THE UNIVERSITY OF MICHIGAN
INDUSTRY PROGRAM OF THE COLLEGE OF ENGINEERING

NUCLEAR DECAY SCHEME ANALYSIS AND CHARACTERIZATION STUDIES OF (d, alpha) REACTION PRODUCTS

Donald Glenn Gardner

This dissertation was submitted in partial fulfillment of the requirements for the degree of Doctor of Philosophy in the University of Michigan, 1957.

May, 1957

IP-220

Doctoral Committee:

Assistant Professor W. Wayne Meinke, Chairman
Professor Philip J. Elving
Associate Professor Peter A. S. Smith
Assistant Professor Milton Tamres
Associate Professor Marcellus L. Wiedenbeck

ACKNOWLEDGEMENTS

The author wishes to express his sincere appreciation for the guidance and encouragement continuously given by Professor W. Wayne Meinke throughout the course of this work.

The many helpful discussions with Professor M. L. Wiedenbeck are especially valued.

The section of this work concerned with the Fourier analysis of radioactive decay curves has benefited from the advice of many persons. In particular, the author is indebted to Professor J. W. Carr III who first suggested that the Fourier approach be tried, and to Professor A. J. Perlis, of the Carnegie Institute of Technology, who aided in many details of the solution. The careful reading and criticism of this section by Dr. B. Galler is appreciated.

It is a pleasure to acknowledge the assistance of Mr. Ronald W. Shideler in the design and construction of the photographic coincidence apparatus, and in the maintenance of the electronic equipment. Thanks are also due to Mrs. Rosemary S. Maddock who assisted in various phases of this work. The cooperation obtained from the crews of the University of Michigan cyclotron, the Argonne National Laboratory cyclotron, and the University of California (at Berkeley) cyclotron is appreciated.

The author is indebted to the U. S. Atomic Energy Commission for partial financial support of this research, and to the Eastman Kodak Company for the receipt of a research fellowship. Both the enriched and radioactive isotopes used in this work were supplied by the Isotopes Division of the U. S. Atomic Energy Commission. Thanks are due to the Industry Program of the College of Engineering for the typing of this manuscript.

Finally, the author is truly grateful to his wife, Jeanne, who made many valuable contributions to all phases of this work related to data analysis and computers, and who painstakingly helped in the preparation of the manuscript.

TABLE OF CONTENTS

TABLE OF CONTENTS (CONT.)

TABLE OF CONTENTS (CONT.)

TABLE OF CONTENTS (CONT.)

LIST OF TABLES

LIST OF TABLES (CONT.)

LIST OF FIGURES

LIST OF FIGURES (CONT.)

LIST OF FIGURES (CONT.)

LIST OF FIGURES (CONT.)

LIST OF FIGURES (CONT.)

ABSTRACT

The objectives of this work were to develop the necessary instrumentation , chemical procedures and aids in data analysis so that nuclear characterization studies of certain (d, α) reaction products could be made.

A study was made to assess the value of a fluorescent plastic detector for use in β-ray spectroscopy. This led to the design, construction and evaluation of a hollow-type scintillation β-ray spectrometer. The performance of the device was evaluated with respect to such aspects as back-scattering from sample backing and sample holder, thick samples, geometry of detector, complex and forbidden spectra, and the useful energy range. A comparison was made with the conventional flat-type scintillator. When corrected for instrument resolution, the hollow-type spectrometer enables β-spectral distributions to be accurately studied down to energies of less than 0.1 Mev. Other instrumentation improvements include a photographic method of obtaining coincidence information.

Existing methods for the analysis of complex radioactive decay curves were studied, and a resolution program was written for the IBM 650 digital computer using the method of weighted least squares. A new method of solution, based on a Fourier analysis, is proposed which seems to have advantages over all previous approaches. Here prior knowledge of the number of components in the decay curve is not needed since it automatically appears in the solution, and the calculation is not endangered by the presence of half-lives of similar value. Regarding β-spectral analysis,

one computer program was written to provide a Kurie analysis, and a second for general linear curve fitting using the method of unweighted least squares.

Characterization studies were made of the isotopes Co^{62}, Y^{92}, Ir^{196}, and Sc^{47} which were produced by the (d, α) reaction in cyclotron-bombarded targets. Isotopically enriched samples were used with the Co^{62} and Ir^{196} studies. Chemical separations were required in all cases, and carrier-free procedures were developed for cobalt, yttrium, and scandium. New decay schemes are proposed for Co^{62} and Y^{92}, and are substantiated by arguments based on nuclear shell structure theory. The previous assignment of an $\sim$ 8-day activity of iridium to Ir^{196} is shown to be incorrect, the activity being due rather to Ir^{189} and Ir^{190}. New γ-ray information is given for Ir^{189} and Ir^{190}, together with excitation functions for the (d, α) reaction on Pt^{194} and Pt^{196} for deuteron energies in the range of 9.6 to 20.4 Mev. The γ-ray information obtained from the scandium work verifies the data reported recently by other workers.

CHAPTER I

INTRODUCTION

The subject fundamental to this work is the analysis of nuclear decay schemes. Basically, a decay scheme is a schematic representation of the decay process which includes the available information concerning the energy levels of the nuclei involved. In some respects, then, the nuclear decay scheme may be compared to the energy level diagrams associated with atomic or extra-nuclear excitation as in the case of the atom or molecule. The quantized excited states in an atom with orbital angular momentum and spin have their analogue in the nucleus, where protons and neutrons are believed to be in somewhat similar energy shells. Even what may be called "rotational" states occur in certain nuclei. As an atom gains energy, the number of available quantum states increases while the energy difference between the higher states decreases until finally ionization is reached. A similar situation occurs in the nucleus, only here the "ionization" would correspond to the loss of a nuclear particle when its binding energy was exceeded.

An isolated excited atom may lose its energy only by the process of photon emission when ionization cannot occur. It is here that the atomic and nuclear cases basically differ. An excited nucleus will also tend to lose its energy by the emission of photons or γ rays. However, under certain conditions, the de-excitation may proceed by particle emission or capture, with the formation of a new element. This new element may or may not be formed in an excited

state. The above radioactive decay will proceed until eventually the ground state of a stable isotope is reached.

The process of decay scheme analysis involves observing the radiation emitted during the decay and deducing properties of the energy levels such as spin and parity in the associated nuclei. In Figure 1 the decay scheme of Co^{60} is given, omitting some of the finer details. Co^{60} is observed to decay by the emission of a 0.3-Mev β ray to an excited state of Ni^{60}, which then drops to the ground state by the emission of two γ rays. The half-life of the β-ray transition is 5.2 years. After the number, energies, and relative intensities of the β-ray and γ-ray transitions have been determined, the data must then be assembled in the form of an energy

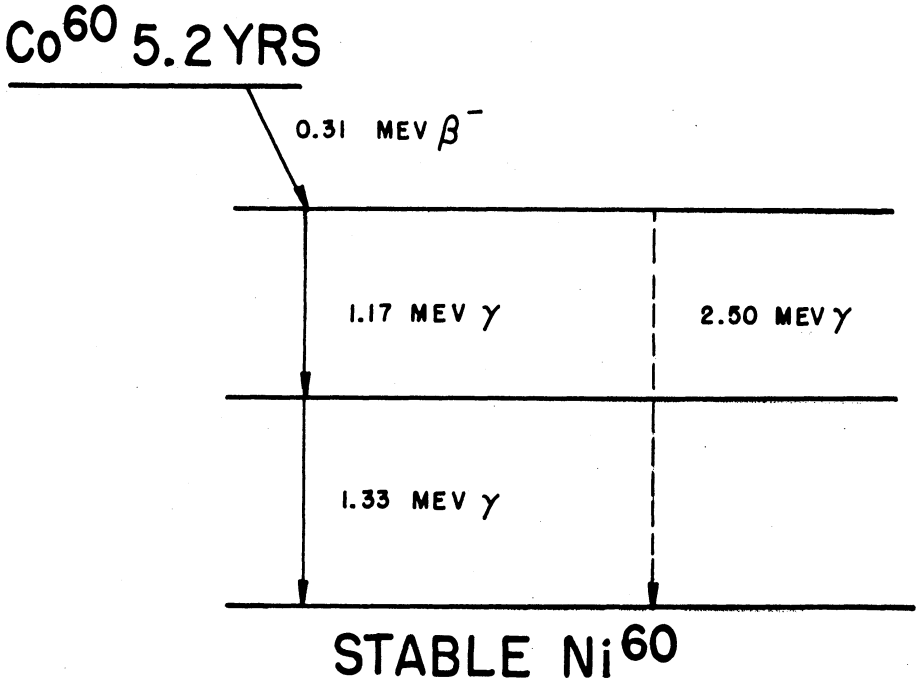

Figure 1. Decay scheme of Co^{60}

level diagram. One technique of value here is called "coincidence" analysis. Using suitable electronic equipment it is possible to determine which radiations produced in a given decay occur simultaneously or "in coincidence," within the resolving time of the equipment. In Figure 1 it would be observed that the β ray and both γ rays were in coincidence. However, if the dotted γ-ray transition could occur, it would only be in coincidence with the β ray. This is because once the second excited state of Ni^{60} has been reached, it may lose energy either by the emission of the 2.50-Mev γ ray or else by the emission of the two lower energy γ rays. In a given decay only one of the two paths may be followed.

Coincidence information is of great value in the construction of decay schemes, but in general other information must be obtained before spin and parity assignments may be made. The term "spin" will be used here to mean total angular momentum. Some other types of information that are a measure of the spin and parity changes are:

1. The half-life and maximum energy of the β-ray transition.

2. The form or "shape" of the β-spectral distribution.

3. The presence of meta-stable or isomeric states that may decay by the γ-ray and/or β-ray emission.

4. The presence of monoenergetic peaks, called conversion electron peaks, in the β-ray distribution.

A great deal of the evidence (91) points to the possibility that the nucleus has, at least in low excitation states, a structure

similar to that of the electrons in an atom. It seems that certain numbers of nucleons produce a more stable nucleus, analogous to the completion of electronic shells. All but one of the isotopes studied here are within $\pm$ 1 nucleon of one of these stable shells. This was done to facilitate the theoretical discussion of each nuclide. Furthermore, all but one of the isotopes contained an odd number of protons and an odd number of neutrons. These "odd-odd" nuclei have been in general less well characterized than other classes of nuclei, primarily because chemical separations are usually required. Finally, odd-odd nuclei are of interest because the arrangement of their energy levels differs on occasion from the arrangement found in other types of nuclei.

The isotopes that were studied were all produced by the (d, α) reaction in the 42-inch cyclotron at the University of Michigan, the Argonne National Laboratory 60-inch cyclotron, or the 60-inch cyclotron located at the University of California at Berkeley. The product nuclei had therefore an atomic number of one less, and a mass number of two less than the target nuclei. The (d, α) reaction, at the energies used here, is a less favorable reaction by a factor of roughly 100 to 1000 than the competing (d, n) and (d, p) reactions. Hence it was necessary to devise a chemical separation procedure in all cases. The investigation was facilitated in two cases by the use of isotopically enriched targets. For example, Co^{62} was produced by the (d, α) reaction on a nickel target. The natural abundance of Ni^{64} is about 1%. With the enriched target this was raised to about 97%, which made possible the study of this isotope's reaction product.

Chemistry has become invaluable in present day nuclear scientific research. In many cases nuclear information cannot be obtained unless a prior chemical separation has been accomplished. The restrictions on the chemical separation are usually quite stringent. Frequently the separation must be rapid, as is obvious when half-lives in the order of minutes are involved. Furthermore, chemical separation factors may be required that are much greater than normally found in analytical chemistry. It is not uncommon to require separation factors of 10^6 or greater from all other elements present. It is here that such techniques as, for example, ion exchange (57, 76) and solvent extraction (29) are used to good advantage. Still further restrictions may be placed on the separation, such as the requirement that no inactive carrier may be used. This is quite common when β-spectral measurements are involved, since any weighable sample will distort the β-ray spectrum to a certain extent. In dealing with such minute amounts of materials as, say, 10^{10} atoms or less, new and interesting chemical problems arise that are not found in the macroscopic case.

The contents of this thesis may be roughly divided into four general classifications, although this division is not adhered to in the text. Separations chemistry is one of these classifications. Carrier-free chemistries with good decontaminations were devised for the studies of Co^{62}, Y^{92}, and Sc^{47}. The chemical separation used to separate iridium from platinum and gold did not need to be carrier-free, since the iridium activity was found to decay by electron capture.

Another category is instrumentation. Much of the equipment used in this work, in particular the two-channel coincidence scintillation spectrometer, has been in use in the nuclear chemistry laboratories of the University of Michigan for several years (20). In many cases, however, it was necessary to modify the previous equipment or to design and construct new devices in order to cope with the specific problems found in this work. One of the new devices is a scintillation β-ray spectrometer whose detector is a specially constructed hollow plastic scintillator. This spectrometer has been thoroughly investigated, and has replaced the older 180° magnetic spectrometer (97) which now finds its best use in separating positron from negatron spectra. Several new scintillation detectors were obtained for γ-ray and x-ray work. As new and better phototubes have become available, these were incorporated into the equipment. A new automatic sweep device was constructed in the laboratory that will, in connection with the count-rate meter and Speedomax strip-chart recorder, continuously scan and record spectra over energy ranges governed by completely variable limits. A photographic coincidence technique was developed to handle short-lived activities.

A third category involves data analysis. In the case of β counting, techniques have progressed far enough so that using 4π proportional counters, essentially every β particle down to energies of the order of 1 kev or less may be detected. Very accurate decay curves are routinely obtained. And yet the half-lives, particularly in the case of complex decay curves, are usually measured graphically. Mention is made of some mathematical methods that have been tried

in the past for analysing decay curves, and a method making use of Fourier analysis is proposed. Due to the size of the problem this method has not been programmed for the IBM 650 computer. An alternative, although admittedly less elegant, method involving a weighted least-squares scheme has been programmed for the IBM 650.

Two computer programs were written for use in the analysis of β-ray spectra. The first is a Kurie analysis program and the second is a simple least-squares program. The latter has been used to determine maximum β-ray energies from Kurie plots, but may also be used for any straight-line curve fitting problem. The Kurie analysis program was considered a necessity in the evaluation of the hollow scintillation β-ray spectrometer since over sixty β spectra were analyzed during the evaluation. Several months would have been required had the analysis been done on a desk calculator, while once the data on a β-ray spectrum has been fed into the computer the computational time required for a thirty-point spectrum is less than one-half minute.

The last category is decay schemes. Using the techniques developed here the decay schemes of Co^{62} and Y^{92} were determined, and are discussed from the point of view of nuclear shell structure. Spin and parity assignments were given to each energy level.

An investigation of an activity previously assigned to Ir^{196} was made using both natural platinum and also platinum enriched in the isotope Pt^{198}. The results showed that the activity did not belong to Ir^{196} but to other iridium isotopes. Excitation functions for the (d, α) reaction on two platinum isotopes were obtained. Finally, a preliminary investigation

of the decay of Sc^{47} was made, although the project was not completed since several excellent studies of this isotope were published while this work was underway.

CHAPTER II

NUCLEAR THEORY

In the following sections, the subjects of nuclear shell structure and β decay are briefly discussed. An understanding of these subjects is vital in the analysis of nuclear decay schemes.

A. Nuclear Shell Structure

The development of the theory of nuclear shell structure must be considered to be only in a formative stage. It is not as yet possible to predict in advance energy levels and spins in any given nuclei. Actually, more experimental evidence must be obtained before the present theory and its modifications may be improved. When used as a guide, the present theory will at least limit the possible choices as to nuclear states, and in some cases will allow unambiguous assignments of spins and parities to be made.

1. The Shell Model of the Nucleus

Since the earliest days of nuclear physics, attempts have been made to detect regularity in the structure of the nucleus analogous to the construction principle and electron catalogue (102) for atomic electrons. The distribution of stable nuclei is shown in Table I with respect to even and odd proton, neutron, and total mass numbers (52).

Table I suggests that like nucleons are paired off with opposite spins. This is further confirmed by the fact that according to all known nuclear spins, nuclides with odd mass numbers have half-integral spins, and nuclides with even mass numbers have integral spins. In particular, nuclides with A and Z both even have zero spin. Binding

TABLE I. DISTRIBUTION OF STABLE NUCLIDES

Mass number, A	Even	Even	Odd	Odd
Proton number, Z	Even	Odd	Even	Odd
Neutron number, N	Even	Odd	Odd	Even
Cases	162	4	55	53

energy considerations also indicate paired nucleons. However, some obvious shape irregularities are found in the binding energy curve at certain proton and neutron numbers. If one goes further, it is possible to correlate additional facts by assuming that the paired nucleons are arranged in shells after the fashion of the planetary electrons. Neutral atoms with electronic configurations of 2, 8, 18, etc. are exceptionally stable, and closed electron shells are spoken of. Atoms with one more or one less electron than that needed to complete a shell are exceptionally active chemically. While in the nuclear case, the effects aren't so dramatic, nuclei with 2, 8, 20, 28, 50, 82, and 126 nucleons of the same kind are particularly stable. These numbers are termed "magic numbers".

A great deal of empirical evidence has been brought forth, particularly by M. G. Mayer, to support the concept of "magic" numbers (40, 52, 88, 90, 91). Several systems have been proposed to predict in a logical way the magic numbers by a proper quantum mechanical treatment usually based on the one-body model. The one by Mayer (89, 90, 91) seems to be the most satisfactory, and will be described qualitatively here. Other treatments (39, 40, 102) including a modification of Mayer's scheme will not be discussed here.

The first assumption is that each nucleon moves in a spherically symmetrical field of force, which is independent of the exact instantaneous position of all of the other nucleons. Since proton and neutron magic numbers are the same, it may also be assumed that the nucleons inside the nucleus retain their individuality to a fair degree. The quantum numbers (n, l, j, m_j) characterize the nuclear orbits, and the corresponding energy levels are filled in succession by neutrons and protons. Proton and neutron shells are separate and are filled independently. Proton and neutron levels with the same quantum numbers do not coincide since the protons are subject to Coulomb forces which shift their levels to higher values. This Coulomb effect may even change the order of the proton levels slightly from that of the neutrons, because the lower l orbits penetrate more deeply and are consequently less favored for the protons.

The nuclear potential differs considerably from the atomic force field, and the nuclear levels have very little correspondence with their atomic analogues. The actual potential lies somewhere between a square-well and a harmonic-oscillator potential. A rough estimate of the level order may be obtained by interpolating between these limits. Since the character of the nuclear forces is essentially unknown, and the level order is greatly dependent upon the potential chosen, there is little use in making exact calculations at this stage. What is done is to try to determine the exact order of the levels from evidence that lead to spin and parity values. Since the parity of the eigenfunctions is $(-1)^l$ it follows that all eigenfunctions belonging to one shell will have the same parity.

The above approximations show that up to N or Z = 20 a wide level spacing occurs beyond the occupation numbers 2, 8, and 20. However, there is no indication of gaps at 28, 50, 82, and 126. Mayer has resolved this difficulty by considering the spin-orbit coupling. In the atomic case, this coupling causes a splitting of the levels $j = \ell \pm 1/2$. This splitting is relatively small compared to the distance between levels of different ℓ. In the nuclear case, however, this coupling has been shown to be quite pronounced (56), and the splitting considerably larger than for electrons. The energy splitting is proportional to $(2\ell + 1)$, and also depends upon the radial quantum number n. Proton scattering experiments show that the level $j = \ell + 1/2$ has a lower energy than the $j = \ell - 1/2$ level, which is reversed in the atomic case. Since the level splitting decreases with increasing n, this means that the split will be the greatest when an angular momentum ℓ appears for the first time. This is precisely where the higher "magic" numbers occur.

Because of the fact that the energy of a given level depends strongly on the way the spin and orbit are aligned, a level must be characterized by its j value as well as its ℓ value. The levels will be filled for both neutrons and protons such that the $2j + 1$ states of $j = \ell + 1/2$ will be filled before the 2ℓ states with $j = \ell - 1/2$. The level sequence proposed by Mayer, with strong spin-orbit coupling is shown in Fig. 2. On the left are the levels first found by extrapolating between the square well and the harmonic oscillator. These are connected by dotted lines to the resultant pairs of split levels. The degeneracy of the level is given in the parentheses,

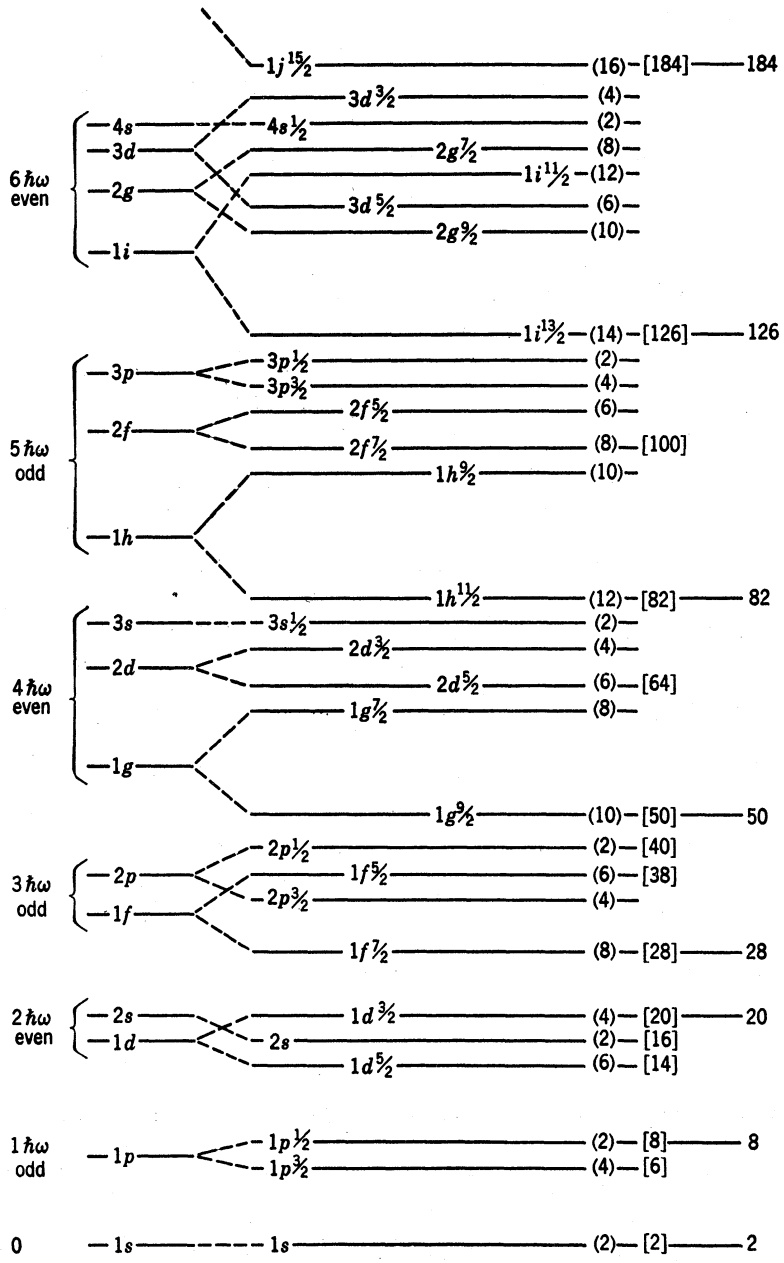

Figure 2. Nuclear Level Sequence Proposed by Mayer

while the total occupation number of all levels up to and including the level under consideration is given in square brackets. It is seen that the nuclear shells are not the same as the oscillator shells because of the coupling. The precise order of the levels cannot be predicted without knowing the precise form of the potential well and the magnitude of the spin-orbit coupling. Furthermore, the order apparently differs slightly for protons and neutrons. The magnitude of the splitting, for the 1g and 1h levels at least, appears to be about 2 Mev.

Essentially then, Mayer (90) proposes that: (1) the succession of energies of single particle orbits is approximately that of a square well with strong spin-orbit coupling giving rise to inverted doublets, (2) for a given ℓ the levels $j = \ell + 1/2$ have invariably lower energy and will be filled before $j = \ell - 1/2$ levels, (3) pairs of spin levels within one shell, which arise from adjacent orbital levels in the square well in such a way that spin-orbit coupling tends to bring their energies closer together can, and very often will, cross, (4) an even number of identical nucleons in any orbit will always couple to give a spin of zero and hence will not contribute to the magnetic moment, and (5) an odd number of identical nucleons in a state j will usually couple to give a total spin of j and a magnetic moment equal to that of a single particle in that state. Very rarely, the total j will be one less than the single particle j.

2. Ground States

In dealing with nuclear ground states the simplest case, other than when both neutron and proton numbers are even, occurs when

there is either one nucleon more or less than a closed shell in odd-A nuclei. Here the spin is due to the odd particle or hole and is just the j value for the level. When there are several neutrons and protons in incompletely filled shells the situation becomes more complex. In order to describe nuclear configurations the terminology of Mayer (91) will be used. The number of neutrons and protons in a level will be denoted by K and λ, respectively. The levels will be designated by the radial quantum number n, orbital angular momentum ℓ, and total angular momentum j, $(n\ell j)$. π will be used for protons and ν for neutrons. For example, $(1d5/2)$ is the first neutron level with orbital angular momentum $\ell = 2$ and parallel intrinsic spin. If there are K neutrons in this state and they couple to give a resultant spin of $\underline{j}$, K and $\underline{j}$ will be used as superscript and subscript. Suppose three neutrons are in the $1d5/2$ level, and the resultant spin is $5/2$, the configuration of the state would be $(\nu 1d5/2)^{3}_{5/2}$. Table II (91) lists the allowed levels of total angular momentum J for populations up to $2j + 1$. For larger populations, the spin states are the same as for $(2j + 1) - K(\lambda)$. If there are π protons as well as ν neutrons in incompletely filled levels, all vector sums are possible:

$$|J\nu - J\pi| \leq J \leq J\nu + J\pi.$$

Mayer (91) states the following rules for ground state coupling:

1. The ground states of all nuclei with an even number of protons and of neutrons have zero angular momentum and even parity.

TABLE II. POSSIBLE TOTAL ANGULAR MOMENTA IN THE CONFIGURATION $(j)^K$ WHERE K EQUALS THE NUMBER OF NUCLEONS IN THE STATE

	j = 3/2
K = 1	3/2
K = 2	0, 2
	j = 5/2
K = 1	5/2
K = 2	0, 2, 4
K = 3	3/2, 5/2, 9/2
	j = 7/2
K = 1	7/2
K = 2	0, 2, 4, 6
K = 3	3/2, 5/2, 7/2, 9/2, 11/2, 15/2
K = 4	0, 2(twice), 4(twice), 5, 6, 8
	j = 9/2
K = 1	11/2
K = 2	0, 2, 4, 6, 8
K = 3	3/2, 5/2, 7/2, 9/2(twice), 11/2, 15/2, 17/2, 21/2
K = 4	0(twice), 2(twice), 3, 4(three times), 5, 6(three times), 7, 8, 9, 10, 12
K = 5	1/2, 3/2, 5/2(twice), 7/2(twice), 9/2(three times), 11/2 (twice), 13/2(twice), 15/2(twice), 17/2(twice), 19/2, 21/2, 25/2

2. In nuclei consisting of an even number of one type of nucleon, the ground state properties are determined by the odd type nucleons alone.

3. In a nucleus of odd-A, the nucleon of the type which is present in odd number will usually couple so that the total angular momentum is that of the last partially filled orbit, j. Occasionally, $J = j - 1$ is encountered.

Rule 1 implies that pairs of nucleons with zero angular momentum are energetically favored. This means that the binding energy of the nucleus is increased by an amount P for each such pair. It has been observed that this "pairing energy" P increases with increasing j. When closely adjacent levels with different j values occur, the sequence of filling of these levels may be greatly affected by the difference in pairing energies for the two levels.

Odd-A nuclei have been of prime importance in evaluating the shell theory presented above. That such a simple picture should be surprisingly accurate is attested to by the following facts. There are 101 odd-A nuclei with N or Z less than 84, and with experimentally determined spins. Of these, 93 fit the theory perfectly, 4 have spins of 1 less than the orbit of the last particle, and 4 show minor irregularities in the level order. In the same Z or N range there are 89 entries of data on magnetic moments. In 86 cases the magnetic moments agree with prediction, 2 are ambiguous, and 1 is a definite contradiction. Thus, for odd-A nuclei in which the odd nucleon is less than the 84 of its kind, the ground state characteristics are very nicely predicted by the shell model.

3. Excited States

It is not in general possible to predict the energy of excited nuclear states from shell theory alone. In a great many cases, spin predictions must be considered only as tentative, particularly in the higher excited states. However, in certain cases, shell theory can be used to limit at least the possible spin choices for a given state, and occasionally to give definite assignments. When experimental evidence such as beta decay, angular correlation, and/or conversion coefficient information is available, then spin and parity assignments of a more concrete nature may be made.

One correlation of the excited states of even-even nuclei is called the "interval rule." This rule states that for nuclei with easily deformable cores, the lowest excited states will be due to intrinsic nuclear distortions similar to rotating surface waves. These states will all have even parity and carry an angular momentum $J = 2$ in the first, $J = 4$ in the second, and $J = 6$ in the third excited states. The corresponding energies will be a function of the J values as follows:

$$E \propto J(J + 1)$$

For most nuclei where the cores are not easily deformable the single-particle excitations and energy splitting for different couplings are smaller than the states of rotating surface distortions, and such states are hard to identify among the lower excitation states of even-even nuclei.

In systems of "mirror" nuclei, that is, in pairs of nuclei such as ${}_5B_6^{11}$ - ${}_6C_5^{11}$ which differ only in an exchange of proton and

neutron numbers, the level systems are expected to be similar. This is because the forces between proton pairs and neutron pairs are the same (as a first approximation).

When all of one type of nucleon are in closed levels and the other nucleons are in an incompletely filled level, the lower excited states will be due to the latter type of nucleons. The available spin states are listed in Table II. For odd-A nuclei the order of these states with respect to increasing energy cannot be obtained from the table.

For even-even nuclei, the first excited state is almost always 2+, that is, J = 2 and even parity. In fact, out of 69 known cases there are only 3 exceptions to this rule. The second excited state is also 2+ in about 1/3 of the cases, 4+ in another third, and the remaining third have various spins and occasionally odd parity. If the excited states arise from the same configuration as the ground state they must have the same parity, namely even. When both the proton and the neutron levels are completely filled the excited states arise from the promotion of one or more nucleons to a higher level. In this case, states of odd parity can occur. In a paper by Scharff-Goldhaber (123) the energies of the first excited states of even-even nuclei are plotted against the number of neutrons or abscissa. General trends, such as low excitation energies when both proton and neutron numbers are in the middle between two magic numbers, may be obtained from this curve. Another fact concerning even-even nuclei with incompletely filled shells is that there is always at least one excited state with J = 2, both for protons and neutrons, and often more than one.

Odd-odd nuclei present a very complicated case. Here both the proton and neutron shells have spins which couple together. The parity of the state is even if the values j_n and j_p are either both even or both odd. If one is odd and the other even, then the parity is odd. In excited states, j_n and j_p may change in accordance with Table II. The new j values may then couple vectorally $|j_n - j_p| \leq J \leq j_n + j_p$. Nordheim (103) has formulated two rules for coupling in odd-odd nuclear ground states. These are:

1. If both proton and neutron are in levels in which intrinsic spin and orbital angular momentum are parallel, as in $j_n = \ell_n + 1/2$, $j_p = \ell_p + 1/2$, or if both are in levels where $j_n = \ell_n - 1/2$ $j_p = \ell_p - 1/2$, then j_n and j_p tend to add but not necessarily to the highest value $J = j_n + j_p$.

2. If one of the nucleons is in a level with intrinsic spin and orbital angular momentum parallel and the other in an anti-parallel level, that is, $j_n = \ell_n + 1/2$, $j_p = \ell_p - 1/2$, or $j_n = \ell_n - 1/2$, $j_p = \ell_p + 1/2$, then the total angular momentum of the ground state is the smallest possible one, $J = |j_n - j_p|$.

These rules are not as successful when applied to excited states, as they are in ground state predictions.

Another complicating fact associated with excited states of odd-odd nuclei is that the order of adjacent levels may not be exactly the same as in odd-A nuclei. When there is one proton and one neutron hole in the same level, j (except $j = 1/2$), they will couple to give a $J = 2j - 1$ or 1 less than the maximum. In the case where the last nucleon of one type is an S 1/2 level one expects to find an excited

level close to the ground state. This is because the S 1/2 nucleon's spin can only be added or subtracted from the angular momentum of the configuration of the other nucleons, and it is generally assumed that the spin-dependent forces are only about 20% of the total forces.

4. Shell Structure and Beta Decay

Information derived from the study of β spectra is of great value both in testing the theory of shell structure and also in gaining information about levels where shell predictions are ambiguous. Mayer (91) lists 200 cases of β decay from odd-A nuclei. Only 2 of these transitions definitely do not agree with shell model predictions. In the complicated case of odd-odd nuclei little direct experimental evidence is available concerning spins and parities since all but four of these nuclei are unstable. Beta-spectral analysis, however, can give information concerning the spin and parity change that occurred during the β transitions. When this information is combined with the γ-decay data of the even-even daughter, in many cases the odd-odd ground state properties may be deduced. A discussion of the theory of β decay is given in the following section.

B. Beta Decay

There are several types of radioactive decay which are classified as β processes. These are (1) negatron emission, (2) positron emission, and (3) orbital electron capture. Positron and negatron emission may be represented by

$$Z^A \rightarrow (Z \pm 1)^A + e^{\mp} + \nu \qquad (1)$$

and orbital electron capture by

$$Z^A + e^- \rightarrow (Z - 1)^A + \nu \qquad (2)$$

where ν represents the possibility of accompanying neutral particles.

One of the first difficulties encountered in the theory of β decay was that unlike α and γ rays the electrons seemed to be emitted in a continuum of energy states from zero to a maximum energy. This would indicate that the total energy of the system was not being conserved. This, along with the fact that linear momentum, angular momentum, and statistics (130) were also not being conserved, lead Pauli in 1927 (52) to postulate a new particle, the neutrino, with the following characteristics: (1) very small or zero rest mass, (2) spin of 1/2, (3) obeys Fermi statistics, and (4) no charge. It is then the simultaneous emission of the β particle and neutrino, both sharing the available energy, which produces the continuous β-ray spectra.

In 1934 Fermi set forth his theory of β emission. This theory, set up in direct analogy to the Dirac theory of γ emission, predicts the shape of the β spectrum and a relationship between the maximum energy and the half-life. In it, Fermi postulated an interaction between the initial and final nucleus and the electron-neutrino field, analogous to the coupling between an atom and its electromagnetic field wherein photons are created. The electrons and neutrinos do not exist in the nucleus any more than photons are thought to exist in excited atoms. Both are created during the emission process. This type of interaction seems to apply not only to β decay but to all known types of processes involving fermions. The known fermions

are: the nucleon (N or P), the electron ($e^{\pm}$), the neutrino (ν), and the mu meson ($\mu^{\pm}$).

A derivation of the equation for the momentum distribution of a β spectrum will not be given here since it is available in several references (12, 75, 128). However, neglecting for the moment the Coulomb interaction between the emitted β particle and the residual nucleus, the momentum distribution of the β particles can be shown to be

$$N(p)dp \propto p^2(E_o - E)^2 dp \qquad (3)$$

where E_o is the maximum energy of the transition. This expression qualitatively describes the shape of observed β-ray spectra. A plot of this expression is given in Figure 3.

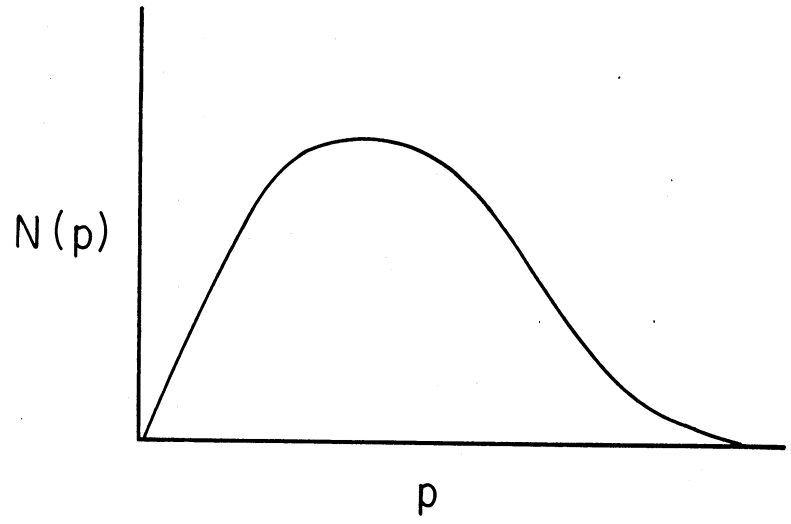

Figure 3. Shape of momentum distribution for beta particles

For large momenta $N(p)dp$ is proportional to $(E_o - E_o)^2$, for small momenta it is proportional to p^2. The distribution vanishes at both limits and has a maximum in the middle.

So far we have ignored the Coulomb force between the β particle and the daughter nucleus. This force can only be neglected for the lightest nuclei, and high electron energies. The effect of the force is simply to accelerate the positive electrons and to decelerate the negative ones. Hence, the spectrum of a positron emitter will show relatively few slow particles, while the negatron spectrum shows more slow particles than it would in the absence of the Coulomb effect. An approximate expression for $F(Z, E)$, the Coulomb correction factor is

$$F(Z, E) \approx \frac{2\pi\eta}{1 - e^{-2\pi\eta}} \qquad (4)$$

where

$$\eta = \pm \frac{Ze^2}{\hbar v} \quad \text{and} \qquad (5)$$

v = Velocity

The upper sign in η is for negatrons, and the lower for positrons. This is given in Reference 12 and was obtained by treating the electon non-relativistically.

The relativistic treatment is also given, but the simple form of the above expression shows more clearly how $F(Z, E)$ varies with energy. With no Coulomb force the momentum distribution is proportional to p^2 at low energies. For negatron emission with low momenta, $F(Z, E)$ becomes inversely proportional to p, and the distribution is proportional

to p rather than p^2. For positron emission F(Z, E) becomes proportional to $\frac{1}{p} e^{-c/p}$ (c is a constant), and the distribution is proportional to $pe^{-c/p}$. It is seen then that the positron spectrum drops to zero much faster than the negatron spectrum. At high energies and low Z, where η is small and changes slowly with energy, F(Z, E) becomes more like a constant and doesn't affect the shape of the spectrum as much.

We now have the relationship

$$N(p)dp \propto F(Z, E)p^2(E_o - E)^2dp \qquad (6)$$

1. Forbidden Transitions and Selection Rules

Consider a nuclear factor represented by the symbol $[M^2]$ This is a sum of terms, some of which are energy dependent and others are not. Whether $[M^2]$ is a function of energy depends on the magnitude of the various terms.

Let the orbital angular momentum of the electron and neutrino be ℓ_e and ℓ_ν, respectively. Now the wave function ψ_e for an electron emitted with a wave number $k_e = P_e/h$ and orbital angular momentum ℓ_e is proportional to $(k_e r_e)^{\ell_e}$ for small distances r_e from the center of the nucleus. It would appear then that ψ_e at the center of the nucleus would vanish except when $\ell_e = 0$.

The same holds for the neutrino. If the above approximations were true, then only electrons and neutrinos with zero orbital angular momenta would be emitted. Actually, the particles may be emitted with ℓ_e and ℓ_ν different from zero; however, the probability for such emission is much smaller. Therefore, transitions where $\ell_e = \ell_\nu = 0$ are called

"allowed" transitions. "Forbidden" transitions are those where one or both of the particles have $\ell \neq 0$.

Both the neutrino and the electron have spins of 1/2. These may combine to give a total spin of 0 or 1. As the orbital angular momentum carried off during emission is zero for allowed transitions, the change in the total angular momentum ΔJ may be 0 or $\pm$ 1. The parity of the system is determined by the sum of the individual ℓ's and is even if L is even and odd if L is odd. It follows that for allowed transitions there is no change in parity. Selection rules for some β transitions are given below.

TABLE III. SELECTION RULES IN BETA DECAY

Transition	Parity Change	ΔJ = "Spin" Change
Allowed	no	0, 1
1st Forbidden	yes	0, 1, 2
2nd Forbidden	no	2, 3
3rd Forbidden	yes	3, 4

For allowed transitions $[M^2]$ is approximately equal to one and independent of energy. Each successive degree of forbiddenness decreases $[M^2]$ by at least a factor of 100. In forbidden transitions $[M^2]$ is usually a function of energy, but many cases are known in which $[M^2]$ varies only slightly.

Thus, we are lead to the result:

$$N(p)dp \propto F(Z, E)p^2(E_o - E)^2[M^2]dp \qquad (7)$$

The spectrometer to be described in a later section measures energy (E) rather than momentum (p), and so it is convenient to rewrite equation (7) in terms of energy. Instead of using E which is measured in terms of Mev (million electron volts), it is more convenient to use the term W in relativistic or rest mass units. See Appendix B.

Here
$$W = \frac{E}{mc^2} + 1 \qquad (8)$$

where mc^2 is the rest mass of the electron. Therefore,

$$N(W)dW \propto pW(W_o - W)^2F(Z, W)[M^2]dW \qquad (9)$$

In general, forbidden transitions are difficult to study because of the complexity of the factor $[M^2]$. There is, however, one class of forbidden spectra which may be analyzed rather easily. These are said to be "unique" forbidden spectra, and occur when the spin change is $\Delta J = n + 1$, where n is the order of forbiddenness. These spectra were theoretically predicted to be unique since only one nuclear matrix element fails to vanish. In this case $[M^2]$ can be represented by the shape factor $\alpha_n(W)$ where n is again the order of forbiddenness. The three shape factors for first, second, and third forbidden spectra are listed below.

TABLE IV. UNIQUE SHAPE FACTORS

$\alpha_1(W) = (W^2 - 1) + (W_o - W)^2$
$\alpha_2(W) = (W^2 - 1)^2 + (W_o - W)^4 + 10/3(W^3 - 1)(W_o - W)^2$
$\alpha_3(W) = (W^2 - 1)^3 + (W_o - W)^6 + 7(W^2 - 1)(W_o - W)^2[(W^2 - 1) + (W_o - W)^2]$

2. Kurie Plots

Referring to equation (9) it may be seen that in the case of allowed transitions where $[M^2]$ is close to unity and independent of energy,

$$\left[\frac{N(W)}{pWF(Z, W)}\right]^{1/2} \propto W_o - W \qquad (10)$$

If the observed energy spectrum is used to compute $\left[\frac{N(W)}{pWF(Z, W)}\right]^{1/2}$ which is then plotted against W, an allowed spectrum will yield a straight line intersecting the abscissa at W_o. This plot is referred to as a Kurie plot after the author who suggested this method of analysis (80). Tables of pWF(Z, W), called the Fermi function, are available from the National Bureau of Standards (99). The Fermi function must be corrected for the effect of the outer atomic electrons, but this may be done using Table 6 of Reference 99. A necessary parameter is the "outer screening potential," V_o, which is available from Figure 13 of the same article. The effect of the screening correction is to reduce the value of the Fermi function for β^- particles, since the energy of the negative β particles which must penetrate the outer screen of electrons is not as high as it would have been in the absence of the screen. Conversely, a positron would have a higher kinetic energy. The beauty of the Kurie representation is that the end-point value need not be known.

Because the more accurately determinable points in the body of the spectrum may be used in a linear extrapolation to give the value at E_{max}, it is not necessary to experimentally determine points in the

low counting rate region near E_{max}. The plot is also a simple means of testing a spectrum to see if it has the allowed shape.

The presence of more than one group of β rays can sometimes be recognized immediately from the shape of the spectrum, as in the case of Sr^{90} - Y^{90}. More frequently it is only by means of a Kurie analysis that the presence of more than one group will be recognized. Since an allowed Kurie plot is linear, a straight-line extrapolation of the highest energy group can be made. This is subtracted from the total curve, just as one resolves half-lives in the case of complex decay curves, and a new Kurie plot made from the difference. Since the number of electrons in each group is proportional to the area under each straight-line curve, one can easily obtain the relative abundance of each β-ray group. Because of the errors involved in the subtraction procedure, the shapes of the lower energy components may be inconclusive. More accurate information concerning the lower groups may sometimes be obtained using coincidence methods.

Where forbidden transitions are involved, one must have information on the factor $[M^2]$. If this can be obtained, as in the case of unique transitions, the corrected Kurie plot may be obtained by dividing the uncorrected plot by $[M^2]^{1/2}$.

Kurie plots will all show an upward curvature at the low energy end due to source thickness, scattering from the backing material, etc. Still, if the spectrum does not contain lower energy groups there will be an appreciable straight section. If there is not, then this is a strong indication that the transition is forbidden. Merely because the Kurie plot is straight does not, however, mean that the transition

is allowed. For example, most first forbidden spectra show allowed shapes. In fact, until 1949, all β spectra investigated appeared to have an allowed shape except that of RaE. This is because the energy dependent terms are overshadowed by large energy-independent terms. All second and third forbidden spectra so far measured have shapes that differ from the allowed shape. If the Kurie plot is straight, the selection rules for allowed transititions fulfilled, and/or a function called log ft (to be discussed in the next section) is in the allowed range, one would conclude that the transition is allowed.

3. Comparative Half-life

Another item of interest is called the "comparative half-life." If the equation for the energy distribution is integrated from zero to the maximum energy, one obtains the total probability per unit time that a β-active nucleus will decay. This probability defines the half-life.

β^- decay probability

$$\lambda = \frac{\ln 2}{t_{1/2}} = \int_1^{W_o} N(W)dW \; \alpha \; f_-(Z, W_o)$$

where

$$f_-(Z, W_o) = \int_1^{W_o} F(Z, W)pW(W_o - W)^2[M^2]dW \qquad (11)$$

Thus, $f_-(Z, W_o)$ times $t_{1/2}$, or simply "ft," is a constant of the disintegration. The value of ft is characteristic of the type of transition, i.e. allowed transitions have a value of ft smaller than the 1st forbidden transitions, and so on. Since the values of ft for known transitions are large and tend to scatter, what is usually done is to compare $\log_{10}(ft)$ values. It is found that there are no distinct separations

between the various orders of forbiddenness, only trends as is shown below in Table V.

TABLE V. LOG(ft) RANGES FOR BETA TRANSITIONS

Transition	Log ft
Supperallowed	3.0 - 3.7
Allowed	4.4 - 5.9
1st Forbidden	$\sim$ 7
2nd Forbidden	8.0 - 11.0

The "superallowed" transitions are a favored case, as in transitions between "mirror" nuclei. In spite of the fact that the ranges overlap, log ft values are of use in characterizing transitions if other information such as parity change or spectral shape are known. The values of $f(Z, W_o)$ have been extensively tabulated by Feenberg and Trigg (41).

CHAPTER III

GAMMA SPECTRAL ANALYSIS

When a γ ray passes through a substance it may lose its energy by three processes:

1. Photo-electric effect. The entire energy of the γ ray is given to an electron in the substance, causing ionization.

2. Compton scattering. Here the initial γ ray gives only part of its energy to an electron, and the secondary, lower energy γ ray is scattered from the point of collision.

3. Pair-production. When the initial γ-ray energy exceeds 1.02 Mev the creation of a positron-negatron pair may take place.

If the substance struck by the γ rays is fluorescent, such as a Tl activated NaI crystal, then the light out-put is a measure of the γ-ray energy. It is most convenient to use the monoenergetic peak caused by the photoelectric effect, since here the light intensity is directly proportional to the γ-ray energy.

In the Compton scattering case, the energy of the secondary γ ray is a function of the energy of the primary γ ray and the photon scattering angle. Therefore, the energy transferred to the substance will vary continuously from 0 to a maximum energy, known as the Compton edge, where the photon scattering angle is 180°. The resulting γ-ray spectrum will then appear as a continuous distribution from 0 to the Compton edge followed by the photo-electric peak.

The relative intensities of γ rays were determined by integrating under the respective photo-peaks. Due to the fact that the

absorption coefficient for the photo-electric process is dependent upon the energy of the incident γ ray, the size of the detector, and atomic number of the atoms in the detector, a correction must be made on the measured relative intensities. McLaughlin and O'Kelly (92) discuss how the correction should be made.

The application of the methods of coincidence counting to experiments in nuclear physics has been described by Dunworth (37), Wiedenbeck and Chu (147) and others (85, 98), and so this subject will not be discussed here.

A. Scintillation Coincidence Spectrometer

The dual channel scintillation coincidence spectrometer used in this work is a slight modification of the apparatus originally built and described by W. A. Cassatt (20). An overall block diagram of the system is shown in Figure 4, while a photograph of the spectrometer appears in Figure 5.

1. Components

a. Scintillation Detectors. Three sodium iodide, thallium-activated scintillation detectors are available for use with γ rays. The crystals are right circular cylinders 1-1/2" in diameter by 1" thick mounted in hermetically-sealed aluminum housings, using magnesium oxide as a light reflector. One of these detectors was purchased already assembled from Harshaw Chemical Company, Cleveland, Ohio. The other two had been purchased in rough form from Harshaw and polished and assembled by Cassatt. One of the latter two detectors was remounted by the author when the crystal lost its optical coupling with the glass window cemented

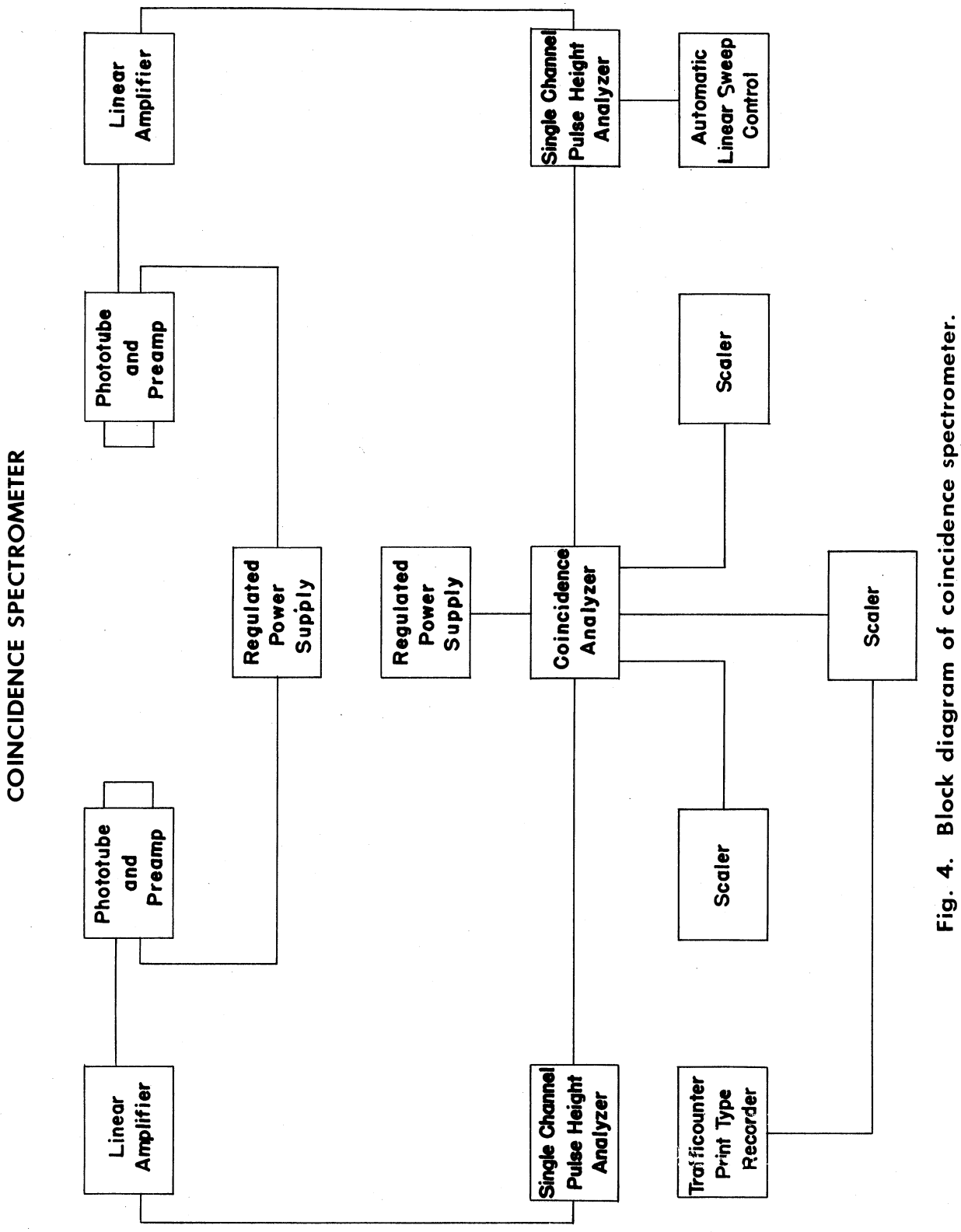

Fig. 4. Block diagram of coincidence spectrometer.

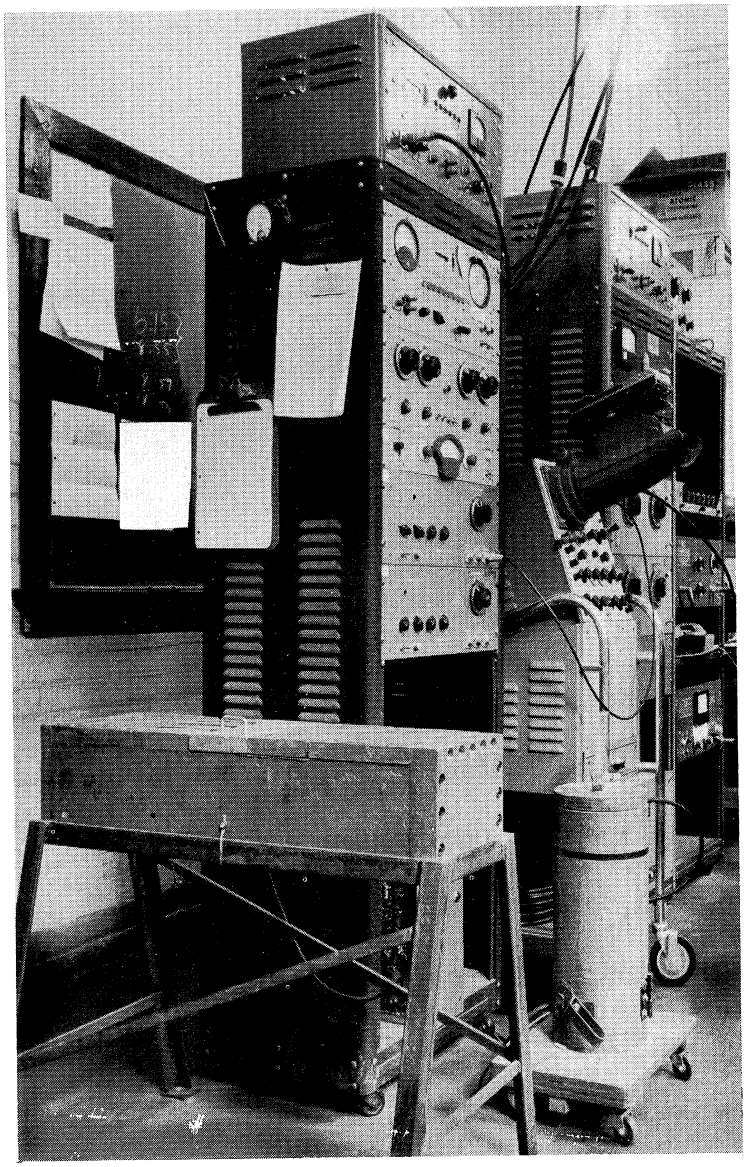

Figure 5. Scintillation Coincidence Spectrometer

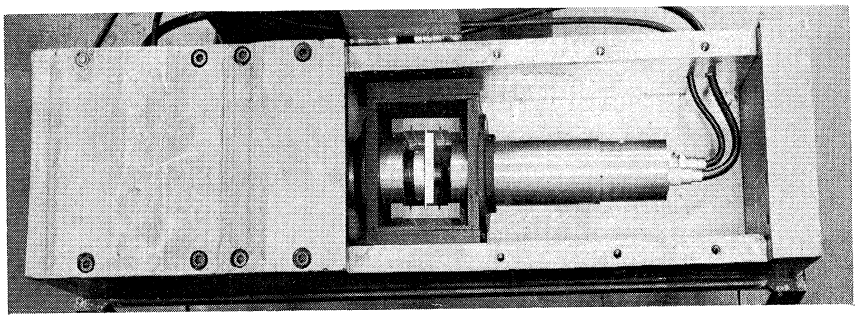

Figure 6. Photomultiplier and Detector in Lead Housing

to one end of the aluminum housing. For details on polishing and mounting crystals see Reference 20.

One x-ray detector was obtained in assembled form from National Radiac, Inc., Newark, New Jersey. This consists of a thin slice of thallium-activated sodium-iodide crystal in the form of a right circular cylinder 1-1/2" in diameter by 2 mm thick. It is thin enough to be reasonably transparent to γ rays and yet thick enough for use with x-rays.

Several different β-scintillation detectors are available. One is a 3/16" thick by 1-1/2" diameter trans-stilbene crystal. Others are flat cylinders of Sintilon-brand plastic scintillator manufactured by National Radiac. These are available in several diameters and thicknesses. One type of specially constructed plastic β-ray detector will be described in detail in a later section.

A detector is connected to the spectrometer by optically coupling it to the flat photocathode of a Dumont 6292 multiplier-phototube with Dow-Corning 200 silicone fluid. A mu metal shield is then placed around the phototube to reduce the effects of magnetic fields, and the phototube is enclosed in a light tight housing which also contains a cathode follower preamplifier. A lead enclosure houses two such detector-preamplifier units placed at 180° to each other. Figure 6 shows the detector arrangement, while Figure 7 is the preamplifier schematic. Low voltage is supplied to the preamplifiers from the linear amplifiers.

b. <u>High Voltage Power Supply</u>. High voltage is supplied to the preamplifiers by an Atomic Model 312 Superstable High Voltage Power

VOLTAGE DIVIDER AND PREAMPLIFIER CIRCUIT

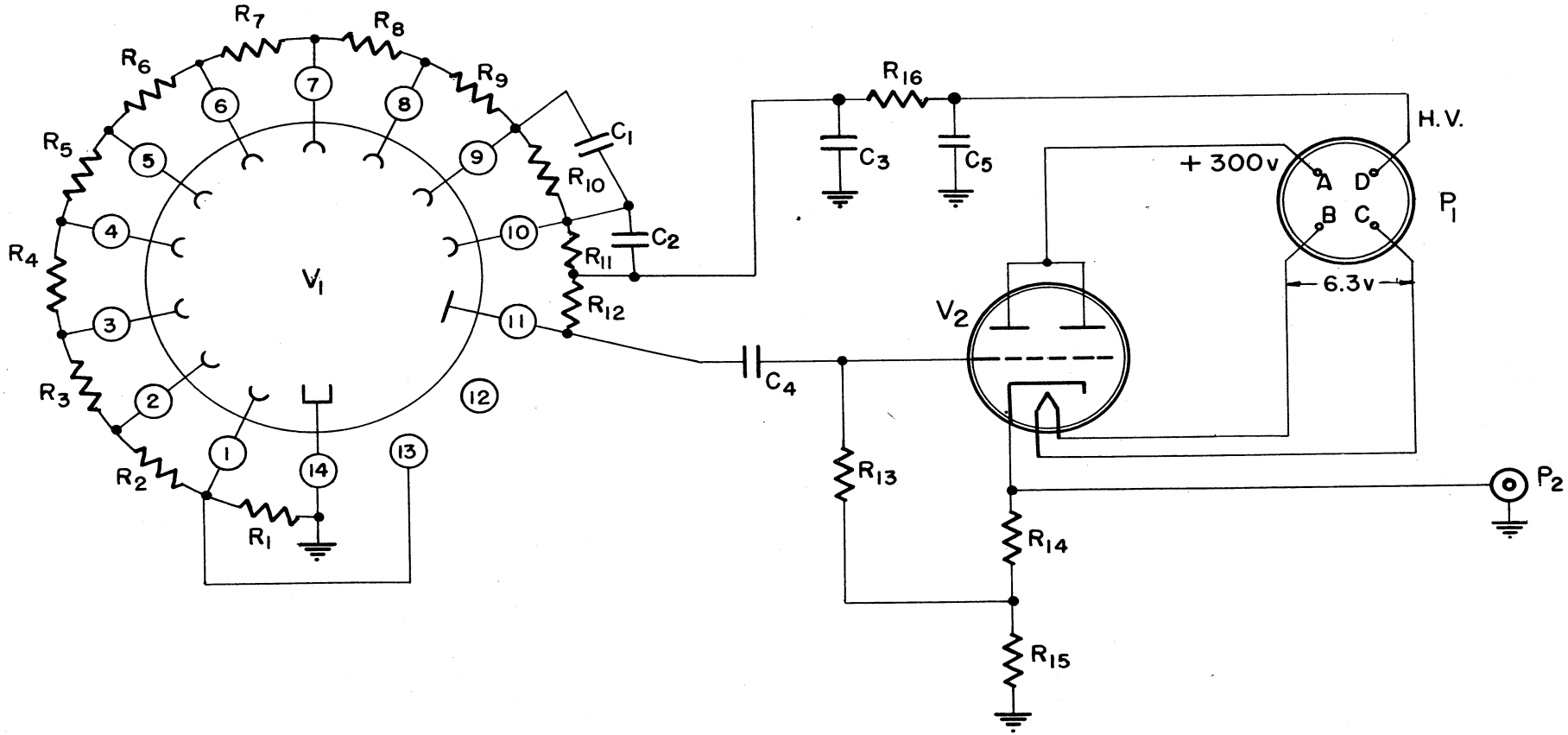

R_1 = 2.2 Meg, 1/4 w
R_2 - R_{12} = 1 Meg, 1/4 w
R_{13} = 1 Meg, 1/4 w
R_{14} = 4.7 K, 1 w
R_{15} = 30 K, 1/2 w
R_{16} = 1 Meg, 1/4 w

C_1 = .001, 600 v
C_2 = .001, 600 v
C_3 = .05, 1600 v
C_4 = .001, 3500 v MICA
C_5 = .05, 1600 v

V_1 = Dumont 6292
V_2 = 6J6
P_1 = Amphenol AN 3102-145-25
P_2 = Amphenol 831R

Figure 7. Scintillation detector preamplifier and photomultiplier voltage divider

Supply. This replaces the power supply originally constructed for the spectrometer. The new power supply has increased the resolution of the spectrometer by reducing the ripple in the output, and shows much better resistance to variations in line voltage and long-time drift. In normal operation a potential of 830 volts is used. Since the gain of a photomultiplier is very sensitive to variations in voltage a Sorensen Model 2000S voltage regulator is used between the power supply and the 110 a.c. line. This particular regulator is a saturable reactor type, and gives a regulation accuracy of ± 0.1% over an input range of 95 to 130 volts. Most of the other units of the spectrometer also have their power supplied by the Sorensen.

c. Linear Amplifiers. The linear amplifiers are both Atomic's Model 204B. The gain may be varied from 3,500 to 15,000 by means of a course and a fine gain control. The original variable controls were replaced by two 11-position step switches for the sake of better reproducibility.

d. Pulse-Height Analyzers. The single-channel differential pulse-height analyzers are Atomic's Model 510. Ten turn heliopots are provided for setting the base-line descriminator from 0 to 100 volts, and for setting the channel width from 0 to 7 volts. At a window setting of more than 7 volts there is no upper limit to the window, and consequently all input pulses larger than the base line setting will produce an output pulse.

The analyzers have been modified so that the base-line height can be varied either manually or by an automatic sweep mechanism. A new sweep drive has been constructed which will allow a spectrum to be swept

continuously, back and forth while a "slide-rule" dial indicates the position of the sweep at all times. Finally, the positions of the reversing switches are completely variable so that any given portion of the spectrum may be scanned at any of five different sweep speeds. In addition, a step sweep is provided which will advance the base line in discrete steps. A preset counter will advance the step sweep mechanism upon the accumulation of a given number of counts from the single-channel analyzer.

e. Count-Rate Meter. The count-rate meter, used in connection with the linear sweep, receives its pulses from the pulse height analyzers. The output of the meter is fed directly into the chart recorder. A selection of eight linear scales ranging in full scale counting rates from 100 to 20,000 counts-per-minute, and four values of the charging condenser from 1 to 16 microfarad are available. A 7,200 counts-per-minute pulse generator is built in for calibration purposes, and a meter in the output circuit may be used for visual monitoring.

f. Recorder. A Leeds and Northrup # 60352-M02-191-Spec Model S Speedomax, four point, printing chart recorder with a 10 millivolt full scale sensitivity is used. Other features include: multi-color printing, dots only; strip chart tear-off device without indices; three seconds per point with two second balancing speed; and a standard cell against which the instrument automatically calibrates itself periodically. The recorder is connected so that during a measurement every fourth dot printed indicates the baseline voltage. The other three dots record the output of the counting-rate meter.

g. Oscilloscope. The Tetronix scope Model 514D is used. The scope is provided with a blanking circuit which cuts off the trace except when a pulse is being viewed. This prevents an objectionable spot from appearing at the zero position of the trace between pulses.

h. Cameras. Two cameras are available. The first is a DuMont Model 295 Polaroid Land Camera. With it oscilloscope pulse traces can be photographed directly. When suitably calibrated, the picture may be measured to determine γ-ray energies (35). By means of a sweep expander and a neutral gray wedge filter (10, 22, 122) the relative intensities of the γ rays may be determined. Due to the relatively low contrast of polaroid film, a DuMont 35 mm oscillograph camera is sometimes substituted for the Polaroid Land Camera. Kodak Linagraph Ortho film is used for these pictures. The Land Camera is very good for taking rapid survey pictures, since the finished positives are ready one minute after exposure.

i. Coincidence Analyzer. The two twin single channels, each consisting of detector, preamplifier, linear amplifier, and pulse-height analyzer, are connected to an Atomic Model 502A coincidence analyzer. Actually, the instrument has four input channels. Any combination of the channels may be operated in coincidence, or any set of the other three channels may be used in anticoincidence with channel one. The resolving time of each channel may be set at 1/4, 1/2, 1, or 2 microseconds. In normal use coincidences are sought between certain pulses appearing in one detector and the entire spectrum, scanned in discrete steps, as it appears in the other detector. β-γ or γ-γ coincidences are observed with the proper choice of detector and

absorbers. When pulses generated in each detector arrive at the coincidence analyzer within the resolving time of the instrument, an output "coincidence" pulse is obtained.

j. Scaler. The gross output of each channel, along with the coincidence output, is fed to a specially constructed three-channel scaler. The scaler was built by Radiation Instrument Development Laboratory, Chicago, Illinois, especially to fit our need. Each scaler channel has a scale of 100, composed of Berkeley decimal counting units, and an electric reset mechanical register. Provision has also been made for making the pulses from the scale-of-100 decimal stage available at the rear of the scaler.

2. Calibration of Spectrometer

The coincidence spectrometer was checked for linearity and calibrated in the usual manner using radioactive samples emitting γ rays of known energy. Some of these sources and their energies are shown in Table VI.

TABLE VI. GAMMA-RAY CALIBRATION SOURCES

Source	Principle γ-Ray Lines (Mev)
In^{114}	0.190
Cr^{51}	0.32
Sn^{113}	0.394
Cs^{137}	0.662
Zn^{65}	1.12
Co^{60}	1.17, 1.33

Two typical γ-ray sweeps and pictures are shown in Figures 8 and 9 for Cs^{137} and Co^{60}, respectively.

The coincidence apparatus was checked using isotopes with known decay schemes such as Cs^{137} and Co^{60}. The resolving times were checked by the method described by Bleuler and Goldsmith (13), and found to agree with the dial readings within experimental error.

B. Photographic Coincidence Method

When it is necessary to obtain coincidence data on short-lived materials, and when multichannel pulse-height analyzers are not available, some type of photographic technique is generally used. A point-by-point manual sweep of the coincidence spectrum would necessarily take many half-lives to complete if good statistical results were to be achieved. A photographic method, on the other hand, is much faster since an entire spectrum may be viewed at one time for coincidences with the other channel, rather than only a narrow window width which sweeps the spectrum in discrete steps. Also, since all parts of the spectrum are viewed simultaneously, no correction for decay is necessary when relative peak intensities are to be measured.

Several photographic methods have been described in the past (10, 18, 22, 33, 49, 67, 122). Some of these require motion picture cameras, while others require specially modified oscilliscopes. All require additional circuitry of various degrees of complexity to produce the desired results. The photographic method described here requires a minimum of additional circuitry, is simple to construct and operate, and is easily adaptable to Gray-Wedge analysis (see Section 1Bh on Cameras). The results are simple to interpret since the coincidence spectrum may be directly compared to the total or "single" spectrum.

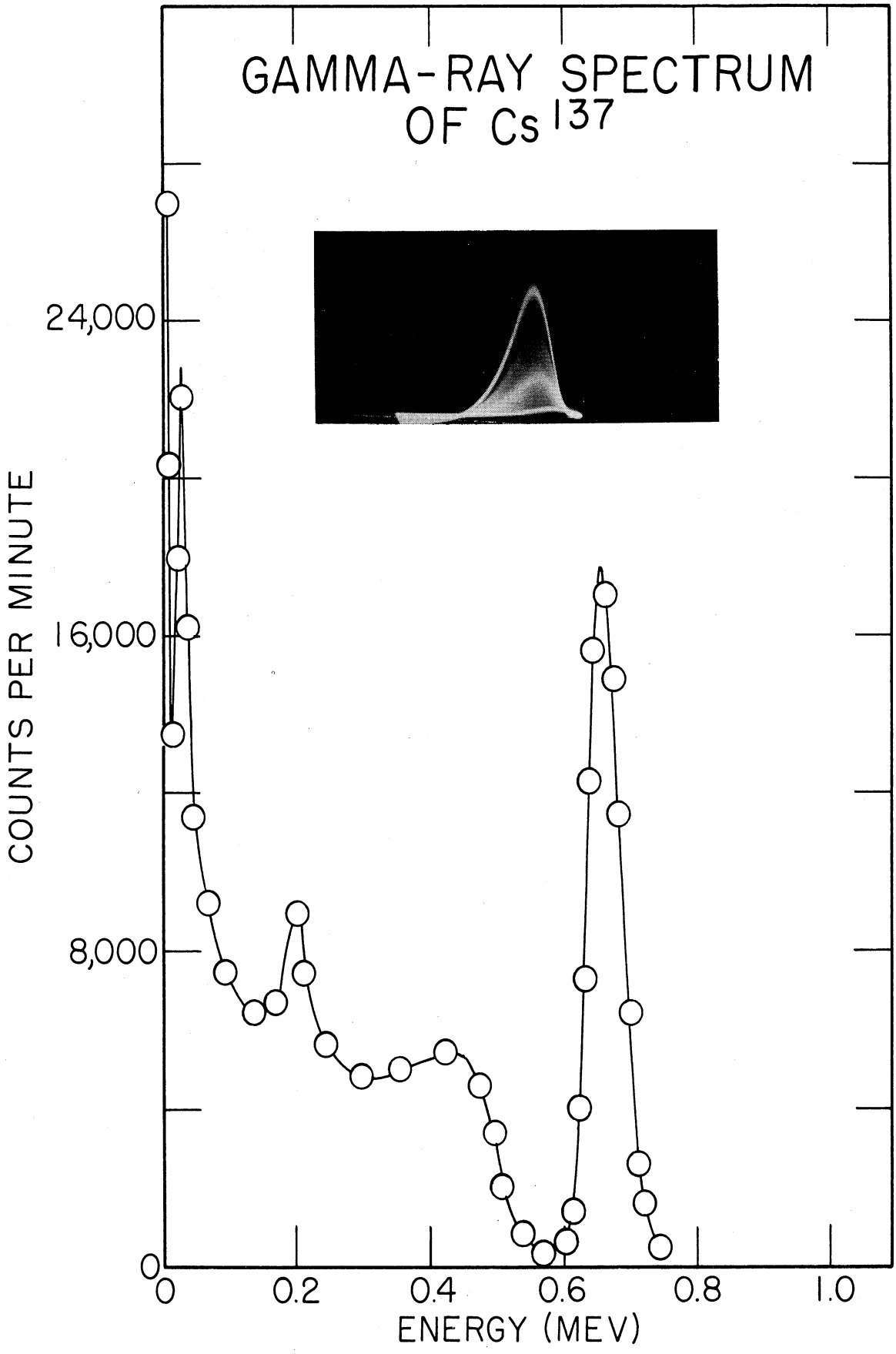

Figure 8. Gamma-ray spectra of Cs^{137}

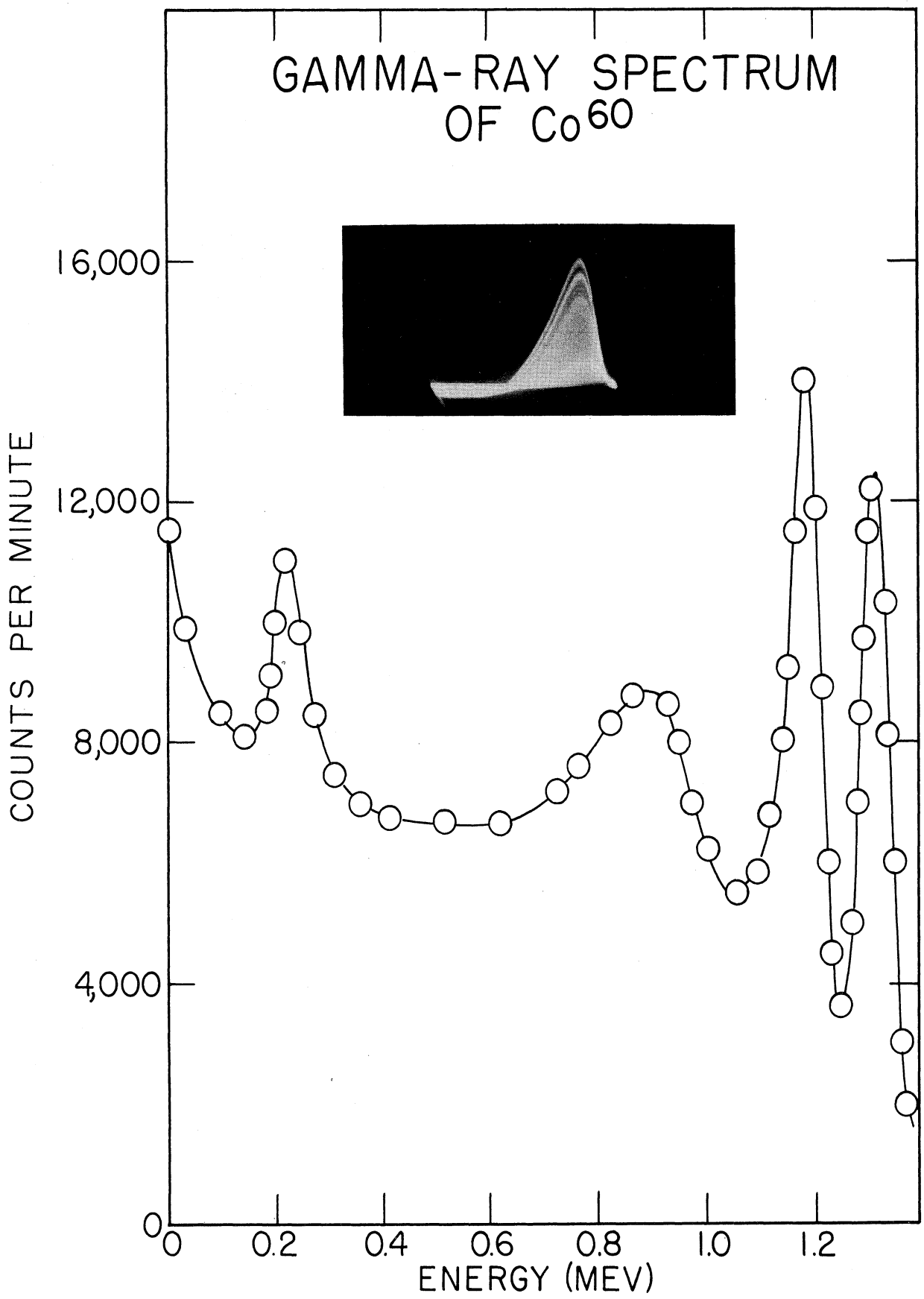

Figure 9. Gamma-ray spectrum of Co^{60}

Figure 10 is a block diagram illustrating the coincidence set-up. The detecting phosphors are chosen for β-γ or γ-γ coincidences. Channel II is the interdicting channel and is set on the pulses with which coincidences are sought. The base line of the channel I pulse height analyzer is set below the lowest energy point in the spectrum above which information is desired, and the window opened completely so as to view all of the spectrum above that point. Usually the baseline is set just above the noise level. Occasionally, when there is an intense γ ray which is obscuring γ rays immediately above it by overexposing the photographs, the intense γ ray may be eliminated merely by setting the baseline just above it.

Pulses from the channel I linear amplifier are fed to the normal oscilliscope input with internal trigger after first passing through a 4-μ sec. delay line terminated by a reostat of 2500 ohms. When a coincidence occurs, the coincidence analyzer's output pulse triggers a monostable multivibrator unblanking gate whose output is an $\sim$20 μ sec. square wave. Figure 11 is the schematic of the gate circuit. The square wave pulse is applied across the oscilliscope's CRT cathode terminal and ground. With the brightness control on the oscilliscope turned all the way down, and the pulse height of the square wave adjusted to $\sim$60 volts, a coincidence event will then illuminate the trace for $\sim$20 μ sec. and reveal the pulse that gave rise to the coincidence. At least 10^6 pulses per minute from channel I may be applied to the scope before the chance occurence of two pulses appearing within a few μ sec. of one another becomes objectionable.

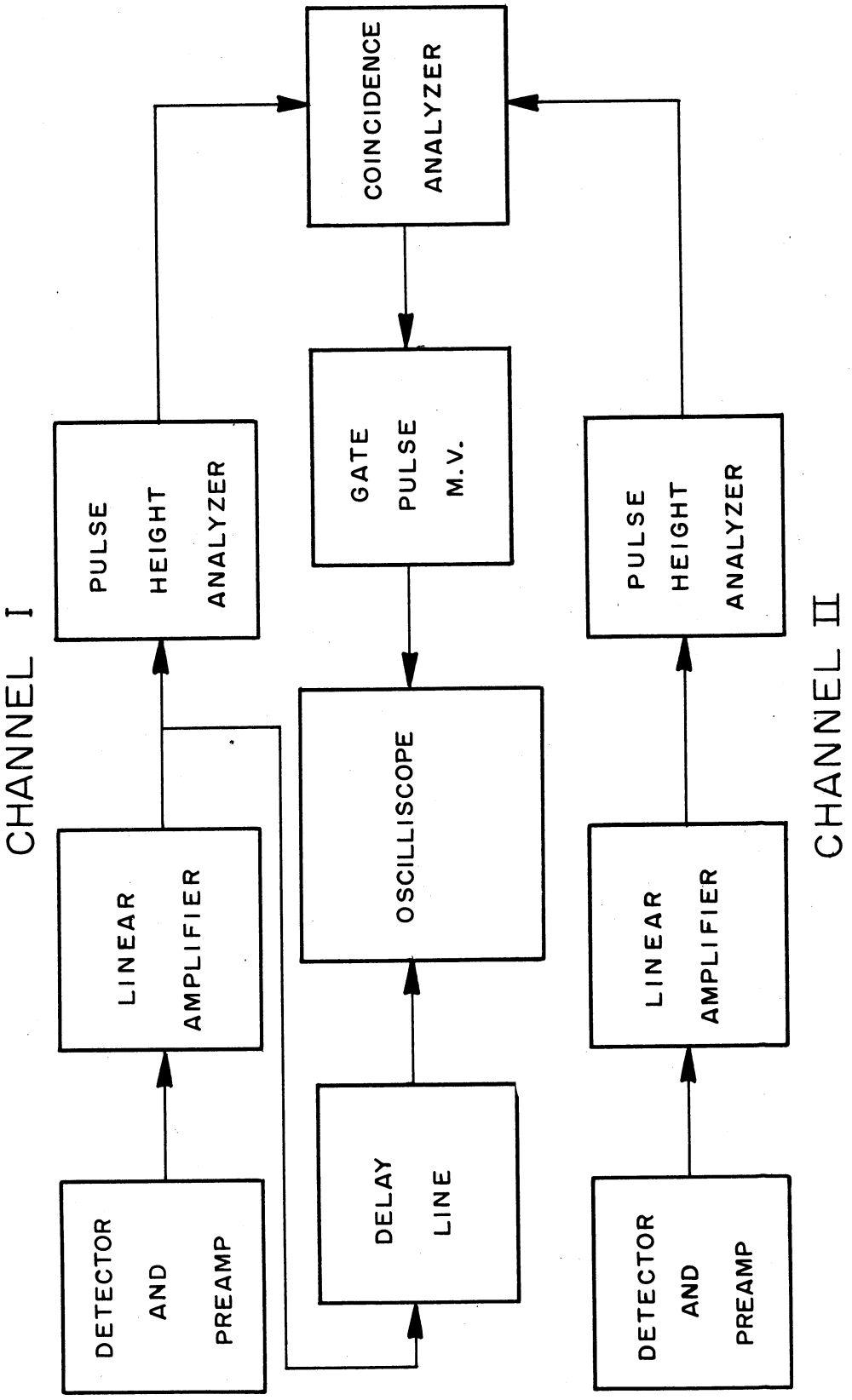

Figure 10. Block diagram of the photographic coincidence arrangement

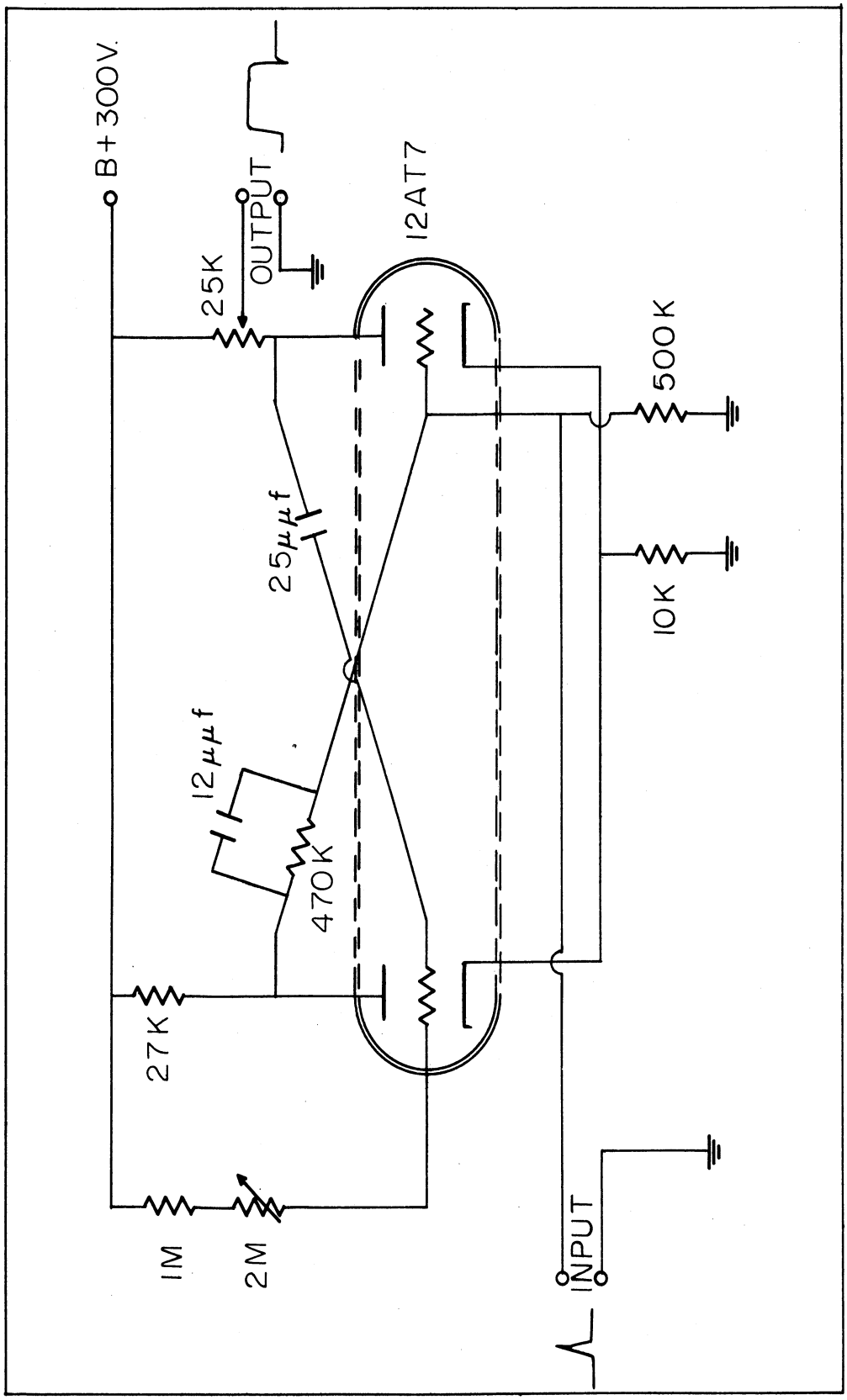

Figure 11. Circuit diagram of the multivibrator unblanking gate

Still pictures are then taken of the ocsilliscope's presentation using either a Land polaroid camera or else a 35-mm camera. If desired, the pulses may be stretched and Gray-Wedge pictures taken. Since the gating pulse is quite flat on top the trace intensity remains constant and independent of when the coincidence pulse appears. The singles spectrum may be observed merely by switching off channel II on the coincidence analyzer, thereby producing an output pulse for each channel I pulse. Figure 12 shows the results obtained for Co^{60}. Good results have also been obtained in β-γ coincidence work. Gamma rays in coincidence with portions of the β spectrum have been measured, using a plastic phosphor as the β detector.

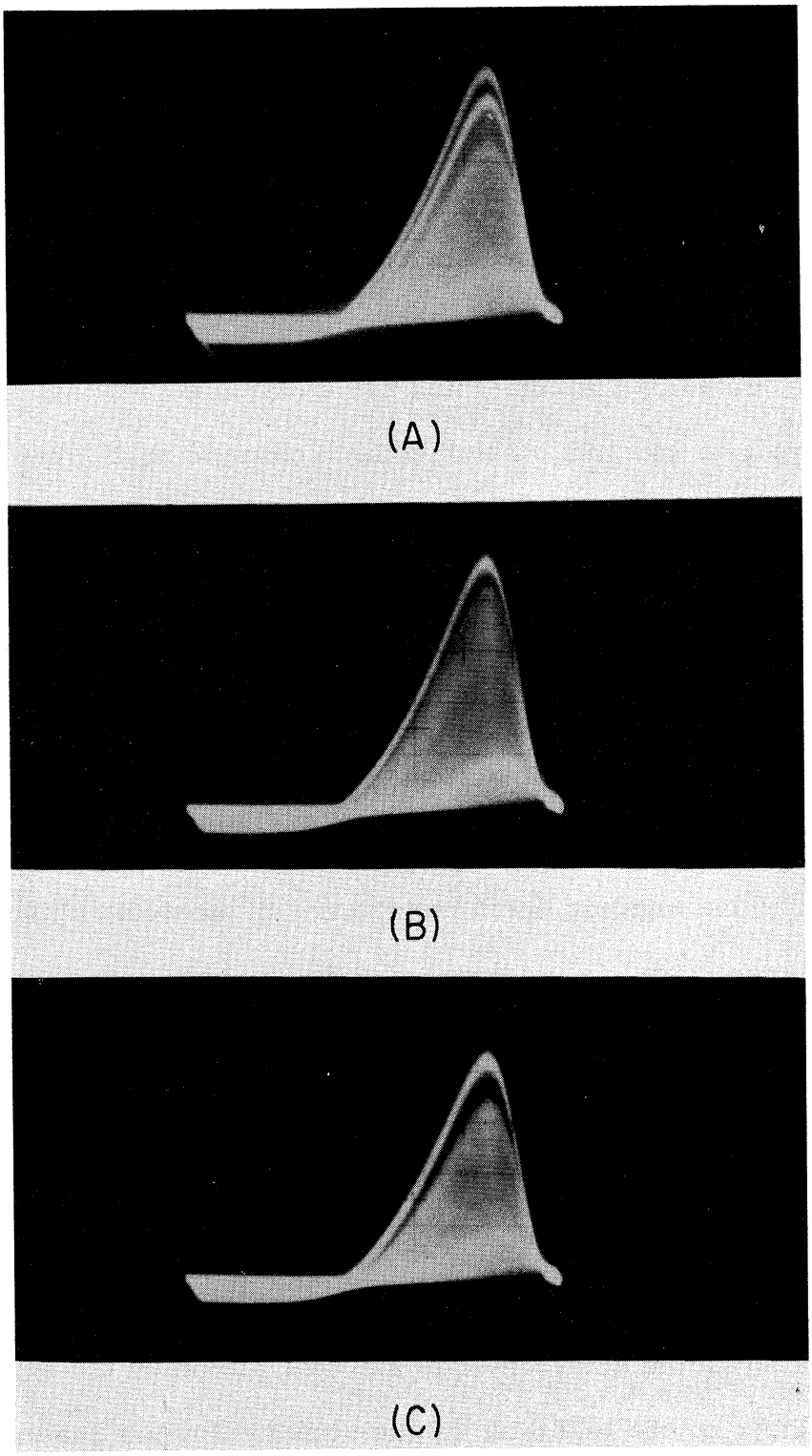

Figure 12. Gamma-ray Spectra of Co^{60}. (A) Singles Spectrum. (B) Spectrum in Coincidence with 1.17-Mev Gamma Ray. (C) Spectrum in Coincidence with 1.33-Mev Gamma Ray

CHAPTER IV

BETA SPECTRAL ANALYSIS

In order to utilize the potentialities of the Kurie analysis previously discussed, the spectrum measured by a β-ray spectrometer must either be essentially free of distortion, or else a suitable procedure for correcting the spectrum must be available. Certain types of spectral distortion are common to most types of spectrometers. These include distortions due to thick β-ray sources and backscattering from the source mounting and surrounding equipment, which tend primarily to distort the lower energy section of the curves. These errors cannot in general be removed by subsequent data treatment.

Another source of distortion is due to instrument resolution. The extent of this effect depends upon the type of spectrometer involved. Certain magnetic spectrometers are in use today which have excellent resolution, in the order of a few percent or less. While undoubtedly these spectrometers will provide one of the best spectral determinations available, they do in general present certain drawbacks. The excellent resolution is counteracted by the requirement of high sample activity, of the order of tens of millicuries, due to low transmission. In many instances the time required to pump the spectrometer down to vacuum after a sample has been placed in the system sets a definite limit on the half-life of the source. Further restrictions include the cost of the spectrometer, and the occasional difficulties encountered in constructing β-γ coincidence equipment. The ability to separate positrons from negatrons is quite a definite advantage, however.

Another type of spectrometer, whose resolution is inherently poorer than the magnetic type, utilizes a fluorescent detector after the fashion of the scintillation γ-ray spectrometer. One method (63, 113) involves the use of a thin flat phosphor covered with a reflecting material such as aluminum foil. This arrangement, however, tends to distort the low-energy portion of the β spectrum since some of the β particles will be scattered out of the phosphor leaving only part of their energy behind. In many cases only about the highest third of the spectrum is undistorted.

A method designed to circumvent the scattering effect (129) uses two separate phosphors placed very close together with the source in between. The light is taken out of the phosphor edges and is viewed by one photomultiplier. This gives in effect 4π geometry. The method is quite good for pure β emitters with none of the β transitions in coincidence, since electrons scattered out of one phosphor will be stopped by the other phosphor. The method is restricted since the γ background cannot be subtracted, and also since coincident radiations will tend to add, producing a pulse representing the sum.

In 1950, P. R. Bell suggested an arrangement known as the Hollow Crystal Spectrometer (69, 108, 109, 129). In this method, the β rays are collimated into the bottom of a conical hole in the phosphor. The scattered β rays will then have small probability of escaping by way of the entrance hole. Bell found that considerable scattering occurred in the air inside the crystal. This was eliminated by either evacuating the equipment or else using an H_2 atmosphere. Hydrogen was more satisfactory since there was little difference between the pulse

height distribution in H_2 and in vacuum, and the organic crystals such as anthracene and stilbene volatize slowly in a vacuum. While the method seems excellent, only one article was found in the literature up to April, 1956 that used the hollow crystal in a spectrometer (111) other than review articles covering the initial work done by Bell and co-workers on the spectrum of Ca^{45}.

Since the 180° magnetic spectrometer (51) in this laboratory was not designed for accurate spectral measurements, a new spectrometer was required. It was deemed necessary that the spectrometer have the following features:

1. Since the isotopes to be investigated will be cyclotron produced, the instrument must be able to work with small amounts of activity so as not to require excessively long bombardment times.

2. The instrument should be simple to construct and relatively inexpensive.

3. It must be possible to run a spectrum immediately after the source is prepared, as some of the isotopes of interest will have half-lives of the order of minutes.

4. The instrument should not require special source preparation such as vacuum plating, which would be time-consuming.

5. The restriction to pure β emitters must not be required.

6. The instrument should be easily adaptable to the measurements of β spectra in coincidence with γ rays.

7. The resolving time of the instrument must be less than 10^{-7} sec.

8. It must be possible to change samples rapidly, so that calibration of the instrument may be done before and after the spectrum is run, if necessary.

9. It should be possible to examine conversion electron peaks with some degree of accuracy.

10. It must be possible to differentiate between allowed and forbidden spectral shapes.

11. Accurate end point values, and relative intensities of different β groups in a complex spectrum must be obtainable.

While scintillation spectrometers have relatively poor resolution, this may be corrected for, as is shown in the later section. The β distribution is a smoothly varying function, and only the measurement of conversion electron peaks will suffer greatly due to poor resolution. Since a good two-channel γ-ray spectrometer was available, it appeared that a β-scintillation spectrometer would be best since only the phosphor would be needed. And of the scintillation techniques available, it seemed that a reinvestigation and modification of Bell's hollow crystal spectrometer would be the best approach. It was decided to have the spectrometer operate in an air atmosphere rather than using hydrogen gas or a vacuum because of the time requirements mentioned above. A few experiments were run using a helium atmosphere, and the results showed little improvement over air. The only serious drawback in this method is that positron spectra cannot be accurately analyzed due to the annihilation radiation unless a special equipment set-up is made.

A. Description of Hollow Scintillator β-Ray Spectrometer

1. Phosphors.

The first problem is the choice of the phosphor. It is desired to have as large a pulse height per Mev lost in the phosphor as possible, since the resolution is approximately inversely proportional to the square root of the number of photoelectrons in the pulse. Resolution, as used here, is defined as the full width of the pulse distribution at half-maximum counting rate for monoenergetic electrons. Table VII lists various features of a few scintillators.

TABLE VII. CHARACTERISTICS OF SOME SCINTILLATORS

Material	Rel. Light Yield	Decay Const.(sec)	Density	Melting Point (°C)
Sodium Iodide	2.0	25.0×10^{-8}	3.67	651
Anthracene	1.0	3.0×10^{-8}	1.25	217
Stilbene	0.65	0.8×10^{-8}	1.16	126
Sintilon Plastic	0.6	0.8×10^{-8}	1.05	110

While NaI crystals produce the largest pulses, scattering of electrons increases rapidly with atomic number and only about 10-20% of the electrons impinging on a flat NaI crystal will lose their entire energy in the crystal. This may be compared to 90% for anthracene (129). However, organic crystals are expensive, difficult to machine, and subject to shock. Therefore, it was decided

to try a plastic phosphor. The plastic phosphor chosen was Sintilon, produced by National Radiac Company, since it appeared to have properties at least as good as other plastics available. A detailed comparison of various scintillators is given by Dhar (36) and others (11, 32).

A discussion of the fabrication and assembly of the hollow scintillators used here is given in Appendix A. The result of this work was the construction of three detectors to be used with β-ray energies up to maximums of 1.5, 2.2, and 3.6 Mev, respectively. Each phosphor was constructed in two parts which consisted of a flat, solid, right circular cylinder used as the base, and a top piece consisting of a hollowed-out cylinder or truncated cone. Figure 13 shows the drawings for the three phosphors which appear in Figure 14. A phototube holder and lead shield constructed to hold the detectors is shown in Figure 15.

The radioactive samples whose spectra are to be examined should be carrier free, or else have as high a specific activity as possible. The samples are prepared as follows:

1. An aluminum disc, 1" in diameter with a 7/16" hole punched in the center, is used. The disc is usually $\sim$ 10-20 mils thick. A piece of 1/4-mil Mylar coated with a thin aluminum layer is used as a backing film. This is glued so that the organic film is next to the disc.

2. A solution of the radioactive substance is evaporated onto the organic side of the film in the center of the disc.

3. The sample is covered with a layer of 1/4-mil Mylar or Teflon film.

Figure 16 shows a cross-section view of a mounted β detector. The purpose of the aluminum film evaporated onto the Mylar film is to prevent

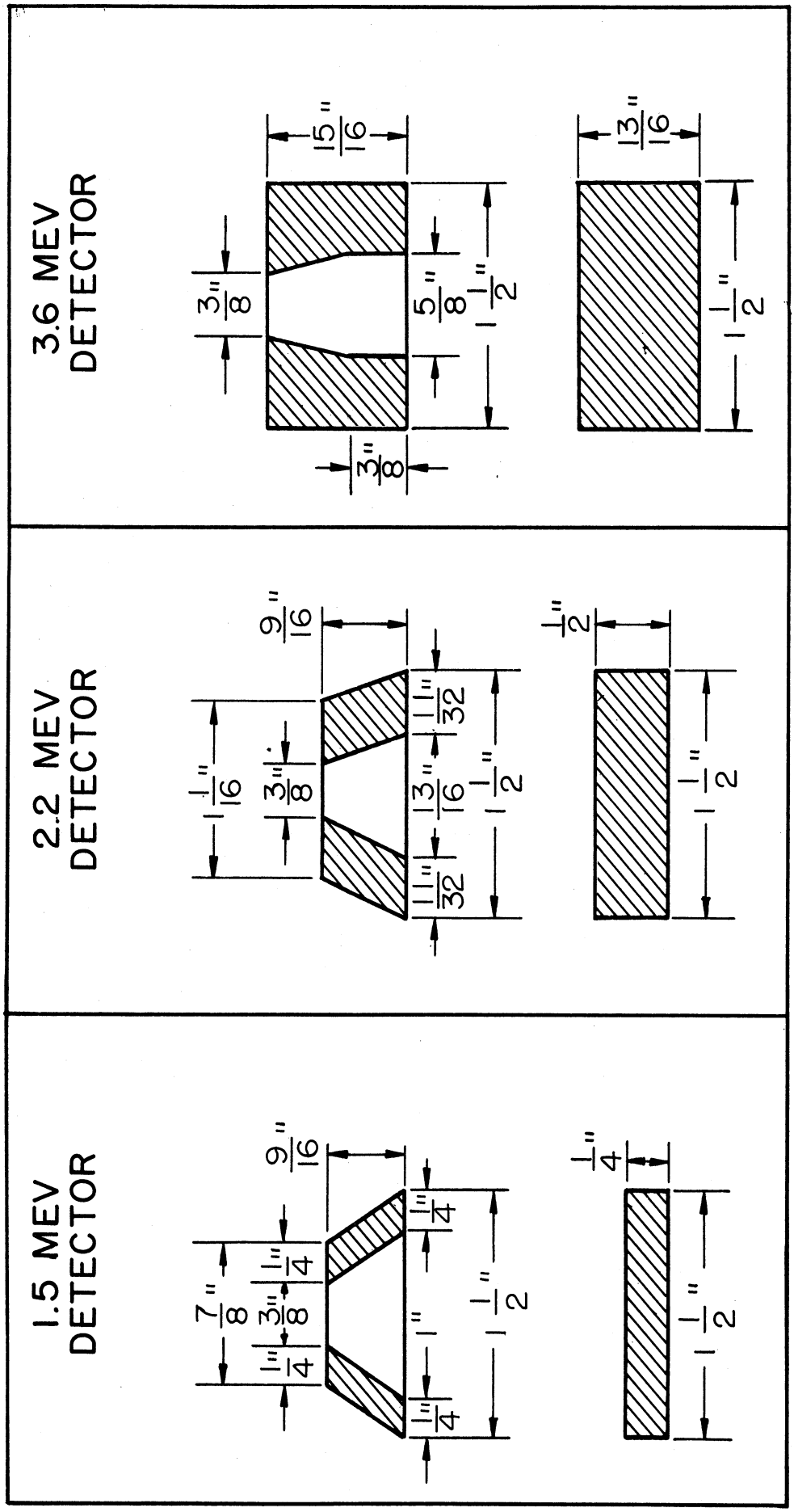

Figure 13. Cross-sections of the three hollow plastic scintillators

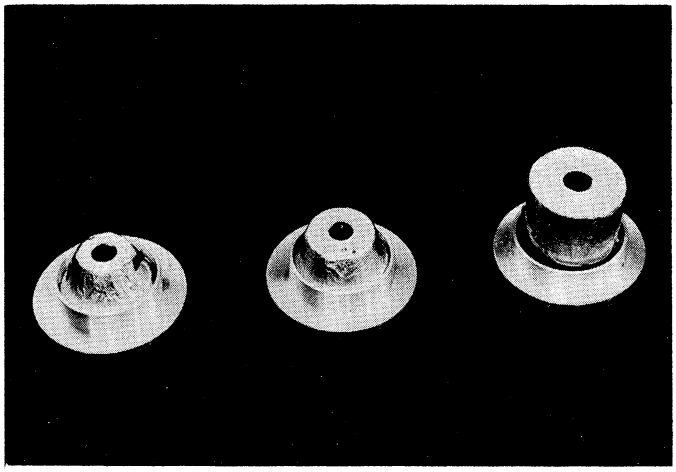

Figure 14. The Three Hollow Plastic Detectors

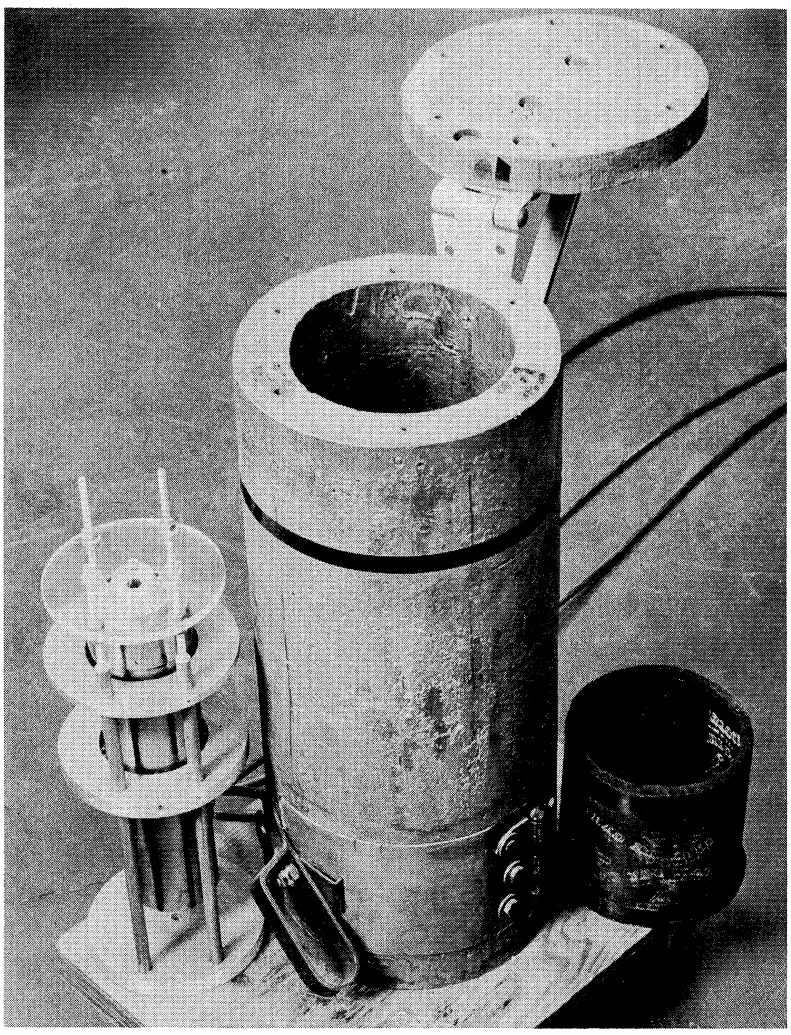

Figure 15. Phototube Holder and Lead Shield for Hollow Scintillator Beta-ray Spectrometer

light from entering or leaving the detector through the hole in the top.

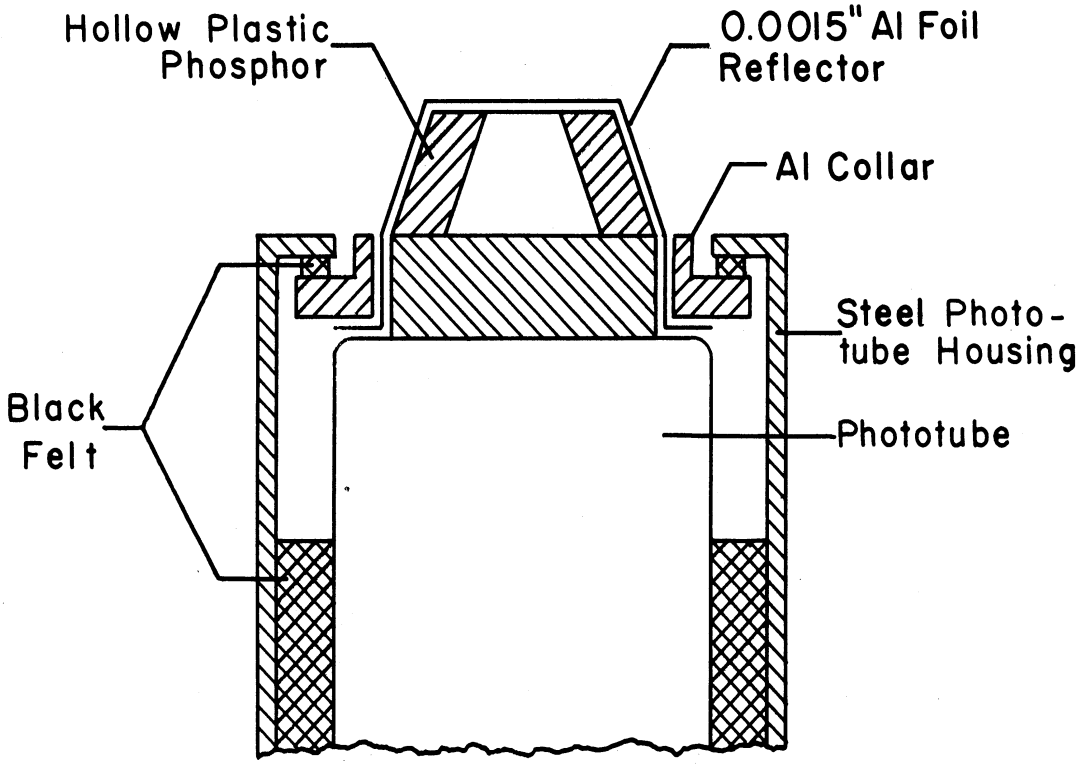

Figure 16. Cross-section of beta-ray detector mounting

2. Operation

If coincidence spectra are to be run, the β detector is simply mounted on a phototube in the housing described in the section on the γ-ray spectrometer. Otherwise, the detector is mounted as shown in the previous section. The lucite sample holder is then centered over

the phosphor and placed in contact with it, with the locking nuts holding it tightly in position. A sample is put into position with the aluminum coated film away from the hole over which is placed the lucite retaining ring. A light-tight cap, made of rubber sheet 1/4" thick which also serves to shield the phosphor from electrons knocked out of the lead shield, is placed over the top of the phototube housing. The top and bottom doors of the shield are then closed. The spectrum may now be taken.

It has been found that increasing the high voltage from 650 to 1300 volts does not affect the resolution of the spectrometer appreciably. Therefore, in order to reduce the noise in the phototube, a voltage of 830 volts is commonly used.

The pulse-height analyzer channel width used depends upon the counting rate of the sample. The "window" may be opened to $\sim$ 1.5 volts before the resolution, position of peak, or peak to valley ratio for the conversion peak of Cs^{137} are affected. With a wider window the resolution and peak to valley ratio become poorer. This is illustrated in the set of curves shown in Figure 17. Table VIII shows the peak to valley ratio and apparent resolution at the various window settings.

TABLE VIII. RESPONSE OF Cs^{137} CONVERSION PEAK TO PULSE HEIGHT ANALYZER WINDOW SETTING

Window (volts)	Peak/Valley	Resolution %
0.10	5/1	14.0
0.20	6/1	14.0
0.40	5/1	13.5
1.00	5.5/1	14.0
1.75	5/1	15.0

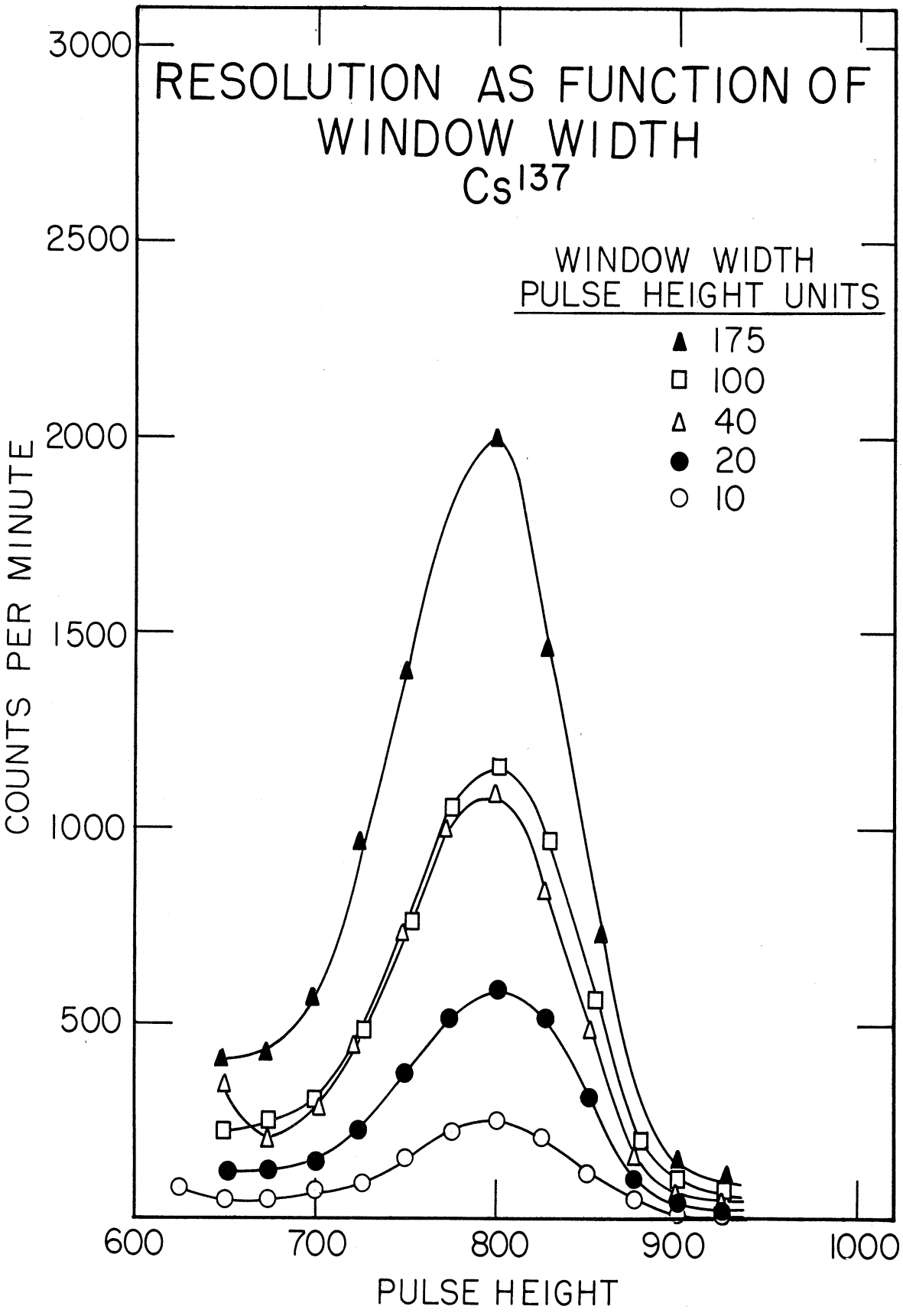

Figure 17. Effect of window width on resolution of Cs^{137} conversion peak. Ordinate scale for top two curves is 2.5 times indicated scale.

3. Calibration.

Since the linear amplifiers are dependably linear only from $\sim$ 10 to $\sim$ 80 volts, the gain must be adjusted so that the spectrum to be analyzed, along with the calibration points of In^{114}, Sn^{113}, and Cs^{137}, falls in this range.

The spectrometer is first calibrated by means of the conversion electron peaks of known energy shown in Table IX.

TABLE IX. CONVERSION ELECTRON PEAKS USED IN CALIBRATION

Isotope	Energy (Mev)
In^{114}	0.162
Sn^{113}	0.364
Cs^{137}	0.624

The stated energies are not, however, the energies of the conversion electrons striking the phosphor. Corrections must be made for the amount of energy lost in the 1/4-mil Mylar film covering the sample, and also in the air in between the sample and the phosphor. This can be done if the rate at which energy is lost, as a function of energy, as the β particle passes through an absorber is known. Using Equation (12),

$$-\frac{dE}{dx} = \frac{2\pi N e^4 Z}{mc^2\left[\frac{u^2+2u}{(1+u)^2}\right]}\left\{\log_e 1/2\left(\frac{mc^2}{I}\right)^2\right\}$$

$$+ \log_e[u(u^2+2u)] - \left[1-\left(\frac{u}{1+u}\right)^2\right]\log_e 2 + \frac{1}{(1+u)^2}\Bigg\} \qquad (12)$$

and information given in Reference 5, the curves in Figure 18 were calculated. $-dE/dx$ is in units of Mev/mg cm^{-2}, and $u = E/mc^2$. The rest of the symbols have their usual meaning. While the curves in Figure 18 are only shown to 1.0 Mev, they may be extrapolated out to $\sim$ 10 Mev with little error.

No attempt was made to calculate a mean path length in the air within each phosphor. It was simply assumed that a good average distance was $\sim$ 1.6 cm. The value of 1.18 mg/cm^3 was used as the density of air. For the Mylar film a surface density of 0.635 mg/cm^2 (of aluminum) was used.

The pulse height analyzer was calibrated by assuming a linear relation between the dial reading and the observed energy of the conversion peaks in the range from 0.16 to 0.62 Mev. It has been found that a linear extrapolation to higher energies is valid at least to 3.6 Mev, the endpoint of the most energetic spectrum measured in this work. For lower energies a linear extrapolation is made to 0.1 Mev, and then a smooth curve is drawn from the end of the line to the origin. It must be remembered that this is at best a guess, and this portion of the spectrum cannot be relied upon. However, in most cases this portion of the curve falls in the non-linear lower range of the amplifier and should be discarded anyway.

As a further check on the calibration, spectra with known maximum energies and shapes were obtained either before or after an unknown is run. After each run the energy assigned to each pulse height amplifier reading was corrected using the curves in Figure 18 to obtain "true" energies.

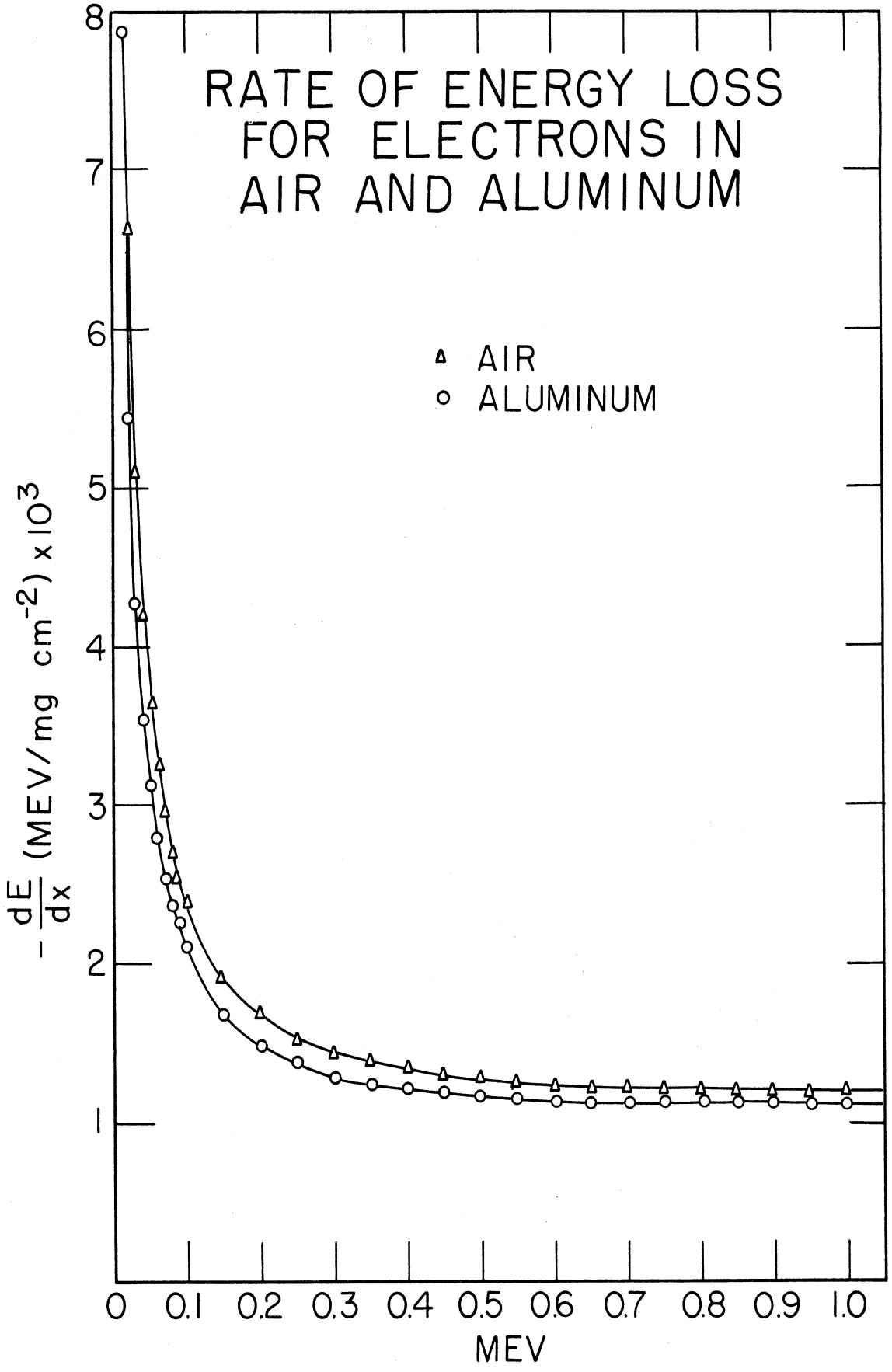

Figure 18. Rate of energy loss as a function of energy for electrons in aluminum and air

A word should be said about drift in the equipment. As long as the ambient temperature remains reasonably constant, say within 5° or so, no drift of over $\sim$ 1.5% was found during three continuous weeks of operation.

B. Performance of Hollow Scintillator β-Ray Spectrometer

An investigation was made to determine the capabilities and limitations of the hollow scintillator spectrometer. Near the end of this section a comparison is made with a flat detector constructed from the same scintillating plastic. The last subsection deals with the problem of instrument resolution. None of the spectra presented up to this last section have been corrected for instrument resolution except near their endpoints.

1. Effect of Detector Size

As mentioned earlier, the three detectors available are for maximum β energies of 1.5, 2.2, and 3.6 Mev. Any γ radiation accompanying the β particles must be subtracted from the gross curve to yield the β component. Since error will invariably be introduced by this subtraction procedure, it is preferable to have the γ component as small as possible. Figure 19 shows the γ-ray background in each detector with respect to a normalized Cs^{137} β-ray spectrum. While in general quite small, the γ-ray background is comparable to the β-ray spectrum near E_{max}. It is to be understood that the "γ background" refers to the gross spectrum minus the β spectrum. Hence, the "γ background" includes also the cosmic and background radiation, along with the noise in the amplifier and phototube. No distinction will be made between the true

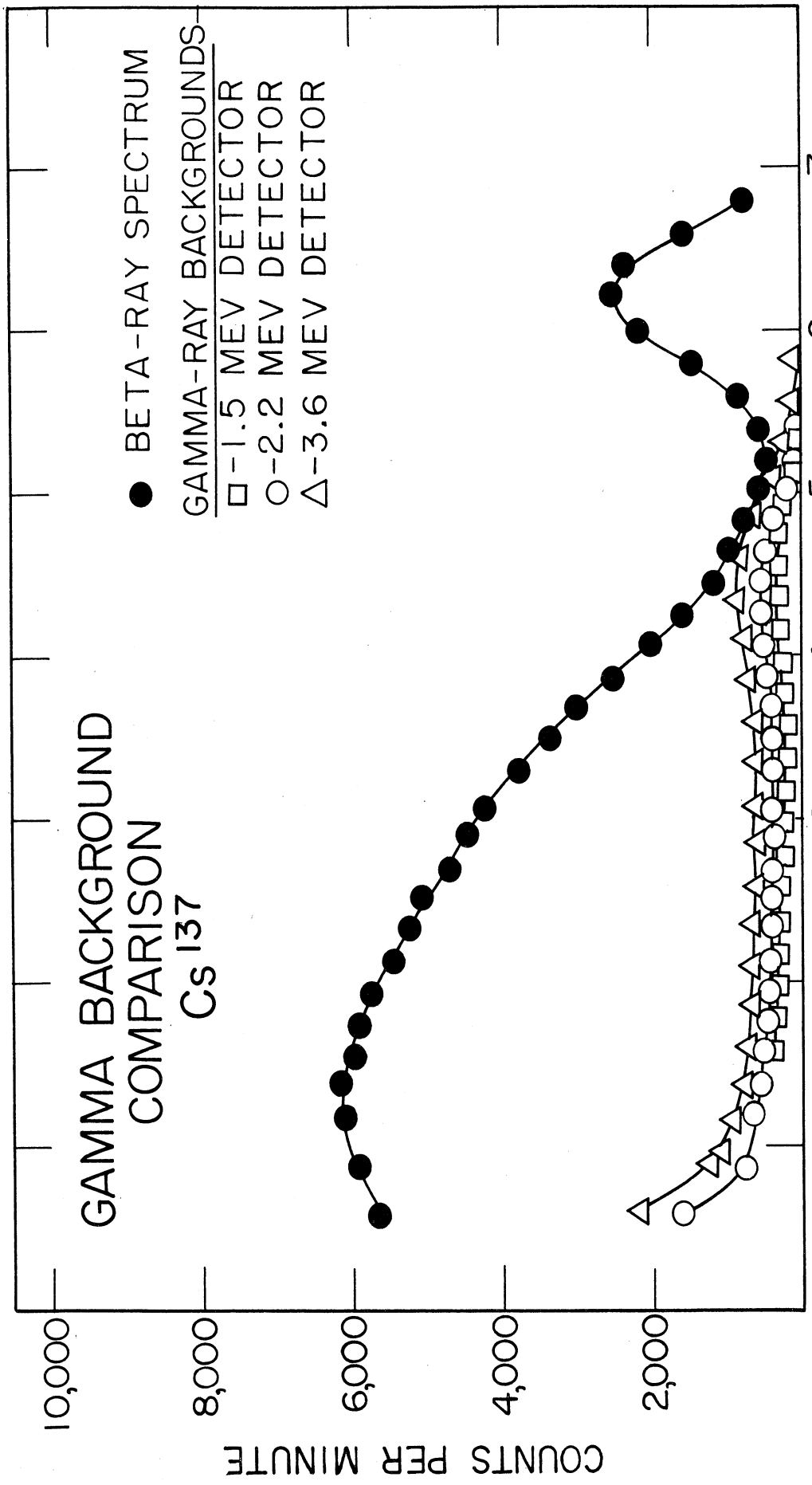

Figure 19. Gamma-ray backgrounds in the three plastic detectors

γ background and the term as used above. It is interesting to note the detection efficiency of the phosphor for β rays and γ rays. Assuming an equal number of β rays and γ rays in Cs^{137}, the ratio of the γ to β efficiencies in the usual experimental set-up is roughly 0.23 for the 3.6-Mev phosphor, and 0.15 and 0.11 for the 2.2 and 1.5-Mev phosphors, respectively.

Figure 19 suggests that for maximum β-ray energies less than 1.5 Mev the smallest detector should be used. There is, however, another point to keep in mind, i.e. the phosphor shape. Two important effects are: (1) the thickness of the phosphor, and (2) the amount of optical coupling between the top and bottom pieces of the phosphor. As the size of the phosphor increases the resolving power and the light output decreases. The change in resolving power is only in the order of 1 or 2% for the phosphors used here, but the decrease in light output may be as much as 5%. As the volume of the phosphor decreases, for a given base diameter the walls of the hollow top of the phosphor become thinner. This means that the optical interface becomes smaller. This interface should be as large as possible to reduce the scattering in the phosphor. As it is, the interface is located over the periphery of the photo-cathode and reducing the wall thickness will just make things worse. Since these two effects are in opposite directions, the 2.2-Mev phosphor is used for energies up to $\sim$ 2 Mev. The 1.5-Mev phosphor is used only when the small difference in γ backgrounds becomes important.

In Figure 20 the Kurie plots for the three Cs^{137} spectra connected with Figure 19 are shown. All three spectra have essentially

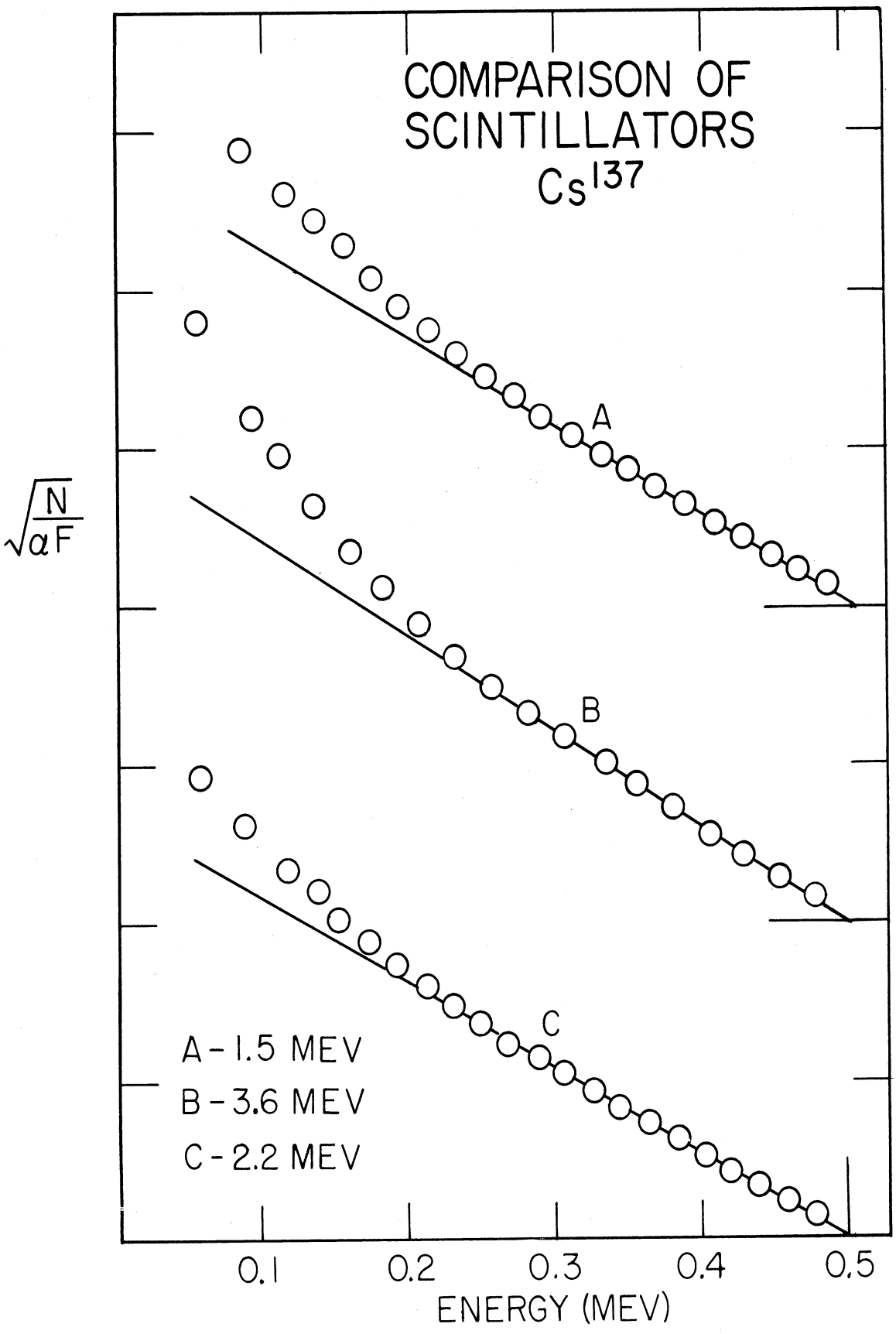

Figure 20. Kurie plots of Cs^{137} from each detector

the same endpoint value of 0.51 Mev as compared with the literature value of 0.517 Mev. As expected, the 2.2-Mev detector yields the best Kurie plot, which is linear down to about 0.18 Mev. Each curve was corrected by the unique first forbidden correction factor $\alpha_1(W)$, where $W_o = 2.01$. To find out how the linearity behaves as a function of E_{max}, a similar set of curves were run on Pm^{147} and P^{32}.

Pm^{147} yields a single allowed β-ray spectrum with $E_{max} = 0.224$ Mev. Figure 21 shows the resulting Kurie plots. There seems to be little difference between the two detectors.

P^{32} also has a single allowed β transition with $E_{max} = 1.7$ Mev. No γ rays are present. Figure 22 shows the Kurie plots. The source contained P^{33} which caused part of the upward curvature at lower energies.

As a final means of comparison, the resolution of the three phosphors for the Cs^{137} conversion electron peak are listed in Table X.

TABLE X. RESOLUTION OF THE THREE PHOSPHORS FOR THE Cs^{137} CONVERSION ELECTRON PEAK

Phosphor	% Resolution Uncorr.
1.5 Mev	14.7
2.2 Mev	14.0
3.6 Mev	15.8

These resolutions have not been corrected for the higher energy β ray in Cs^{137}, nor for the smearing of the low energy edge of the peak. The true % resolution would be somewhat smaller in each case.

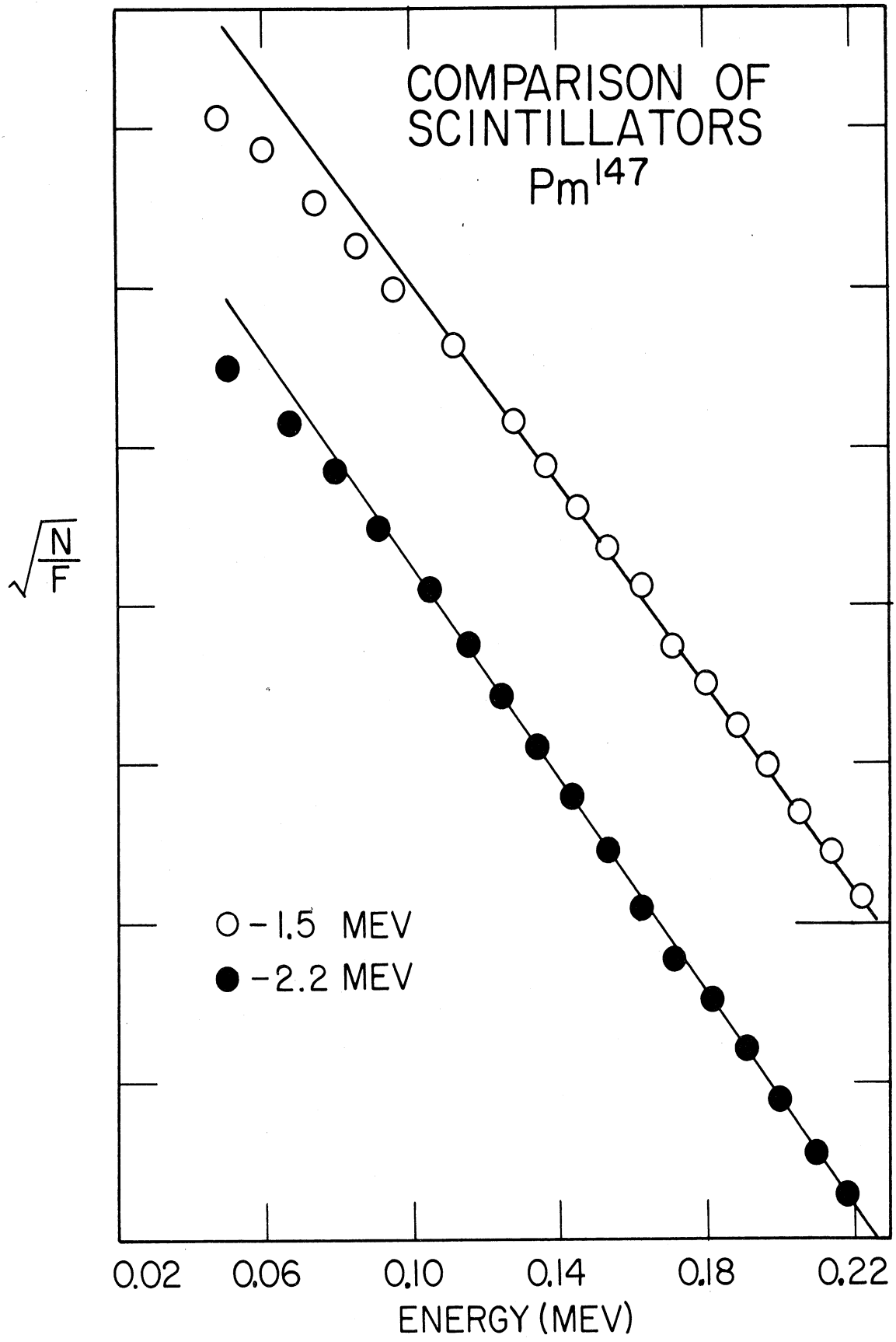

Figure 21. Kurie plots of Pm^{147} from the 1.5-Mev and the 2.2-Mev detectors

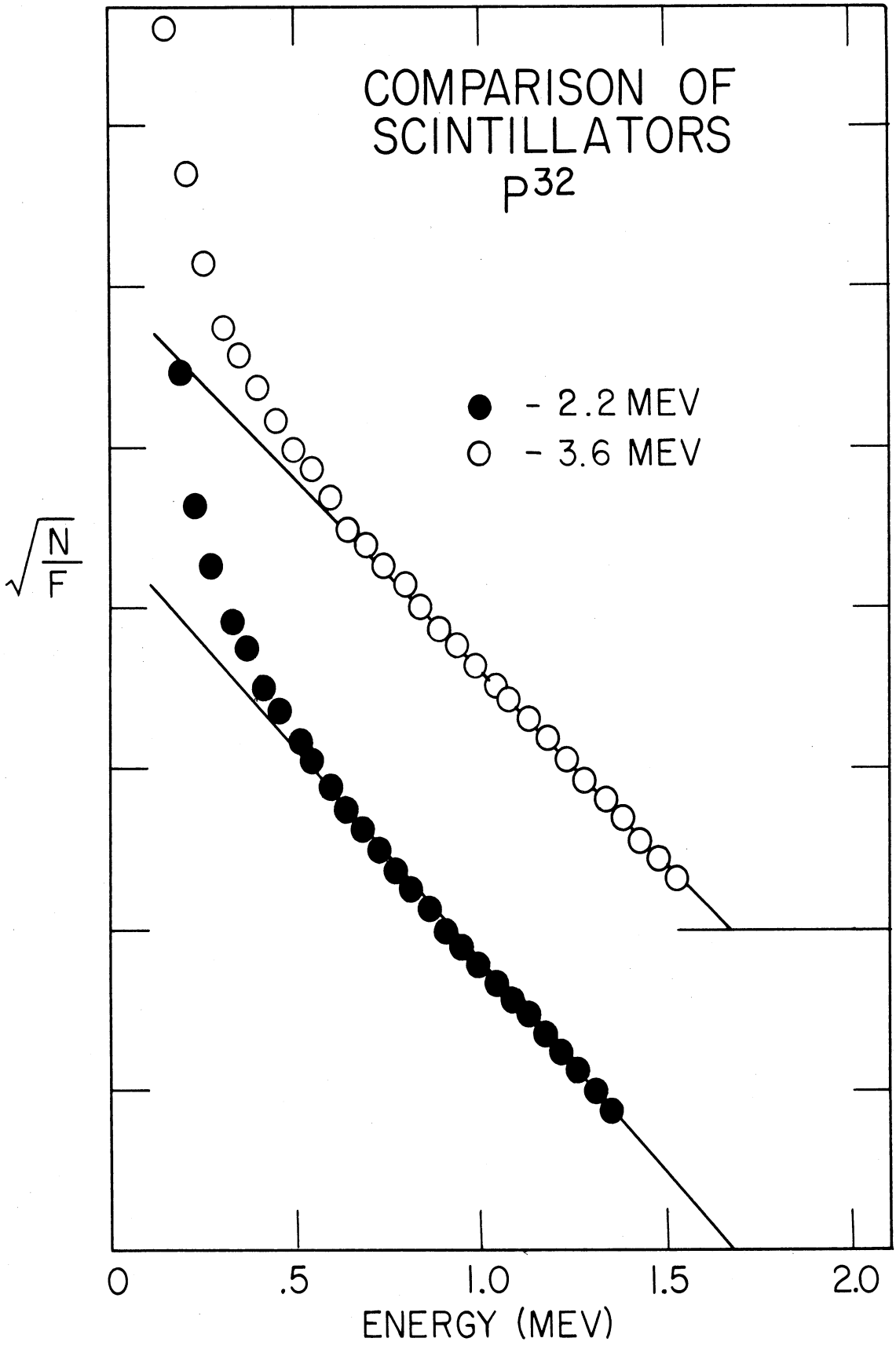

Figure 22. Kurie plots of P^{32} from the 2.2-Mev and the 3.6-Mev detectors

The evidence presented above indicates that the 2.2-Mev phosphor is the best for general use for β rays up to 2.2 Mev. The advantage is only slight, however, and good results may be obtained with both of the detectors.

2. Effect of Sample Backing

Essentially any amount of backing upon which the sample rests will cause some distortion of the β spectrum due to backscattering. It is also of interest to compare light reflecting backings with transparent ones. It would naturally be supposed that a reflecting backing would be better since any light loss would distort the spectrum and decrease the resolving power. But the magnitude of this effect was not known.

In Figure 23 the Kurie plots of Cs^{137} are shown for the following backing materials:

1. 1/4-mil Mylar (0.64 mg/cm^2).
2. 1/4-mil Mylar coated with aluminum (0.7 mg/cm^2).
3. One 6-mil aluminum disc behind 1/4-mil Mylar (38.1 mg/cm^2).
4. Nine 6-mil aluminum discs behind 1/4-mil Mylar ("infinite" backing).

Comparing the transparent Mylar backing alone with the same backing covered with one aluminum disc, it would seem that the distortion caused by light loss in the first case is about equal to the backscattering distortion in the second case. The aluminum-coated Mylar is by far the best backing.

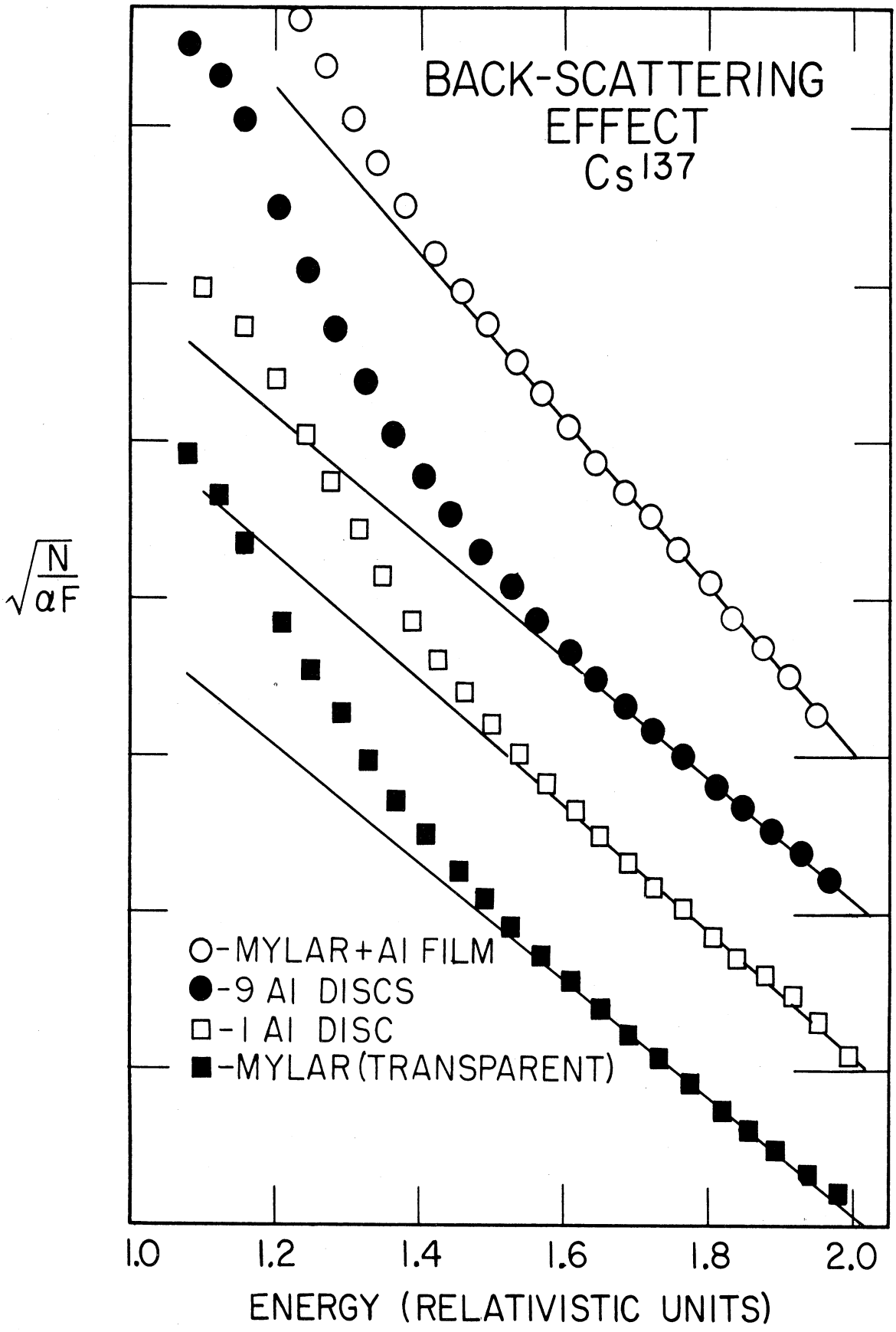

Figure 23. Effect of sample backing on shape of the Kurie plot of Cs^{137}. For energy in Mev see Appendix B, Figure 67.

3. Backscattering From Sample Holder.

When the phototube assembly was first constructed it was not known if backscattering from the sample holder would be a problem. Two sample holders were built, one of aluminum and the other of lucite, both of the same design. The design was such as to minimize backscattering as much as possible. Figure 24 shows a P^{32} spectrum obtained with each sample holder. As may be seen, the aluminum sample holder caused enough backscattering to make the Kurie plot linear from $\sim$ 0.65 Mev to E_{max}, whereas the other Kurie plot is linear down to $\sim$ 0.45 Mev.

4. Backscattering Shields and Collimators.

A disc of 18-mil copper with a 7/16" hole in its center was placed over the phosphor to prevent electrons from striking the phosphor except through the entrance hole. The resulting Kurie plots showed very little if any improvement. Hence, this phase of backscattering appears to be a negligible effect in the geometry used.

Another possible detrimental effect is that the optical interface between the top and the bottom of the crystal might cause some scattering and loss of light. This would tend to cause the Kurie plot to bend up at low energies. To investigate this effect a collimator was made from a disc of 18-mil copper with a 3/16" hole in its center. This was placed between the source and the detector so that more of the electrons would strike the base of the detector. Again, the Kurie plots showed little if any improvement. This would indicate that the optical interface was good, and that light loss in the phosphors was not important.

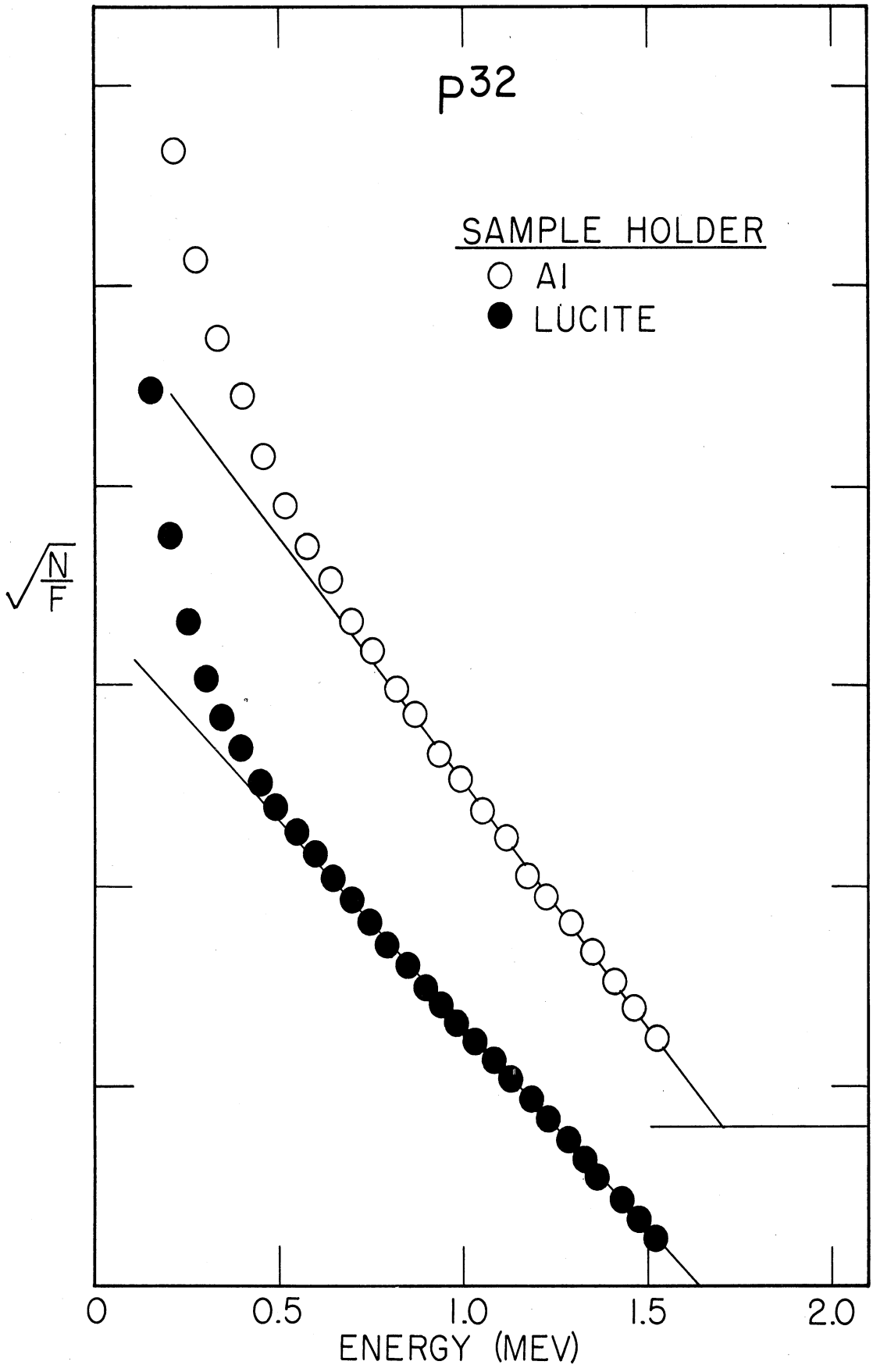

Figure 24. Effect of backscattering from sample holder on the Kurie plot of P^{32}

5. Thick Samples.

Occasionally carrier-free β sources are not available, due perhaps to difficulties in the chemical separation or more commonly when the radioactive isotopes produced in a nuclear reaction have the same atomic number as the target material. The best one can hope for then is to have a high specific activity. Since any weighable sample will distort the β spectrum, it is of interest to determine the magnitude of this effect.

Finely powdered $BaCO_3$ was mixed with a carrier-free solution of Cs^{137}. A more or less uniform sample ~ 3.6 mg/cm^2 in surface density was then made by evaporating a portion of the $BaCO_3$ suspension onto the usual aluminum coated Mylar film. The sample was covered with a layer of 1/4-mil Mylar. Figure 25 compares the Kurie plot for the thick sample with a plot obtained for a carrier-free sample mounted in the same way. It can be seen that while the thick sample shows more distortion than the other, it still yields a good curve down to about 1.6 relativistic units ($W = \frac{E}{mc^2} + 1$) or ~ 0.3 Mev.

6. Gamma Attenuation in Absorber.

To determine the γ background an absorber is placed between the source and the detector. Since the absorber normally used is 4.53×10^3 mg/cm^2 thick, it was thought that the attenuation of low-energy γ rays, say up to 0.1 Mev, might become important. A comparison between the normal absorber and an 18-mil copper disc showed no detectable difference in the Kurie plots for Cs^{137}. The normal absorber is therefore the one that is routinely used.

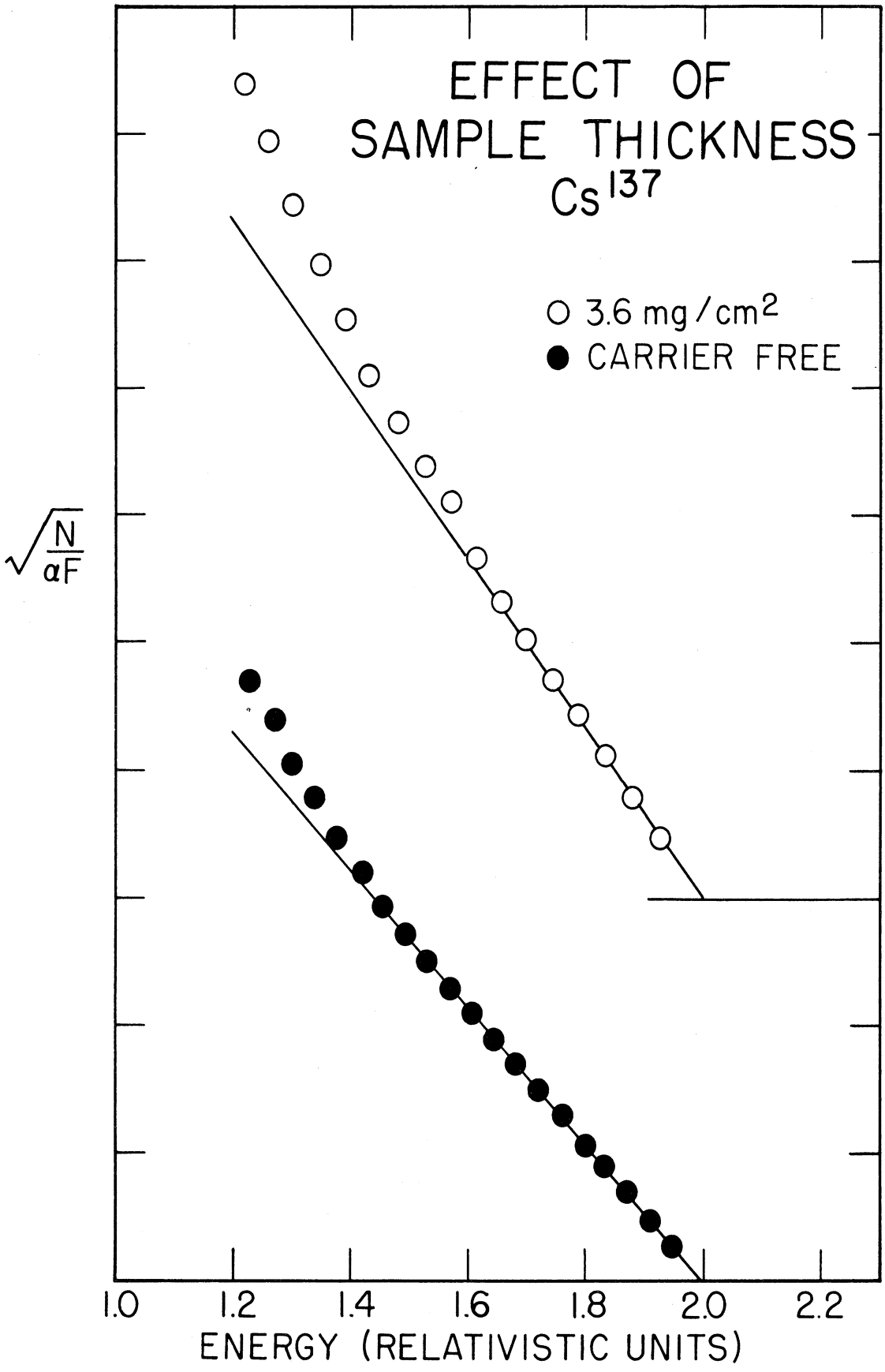

Figure 25. Effect of sample thickness on the Kurie plot of Cs^{137}. For energy in Mev see Appendix B, Figure 67.

7. Amplifier Overload and Drift.

Occasionally it is of interest to examine only the lower portion of a spectrum, such as in the case of a complex spectrum. For the sake of accuracy, as much of the amplifier range should be used as possible. For example, if a spectrum contains a 2.0 Mev and a 0.5-Mev β ray, and the amplifier is adjusted so that the entire spectrum is viewed, then only the lower quarter of the range contains the weaker β ray. Due to the non-linearity of the amplifier, about 1/3 of the lower quarter will be distorted. If the amplification were changed so that the 0.5-Mev portion occupied one-half the available range, then only about 1/5 of the lower energy spectrum would be distorted.

In the latter case, the amplifier would overload at the higher end. It is of interest to know how much distortion this overload would cause, and if it is still possible to obtain useable Kurie plots. Normally only about 80% of the amplifier range is used since the upper 20% is somewhat non-linear. A P^{32} spectrum was run where the amplification was such that the endpoint of the spectrum fell outside the full range of the amplifier by $\sim$ 15%. The Kurie plot is shown in Figure 26. It can be seen that while the upper one-third of the spectrum is distorted a straight Kurie plot is still obtainable with an endpoint within 2% of the correct value.

Amplifier overload is a relatively easy type of distortion to recognize. It is not readily confused with a forbidden spectral shape. A more subtle type of distortion occurs when drift occurs in the system. Sometimes the drift is obvious as shown in the second Kurie plot in Figure 26. Here a power failure occurred for approximately

five minutes. Although the equipment was allowed to stabilize for over an hour, the gain of the system had definitely changed.

By far the most common effect of drift is to yield a Kurie plot that is almost but not quite straight, with the wrong endpoint value. An example is the top plot in Figure 26. The solid line shown is only one of many straight lines, each of which would fit the data about equally as well. Corresponding endpoint values would vary by 7% or more. Probably the worst danger in the analysis of a drift-distorted spectrum is the temptation to "resolve" the curve into several fictitious components. For example, the top plot in Figure 26 might be "resolved" to give a weaker component with a forbidden shape and an endpoint of $\sim$ 0.9 Mev. Checking the energy calibration before and after a spectrum is taken seems to be the only answer.

8. Range of Spectrometer

The highest energy β-ray spectrum examined in this work belonged to Y^{92}, E_{max} = 3.60 Mev, and will be discussed in a later section. The weakest β transition analyzed was that of S^{35} where E_{max} = 0.17 Mev. The resulting Kurie plot using the 2.2-Mev phosphor is shown in Figure 27. An intermediate range transition of use in calibration is that of In^{114} where E_{max} = 1.98 Mev. This allowed spectrum and Kurie plot is shown in Figure 28.

For most purposes the size of the phosphor is the only limitation on the maximum β energy that may be examined (below $\sim$ 10 Mev) with this spectrometer. This is not true for the lower energies. All phosphors including NaI tend to be non-linear at low energies. Table XI lists a few phosphors and the energy below which their response is non-linear (11, 32, 36).

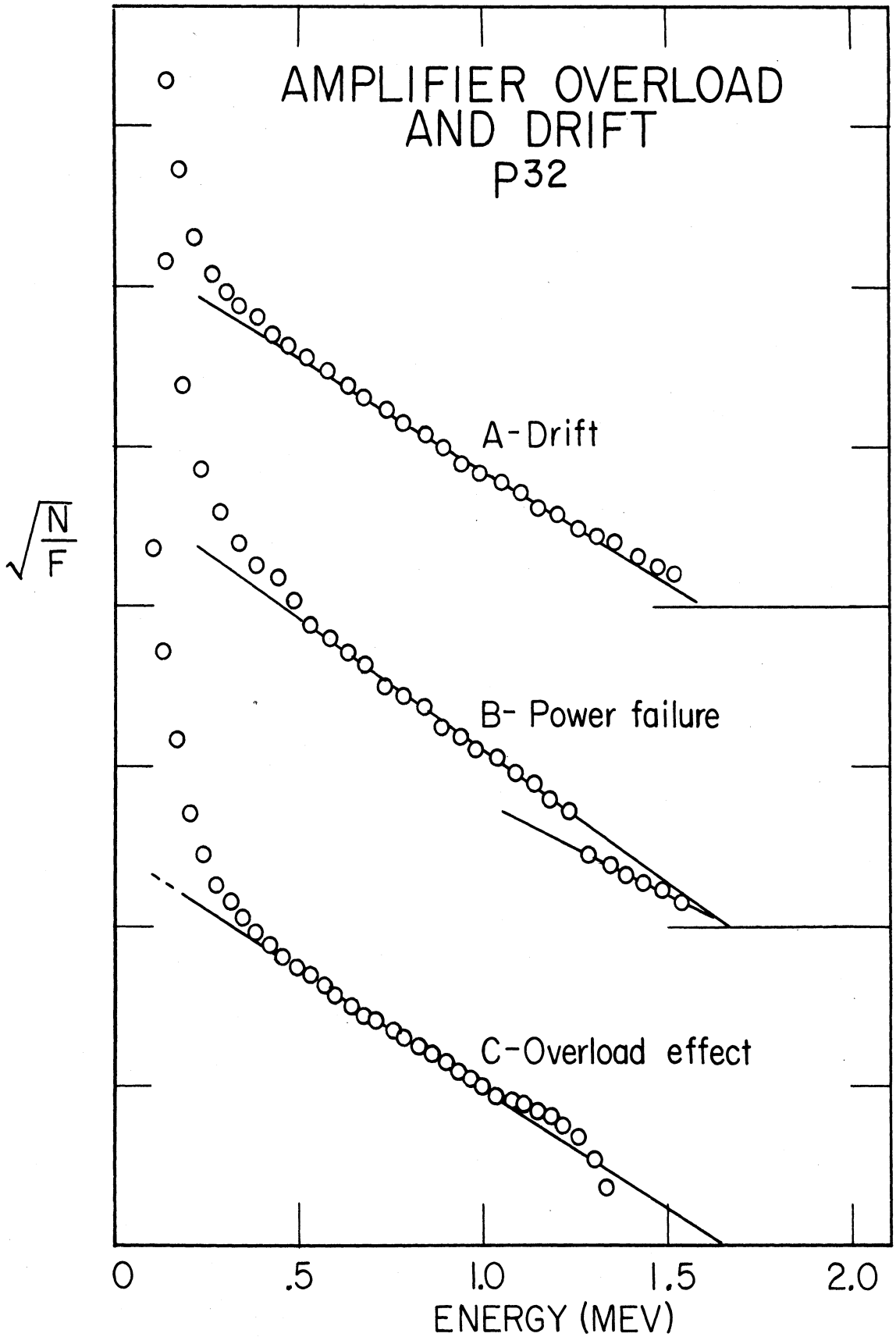

Figure 26. Effect of amplifier overload and drift on the Kurie plot of P^{32}.

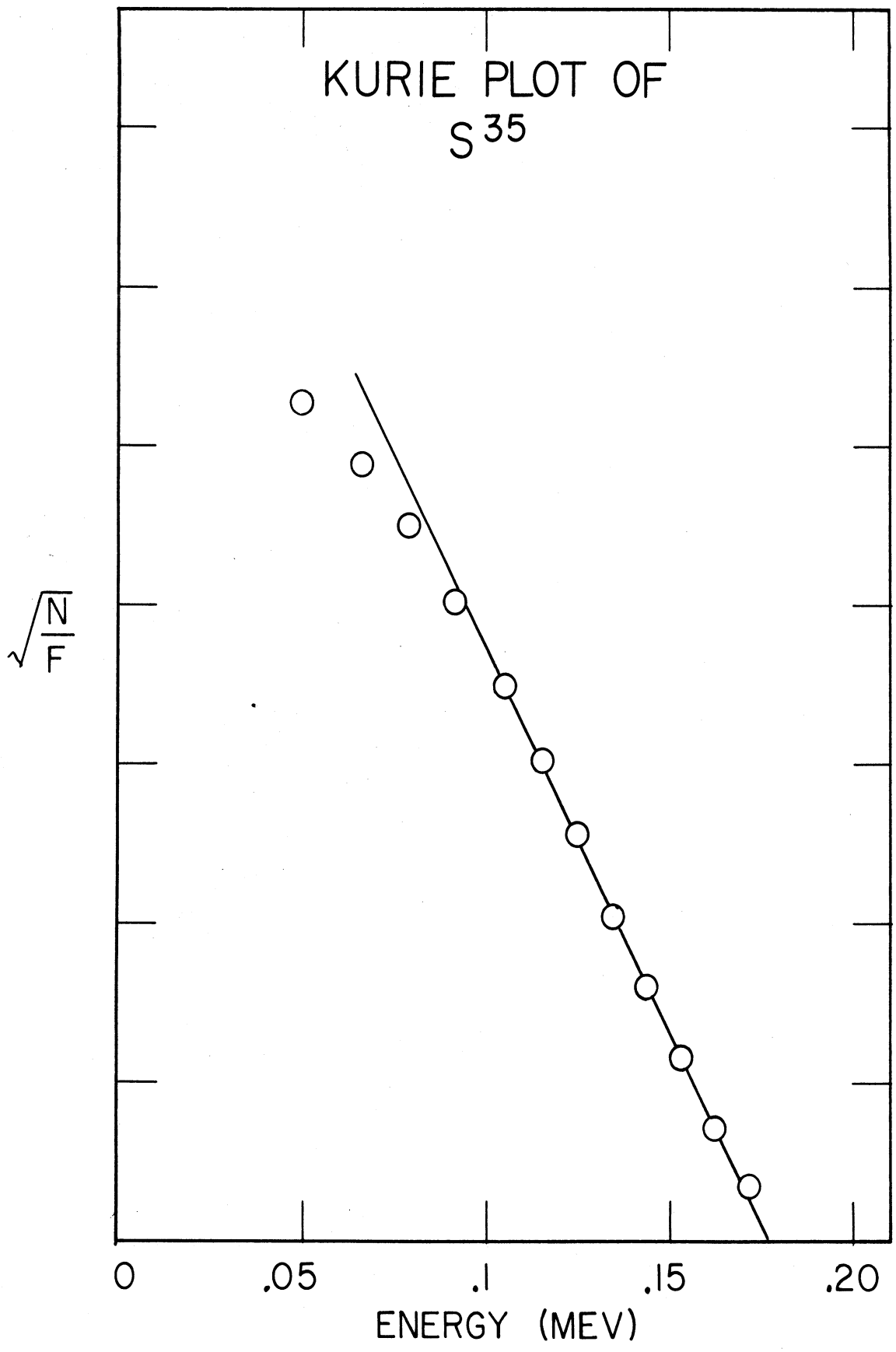

Figure 27. Kurie plot of S^{35}

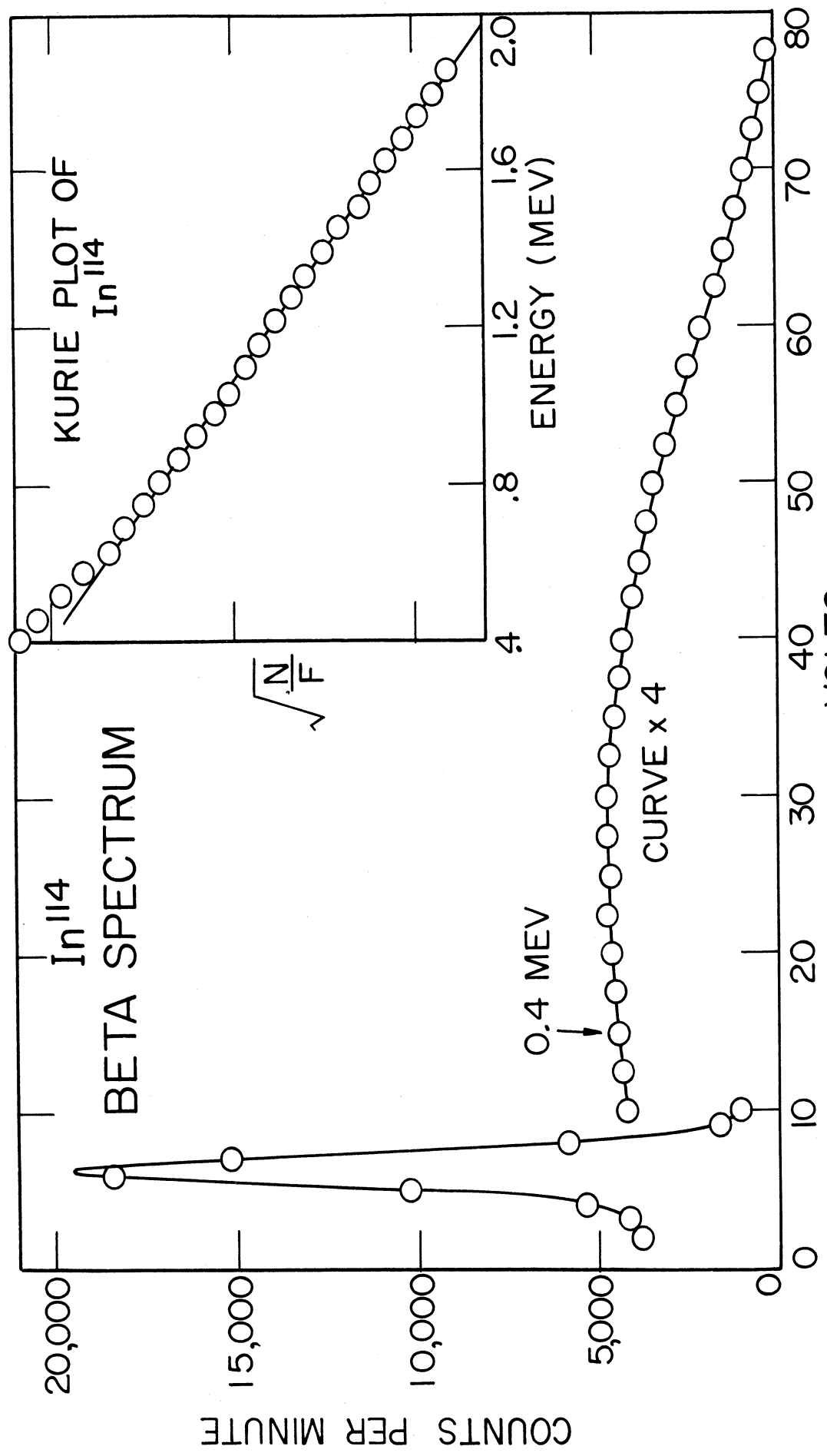

Figure 28. Beta spectrum and Kurie plot of In^{114}

TABLE XI. LOW ENERGY RESPONSE OF SOME PHOSPHORS

Phosphor	Lowest Energy in Linear Portion of Response Curve (kev)
NaI	~ 1
Anthracene	1.00×10^2
Stilbene	1.25×10^2
Terphenyl	2.40×10^2
Sintilon	$\sim 1 \times 10^2$

9. Forbidden Spectra.

It is imperative that a spectrometer be accurate enough to distinguish between the shapes of allowed and forbidden spectra. With this information a great deal more may be said about the nuclear transition generating the spectrum. Without this information the resolution of complex spectra into components may be difficult if not impossible. To evaluate the spectrometer used here a number of "unique" forbidden spectra have been examined. In the cases where the spectra are complex, only the highest energy component will be shown. The resolution of complex spectra will be discussed in the next section.

In Figures 29, 30, 31, and 32 the Kurie plots for Cs^{137}, Rb^{86}, Y^{90}, and Y^{91} are presented. Both the plot which is produced when the spectrum is assumed to be allowed, and also the plot corrected by the unique first forbidden correction term are shown. The pronounced difference in shape, i.e. the skewing of the spectrum toward higher

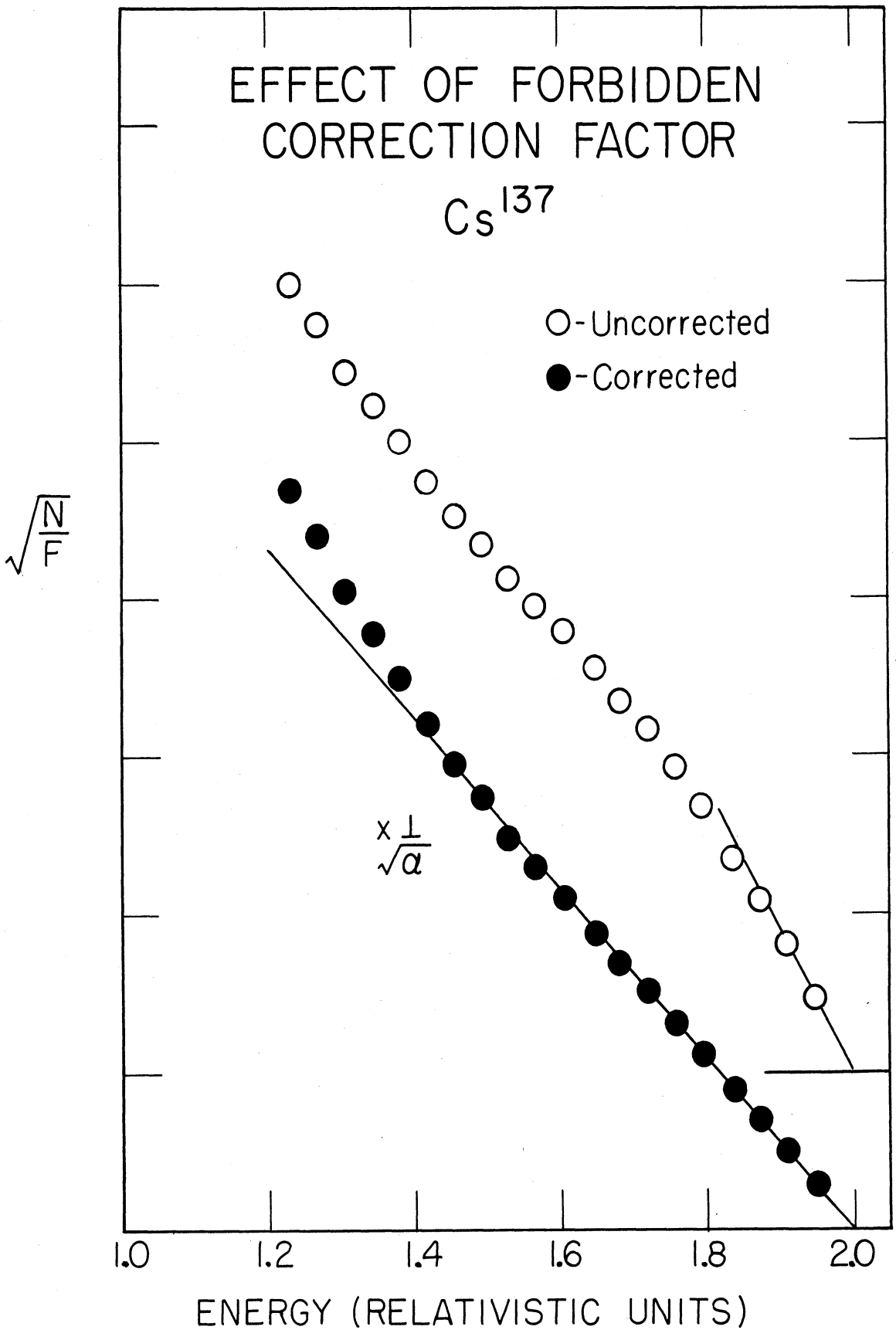

Figure 29. Kurie plot Cs^{137} showing effect of forbidden correction term. For energy in Mev see Appendix B, Figure 67

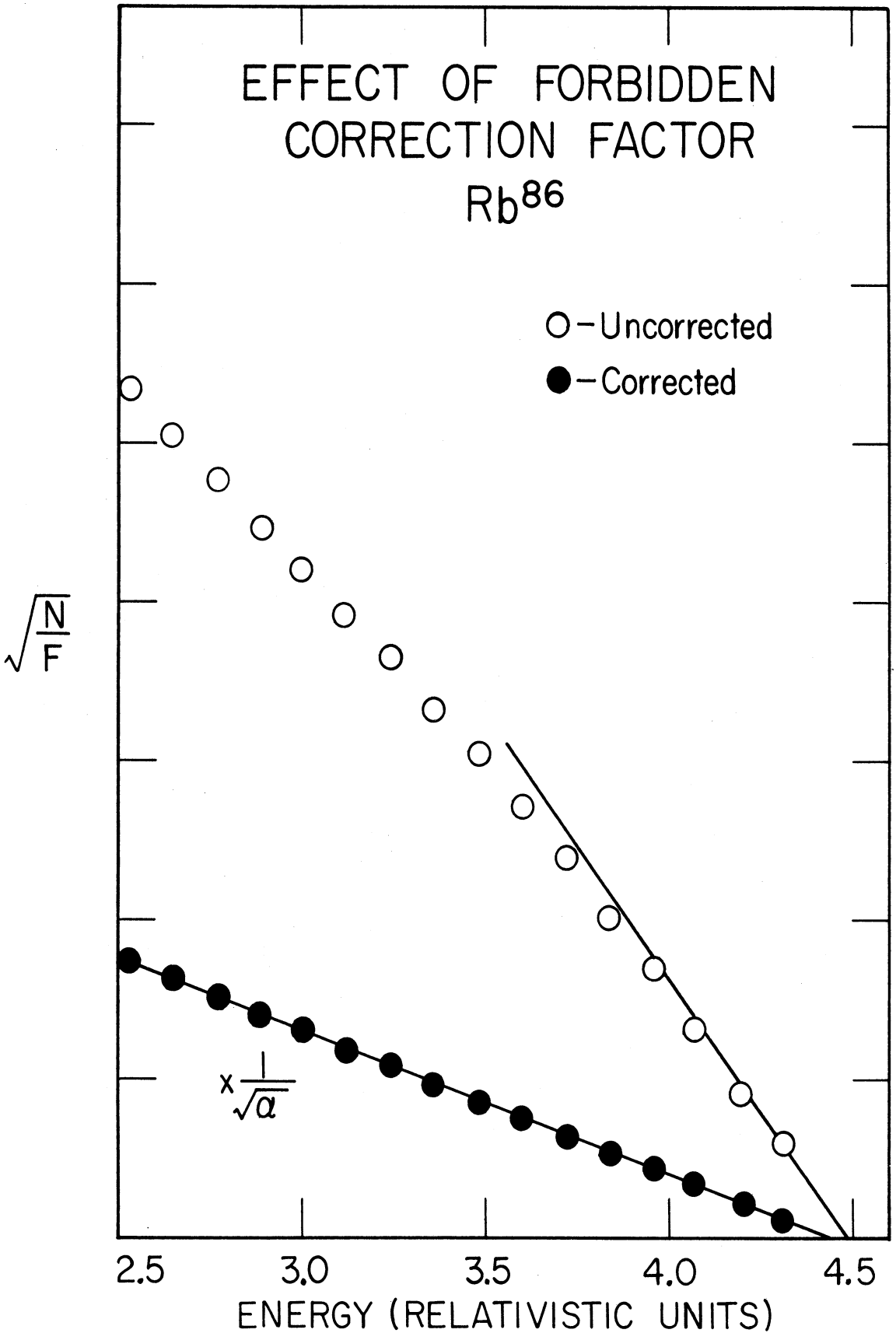

Figure 30. Kurie plot of Rb^{86} showing effect of forbidden correction term. For energy in Mev see Appendix B, Figure 67.

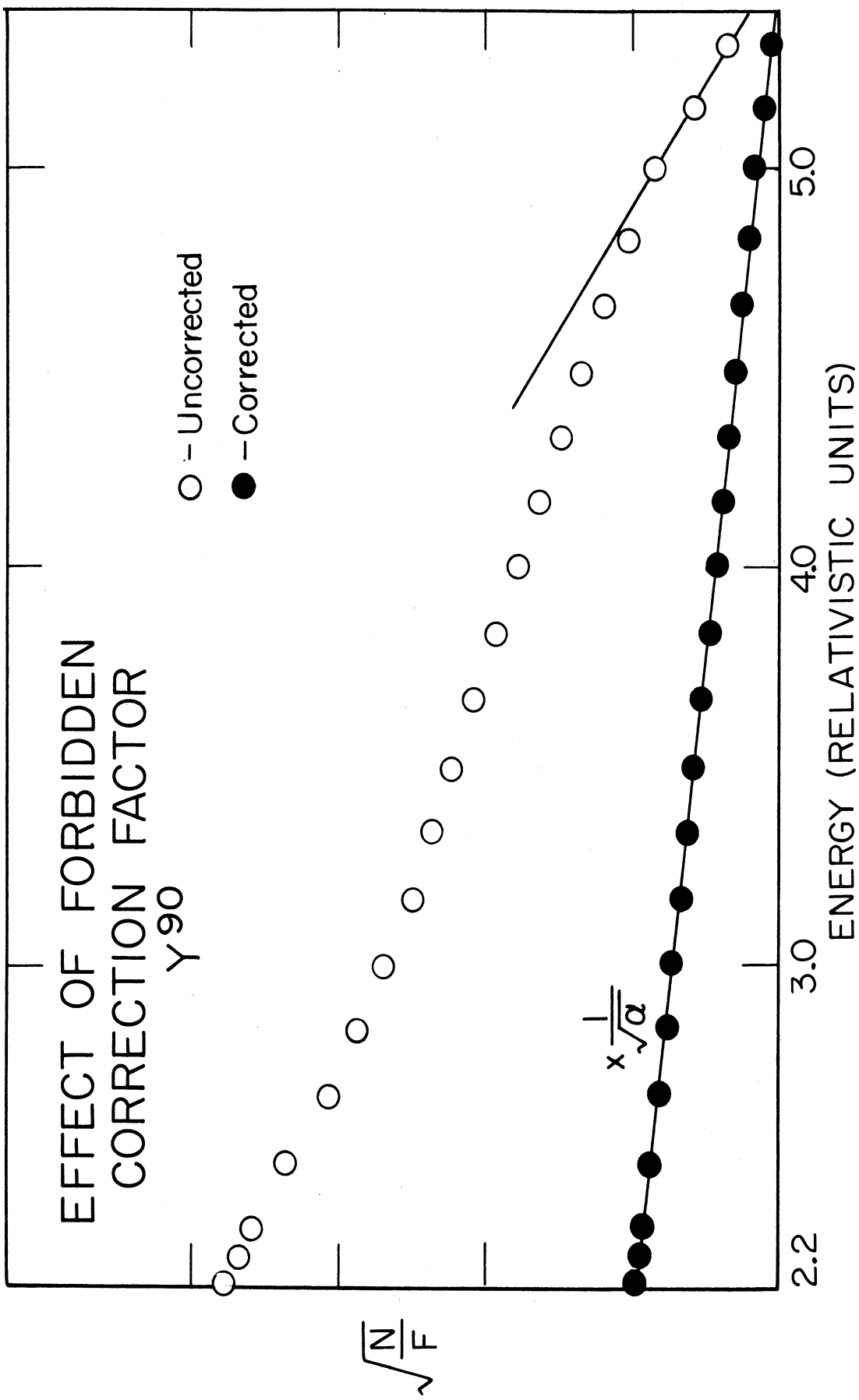

Figure 31. Kurie Plot of Y^{90} showing effect of forbidden correction term. For energy in Mev see Appendix B, Figure 67.

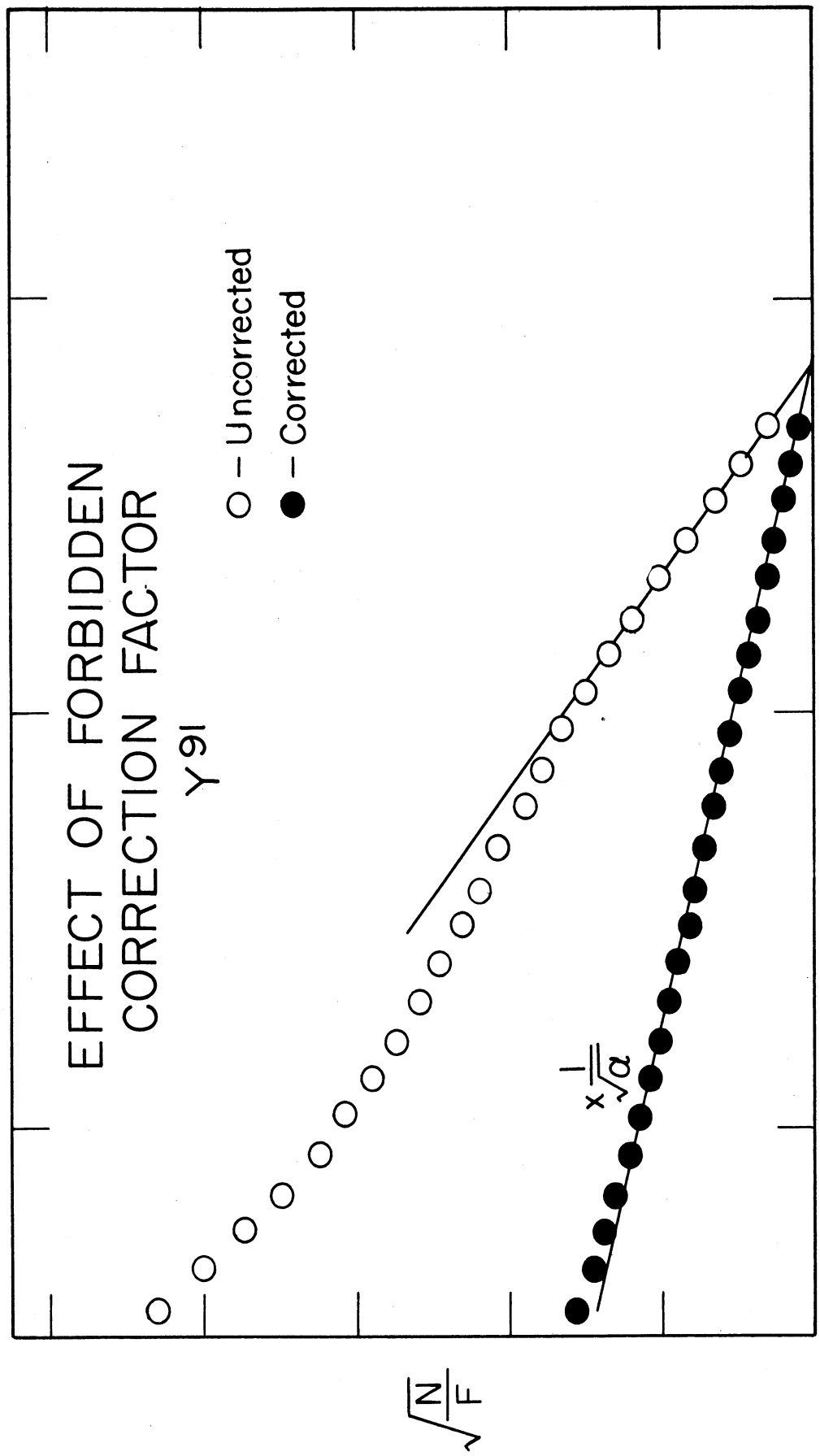

Figure 32. Kurie plot of Y^{91} showing effect of forbidden correction term. For energy in Mev see Appendix B, Figure 67.

energies, is typical of forbidden spectra. In the case of a complex spectrum where one or more of the β groups is forbidden, it is obvious that the spectrum could not be resolved with any accuracy at all unless the forbiddenness is taken into consideration.

10. Complex Spectra.

Besides knowing the E_{max} and the forbiddenness of a transition, it is also important to know the branching ratios in a complex spectrum. These ratios must be known, for example, if the log (ft) values are to be calculated. One means of measuring these ratios is to compare the areas under the respective Kurie plots. Naturally, these areas must be compared on an equal basis. If two components are present, say, and one is forbidden, then the area under the plot corrected for forbiddenness cannot be directly compared with the area under the allowed plot since the forbidden spectrum has been multiplied by a correction factor. In this case, the areas are compared when each spectrum is assumed to be allowed. One might alternately calculate back from each Kurie plot to find the true spectrum and then compare those areas.

To simulate a complex spectrum, a Pm^{147} and a Cs^{137} sample were examined simultaneously. The samples were on separate plates placed such that the Pm^{147} sample was closest to the phosphor. Here the 2.2-Mev detector was used. The spectrum was analyzed as if it were due entirely to Cs^{137}. After correcting for forbiddenness the Kurie plot shown in Figure 33 was made. The Cs^{137} component was subtracted out, and the remaining plot corrected back to give the Pm^{147} spectrum. The resulting Pm^{147} Kurie plot appears in Figure 34. The areas under

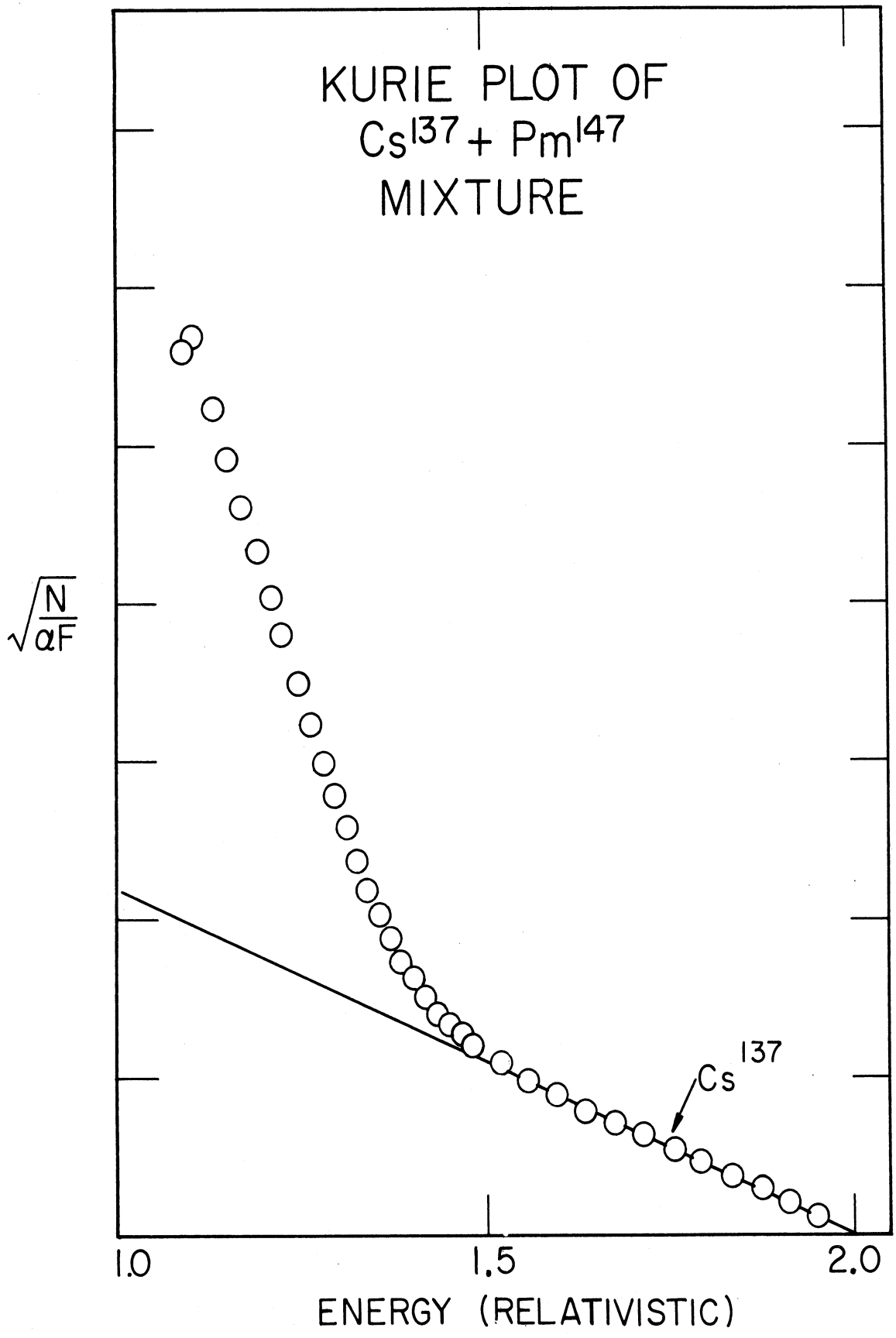

Figure 33. Kurie Plot of Cs^{137} + Pm^{147} mixture

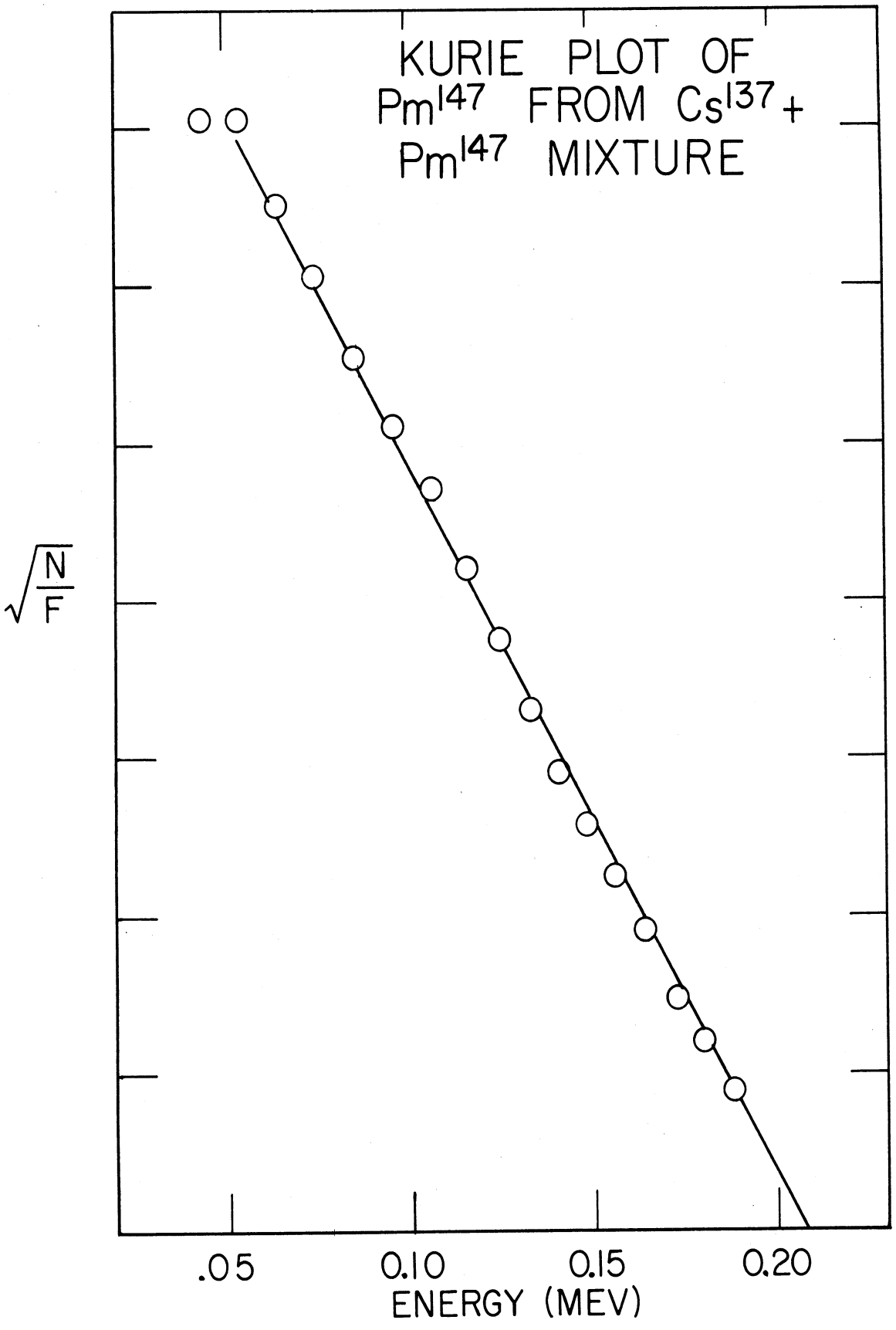

Figure 34. Kurie plot of Pm^{147} resolved from Cs^{137} + Pm^{147} mixture

both Kurie plots were compared with the Kurie plots taken individually on each sample. The ratio of the areas in the mixture was within 4% of the ratio from the individual samples. This is considered to be within the experimental error since the phosphor had been remounted before the mixture was analyzed.

Consider next the complex spectrum of Rb^{86}. Of the β rays present, the first has a reported energy of 0.68 Mev and a relative abundance of ~ 10%. The second β ray is ~ 90% abundant with E_{max} = 1.77 Mev. The branching ratio is not accurately known; some relative values for the higher energy component go as low as 80% and as high as 92%. While the higher energy component is forbidden, several investigators have found an allowed shape for the lower transition. Figure 35 shows the Kurie plots obtained with the 3.6-Mev phosphor. The branching of the lower component as determined here is ~ 12%. The endpoint of 0.60 Mev is considerably lower than is indicated in the literature. Since the higher energy component's endpoint is within 1% of the literature value of 1.77 Mev, it is assumed that any errors must lie in the graphical resolution. In a spectrum like this, coincidence techniques are of great value.

11. Positron Emitters.

The β spectrum of a positron emitter may also be obtained using the scintillation detector if a three-channel coincidence spectrometer is available. With positron emitters the difficulty lies in the presence of annihilation radiation. When the positron reaches the end of its range and is annihilated, the resulting energy is given off primarily in the form of two γ rays, each 0.511 Mev in energy, and emerging

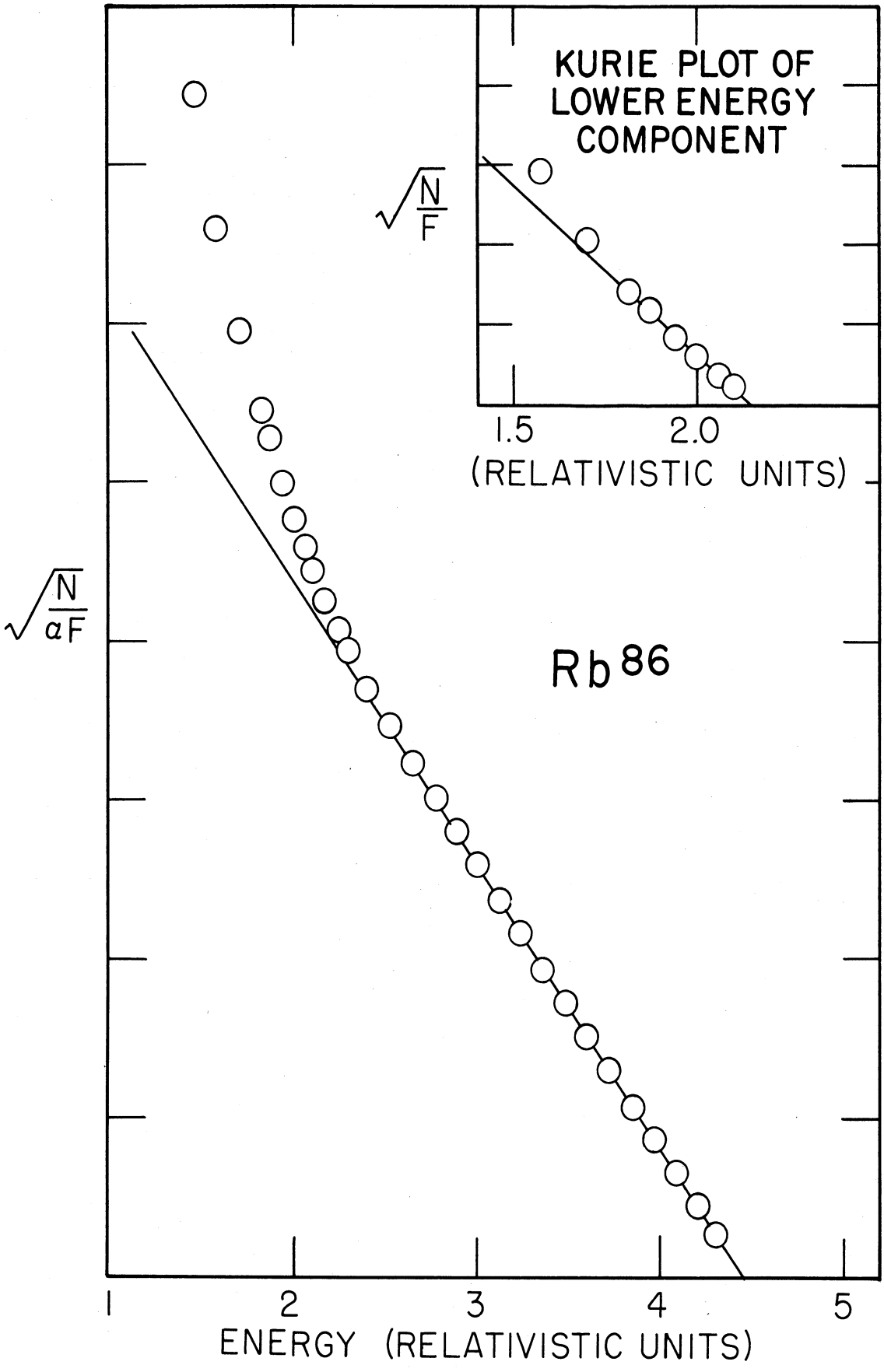

Figure 35. Kurie plot of Rb^{86}. For energy in Mev see Appendix B, Figure 67.

at 180° to each other. Since the γ rays will originate in the detector itself, there is no simple way of determining the γ background. Furthermore, since the γ radiation is in coincidence with the β pulse, an unknown amount of energy, from zero up to the Compton Edge ($\sim$ 0.34 Mev) of the 0.511-Mev γ pulse distribution, will be added to the energy of each β pulse. Actually no positron spectra were measured in this work, but a method for obtaining these spectra is given below.

Using the three-channel coincidence arrangement shown in Figure 36, the distortion will be for the most part eliminated. The detectors marked 1 and 2 are NaI(Tl) crystals, and their associated pulse-height analyzers are set on the 0.511-Mev γ energy. When the positron is annihilated in the β detector (say at the place marked with an x), the two γ rays will have a certain probability, dependent upon the geometry, of one entering each NaI(Tl) detector as shown. Thus, disregarding chance coincidences, if both detector 1 and 2 simultaneously "see" a 0.511-Mev γ ray, this means the β pulse is undistorted since neither γ ray lost any energy going through the β detector. By setting all three channels in coincidence only those positrons whose energy pulses are undistorted will be detected, and the β spectrum may be scanned in the usual way. In this arrangement positron spectra may be determined in the presence of accompanying negatron radiation.

As in all coincidence work relatively intense sources or long counting times are necessary in order to achieve good statistical results. Particularly so in this case, since in order to register a coincidence count both γ rays must pass through the β detector without

losing energy, both must strike a γ detector, and both must produce a pulse in the photopeak region. Using 1" x 1-1/2" NaI(Tl) crystals and the 2.2-Mev β detector previously described in a reasonable geometry, one might expect to find a coincidence counting rate down by a factor of $\sim 10^3$ from the true β counting rate.

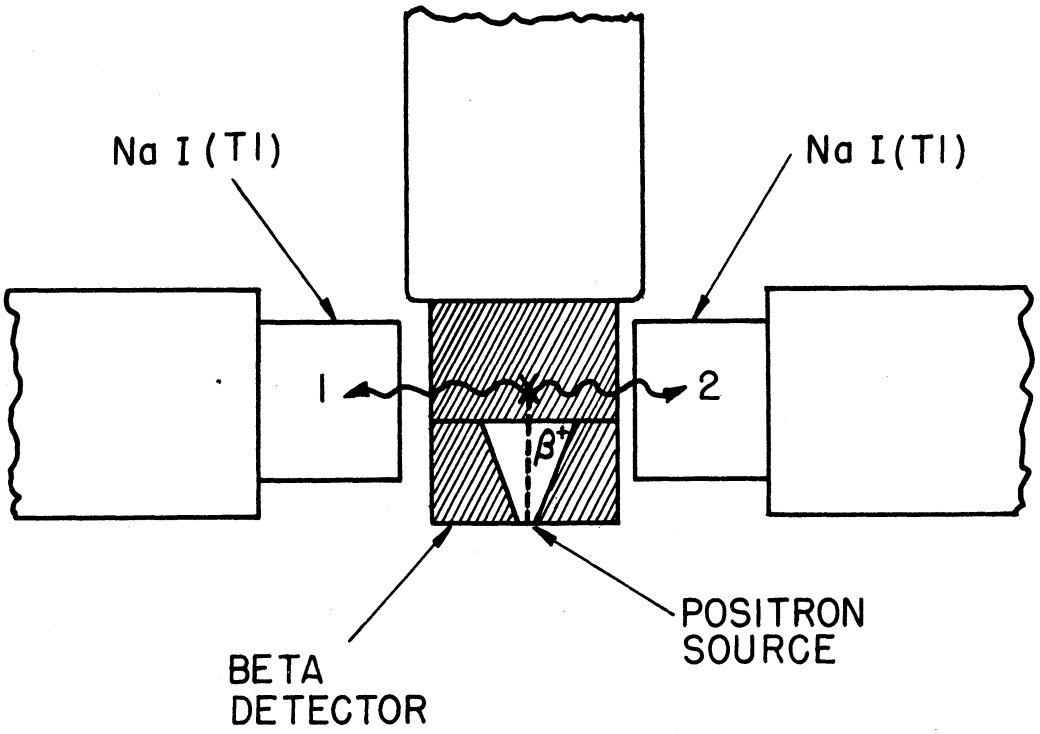

Figure 36. Three-channel coincidence arrangement for positron emitters

12. Conversion Coefficients.

An excited nucleus, which would normally make a transition to a lower state by emitting a γ ray, may lose energy by another process. The alternative process, called internal conversion, involves the ejection of one of the orbital electrons. Here the electron appears with the energy of the γ ray minus the binding energy of the shell from which it was ejected. A third process wherein an electron-positron pair is emitted occurs relatively seldom compared to internal conversion. It is primarily found at high energies and/or low atomic numbers. The transition energy has to be greater than 1.02 Mev. For $0 \rightarrow 0$ transitions no conversion or γ-ray emission is possible and pair emission becomes important.

We shall define the conversion coefficient α as follows:

$$\alpha = \frac{N_e}{N_\gamma} = \alpha_K + \alpha_L + \alpha_m + \ldots \qquad (13)$$

where N_e is the number of conversion electrons emitted, and N_γ is the number of γ rays. As defined, α is the total conversion coefficient, and is the sum of the conversions coefficients for each electron shell as indicated by the subscripts. It is understood that α_L, for example, is the sum of the subshell coefficients:

$$\alpha_L = \alpha_{L_I} + \alpha_{L_{II}} + \alpha_{L_{III}} \qquad (14)$$

Conversion coefficients are of interest because they are quite sensitive to the following parameters:

1. The atomic number of the emitter.
2. The transition energy.
3. The particular shell or subshell.

4. The multipolarity L of the competing γ radiation.

5. The character of the nuclear transition, i.e. electric or magnetic.

Gamma rays may be classified by multipole orders L, according to the angular momentum carried off by each quantum. For each order there are two subclasses electric 2^L pole (EL) and magnetic 2^L pole (ML). These differ with respect to parity as is shown in the table below.

TABLE XII. POSSIBLE MULTIPOLARITIES FOR GAMMA RADIATIONS

Parity Change	Angular Momentum Change				
	0 or 1	2	3	4	5
No	M1(E2)	E2(M3)	M3(E4)	E4(M5)	M5(E6)
Yes	E1(M2)	M2(E3)	E3(M4)	M4(E5)	E5(M6)

The transition in parenthesis is usually not significant. Once L is fixed, the character of the nuclear transition uniquely fixes the parity change. Furthermore, the transition probability is a function of L and the character of the transition. As is expected, the larger the number of units of angular momentum the quantum must carry off, the smaller is the transition probability and the longer is the half-life of the state. In Cs^{137}, where the transition is the type M4, a delayed state exists with a half-life of about 2.6 minutes.

Conversion coefficients are measured in a variety of ways depending upon the particular isotope involved. If no β rays occur the

number of conversion electrons are compared with the number of x-rays or γ rays emitted. In other cases, the number of β rays emitted may be used to calculate the γ-ray intensity. After the coefficient is measured, it is compared with tables such as those by M. E. Rose, et al. (119) in order to deduce the type of transition involved.

In most cases the instrument described here, due to its relatively poor resolution, will not be able to resolve K electrons from L or M electrons. This is unfortunate since $\frac{\alpha_K}{\alpha_L}$, $\frac{\alpha_{L_I}}{\alpha_{L_{II}}}$, and $\frac{\alpha_{L_{III}}}{\alpha_{L_I}}$ ratios are generally more sensitive in energy dependence than the absolute conversion coefficients. Nevertheless, in many cases the coefficients differ sufficiently so that only the total conversion coefficient need be used.

Using Figure 40 and assuming a symmetrical conversion peak, the conversion coefficient for Cs^{137} was measured by integrating under the peak and the β spectrum. Assuming an $\frac{\alpha_K}{\alpha_L}$ ratio of 5 (26), the α_K for the corrected curve was found to be 0.095. For the uncorrected curve α_K was 0.082. These may be compared to 0.094 as given by Rose's tables for M4 radiation, and 0.097 as determined experimentally by Waggoner (26).

The coefficients from both the corrected and uncorrected curves are good enough to determine the type of transition if the transition is assumed to be "pure." If the possibility of mixed transitions is considered, then the uncorrected value would lead to erroneous results.

13. Comparison with Flat Detectors.

As another means of evaluating the hollow-type detector, a comparison was made with the results obtained with a flat detector. The flat detector was made by using the base of the 2.2-Mev hollow scintillator covered with a 1.5-mil sheet of aluminum foil. The detector was coupled as usual to the phototube, while the source was placed 2.2 cm from the detector along its axis.

Figure 37 shows the results for Cs^{137}. The table below presents some of the information obtained from the spectra.

TABLE XIII. COMPARISON OF FLAT AND HOLLOW DETECTORS

Detector	Resolution	Conversion Peak to Valley Ratio
Flat	23%	4/1
Hollow	14%	6/1

The better resolution of the hollow-type detector proves advantageous when dealing with conversion electron peaks, endpoints of spectra, complex spectra, and other cases where the slope of the spectrum changes rapidly. Also, the better resolution facilitates the recognition of forbidden shapes which usually appear smeared out with poorer resolution. It should be noticed that in Figure 37 the flat detector spectrum is badly distorted at the lower end. This is probably due to the fact that for a given angle of incidence, the lower the energy of a β particle the greater is its probability of scattering out of the

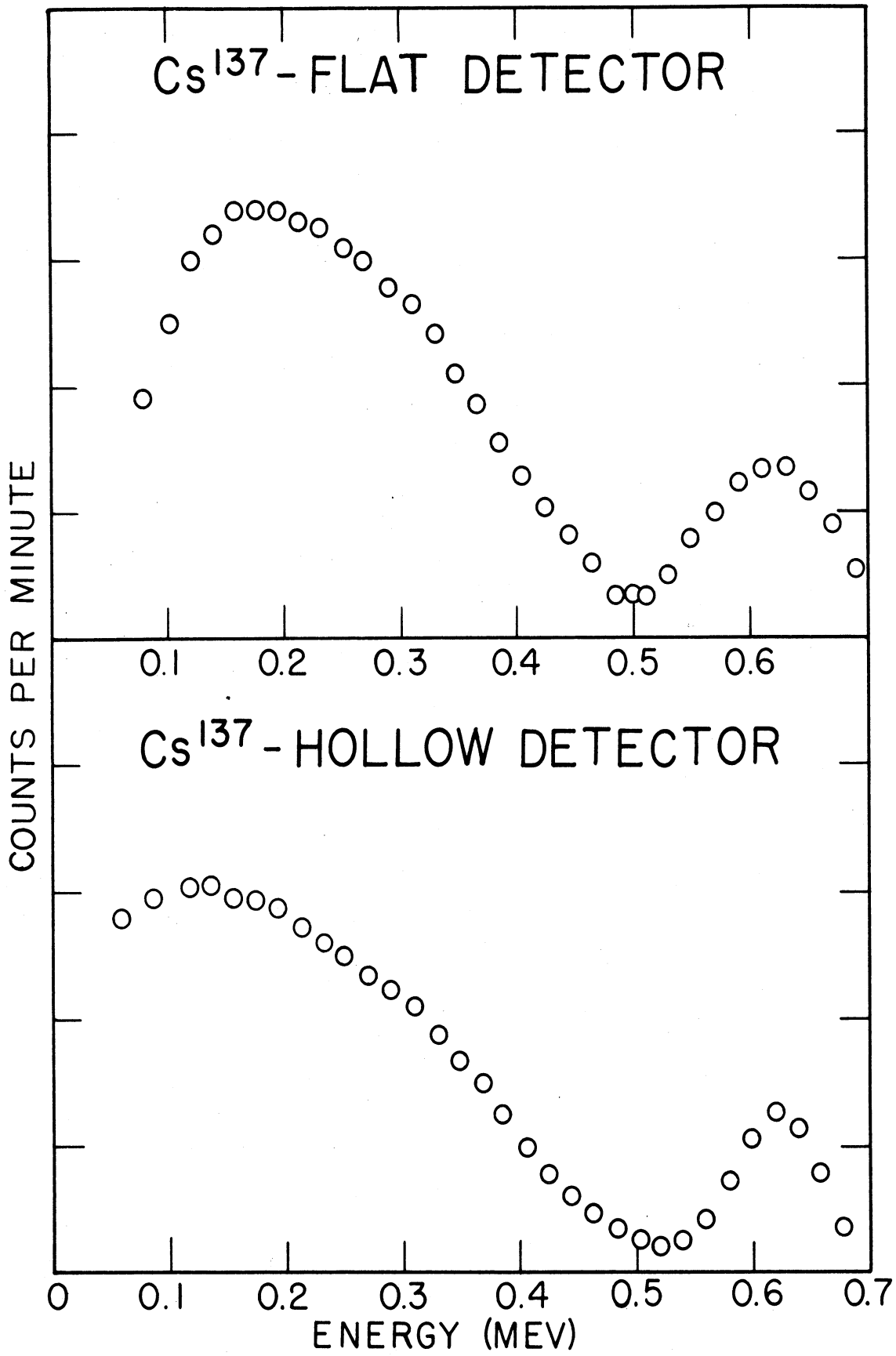

Figure 37. Comparison of flat and hollow detectors

detector. Figure 38 compares the Kurie plots of P^{32} obtained on the two types of detectors. While the flat detector produces a Kurie plot that is linear over about half the range, the hollow detector's plot is linear over more than three-quarters of the range. On both curves the sharp upward curvature at the lower end is due to P^{33} in the sample.

14. Correction for Instrument Resolution.

Because of the low resolving power of β-scintillation spectrometers, the observed spectral shape does not correspond exactly to the true shape. In fact, at both the low energy and the high energy ends the distortion usually proves to be very significant.

The experimentally measured spectrum M(E) is related to the true spectrum N(E) by the equation

$$M(E) = \int_0^{E_{max}} N(E)S(E)dE \qquad (15)$$

$$\approx \sum_i N(E_i)S(E_i)\Delta_i E$$

where S(E) is the so-called instrument profile (112). Until recently, the usual approach to this problem was to assume that S(E) could be represented by a Gaussian distribution of the form

$$S(E) = \frac{A}{\sqrt{2\pi\sigma^2}} e^{-\frac{(E_o - E)^2}{2\sigma^2}} \qquad (16)$$

where A is a normalizing constant, and σ^2 is the variance of the pulse height distribution for a monenergetic beam of electrons of energy, E_o. Katelle (71), and Palmer and Laslett (113) have used this approach, based on the method of Owen and Primakoff (112). In the body of the spectrum this method has uniformly failed to eliminate upturns at low energy. At

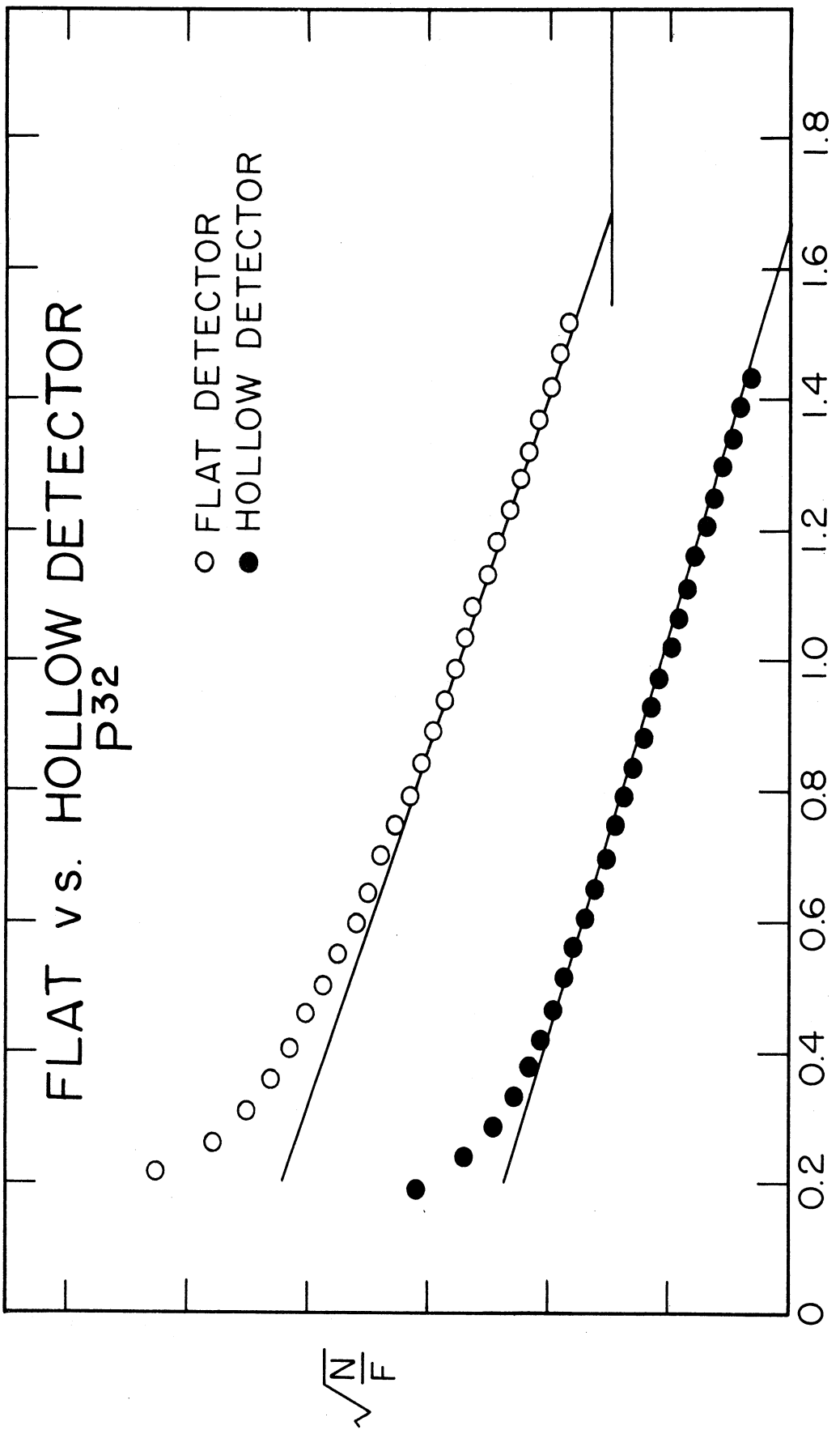

Figure 38. Kurie plots for P^{32} from both flat and hollow detectors

the high energy end near E_{max}, however, the procedure works well. A suitable correction factor is illustrated graphically in Reference 113, and has been used to correct all of the spectra shown in this work up to this point. The correction factor is a function of the maximum β energy. Therefore, in order to determine the correction, an endpoint must first be estimated. Thus, the correction serves only to indicate whether or not the observed data are donsistent with the estimated endpoint. Figure 39 shows the correction applied to the Kurie plots of Cs^{137} and Pm^{147}.

Another method for resolution correction, due to Bracewell (17), also uses a Gaussian distribution. The method has the advantage that it is simple and easy to apply. When applied to the Cs^{137} spectrum, the results are shown in Figure 40. Since the method is graphical, the correction is not too exact. The resolutions calculated from the peaks in Figure 40 are:

Uncorrected - 14.7%

Corrected - 12.7%

Probably the best approach to the resolution problem was put forth by Freedman, et al., in June, 1956 (45). They made the reasonable assumption that the instrument profile was not symmetrical, and that a monoenergetic beam of electrons will produce a profile that is measurable down to zero energy. Figure 41 illustrates this point.

Four conversion peaks were measured in their work, and it was found that the relative height of the tail of the curve remained

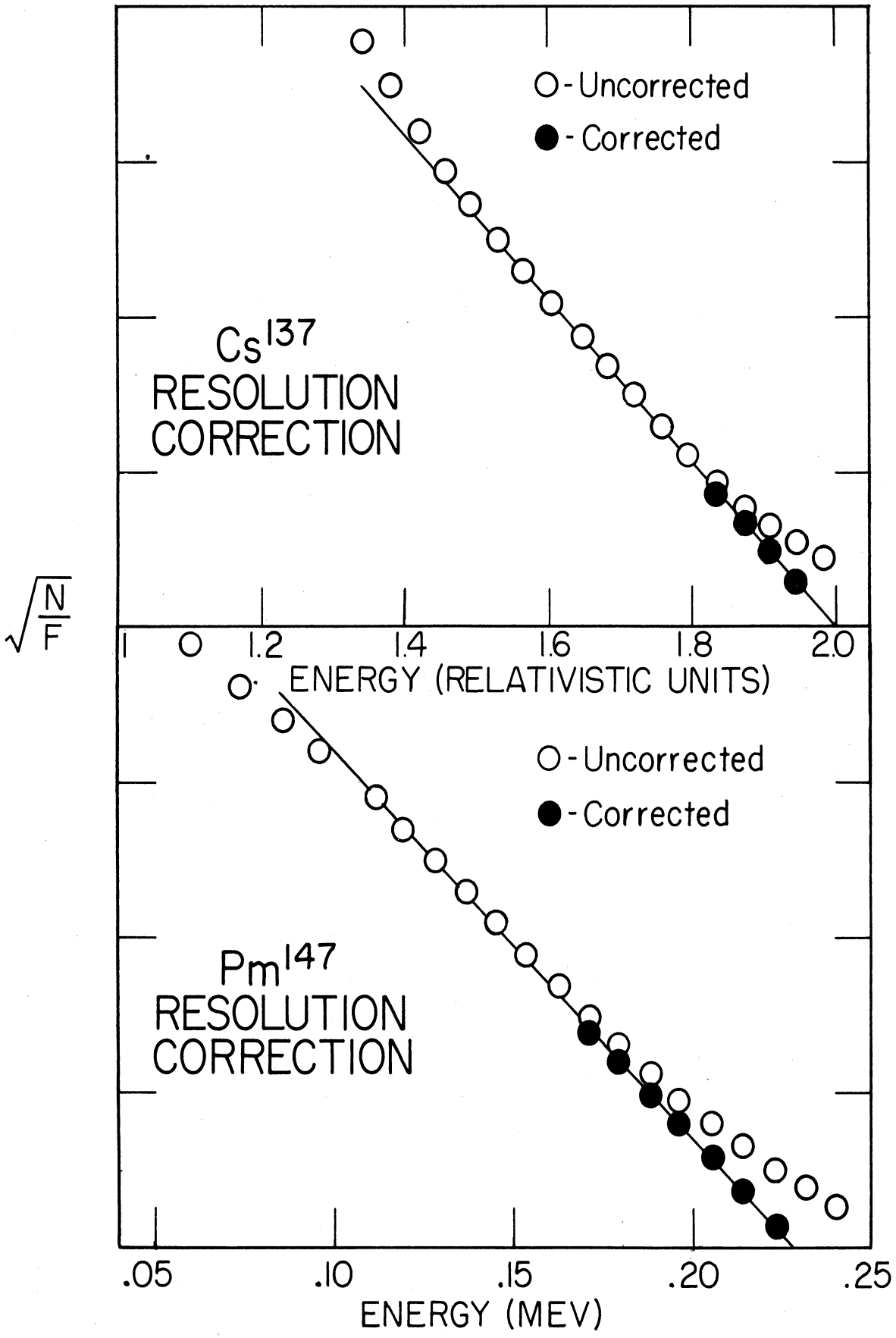

Figure 39. Effect of resolution correction near the endpoint of beta spectra. For energy in Mev see Appendix B, Figure 67.

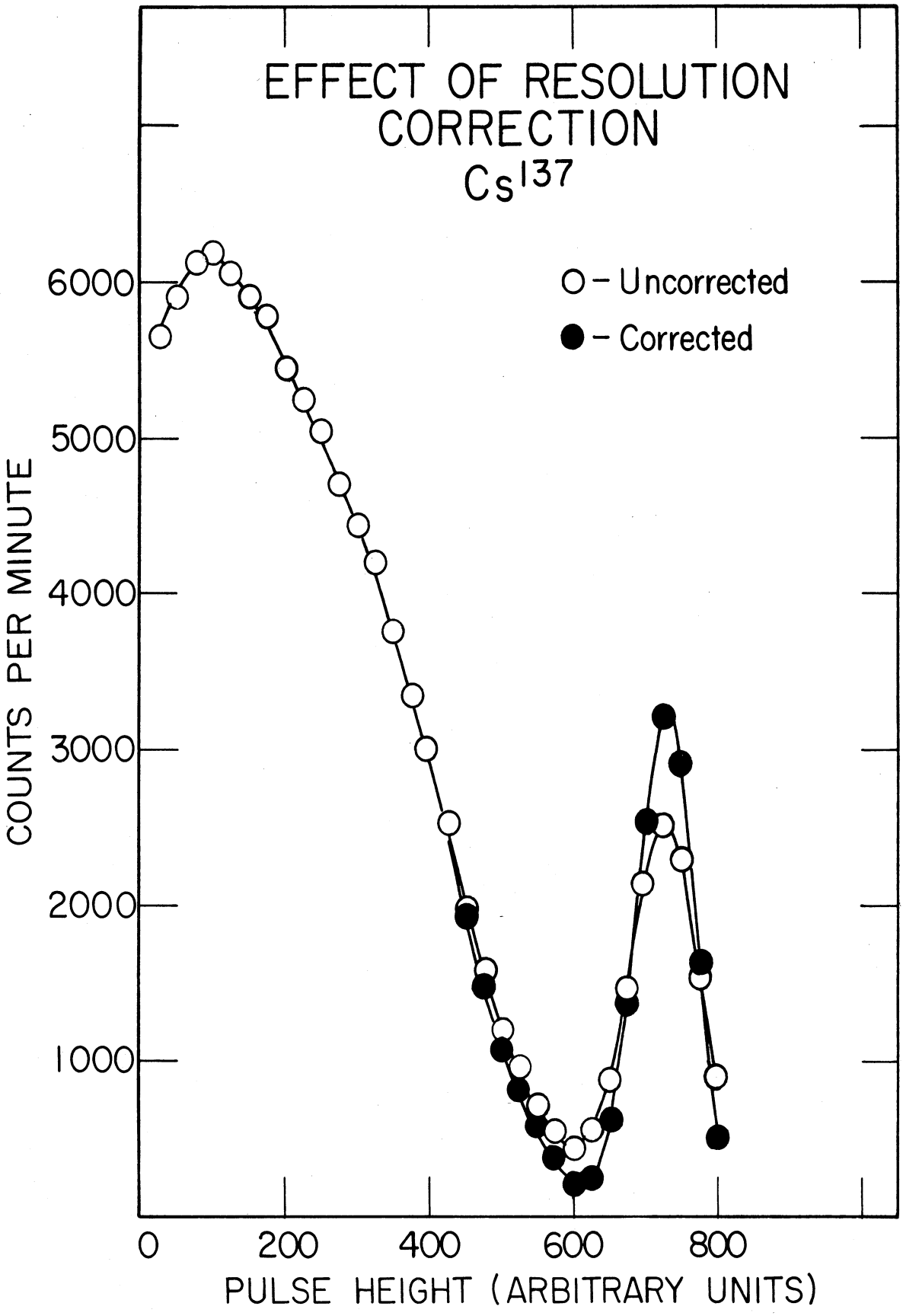

Figure 40. Resolution correction by Bracewell

essentially constant, and was 7.5% of the peak intensity for each conversion peak.

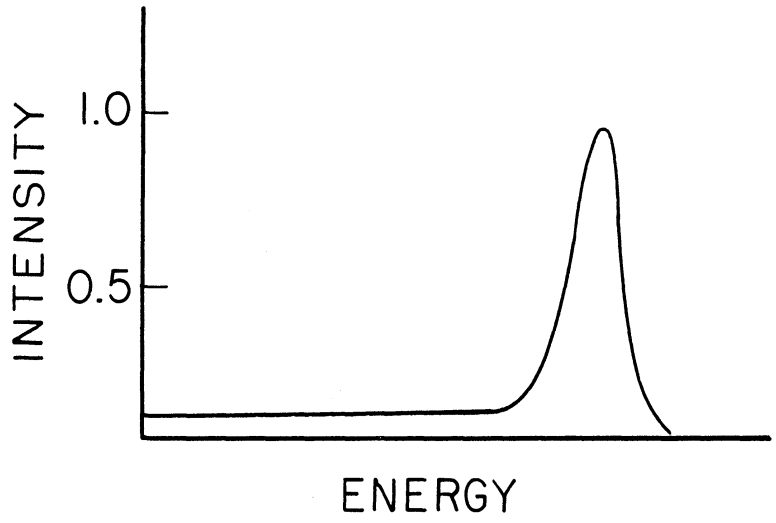

Figure 41. Form of experimental line shape determined by Freedmen, et al

To obtain N(E) from Equation (15), a zero-order approximation to N(E) is made: $M(E)/\Delta E$, where ΔE is the window width. The integration is performed numerically producing a new $M_1(E)$. If S(E) has been absolutely normalized, the new spectrum will have the same area as the

original M(E). A first approximation to the true spectrum is now obtained.

$$N_1(E)\Delta E = M(E) - [M_1(E) - M(E)]$$
$$= 2M(E) - M_1(E) \qquad (17)$$

Next $N_1(E)$ is put into the integral and the numerical integration repeated to obtain a second approximation. Usually two to four approximations were needed to obtain a spectrum which, when used in the integration, reproduced the experimental curve to within 2%.

The above procedure has been used here to correct the Kurie plots of two spectra, and was found to be excellent. Figure 42 shows the profile of the Cs^{137} conversion peak obtained by requiring coincidence with the x-ray. In this work, it was found that the height of the tail of the profile was 5.0% of the peak intensity, for the 2.2-Mev detector. Knowing that the half-width of the peak is a function of energy (113), the following equation was used to construct profiles at any given energy once one profile was measured:

$$W_{1/2} = CE^{1/2} \qquad (18)$$

where $W_{1/2}$ is the half-width, C is a constant, and E is energy.

Figures 43 and 44 show the effect of this type of resolution correction on the Kurie plots of Cs^{137} and Y^{91}. In the case of Cs^{137}, the Kurie plot is straightened out down to 0.05 Mev. For Y^{91} the Kurie plot now is straight down to 1.2 relativistic units or about 0.1 Mev.

15. Summary.

A β-ray spectrometer of the scintillation type has been designed, built, and evaluated. Using a hollow plastic detector the resolution has

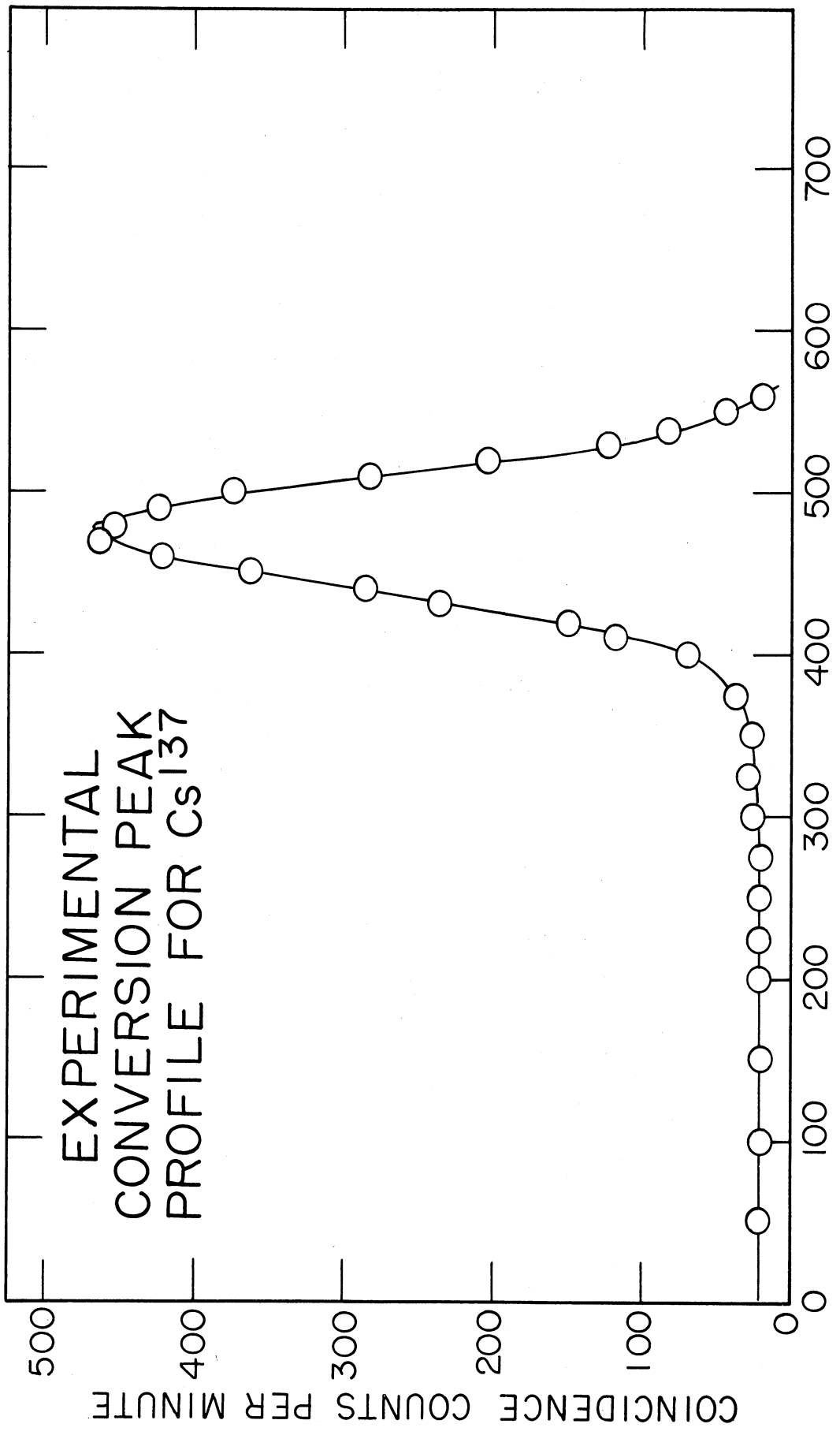

Figure 42. Experimental conversion peak profile for Cs137

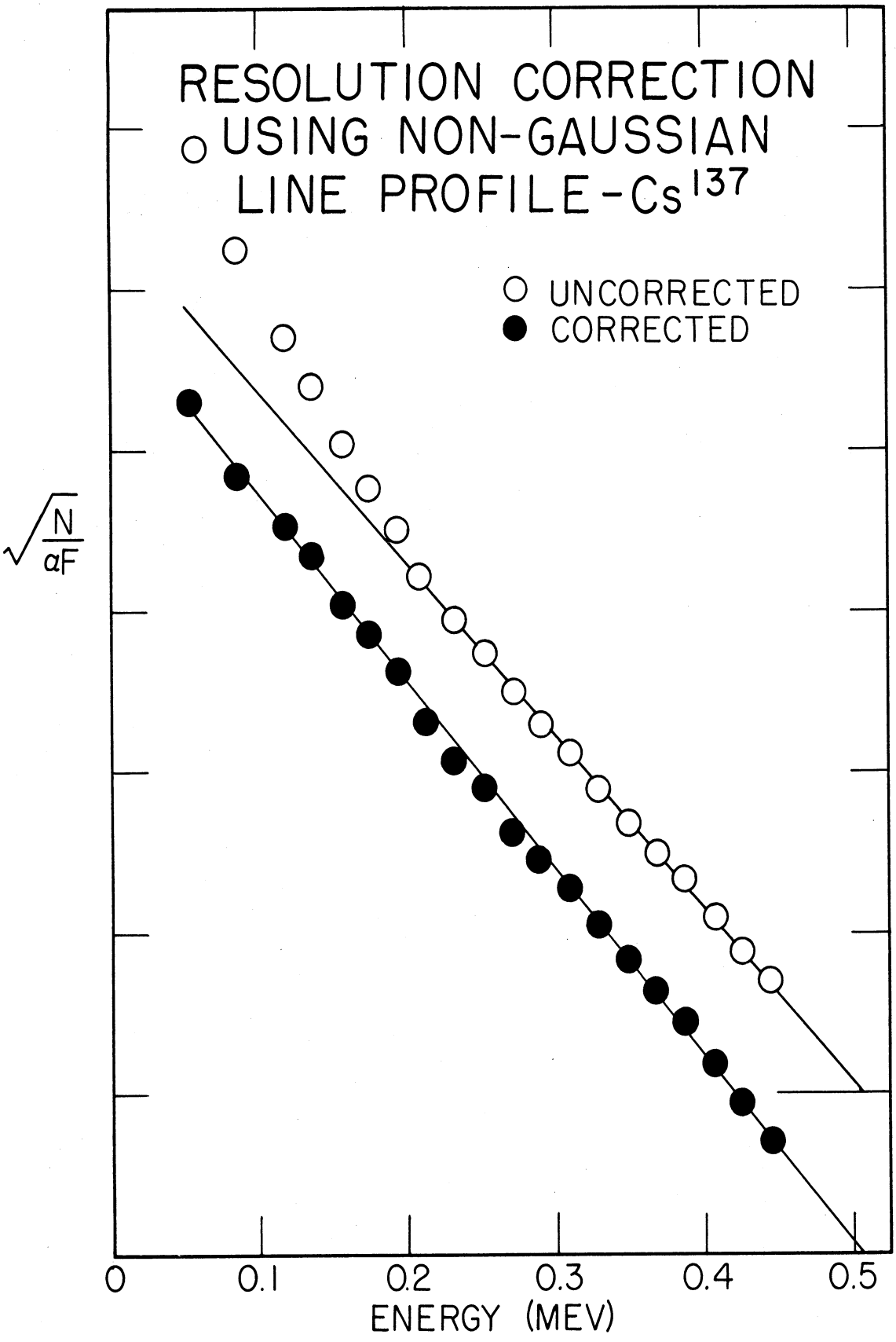

Figure 43. Effect of Non-Gaussian Resolution correction on Cs^{137} Kurie plot

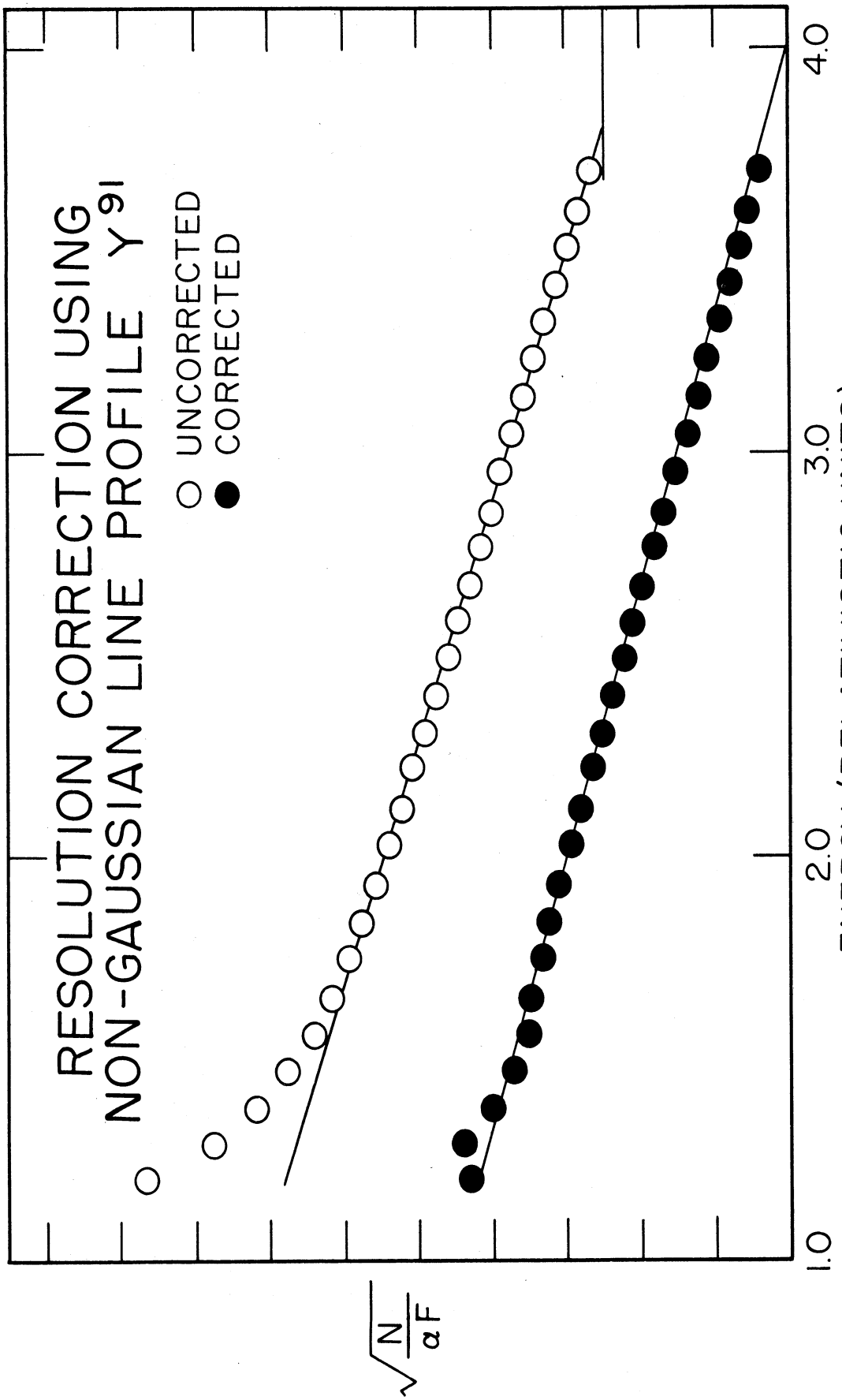

Figure 44. Effect of non-Gaussian Resolution Correction on Y^{91} Kurie plot. For energy in Mev see Appendix B, Figure 67.

been improved by a factor of about 2 over a flat-type detector. Even more important is the fact that electrons scattered out of a flat detector cannot easily be corrected for. This effect has been greatly minimized by using a hollow detector. Finally, when necessary, the still relatively poor resolution may be corrected for using a non-Gaussian instrument profile scheme.

CHAPTER V

DATA ANALYSIS: APPLICATION OF DIGITAL COMPUTERS

Two principal types of problems encountered in this work require lengthy mathematical calculations. These are the Kurie analysis, discussed in Chapter II, and the resolution of complex radioactive decay curves. It, therefore, seemed advisable to make use of the computational facilities availabe at the University of Michigan.

The IBM 650 Digital Computer was used. It is of medium size (2000 words of storage) and has a magnetic-drum type memory. Punched cards are used for input and output. Physically, there are three separate units that comprise the computer. These are:

1. The type 553 Read-Punch Unit. It is here that the instructions are fed into the machine, and where the results are punched out. Maximum input and output rates are 200 cards per minute and 100 cards per minute, respectively.

2. The type 650 Console Unit. This unit contains the magnetic drum on which information necessary to process a problem is stored. There is also a console from which information may be read into the memory, or displayed from the memory on the display lights.

3. The type 655 Power Unit. This contains all of the power supplies for the other units. It also translates the decimal input into the machine code, and the machine code into decimal output.

The set of instructions used by the machine to compute the desired results is called a "program." There are certain routines available which facilitate the writing of programs; these will be re-

ferred to under each specific program. In the program itself, one instruction is written per card.

After the program is read into the machine, the data cards are then entered. The form of the data cards varies, and will be given for each program. After the computation is completed the results appear on punched cards and can then be printed out on the Reproducer.

A. Kurie Analysis

1. Computer Program for Kurie Computation.

The program was first written in symbolic notation in which no definite drum locations or "addresses" were used. This was then assembled and optimized by means of a program known as S.O.A.P., Symbolic Optimal Assembly Program. By means of this program addresses are assigned for the instructions in such a way that a minimum of time is required to perform the program.

All data are punched on cards in eight groups or "words" each containing ten digits. The first word on each data card contains the address of the first piece of data on the card along with the total number of pieces of data on the card. This is the usual seven word format used when data are to be read in by means of the seven word loading routine.

The Kurie analysis program is essentially a data handling program. Seven tables are stored in the computer. The experimental data are modified and correlated by means of extensive "table look-ups," interpolation within the tables, and simple arithmetic calculations. The following tables must be supplied, along with the instructions.

1. Table A contains the disintegration rate for each point in the β spectrum. A maximum of 51 points may be used, and the maximum rate is 99,999.99999 counts per unit time.

2. Table B contains the energy in Mev associated with each point. Again a maximum of 51 points may be used. The maximum energy permitted is 999.9999999 Mev.

3. Table C is the list of energies that serves as the argument for Table D. This table is the same for every element.

4. Table D is the list of values of the Fermi function as listed in Reference 99. A separate table must be made for each different element to be analyzed. There are on hand at present tables for S, P, Pm, Sr, Y, Rb, In, Cs, and Hf.

5. Tables E and F contain the information necessary to correct the Fermi function for the screening effect in the base of the β^- emission. The data come from Table 6 of Reference 99.

6. Table G contains the energy argument for Tables E and F, and is the same for any value of Z.

7. V1 and Z1 are two numbers on a single card, different for each element. V1 is the "outer screening potential" referred to before. It is obtained from the K binding energy data given in Figure 13 of Reference 72. Z1 is a number needed to interpolate in the E and F Tables.

When the output cards are read by the Reproducer, the results of the Kurie analysis appear in two columns. The first column is the list of energy values, directly opposite which, in the second column, appear the appropriate ordinates for the Kurie plot. At present, forbidden spectra are not correct in the machine.

While the IBM 650 computation time for an average Kurie analysis of thirty points is less than one-half minute, the overall time required to analyze a spectrum may be about one-half hour since it is necessary to punch the data on input cards. A hand calculation of the problem might require a day or longer. Over sixty computer analyses have been run to data. Figure 45 is a flow diagram of the program.

2. Simple Least-Squares Line Fit

A simple least-squares program was written primarily to be used to determine more accurately the endpoints of Kurie plots. However, the code is general purpose and may be used whenever a straight line is to be fitted to data. Some examples of its use are: analyzing one or two component decay curves, interpolation in and extrapolation of tables, and accurate calibration of linearly behaving equipment.

The principle of least squares states that the best representative curve that can be fitted to a set of data is that curve for which the sum of the squares of the residuals is a minimum. Using the equation of a straight line:

$$a = a_o + bt \tag{20}$$

the residual r_i for the i^{th} measurement would be:

$$r_i = a_o + bt_i - a_i \tag{21}$$

The least-squares program was coded in MITILAC, an interpretive routine which simplifies coding for small problems. The data are punched in the standard MITILAC data card format. The program was designed to be able to analyze any number of curves without having to read in the MITILAC deck and the instructions each time.

START

↓

Using B table elements interpolate in tables C and D to find Fermi Functions for each energy.

↓

Using B table elements, and Z1, double interpolate in table E, F, and G to find screening correction factors.

↓

Screening correction factors times V1 % corrections.

↓

Modify Fermi Functions by correction terms to get f_{cor}.

↓

$$\frac{\text{Counting rate}}{f_{cor}}$$

↓

$$\frac{\text{Counting rate}}{f_{cor}} \; 1/2$$

↓

Punch out Energy and Kurie Plot ordinate tables.

↓

STOP

Figure 45. Flow diagram of Kurie plot calculation by the IBM 650 computer

The program fits a straight line to a maximum of 200 points in $\sim$ 1 minute. The results of the computation appear on one card. The first word is the ordinate intercept, the second word is the slope of the line, and the third word is the abscissa intercept.

B. Decay Curve Analysis

Accurate knowledge of decay constants is of real value both from a theoretical and also a practical point of view. The determination of cross-sections of nuclear reactions is a good example. The number of atoms produced in a given reaction is usually determined by following the decay of the product nuclei if they are unstable, and extrapolating the decay curve back to a "zero" time. This extrapolation presumes the knowledge of the half-life, and hence the value of the cross-section will be in error by at least the error in the half-life. Log (ft) values described in a previous chapter also require a knowledge of the half-life. Information of a fundamental nature in β-decay theory may be obtained from knowledge of transition probabilities and half-lives of meta-stable states. The identification of components in a radioactive mixture may sometimes best be done by half-life measurements if short half-lives are involved. In any case, a half-life measurement may be used to confirm an identification based on other facts, or if determined first may limit the choice so that further confirmation may be facilitated.

A second and equally as important problem is the determination of the true number of components that make up the decay curve. If the actual number of components is uncertain or arbitrarily determined by the experimenter, the concept of accurately determined half-lives has no meaning.

Since accurately known half-lives are valuable and since it is technically feasible and even convenient to obtain good decay curves, the answer to the question of why half-lives are not measured more accurately must lie in the actual analysis of decay curve data. The decay of radioactive nuclei is a first order process, and may be represented by a differential equation of the type:

$$-\frac{dN}{dt} = N\lambda \tag{22}$$

where λ is the decay constant and N is the number of atoms of a given type that are present at time t. Integration gives:

$$N = N_o e^{-\lambda t} \tag{23}$$

where N_o is the number of atoms present at "zero time." In terms of observed counting rate A, Equation (23) becomes

$$A = A_o e^{-\lambda t} \tag{24}$$

If several different radioactive species are present, the observed counting rate h(t) is then

$$h(t) = \sum_{i=1}^{n} (A_o)_i e^{-\lambda_i t} \tag{25}$$

$$i = \text{integers from 1 to n}$$

The problem may now be stated as follows: a function h(t) is approximated by experimentally determining an estimate of h(t) at a finite number of values of t. From this discontinuous set of data it is desired to obtain n (total number of components) and estimates of the $(A_o)_i$'s and λ_i's. An error analysis is also desired, based on the errors inherent in the method of solution, as well as in the values of h(t) and t. It should be noted that in Equation (25) the exponentials are all assumed to be separate and

unrelated. In the physical case this means that there are no decay chains involved; each radioactive parent decays into a stable daughter product.

The essential difficulties in the solution of this problem are that we are dealing with a series of non-linear equations, and that the data are only approximating the function h(t) over a finite range of t. The importance of the cut-off of h(t) at a finite t depends upon the method of solution. Since there can be no analytic solution to the problem, a numerical approach must be taken. Applications of techniques in numerical analysis make possible an approximation to the solution. The computational labor involved, which would normally be prohibitive, is now no longer a problem due to the advent of high-speed digital computers.

Several approaches to the problem of decay curve analysis will be reviewed, including a method that apparently has not been successfully applied to this problem before. At present the author knows of no truly satisfactory method for solving this problem that has actually been tried. Most methods do not make use of all of the accuracy inherent in the data, impose conditions on the data that cannot realistically be fulfilled, do not necessarily converge to the proper solution, or else are incapable of yielding an error analysis. It would seem that the solution proposed will in part overcome these difficulties.

1. A Review of Previous Methods

a. Graphical Method. By far the most common method used to resolve a decay curve into its components is the graphical approach. Here one plots the counting rate as a function of time on semilog paper.

The last portion of the curve where only one component remains will appear as a series of points to which a straight line may be fitted (see Figure 46). This is arbitrarily done using a straight edge after determining by eye where the straight line segment ends and the upward curvature begins. The straight line segment is extended back to time "zero" and the subtraction or "peeling off" procedure is begun. The ordinate values from the extended line used in the subtraction are read from the graph as is the intercept at time zero. Normally, the half-life is read directly from the graph. The peeling off process is repeated until the entire curve has been analyzed.

The limitations of the method are apparent. Each straight line is fitted with no better criteria than a visual impression. Human judgment rather than some mathematical treatment is used to determine the number of components. Fictitious components may be introduced or real components overlooked in this process. For details on the errors introduced by the peeling off procedure see the next section, titled "Least-Squares Method."

In this graphical method there is no error analysis, and hence no criteria on which to base a judgment as to which combination of components out of many possible combinations is the best. Finally, values are plotted on and read from a graph, which in itself is a practical limit to accuracy. The method is, however, certainly the easiest to perform.

b. Least-Squares Method. The graphical method may be considerably refined by employing a least-squares curve fitting procedure. This procedure may be applied only to equations linear in the coefficients,

or equations that may be reduced to a form linear in the coefficients (121). Consider the form of a single component decay curve written in terms of counting rates:

$$A = A_o e^{-\lambda t} \tag{24}$$

This may be transformed to give

$$\ln A = \ln A_o - \lambda t \tag{26}$$

which is linear in the coefficients ln A_o and t.

Two forms of the least-squares method have been programmed for the computer. The first is the simple, or unweighted, line fit previously described. It may be used to analyze a single component decay curve of the form shown in Equation (26). Even two component curves may be treated in the following way (7):

Assume that the half-lives of the two components are known and it is desired to obtain the activities A_1 and A_2 of the two components at a certain time t_o called the "zero time." This is the case where nuclear reaction cross-sections are concerned. The total observed activity is

$$h(0) = A_1 + A_2 \tag{27}$$

and at any time t the expression becomes

$$h(t) = A_1 e^{-\lambda_1 t} + A_2 e^{-\lambda_2 t} \tag{28}$$

where λ_1 and λ_2 are the decay constants and t is the time interval between zero time and the time of determining h(t).

Two cases present themselves:

Case I. Here the half-life of A_2 is very long compared to A_1, and A_2 remains essentially constant over the period of the decay measurements.

Then $e^{-\lambda_2 t} \approx 1$ and the expression becomes

$$h(t) = A_1 e^{-\lambda_1 t} + A_2 \qquad (29)$$

This expression is in the form of a straight line with h(t) as the ordinate values and $e^{-\lambda_1 t}$ as the abscissa values. A least-squares determination of the slope of this line gives A_1 while the ordinate intercept gives A_2.

Case 2. Here the half-life of A_2 is of the same order of magnitude as A_1. The expression then becomes:

$$\frac{h(t)}{e^{-\lambda_2 t}} = \frac{A_1 e^{-\lambda_1 t}}{e^{-\lambda_2 t}} + A_2 \qquad (30)$$

When $\frac{h(t)}{e^{-\lambda_2 t}}$ is plotted against $e^{-(\lambda_2 - \lambda_1)t}$, the slope is A_1 and the ordinate intercept is A_2. Since the above equation only holds when there is a finite amount of A_1 activity present, a divergence from linearity will occur when the ratio of the activities becomes very small. In practice the curved portion should be neglected when the data are being analyzed.

The second least-squares method involves the use of weighted ordinates. Recall Equation (26):

$$\ln A = \ln A_o - \lambda t \qquad (26)$$

Define $\ln A = a$, $\ln A_o = a_o$, and $-\lambda = b$. The equation now becomes

$$a = a_o + bt \text{ (equation of straight line)} \qquad (20)$$

The residual for a given measurement is defined as:

$$r_i = a_o + bt_i - a_i \qquad (21)$$

If the measurements are not all of equal precision, or as in the present case the residuals are of a function of a variable rather than of the variable itself, then the residuals are not all of equal weight. In this discussion it will be assumed that the variable t is not subject to error, and that the measurements of A are of equal precision. However, since the straight line is being fitted to values of lnA, the squares of the residuals must be weighted by the quantity w_i, and for lnA functions w_i is proportional to A^2 (see Scarborough, Reference 121). Hence, it is desired that:

$$\sum w_i r_i^2 = \sum A_i^2 (a_o + bt_i - a_i)^2 = \text{minimum} \qquad (31)$$

Taking partial derivatives with respect to a_o and b and setting them both to zero the normal equations are found:

$$a_o \sum A^2 + b \sum A^2 t = \sum A^2 a \qquad (32)$$

$$a_o \sum A^2 t + b \sum (A^2 t^2) = \sum A^2 ta \qquad (33)$$

These yield

$$a_o = \frac{\sum A^2 a \sum A^2 t^2 - \sum A^2 at \sum A^2 t}{\sum A^2 \sum A^2 t^2 - (\sum A^2 t)^2} = \frac{\sum A^2 a \sum A^2 t^2 - \sum A^2 at \sum A^2 t}{L_T} \qquad (34)$$

and

$$b = \frac{\sum A^2 \sum A^2 at - \sum A^2 t \sum A^2 a}{\sum A^2 \sum A^2 t^2 - (\sum A^2 t)^2} = \frac{L_{AT}}{L_T} \qquad (35)$$

Certain combinations of sums are defined as L_T, L_{AT}, and L_A for convenience in writing.

The sum of the squares of the deviations of the points from the fitted line divided by (n - 2), where n is the number of points, is

a measure of the scatter of the points and is called S^2 or the "variance of the estimate" of a single a_i measurement (137, 150, 151). S^2 may be calculated from the following equation:

$$S^2 = \frac{[\Sigma A^2 \Sigma A^2 t - (\Sigma A^2 t)^2][\Sigma A^2 \Sigma A^2 a^2 - (\Sigma A^2 a)^2] - [\Sigma A^2 \Sigma A^2 ta - (\Sigma A^2 t)(\Sigma A^2 a)]^2}{(n-2)(\Sigma A^2)[\Sigma A^2 \Sigma A^2 t^2 - (\Sigma A^2 t)^2]} \tag{36}$$

or in abbreviated notation:

$$S^2 = \frac{[L_T][L_A] - [L_{AT}]^2}{(n-2)(\Sigma A^2)L_T} \tag{37}$$

The standard deviation of the estimate $\sigma_e = \sqrt{S^2}$.

The other standard deviations of interest are:

$$\text{Intercept:} \quad \sigma_{a_o} = \sigma_e \sqrt{\frac{\Sigma A^2 t^2}{L_T}} \tag{38}$$

$$\text{Slope:} \quad \sigma_b = \sigma_e \sqrt{\frac{\Sigma A^2}{L_T}} \tag{39}$$

The following procedure was used in the IBM 650 program for the resolution of complex decay curves. Consider the two component decay curve shown in Figure 46. Let the total number of points on the curve equal n, and the number of points on the "tail" of the longest-lived component equal p. First the p points, each with coordinates A_i and t_i are read into the computer in order beginning with the highest t value, one point per card. From these points the slope, intercept, σ_e, σ_{a_o}, and σ_b are calculated. The quantities $(a_o + \sigma_{a_o}) = a_o^+$ and $(a_o - \sigma_{a_o}) = a_o^-$ are then formed. Finally, the values of the slope, σ_e,

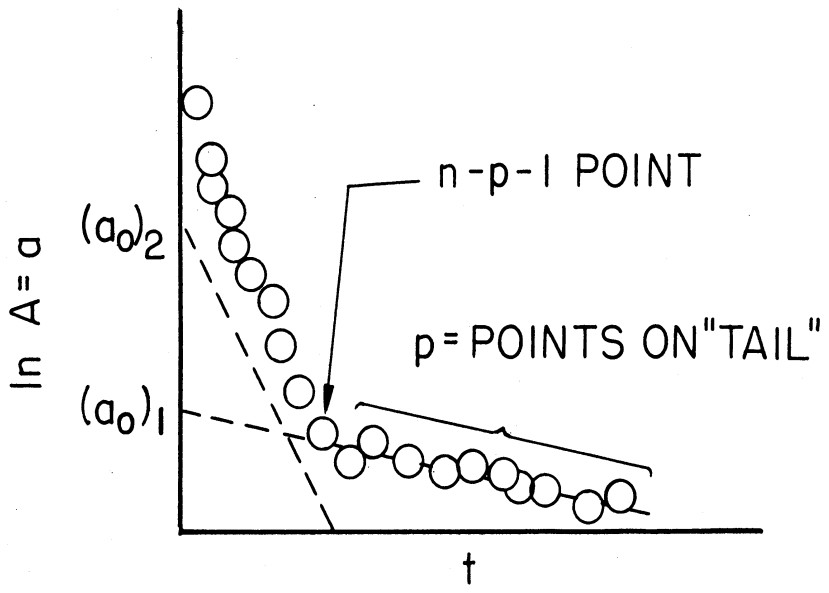

Figure 46. Two component decay curve

the intercept A_o, and the range limits of the intercept $e^{a_o^+} = A_o^+$ and $e^{a_o^-} = A_o^-$ are punched out. The next data card containing the coordinates for the point n-p-1 is then read. Call the coordinates A_r and t_r. The value of a at t_r for the previous component is calculated and the quantity $e^a = A$ is found. A is then subtracted from A_r giving A_r' or the value of

A of the second component at t_r. Finally the values of A_r' and t_r are punched out. The next data card is read in and the procedure repeated until all data cards have been read. The output cards are punched out in such form that they can be used for input cards, when the program is rerun for the next component.

An automatic programming routine called S.I.R., Symbolic Interpretive Routine, was used to program the problem. It is similar to S.O.A.P., with the addition of floating point arithmetic (automatic scaling) and several additional operations such as SINE, EXP, LOG, etc. The program can handle up to approximately 300 points on the experimental curve at one time.

Errors. Actually, the weight of each residual should be $w = A^2 w_A$ where w_A is the weight of the ordinate A due to the uncertainty in the determination of A. This uncertainty may be due just to the statistical nature of the counting process, or it may also contain experimental errors such as variations in the sensitivity of the counter or in counter geometry. Experimental errors of the above class are usually impossible to describe mathematically, and so the best one can do is to try to minimize these errors and to leave them out of the mathematical treatment.

Since the statistical errors in the counting rates usually follow a Poisson distribution ($\lambda t \ll 1$, $N_o \gg 1$, and $(At) \ll N_o$, where N_o = number of atoms at t = 0 and t = time of the count), the standard deviation in the counting rate is just $\sigma_A = \sqrt{\frac{A}{t}}$. When these deviations vary over a large range from point to point they should be taken into

account when the residuals are weighted. This may be done by calling

$$w_A = \frac{1}{(\sigma_A)^2} \tag{40}$$

Then the total weight is:

$$w = \left(\frac{A}{\sigma_A}\right)^2 \tag{41}$$

The factor σ_A was not included in this scheme because in a good decay curve the value of σ_A is of the order of 1 or 2% and does not vary greatly from point to point. Furthermore, the inclusion of σ_A would complicate the computer program and place much greater limitations on the size of the problem that can be handled. Finally the results obtained using σ_A after the first component has been subtracted are subject to criticism from a mathematical point of view. The omission of σ_A has two important effects. First, in dealing with short half-lives where the decay is followed automatically by recording the number of decays that occur in a fixed time interval, the σ_A becomes progressively larger. If all points are considered to have equal precision the standard deviations of the fitted curve will be larger than necessary. However, in just such a case the error in the time interval may become important and may not justifiably be ignored. Therefore, the least-squares procedure employed here would no longer be truly valid, and a new one would be required which took into account the errors in both the ordinate and the abscissa (53). It should be remembered that with short half-lives where the time of a single count is say 1% or more of the half-life a correction must be made for the decay that occurs during a count.

If N_o atoms are present at the beginning of a count lasting for time t, then the number of disintegrations that occur will be ΔN.

$$\Delta N = N_o - N_o e^{-\lambda t} = N_o(1 - e^{-\lambda t}) \tag{42}$$

If

$$A_o = \frac{dN}{dt} = N_o \lambda, \tag{43}$$

then

$$A_o = \frac{\lambda \Delta N}{1 - e^{-\lambda t}} \tag{44}$$

Thus, each count may be corrected to find the disintegration rate at the beginning of the count.

The second effect caused by the omission of σ_A is to further emphasize what is probably the chief disadvantage of this resolution scheme. The "peeling off" process, that is, the procedure of subtracting off the line fitted to the longest-lived component, automatically throws all of the error due to the scatter of the gross points into the remaining curve of the shorter-lived components. This is inherent in any peeling process, be it graphical or mathematical. Assuming no errors of the experimental type, the scatter of the gross curve is a function only of the actual number of disintegrations recorded at each point. Consider a point on a two-component curve where each component contributes to the gross point. Let us say that the counting rate and standard deviation is 10,000 $\pm$ 100 counts per minute. Assume that the extrapolation of the longer-lived component gives a value of 9,000 c/m at this point. Upon subtraction the shorter component would have a value of 1,000 c/m. Yet the absolute value of the scatter of the points

is the same for the second component as it was for the gross curve. Percentwise, the error has increased from 1% to 10%. Merely because a subtraction has taken place, the uncertainty in the second component has increased.

While no smoothing of the original data based on an assumed knowledge of the error in the longer-lived component is justified, the following procedure may be used to get a better estimate of the second component. The standard deviation of each point in the gross curve is calculated and carried along with each point. After the first component is subtracted the numerical standard deviation of the points on the gross curve are given to the points on the remaining curve at the same abscissa values. These are then converted to percent errors and squared to get the variances. The value of σ_e^2 for the first curve is added to the above variances to give a new σ_{A1}^2. The weight of the residual for the second curve would be as before:

$$W = \left(\frac{A}{\sigma_{A1}}\right)^2 \qquad (45)$$

Using this weighting scheme a somewhat better line and a smaller error are obtained. Two things must be remembered: first, the weight factor must be carried to as many decimal places as the rest of the data; and second, the weighting procedure just described is not mathematically rigorous. The latter is due to the fact that the error in the second component was calculated using only those points on the gross curve where the contribution of the shorter-lived component was essentially zero. The information present in the first portion of the curve was not used to determine the longer-lived component. Furthermore, the errors in the

original data are homogeneous, thereby producing skewed errors in the logarithm form. The above procedure has assumed homogeneous errors in the logarithm form, which leads to a skewing of the errors in the final result.

In summary, it may be said that there are several disadvantages to a least-squares "peeling" process. Every time a subtraction takes place the scatter of the original points automatically falls into the lower component. This is because the residuals of the entire curve are not made a minimum. Therefore, the shorter components cannot be determined with the accuracy that is inherent in the original data. The number of components has to be decided upon, it does not fall out of the method. This usually requires a prior rough graphical resolution. All but the shortest-lived component are determined using fewer points than are available in the original data. This again introduces error. Also half-lives that are very close together may not be resolvable. The reasons for using the method are as follows: better results are obtained compared to the graphical method, and an error estimation is available. The method is simple to program and the problem is of such a size that it could be put on a medium size digital computer, such as the IBM 650, which was immediately available.

A possible modification of the above resolution scheme that would place more of the burden of analysis on the computer would be to allow the machine to decide how many points should be used to fit a line to the long-lived tail. After this has been decided, the subtraction could take place, and the desired information pertaining to the first curve punched out. Next the machine could automatically begin to fit

a line to the next component, and so on until the entire curve was analyzed. This would mean no prior graphical resolution would be necessary, although it might be necessary to tell the machine how many components make up the curve. The procedure for accepting points might be as follows: Arbitrarily select a minimum number of points that will surely fall on each component's tail; this number will depend on the nature of the curve and how many points were taken. Let us say that the minimum number of points is 3. Have the machine fit a line to these three points, and then calculate the variance of the estimate. Let the next point be accepted, fit a new line to the now 4 points, and calculate a new variance of estimate. If the new variance is less than the first variance, the fourth point was good. The process is repeated until a variance is found that is larger than the preceding one. The last point would then represent a contribution from the second component and should be rejected. This procedure presumes reasonably smooth data, and might break down if the gross points scattered greatly.

c. Prony's Method. A rather elegant method of fitting exponentials was suggested by A. L. Prony (58). As usual it is desired to determine an approximation of the form

$$h(t) \approx \alpha_1 e^{-\lambda_1 t} + \alpha_2 e^{-\lambda_2 t} + \ldots + \alpha_n e^{-\lambda_n t} \qquad (46)$$

which is equivalent to

$$h(t) \approx \alpha_1 \mu_1^t + \alpha_2 \mu_2^t + \ldots + \alpha_n \mu_n^t \qquad (47)$$

where

$$\mu_i = e^{-\lambda_i} \qquad (48)$$

Prony's method requires that h(t) be determined at N equally spaced points, t = 0, 1, 2, ..., N-1. This restriction is a distinct disadvantage, because decay data are usually not taken in this manner. However, this restriction is common to all of the following methods, and may be attained by an interpolation procedure of whatever degree of accuracy is justified by the original data. Once equally spaced points are determined a simple linear transformation of the variable t will yield the required integral values of t.

Now if Equation (47) were actually an equality, we would have

$$\begin{aligned} \alpha_1 + \alpha_2 + \ldots + \alpha_n &= h(0) \\ \alpha_1\mu_1 + \alpha_2\mu_2 + \ldots + \alpha_n\mu_n &= h(1) \\ \cdots\cdots\cdots\cdots\cdots\cdots\cdots\cdots\cdots\cdots & \\ \alpha_1\mu_1^{N-1} + \alpha_2\mu_2^{N-1} + \ldots + \alpha_n\mu_N^{N-1} &= h(N-1) \end{aligned} \tag{49}$$

If the constants $\mu_1, \mu_2, \ldots, \mu_n$ were known, this set would comprise N linear equations in n unknowns, $\alpha_1, \alpha_2, \ldots, \alpha_n$, and could be solved exactly if N = n or approximately using the least-squares method if N > n. However, since the μ's are also to be determined, a minimum of 2n equations are necessary.

The set of Equations (49) is still not linear in the μ's. Therefore, let $\mu_1, \mu_2, \ldots, \mu_n$ be the roots of the equation

$$\mu^n - \beta_1\mu^{n-1} - \beta_2\mu^{n-2} - \ldots - \beta_{n-1}\mu - \beta_n = 0 \tag{50}$$

In order to find the β coefficients, the first equation in (49) is multiplied by β_n, the second by β_{n-1}, and so on. Adding the results

$$h(n) - \beta_1 h(n-1) - \ldots - \beta_n h(0) = 0 \qquad (51)$$

is obtained. In a similar way the N-n-1 equations are obtained

$$\begin{aligned} h(n-1)\beta_1 + h(n-2)\beta_2 + \ldots + h(0)\beta_n &= h(n) \\ h(n)\beta_1 + h(n-1)\beta_2 + \ldots + h(1)\beta_n &= h(n+1) \\ \ldots\ldots\ldots\ldots\ldots\ldots\ldots\ldots\ldots\ldots\ldots\ldots & \\ h(N-2)\beta_1 + h(N-3)\beta_2 + \ldots + h(N-n-1)\beta_n &= h(N-1) \end{aligned} \qquad (52)$$

The set of equations (52) may be solved directly to give the β's if $N = 2n$, or approximately using least squares, if $N > 2n$. Knowing the β's the roots $\mu_1, \mu_2, \ldots, \mu_n$ of Equation (50) may be found. The μ values may be used directly to calculate the λ's from Equation (48) and together with the set of equations (49) may be used in a least-squares method to obtain the α values.

While Prony's method gives the appearance of being a least-squares fit, it is actually not since both the β's and the h(t)'s are subject to error. Hence no error estimate is available. Also, there is no provision for weighting the values of h(t) according to their precision. Another serious drawback is that the number of components must be known. Finally, for large numbers of data, the method becomes cumbersome computationally.

d. Householder's Method. A. S. Householder in 1949 proposed a modification of Prony's method (62) which permitted valid least-square estimates to be obtained. Essentially he applies Prony's

method to obtain initial estimates of the exponents, and then by an iterative procedure arrives at least squares estimates. A test is also included to determine how many exponentials are needed to adequately fit the data. The method was programmed for the ORACLE, a computer at Oak Ridge National Laboratory, and for a reason that is not known, the method sometimes failed to converge, and even occasionally converged to unreasonable estimates (61).

e. Cornell's Method. Another procedure for the estimation of a linear combination of exponentials was put forth by R. G. Cornell in August, 1956, who tested the method on the Oak Ridge National Laboratory's computer, the ORACLE (28). In some respects the method appears to be similar to Prony's method, except that among other things it may also be applied to group means instead of only individual observations. This is quite important in investigations where an observation at a given point may be repeated. Furthermore, Cornell's method does not involve questionable least squares calculations.

In its unmodified form this new method requires not only that equally spaced points be available, but also that the number of components be known and that the number of points N be equal to 2rn, where n is the number of components and r is any integer, if an error estimate is to be made. Ease of computation is comparable to Householder's method or Prony's method.

Actually only the case of a single component exponential was investigated to any great extent. Here the results seem to be at least as good as most other methods provide, and better in many cases, particularly when the half-life was long and smooth data were available.

Since the method is still new and relatively untested a further study must be made before it can be accurately evaluated.

2. Method of Fourier Transforms.

The previously listed methods all contain certain undesirable limitations, and it was felt that a search for a new method was warranted. There is little that is original in the mathematics of the method to be presented. In the main, it consists of a grouping of previously known techniques into a program which appears to have several distinct advantages over other methods. As in the case of Cornell's method, the procedure now to be presented has not been thoroughly tested, and until this is done its actual value is difficult to assess.

One of the most important reasons for desiring a new method is that none of the previous methods, except Householder's, can estimate or determine the actual number of exponentials that comprise the gross curve. It was necessary to rely on human judgment to obtain this information. It seems to this author that it is just as important to be able to accurately estimate the number of components as it is to extimate their constants. In fact, if the number of components is uncertain then any accurate calculation of the constants involved begins to lose its meaning. This would not necessarily be true if it were only required to produce an arbitrary function that would simulate the data. But the constants involved have physical significance and their estimation is fundamental to the entire analysis.

A satisfactory analytical procedure must also include the following features:

1. An error estimation. Without this there is no way of evaluating the results.

2. Full use of the accuracy inherent in the data. The lack of this feature was pointed out in the graphical and least-squares peeling process.

3. The replacement of human judgment by mathematical analysis. This is particularly needed in the case of the number of components.

4. Treatment of all observations as a whole. This is essential if a minimum error is to be obtained over the entire curve. (See also remarks in Least-Squares Method section.)

a. Development of Initial Problem into the Form of a Laplace Integral Equation. Consider first the case where nuclei of type A decays into stable nuclei of type B. Also let $A = A(t)$ and $B = B(t)$ be the numbers of atoms of types A and B present at time t. Assume that $B(0) = 0$

At time $t = 0$	$A = A_o$
	$B = 0$
At time $t = \infty$	$A = 0$
	$B = B_\infty = A_o$
At time $t = T$	$A = A_o e^{-\lambda_A T}$
	$B = A_o - A = A_o(1 - e^{-\lambda_A T})$

The rate of decay of A is equal to the rate of growth of B

$$-\frac{dA}{dt} = \frac{dB}{dt} \tag{53}$$

Also,

$$-\frac{dA}{dt} = A\lambda_A = A_o\lambda_A e^{-\lambda_A t} \tag{54}$$

The actual counting rate obtained experimentally may or may not be the true time derivative of A. It is assumed that the observed counting rate is proportional to the true disintegration rate.

Combining (53) and (54), we may arrive at

$$-\int_{A_o}^{A} \frac{dA}{dt}\,dt = \int_{o}^{B} \frac{dB}{dt}\,dt = \int_{o}^{t} A_o\lambda_A e^{-\lambda_A t}\,dt \qquad (55)$$

Integrating we obtain

$$B = -\left[A_o e^{-\lambda_A t}\right]_o^t = -A_o e^{-\lambda_A t} + A_o \qquad (56)$$

Rearranging gives

$$A_o - B = A_o e^{-\lambda_A t} \qquad (57)$$

Let $f(t) = A_o - B(t)$. Then

$$f(t) = A_o e^{-\lambda_A t} \qquad (58)$$

In a sample containing several radioactive substances decaying independently into stable daughters, Equation (58) can be generalized to give

$$f(t) = \sum_i A_{o_i} e^{-\lambda_{A_i} t} \qquad (59)$$

The following conditions are required:

$$A_{o_i} \neq 0,\ \lambda_i > 0,\ \text{and}\ \lambda_r \neq \lambda_s \ \text{when}\ r \neq s.$$

Equation (59) is in the form of a Dirichlet series (148) and may be expressed in integral form as:

$$f(t) = \int_o^\infty g(\lambda) e^{-\lambda t} d\lambda \qquad (60)$$

It should be noted that a plot of f(t) vs. t is actually a plot of the sum of the decay curves of the radioactive parents on an atom basis. Therefore, in the case of a single component the f(t) is actually the number of atoms of A present at time (t). The function f(t) may be obtained by integrating the disintegration rates from zero to t, for each t, and plotting the results against t to obtain B(t). This curve will approach a limit as $t \rightarrow \infty$ of $\sum_i A_{o_i}$. Each point on the curve is subtracted from the limiting value to give f(t). Equation (60) has the form of a Laplace Integral equation.

b. Solution of Integral Equations by the Method of Transforms. The process of multiplying a function f(t) by a known function k(u, t) and integrating with respect to t from a to b to generate a new function F(u) is a type of transformation whose name depends on the kernel k(u, t). A Fourier transform is an integral equation of the form,

$$F(u) = \int_{-\infty}^{\infty} f(t)e^{iut}dt \qquad (61)$$

where e^{iut} is the kernel k(u, t).

A generalized linear integral equation of the "first type" may be written as

$$f(t) = \int_a^b k(\lambda, t)g(\lambda)d\lambda \qquad (62)$$

where $g(\lambda)$ is the unknown function, $k(\lambda, t)$ is a kernel of known form, and f(t) is a known function or a tabulated set of points. In most cases, an analytic solution does not exist and few numerical methods have been worked out. The method (115) that will be used is limited to cases where $k(\lambda, t)$ is of the form $k(t - \lambda)$, $k(t + \lambda)$, or $k(\lambda t)$.

A simple change of variables will transform each of the above into the form $k(t - \lambda)$. First,

$$f(t) = \int_{-\infty}^{\infty} k(t - \lambda)g(\lambda)d\lambda \tag{63}$$

Now

$$F(u) = \frac{1}{\sqrt{2\pi}} \int_{-\infty}^{\infty} f(t)e^{iut}dt \tag{64}$$

where $F(u)$ is the Fourier transform of $f(t)$ and u is a dummy variable. Substituting for $f(t)$ in Equation (64) the integral in (63) we obtain

$$F(u) = \frac{1}{\sqrt{2\pi}} \int_{-\infty}^{\infty} k(t - \lambda)g(\lambda)d\lambda \int_{-\infty}^{\infty} e^{iut}dt$$

and

$$F(u) = \frac{1}{\sqrt{2\pi}} \int_{-\infty}^{\infty} g(\lambda)d\lambda \int_{-\infty}^{\infty} k(t - \lambda)e^{iut}dt \tag{65}$$

Let $t = x + \lambda$. Then $x = t - \lambda$. Therefore:

$$F(u) = \frac{1}{\sqrt{2\pi}} \int_{-\infty}^{\infty} g(\lambda)d\lambda \int_{-\infty}^{\infty} k(x)e^{iu(x+\lambda)}dx \tag{66}$$

Since $e^{iu(x+\lambda)} = e^{iux} \cdot e^{iu\lambda}$, we have

$$F(u) = \frac{1}{\sqrt{2\pi}} \int_{-\infty}^{\infty} g(\lambda)e^{iu\lambda}d\lambda \int_{-\infty}^{\infty} k(x)e^{iux}dx \tag{67}$$

It is seen from Equation (61) that the first part of Equation (67) is the Fourier transform $G(u)$ of $g(\lambda)$, and the second part is the Fourier transform $K(u)$ of $k(x)$. Therefore,

$$F(u) = \sqrt{2\pi}\, G(u)K(u), \tag{68}$$

and

$$G(u) = \frac{1}{\sqrt{2\pi}} \frac{F(u)}{K(u)} \tag{69}$$

Taking the inverse Fourier transform of G(u) we obtain the original function $g(\lambda)$ which is now a function of the transforms of f(t) and $k(t, \lambda)$.

$$g(\lambda) = \frac{1}{2\pi} \int_{\infty}^{\infty} \frac{F(u)}{K(u)} e^{-iu\lambda} du \tag{70}$$

The results obtained in Equation (70) are purely formal. For a precise statement of the conditions under which Equation (70) holds, see References 139, 141, and 115.

c. Solution of the Laplace Integral Equation. We begin with Equation (60).

$$f(t) = \int_{-\infty}^{\infty} e^{-\lambda t} g(\lambda) d\lambda \tag{60}$$

and proceed to transform the variables λ and t.

Define:

$$\lambda = e^{-y}, \quad t = e^{x} \tag{71}$$

Then

$$f(e^{x}) = - \int_{-\infty}^{\infty} e^{-e^{(x-y)}} g(e^{-y}) e^{-y} dy \tag{72}$$

Multiply both sides of (72) by e^{x}:

$$e^{x} f(e^{x}) = - \int_{\infty}^{\infty} e^{-e^{(x-y)}} g(e^{-y}) e^{(x-y)} dy \tag{73}$$

Define:

$$f(e^x) = \tilde{f}(x), \quad g(e^{-y}) = \tilde{g}(y) \tag{74}$$

Then

$$e^x \tilde{f}(x) = - \int_{-\infty}^{\infty} e^{-e^{(x-y)}} e^{(x-y)} \tilde{g}(y) dy \tag{75}$$

The Fourier transform of the left hand side of Equation (75) is

$$F(u) = - \frac{1}{\sqrt{2\pi}} \int_{-\infty}^{\infty} e^x \tilde{f}(x) e^{iux} dx \tag{76}$$

Let $s = x - y$, and forming the Fourier transform of the kernel of Equation (75)

$$K(u) = - \frac{1}{\sqrt{2\pi}} \int_{-\infty}^{\infty} e^{-e^s} e^s e^{ius} ds \tag{77}$$

Finally we form

$$\tilde{g}(y) = \frac{1}{2\pi} \int_{-\infty}^{\infty} \frac{F(u)}{K(u)} e^{-iyu} du \tag{78}$$

In this case, K(u) can be evaluated analytically. In Equation (77) let $e^s = Z$, $dZ = e^s ds$, $ds = e^{-s} dZ = dZ/Z$.

Also let $iu = n - 1$. Therefore,

$$n = 1 + iu \tag{79}$$

Substituting into Equation (77) we get:

$$K(u) = \int_{-\infty}^{\infty} e^{-Z} Z^{n-1} dZ \tag{80}$$

which is by definition (65) the Γ function, $\Gamma(1 + iu)$.

Therefore, the kernel K(u) turns out to be the Euler integral for

$$\frac{1}{\sqrt{2\pi}} \Gamma(1 + iu).$$

d. Details on the Method of Solution. Briefly, the method of solution was shown to consist of first integrating the initial disintegration rate curve and then forming a new decay curve on an atom basis. This was called f(t). Next, the Fourier transform F(u) of f(t) was needed.

$$F(u) = \frac{1}{\sqrt{2\pi}} \int_{-\infty}^{\infty} e^{x} \tilde{f}(x) e^{iux} dx \qquad (76)$$

K(u) was shown to be the Γ function

$$K(u) = \frac{1}{\sqrt{2\pi}} \Gamma(1 + iu) \qquad (81)$$

Next, the quotient F(u)/K(u) was formed, and the inverse Fourier transform taken to give $\tilde{g}(y)$ where $\tilde{g}(y) = g(e^{-y}) = g(\lambda)$.

$$\tilde{g}(y) = \frac{1}{2\pi} \int_{-\infty}^{\infty} \frac{F(u)}{K(u)} e^{-iyu} du \qquad (78)$$

Basically then, the method requires two integrations and an evaluation of a complex Γ function. The details of the numerical integration will be given later, but it is clear that we cannot integrate numerically from $-\infty$ to ∞ in Equations (76) and (78). [Equation (76) will be discussed here, but the remarks apply also to Equation (78).] Therefore, we must introduce the limits x_o and $-x_o$ into Equation (76). These are the cut-off points of the integral, and naturally we would like to

have $|x_o|$ approach ∞ as closely as possible. Instead of Equation (76) we now have:

$$\sqrt{2\pi}\, F(u) = \int_{-x_o}^{x_o} e^{x}\tilde{f}(x)e^{iux}dx + E(x_o, u) \tag{82}$$

The cut-off at $x = \pm x_o$ and the subsequent dropping of $E(x_o, u)$ is equivalent to folding the transform of $F(u)$ against the transform of the unit step function:

$$m(x) = \begin{cases} 0, & x > x_o \\ 1, & -x_o \leq x \leq x_o \\ 0, & x < -x_o \end{cases} \tag{83}$$

Consider the following sketch:

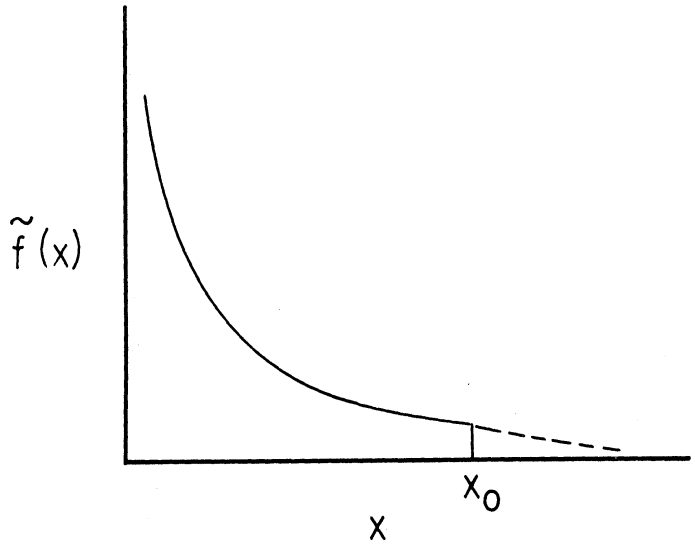

Figure 47. Sketch of $\tilde{f}(x)$ as a function of x

There is no difficulty in choosing a zero on the x axis so that the necessary conditions of symmetry are maintained. However, it is necessary that a finite x_o exist such that the value of $E(x_o, u)$ is sufficiently small to render a good solution possible. Since $\tilde{f}(x)$ is obtained from experimentally measured quantities, knowledge out at least as far as x_o is required. If this knowledge cannot conveniently be obtained experimentally, it must be obtained in some other way. More will be said about this later.

The major difficulty in this method is now apparent. We are trying to simulate a curve with an abrupt cut-off at x_o by a sum of exponentials that extend to $x = \infty$. This process introduces high frequency Fourier components into $F(u)$ which will tend to obscure the results. In fact, if $E(x_o, u)$ is large enough, it will be impossible to obtain a good solution. It is most unfortunate that once the frequency spectrum of $\tilde{f}(x)$ has been warped by folding against the step function $m(x)$, which may be represented by $\sin(ux)/ux$, the warping cannot be removed from $\tilde{g}(y)$ by any unfolding.

It will help in the discussion of the cut-off error if the form of the results is examined. $\tilde{g}(\lambda)$ may be thought of as a sum of Δ functions. However, due to errors in the initial data, the integration process, the evaluation of the Γ function, and in the numerical calculations due to round-off and truncation of numbers, the best that can be hoped for, when cut-off errors are not considered, is a frequency spectrum similar to the one shown in the following sketch which

represents a hypothetical four component curve.

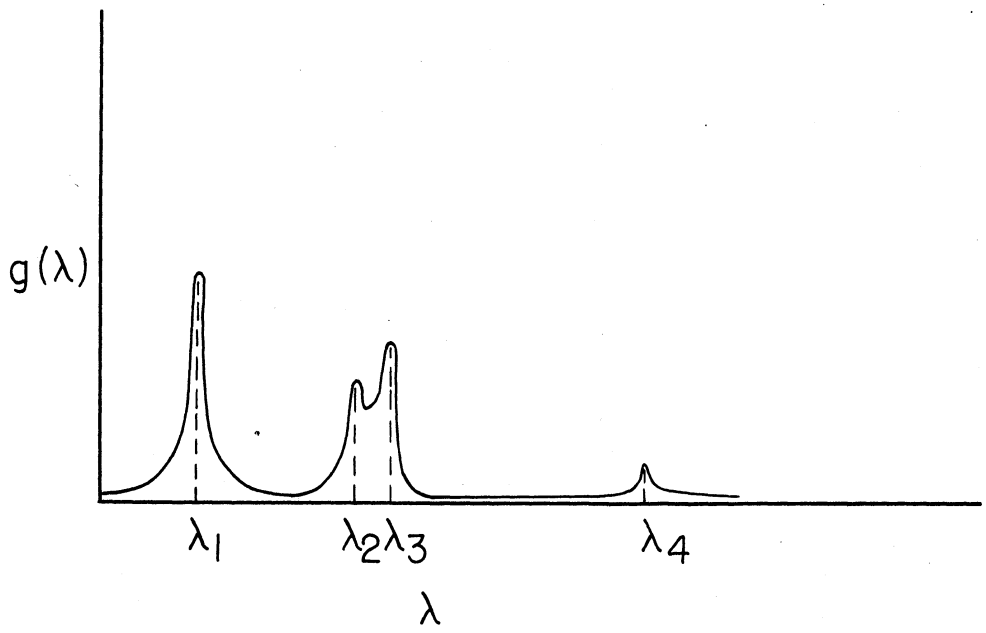

Figure 48. Sketch of $g(\lambda)$ as a function of λ

Each peak in the spectrum indicates a component. The abscissa value at the center of a peak is the decay constant, while the height of the peak gives the number of atoms of the component at time zero. An error analysis would come from the profile of the peak. The beauty of the method lies in the fact that the number of components auto-

matically falls out of the analysis. How well the components may be resolved naturally depends on how good the initial data are, and also on the errors introduced during the numerical calculation. The region of the sketch around λ_2 and λ_3 illustrates the case where two half-lives are close together. A better resolution may be effected by starting at one end of the total curve, fitting a distribution curve to the first peak, and subtracting it from the total curve. In this way, each component may be "peeled" off of the gross curve.

Returning to the discussion of the cut-off error, it is of interest to see how this factor will affect the overall results. It was noted that the cut-off at a finite value of x has the effect of adding into F(u) Fourier components which extend the range in u on which F(u) maintains appreciable value. In order that the integral in Equation (78) converge, F(u) in the quotient F(u)/K(u) must approach zero at infinity faster than K(u). Now,

$$|\Gamma(1 + iu)| \approx \sqrt{\pi}\,\frac{1}{|u|}\,\frac{1}{\sinh(\pi u)} \qquad (84)$$

and so K(u) tends to diminish quite rapidly. Therefore, when F(u) is warped by the cut-off (or by other sources of error), for some value of u the quotient F(u)/K(u) will begin to grow without bound. The result of the extra Fourier components in F(u) is not only to smudge out the peaks but also to cause them to be riding on a function that is tending to increase in value. The sketch below illustrates this case for a hypothetical two component decay curve. Even this

poor solution (and it could be far worse) does yield some information.

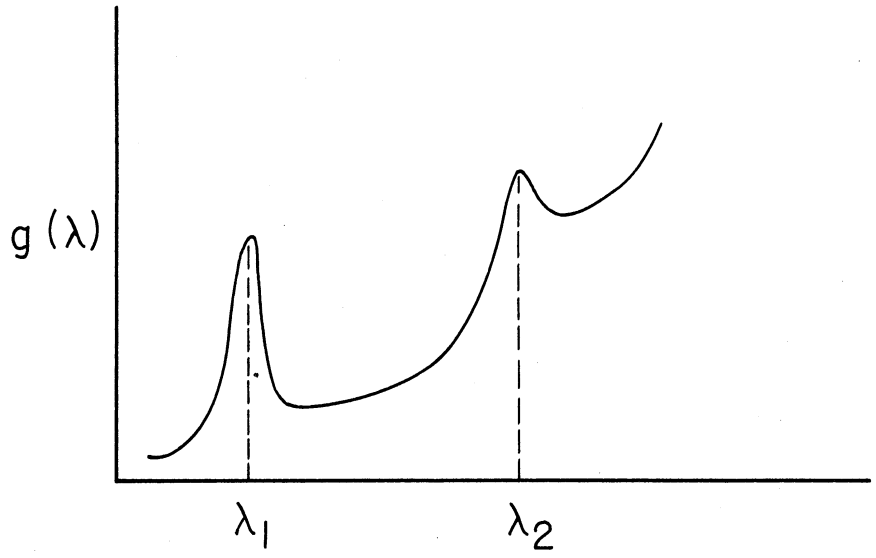

Figure 49. Sketch of $g(\lambda)$ showing effect of cut-off error

The λ's may be determined with some accuracy, and an estimate of $g(\lambda_1)$ and $g(\lambda_2)$ may be obtained if the questionable procedure of trying to subtract off the contribution of the rising function is employed.

If nothing is done to counteract the effect of the cut-off, at least something may be said about error formulae for the cut-off.

There are two cut-off integrals to be evaluated:

$$(a)\quad \int_{x_o}^{\infty} e^{-x_o} f(-x) e^{-iux}\,dx = E^{-}\,,$$

and (85)

$$(b)\quad \int_{x_o}^{\infty} e^{x_o} f(x) e^{iux}\,dx = E^{+}$$

Perlis in Reference 115 states the necessary conditions for the behavior of $f(x)$ at x_o, and obtains the following results:

$$(a)\quad E^{-} \leq \frac{o(e^{(n-1)x_o})}{|n-1| - |u|}$$

$$(b)\quad E^{+} \leq \frac{o(e^{(n+1)x_o})}{|n+1| - |u|} \qquad (86)$$

where $n < 1$ in the case (a) and $n < -1$ in case (b). He obtains a more specific result for the cut-off in forming $K(u)$.

Range	Error
x_o to ∞	$-\Gamma_{x_o}(1+iu) + (1+iu)$
$-x_o$ to $-\infty$	$-\Gamma_{\frac{1}{x_o}}(1+iu)$

(87)

where Γ_j refers to the incomplete Γ function of x with integration limit j.

As $x_o \to \infty$, the above errors $\to 0$. Thus, in both $F(u)$ and $K(u)$, the errors should be quite small at any reasonably large value of x_o. There are two principal approaches to the problem of cut-off errors. The first and less satisfactory approach is to introduce a convergence factor into Equation (78). Through a sacrifice in

"resolution" of g(y) a convergent numerical solution is available. Two convenient factors given in Reference 115 are e^{au^2} and $\sin^2 au/(au)^2$. Therefore, instead of calculating $\tilde{g}(y)$, we find the quantity

$$\tilde{g}^*(y) = \frac{1}{2\pi}\int_{-\infty}^{\infty} \frac{F(u)}{(1+iu)} e^{-iyu}T(u)du$$
$$= \int_{-\infty}^{\infty} \tilde{g}(y-s)t(s)ds \qquad (88)$$

where T(u) may be e^{-au^2} for example. Then Equation (88) becomes

$$\tilde{g}^*(y) = \frac{1}{\sqrt{2a}}\int_{-\infty}^{\infty} g(y-s)e^{-\left(\frac{s}{2a}\right)^2} ds \qquad (89)$$

The solution is seen to be folded against the transform of T(u). The purpose of this is to have the transform of the convergence factor approximate the actions of a unit step function. That is, we would like to have the solution multiplied by a factor that was essentially one up to the point where the solution started to rise without bound. Then the convergence factor should cause the solution to fall to zero. How rapidly the convergence factor falls to zero may be controlled by the constant a. The greater the value in u at which F(u)/K(u) remains well behaved, the closer to zero the constant a may be made. The smaller the value of a, the narrower the spread by which each point in $\tilde{g}^*(y)$ will be weighted.

This solution to the cut-off problem suggested in Reference 115, is undesirable from several respects. First of all, it introduces into $\tilde{g}^*(y)$ oscillations of decreasing amplitude which tend to obscure the results. Secondly, it can at best only try to subtract out the "background noise" on which the peaks are riding and keep the range of

the number size from becoming overly large. Actually, the subtraction might be done graphically. Finally, the $\tilde{g}^*(y)$ produced cannot be unfolded from the transform of T(u), and the $g^*(\lambda_i)$ found are only estimates of the desired $g(\lambda_i)$ being in error by an unknown amount.

A second, and it is believed better, approach to the cut-off problem is that of artificially extending the observed values of f(t) to the point where the cut-off becomes relatively insignificant. We shall consider two cases, in each of which it is assumed that the half-lives of the components are short enough so that it is convenient to follow the gross decay until only the longest lived component remains.

Case 1. Here we require also that there is not a vast difference in half-lives between the shortest- and the longest-lived components. The numerical calculations are to be carried out on a computer, and so the maximum difference in half-lives will be a function of the size of the computer. The procedure in this case would be to follow the decay of the longest-lived component until its decay constant can be determined with sufficient accuracy using a least squares fit. Similarly, its ordinate intercept at time zero is determined. This information will then allow a simple extrapolation to give values of f(t) at appropriate intervals out to where the experimental counting rate becomes comparable with the background. A cut-off at this point will still introduce some error, but this error should be almost negligible and $\tilde{g}(\lambda)$ should be very well behaved over the range of interest.

In the integration scheme to be presented later, equally spaced points are required. It is necessary that small enough in-

tervals be taken so that no appreciable error is introduced when integrating under the shorter-lived components. This implies that if the interval is small enough to suit the shorter-lived components then a great many values of f(t) that define only the longest-lived component will be required. This is a failing of most numerical integration schemes, but may be circumvented to a degree by using an unequal interval integration scheme. It becomes apparent then that if the distribution of half-lives is sufficiently poor so that several hundred values of f(t) are required (obtained by interpolation), then a fairly large computer like the IBM 704 is necessary to handle the problem. It should be remembered that K(u) must be evaluated at the same points as F(u). Finally, $\tilde{g}(\lambda)$ will also be evaluated over a large set of values.

Case 2. This is the case where the half-life of the longest-lived component differs greatly in magnitude from the next longest-lived activity. For example, a three-component system might have the following half-lives: 1 hour, 10 hours, and 200 days. In 60 hours the 10 hour half-life will have been reduced by a factor of 64 while the 200 day activity will still be above 99% of its value at time zero. Therefore, to a good approximation we may subtract off the 200 day activity as a constant factor from the gross experimental decay curve. The remaining two components may then be analyzed much more accurately than if the 200 day component had been extrapolated down to background and the entire system treated. If this system had been followed for 200 days and then cut off, even with a convergence factor the results would probably not have been very good.

e. The Numerical Integration Scheme. The numerical evaluation of an integral such as

$$I = \int_a^b f(p)\cos(xp)dp \tag{90}$$

presents considerable difficulty due to the rapid oscillations of the function cos(xp). An ordinary integration scheme, such as Simpson's rule, would require excessively small intervals of integration in order to approach the accuracy of a method specifically designed to handle trigonometric functions. L. N. G. Filon (42) has developed an excellent method for the evaluation of such integrals that requires integration intervals only as small as would be necessary to evaluate the integral without the trigonometric factor. Since the method does not seem to be well known it will be developed very briefly here.

Let the range of integration be divided into 2n equal parts with an interval h, so that

$$b = a + 2nb \tag{91}$$

The following notation will be used:

$$\begin{aligned} xh &= \theta \ , \\ a + sh &= p_s \ , \\ f(a + sh) &= f_s \ , \end{aligned} \tag{92}$$

where s = an integer. It is assumed that over the range (p_s - h, p_s + h), that is, (p_{s-1}, p_{s+1}) the function f(p) can be approximated sufficiently well by the quadrature formula,

$$f(p) = A + B(p - p_s) + C(p - p_s)^2 \tag{93}$$

Differentiation leads to

$$f'_{s+1} = (3f_{s+1} + f_{s-1} + 4f_s)/2h$$
$$f'_{s-1} = (4f_s - f_{s+1} - 3f_{s-1})/2h \tag{94}$$

If

$$I_s = \int_{p_{s-1}}^{p_{s+1}} f(p)\cos(xp)dp \tag{95}$$

Then

$$xI_s = \left[\left\{f(p) - 2Cx^{-2}\right\}\sin(xp) + f'(p)x^{-1}\cos(xp)\right]_{p_{s-1}}^{p_{s+1}} \tag{96}$$

This reduce to

$$\begin{aligned} x\theta I_s = {} & (f_{s+1} - f_{s-1})(\theta\cos\theta - \sin\theta)\sin(xp_s) \\ & + (f_{s+1} + f_{s-1})(\theta\sin\theta - 2\theta^{-1}\sin\theta + 2\cos\theta)\cos(xp_s) \\ & + 4f_s(\theta^{-1}\sin\theta - \cos\theta)\cos(xp_s) \end{aligned} \tag{97}$$

If we write

$$\begin{aligned} \theta^3\alpha &= \theta^2 + \theta\sin\theta\cos\theta - 2\sin^2\theta \\ \theta^3\beta &= 2\left[\theta(1 + \cos^2\theta) - 2\sin\theta\cos\theta\right] \\ \theta^3\gamma &= 4\left[\sin\theta - \theta\cos\theta\right] \end{aligned} \tag{98}$$

Then Equation (97) can be written as

$$\begin{aligned} I_s = h\Big[& \alpha\left(f_{s+1}\sin(xp_{s+1}) - f_{s-1}\sin(xp_{s-1})\right) \\ & + 1/2\beta\left(f_{s+1}\cos(xp_{s+1}) + f_{s-1}\cos(xp_{s-1})\right) + \gamma f_s\cos(xp_s)\Big] \end{aligned} \tag{99}$$

If I_s is summed for $s = 1, 3, 5, \ldots, 2n-1$, we have the expression

$$\int_a^b f(p)\cos(xp)dp = h\left[\alpha\left\{f(b)\sin(\alpha b) - f(a)\sin(\alpha a)\right\} + \beta C_{2s} + \gamma C_{2s-1}\right] \tag{100}$$

where C_{2s} denotes the sum of all even ordinates of the curve $y = f(p)\cos(xp)$ between a and b inclusive minus one-half of the first and last ordinates, and C_{2s-1} denotes the sum of all of the odd ordinates. The quantities α, β, and γ, given in terms of $\theta = xh$, are determined by the set of equations (98) but for reasonable accuracy at small values of θ it is necessary to expand the trigonometric terms as follows

$$\alpha = \frac{2\theta^3}{45} - \frac{2\theta^5}{315} + \frac{2\theta^7}{4725} - \ldots$$

$$\beta = \frac{2}{3} + \frac{2\theta^2}{15} - \frac{4\theta^4}{105} + \frac{2\theta^6}{567} - \ldots \qquad (101)$$

$$\gamma = \frac{4}{3} - \frac{2\theta^2}{15} + \frac{\theta^4}{210} - \frac{\theta^6}{11,340} + \ldots$$

When $\theta \to 0$, then $\alpha \to 0$, $\beta \to 2/3$, and $\gamma \to 4/3$. This results in Equation (100) becoming

$$\int_a^b f(p)dp = (h/3)[2C_{2s} + 4C_{2s-1}] \qquad (102)$$

which is Simpson's Rule. Values of α, β, and γ have been tabulated for small angles in radians (Reference 141) and in degrees (Reference 42). In a similar way, the formula for the integral containing the sine term can be deduced.

$$\int_a^b f(p)\sin(xp)dp = h[-\alpha f(b)\cos(xb) - f(a)\cos(xa) \qquad (103)$$

$$+ \beta S_{2s} + \gamma S_{2s-1}]$$

where S_{2s} and S_{2s-1} have the same meanings as C_{2s} and C_{2s-1} except that they pertain to the curve $y = f(p)\sin(xp)$. An estimation of the error may be made by first evaluating the integral using an interval h, and then halving the interval and repeating the process. Clearly if halving

the intervals makes no appreciable difference in the results, the process cannot be very far from the limit. An actual error estimation based on this halving procedure is given in Reference 42.

f. Details on the Numerical Solution. The size of this problem necessitates a fairly large computer, something in the range of an IBM 704. It is conceivable that an IBM 650 could be used, but this would at least require that the problem be broken up into several small sections. Even then the number of points would impose a serious problem.

It is not the purpose of this section to present a complete computer program. It is rather to stress a few details in the numerical solution so that when a large enough computer becomes available the programming will be facilitated.

To begin with, the original data will have to be treated to minimize the cut-off error as was mentioned in section d. If it only requires the subtraction of a constant term this might best be done by hand. If an extrapolation is needed, a separate program such as the weighted least squares routine described previously will give the necessary constants enabling the extrapolation to be performed or else an interpolation program (which is also needed later) may be used to interpolate on the "tail." Preferably then the original counting-rate data will have been corrected for background and cut-off before the principal program begins.

In forming f(t) it is first necessary to integrate to form the growth curve of the daughter products. Simpson's rule will serve as the integration scheme. The limit of the growth curve may be taken as the ordinate at t_{max}. F(t) is then formed by subtracting the growth

curve from its limit and plotting the results against t. All these preliminary calculations are carried out automatically in the computer.

We make the change of variable $t = e^x$, and $f(t) = f(e^x) = \tilde{f}(x)$. The function f(t) ranges from 0 to t_{max} while $\tilde{f}(x)$ now ranges from $-\infty$ to $\ln t_{max} = x_{max}$. The point at $t = -\infty$ is dropped. The remaining points are predominantly larger than x = 0. Therefore, since we have to integrate between $\pm x_{max}$, it would be best to choose a new zero so that the experimental points are equally distributed on either side, primarily to make use of the symmetric properties of the sines and cosines used later. Each $\tilde{f}(x)$ must be multiplied by e^x and then the following integral may be set up

$$F(u) = \frac{1}{\sqrt{2\pi}} \int_0^{x_{max}} [f^*(x) + f^*(-x)]e^{iux}dx \qquad (104)$$

or more conveniently,

$$F(u) = \frac{1}{\sqrt{2\pi}} \int_0^{x_{max}} \left\{[f^*(x) + f^*(-x)]\cos(ux) + i[f^*(x) - f^*(-x)]\sin(ux)\right\}dx \qquad (105)$$

where $f^*(x) = e^x f(x)$.

Essentially then Equation (105) and K(u) must be evaluated over the same range of u values.

The Γ function $\Gamma(1 + iu) = \Gamma(Z)$ may be evaluated from a formula such as

$$\frac{1}{\Gamma(Z)} = Ze^{\gamma Z} \prod_{n=1}^{\infty} \left\{(1 + \frac{Z}{n})e^{-\frac{Z}{n}}\right\} \qquad (106)$$

where γ is Euler's constant ($\gamma = 0.57721566...$). It is also tabulated in the form of $\ln\Gamma(x + iy) = U + iV$ in Reference 100 for the ranges

$$x : \quad 0 \text{ to } 10$$

$$y : \quad 0 \text{ to } 10$$

Therefore

$$\Gamma(Z) = e^{U}(\cos V + i \sin V) \tag{107}$$

The range of the table may be doubled by use of a duplication formula given in Reference 100 and further extended by means of extrapolation. By using Equation (106) to calculate first $\Gamma(iu)$ and then obtaining $\Gamma(1 + iu)$ from

$$\Gamma(1 + Z) = Z\Gamma(Z) \tag{108}$$

the computation is facilitated.

$F(u)$ and $K(u)$ are complex numbers. The real part of $F(u)$, termed F_c comes from the cosine terms in the integration, and the imaginary part F_s comes from the sine terms. Similarly, $K(u)$ is composed of K_c and K_s. The quotient of $F(u)$ and $K(u)$ is

$$\sqrt{2\pi}\, G(u) = \frac{F(u)}{K(u)} = \frac{F_c + iF_s}{K_c + iK_s} = \frac{(F_c + iF_s)(K_c - iK_s)}{K_c^2 + K_s^2} \tag{109}$$

Since

$$2\pi\tilde{g}(y) = \int_{-\infty}^{\infty} \frac{F(u)}{K(u)}\, e^{-iyu}du, \tag{110}$$

we get

$$\int_{-\infty}^{\infty} \frac{F(u)}{K(u)}\, e^{-iyu}du = \int_{-\infty}^{\infty} \left\{\frac{F_cK_c + iF_sK_c + iF_cK_s + F_sK_s}{K_c^2 + K_s^2}\right\} (\cos yu - i \sin yu)du \tag{111}$$

Making use of the properties of harmonic functions,

Real	Imaginary
$G(u) = G(-u)$	$G(u) = -G(-u)$

all odd terms vanish in the integration (86), so that

$$\pi\tilde{g}(y) = \int_0^\infty \left\{ \frac{F_c K_c + F_s K_s}{K_c^2 + K_c^2} \cos(yu) + \frac{F_s K_c - K_c K_s}{K_c^2 + K_s^2} \sin(yu) \right\} du \qquad (112)$$

It should be noticed that in Equation (112) all imaginary quantities have vanished. Actually the integral in Equation (112) has the limits 0 to u_{max}, and the integration takes place over the same values of u used to determine F(u) and K(u) or an equidistant subset of u's.

Finally then, a set of values of g(y) are obtained over the range 0 to y_{max}. From these, the plot of $g(\lambda)$ vs. λ is easily obtained. Some prior knowledge about the probable range of λ's would be, of course, of use in determining what the limits on y should be.

g. Summary and Conclusions. A method for the analysis of decay curve type problems, based on the Fourier transform has been proposed. The results appear as a frequency spectrum of $g(\lambda)$ vs. λ. Fundamental to the entire analysis is the assumption that, while in theory $g(\lambda)$ could be represented by a discontinuous set of Δ functions, it is impossible to measure $g(\lambda)$ exactly by an experimental means and so, due to the inherent error in the data, $g(\lambda)$ lapses into a continuous function. However, it is also true that the resolution of the peaks in $g(\lambda)$ may be made as fine as desired merely by extracting an increasing number of values of f(x) from the initial data, and refining the integration scheme accordingly.

An error analysis is available for the integration scheme and also for the cut-off error. The error in the original data plus the error in the numerical calculations due to rounding off numbers, etc., will produce peak profiles showing a normal distribution as long as the cut-off error is very small and the integration scheme employs small enough intervals. Therefore, a standard deviation may be obtained from the peak itself. Under favorable conditions, the standard deviation should not change greatly from peak to peak in a multicomponent system, and hence may be used as a test to see if a peak might contain more than one component for λ's extremely close together. That the number of components present may be determined by counting the number of peaks in the results is one of the best features of this method.

A fairly large computer will be required to handle the problem if the maximum resolution inherent in the method is to be approached. However, the computer program itself should not be logically complex. Most of the subroutines needed, for example the determination of sine, cosine, exponential, logarithm, and routines for simple integration and interpolation, are available at most computer installations. Only the subroutines for the determination of the complex Γ function, and Filon's integration scheme would then be needed.

Besides the fact that the number of components falls out of the analysis, it is felt that this method has certain other advantages over previous methods. For example, the restriction to equal intervals is merely a requirement of the particular integration scheme used, and

is not basic to the procedure as in Cornell's, Householder's, and Prony's methods. Human judgment in the resolution process has been reduced to roughly estimating the spread in half-lives so that a minimum of computational time may be used. This is an advantage over all previous methods. The fact that errors entering the program at different places may be estimated individually may prove advantageous. Finally, the numerical computation itself is not as complicated as in Prony's or Householder's method, and the occurence of two half-lives very close together does not endanger the entire calculation as it does in the former methods.

CHAPTER VI

NUCLEAR DECAY SCHEME STUDIES

In the following sections the results of the investigations carried out on the isotopes Co^{62}, Y^{92}, Ir^{196}, and Sc^{47} are given. Where possible the results are discussed from the point of view of nuclear shell structure. Figure 50 gives a key to the charts of isotopes.

A. The Isotope Co^{62}

Relatively few reports have appeared in the literature on the decay of Co^{62} and the energy levels in Ni^{62}. Parmley, et al.(114)in 1949 found that the half-life of the Co^{62} ground state decay was 13.9 minutes. They measured a maximum β-energy of 2.3 Mev by absorption techniques, and noted the presence of γ rays of about 1.3 Mev. A much shorter lived activity of about 1.6 minutes that emitted both β rays and γ rays also was found, and assigned to an isomeric state of Co^{62}. In 1954, Nussbaum, et al.(107)measured a maximum β-ray energy of 2.8 ± 0.2 Mev for this isotope in addition to a number of γ rays (see Table XIV), and in 1955, Kraushaar, et al.,(79)found in the decay of Cu^{62} a group of γ rays also ascribed to Co^{62} (Table XIV). Since over 98% of the Cu^{62} decay is to the ground state of Ni^{62}, the results obtained for the γ rays are somewhat tentative. A search of the literature up to March, 1957, revealed no further work on this isotope. A chart of the isotopes of cobalt, nickel, and copper is given in Figure 51, to indicate the possible isotopes that might be produced by low energy deuteron bombardment of nickel.

1. Chemical Separation

The Co^{62} was produced by the (d,α) reaction on a nickel oxide

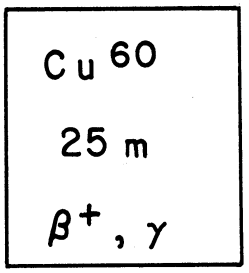

Element, Mass Number

Half Life

Mode of Decay

Radioactive

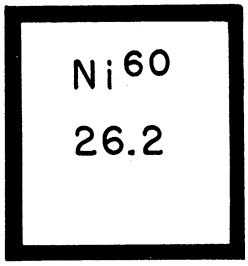

Element, Mass Number

Percent Abundance

Stable

β^-	negative beta particle
β^+	positive beta particle
γ	gamma-ray
K	electron capture
IT	isomeric transition
s	second
m	minute
h	hour
d	day
y	year

Figure 50. Key to the charts of the isotopes

Cu57	Cu58 3s β^+, γ	Cu59 81s β^+	Cu60 25m β^+, γ	Cu61 3.3h β^+, K, γ	Cu62 9.7m β^+, γ	**Cu63 69.0**	Cu64 12.8h β^+, K, γ	**Cu65 31.0**	Cu66 5.2m β^-, γ	Cu67 59h β^-, γ
Ni56 6.4d K, γ	Ni57 36h β^+, K, γ	**Ni58 67.9**	Ni59 8×10^4y K	**Ni60 26.2**	**Ni61 1.2**	**Ni62 3.7**	Ni63 85y β^-	**Ni64 1.0**	Ni65 2.56h β^-, γ	Ni66 56h β^-
Co55 18h β^+, K, γ	Co56 77d β^+, K, γ	Co57 270d β^+, γ	Co58 9h IT | 72d β^+, K, γ	**Co59 100**	Co60 11m β, γ | 5.2y β^-, γ	Co61 1.7h β^-, γ	Co62 14m β^-, γ | 1.6m β^-, γ	Co63	Co64 ~5m	Co65

Figure 51. Chart of isotopes of cobalt, nickel and copper

TABLE XIV. RADIATIONS EMITTED DURING THE DECAY OF Co^{62} AND Ni^{62}

Reference	Energy (Mev)	Relative Abundance
	γ Rays	
114	1.3	γ/β~1
107	1.0	40
	1.17 ± 0.03	100
	1.5	5
	1.7	10
	2.0	15
	2.5	~3
79	0.66 ± 0.03	~1
	0.86 ± 0.03	~1
	1.18 ± 0.02	~1
	1.36 ± 0.02	
	1.46 ± 0.03	
	1.55 ± 0.02	
	1.67 ± 0.02	
	1.98 ± 0.03	
	2.24 ± 0.03	~1
Present Work*	1.17 ± 0.01	100
	1.17 ± 0.01	82
	1.47 ± 0.02	18
	1.74 ± 0.03	18
	2.03 ± 0.03	7
	2.5 ± 0.2	<2
	β Rays	
114	2.3 ± 0.1	
107	2.8 ± 0.2	
Present Work*	0.88 ± 0.04	25 ± 3
	2.88 ± 0.03	75 ± 3

	Coincidence Results	
	Radiation (Mev)	γ Rays "in coincidence" (Mev)
Present Work	β^-, ≥ 1.2	1.17
	γ, 1.17	1.17, 1.47, and higher

* Stated errors are standard deviations, estimated for the β results.

target enriched in Ni^{64}. Table XV lists the isotopic percentages, along with the spectrographic analysis for the target material as given by the Isotopes Division of the Atomic Energy Commission.

TABLE XV. ANALYSIS OF ENRICHED NICKEL ISOTOPES

Mass Analysis

Isotope	Atomic %	Precision
58	1.99	± 0.10
60	1.20	± 0.05
61	0.14	± 0.01
62	0.77	± 0.03
64	95.90	± 0.16

Spectrographic Analysis

Element	%
Cu	0.05
Fe	0.02
Mn	0.01

Eight bombardments were required to complete this work. Usually about 50 mgs. of the oxide was enclosed in a 1.5-mil aluminum envelope for the bombardment in the 7.8-Mev deuteron beam of the University of Michigan cyclotron.

A chemical separation was required to isolate the cobalt in a carrier-free form from the copper and nickel activities produced by the (d,n) and (d,p) reactions in the target element, as well as from the products of these reactions on the impurity elements.

Two approaches to this separation problem were tried, both using ion-exchange as the basis for the separation (77). With Dowex-2 resin, nickel will not adsorb onto the column at any concentration of HCl. Cobalt and copper, however, both show appreciable adsorption in

the range from 6 to 12 N HCl, with cobalt being the more strongly adsorbed element. In 6 N HCl, cobalt and copper are adsorbed about equally. In the range from 6 to 3 N HCl, cobalt rapidly loses its tendency to be adsorbed while copper remains fairly constant.

Using two different sized resin beds, one 8 mm x 140 mm and the other 4 mm x 10 mm, it was found that trying to remove the copper before the cobalt by eluting with solutions in the range of 8 to 10 N in HCl required more time than removing these elements in the reverse order. While the smaller column decreased the time of the separation, the degree of separation was much poorer at elution rates of 1-2 drop/sec. It was therefore decided to perform the separation as indicated in Table XVI using the larger column.

Since it was necessary to use the target material in several bombardments and to return it to the Atomic Energy Commission in purified form, a procedure for reprocessing the target material was required. This was done as follows: The 8 N HCl solution containing Ni(II) was first evaporated to dryness, and then the residue was dissolved in water. Next $Ni(OH)_2$ was precipitated with NaOH. The hydroxide was repeatedly washed in a centrifuge tube with distilled water until the wash water was neutral. Finally, the hydroxide was heated until the oxide was obtained.

The cobalt fraction was mounted directly by evaporation onto a thin cover glass for γ-ray measurements. For the β-ray measurements the cobalt fraction was first evaporated to dryness, then taken up in water, and finally mounted on the aluminum coated 1/4-mil Mylar film previously described.

TABLE XVI. COBALT SEPARATION CHEMISTRY

Element separated: Cobalt

Procedure by: Gardner

Target Material: Nickel Oxide

Time for sep'n: 1/2 hr.

Type of bbdt: 7.8 Mev deuterons

Equipment required: Ion exchange column of AG 2-x8, 200-400 mesh resin obtained from Bio-Rad Labs. Resin bed was 8 mm x 140 mm.

Degree of purification: Estimated $\sim 10^5$ from Ni and Cu.

Advantages: Carrier-free separation with high decontamination.

Procedure:

1. Dissolve NiO in 5 ml of 10 N. HCl. Evaporate to small volume, place in column previously washed with conc. HCl.

2. Remove Ni from column by elution with 15 ml of 8 N HCl at rate of 1 or 2 drops/sec. Both Co and Cu remain on column.

3. Remove Co by elution with 6 - 8 ml. of 4 N HCl. Last ml. or so possibly contaminated with small amount of Cu.

4. Mount for counting.

Remarks:

1. General reference: Hicks, H. G., et al., "The Qualitative Anionic Behavior of Resin, 'Dowex 2' ", Livermore Research Laboratory Report, LRL-65, Dec. 1953.

2. Experimental Methods

γ-ray spectra were obtained using both the photographic technique, and also by automatic plotting of the spectrum from the pulse height analyzer on the strip chart recorder. The β-ray spectrum was measured using the 3.6-Mev hollow plastic scintillator.

The γ-γ coincidence studies were carried out using two 1" x 1-1/2" NaI (Tl) crystals. A 1.6 gm/cm^2 aluminum absorber was placed between the sample and each crystal to absorb the β-rays. For the β-γ coincidence studies, one NaI (Tl) crystal was replaced by the plastic scintillator previously mentioned. No absorber was used between the source and the plastic scintillator. Since the half-life of Co^{62} is so short, it was only possible to obtain coincidence information through the use of the photographic coincidence method described in Chapter III.

3. Results

The half-life of Co^{62} was determined to be 13.909 $\pm$ 0.013 minutes, the error being the standard deviation, by following the decay of the γ rays in a scintillation well-type counter. The decay curve is shown in Figure 52. A small amount of Ni^{65} is seen to be present. No other cobalt activity could be seen. The resolution was obtained using the Weighted Least-Squares program.

Figure 53 shows the Co^{62} γ-ray spectrum taken from the strip chart recorder. Measurements of this type along with the oscilliscope pictures indicated that the primary γ-ray transition was 1.17 $\pm$ 0.01 Mev in energy. Four higher γ rays of lower intensity were also observed. These were 1.47 $\pm$ 0.02, 1.74 $\pm$ 0.03, 2.03 $\pm$ 0.03, and 2.5 $\pm$ 0.2 Mev.

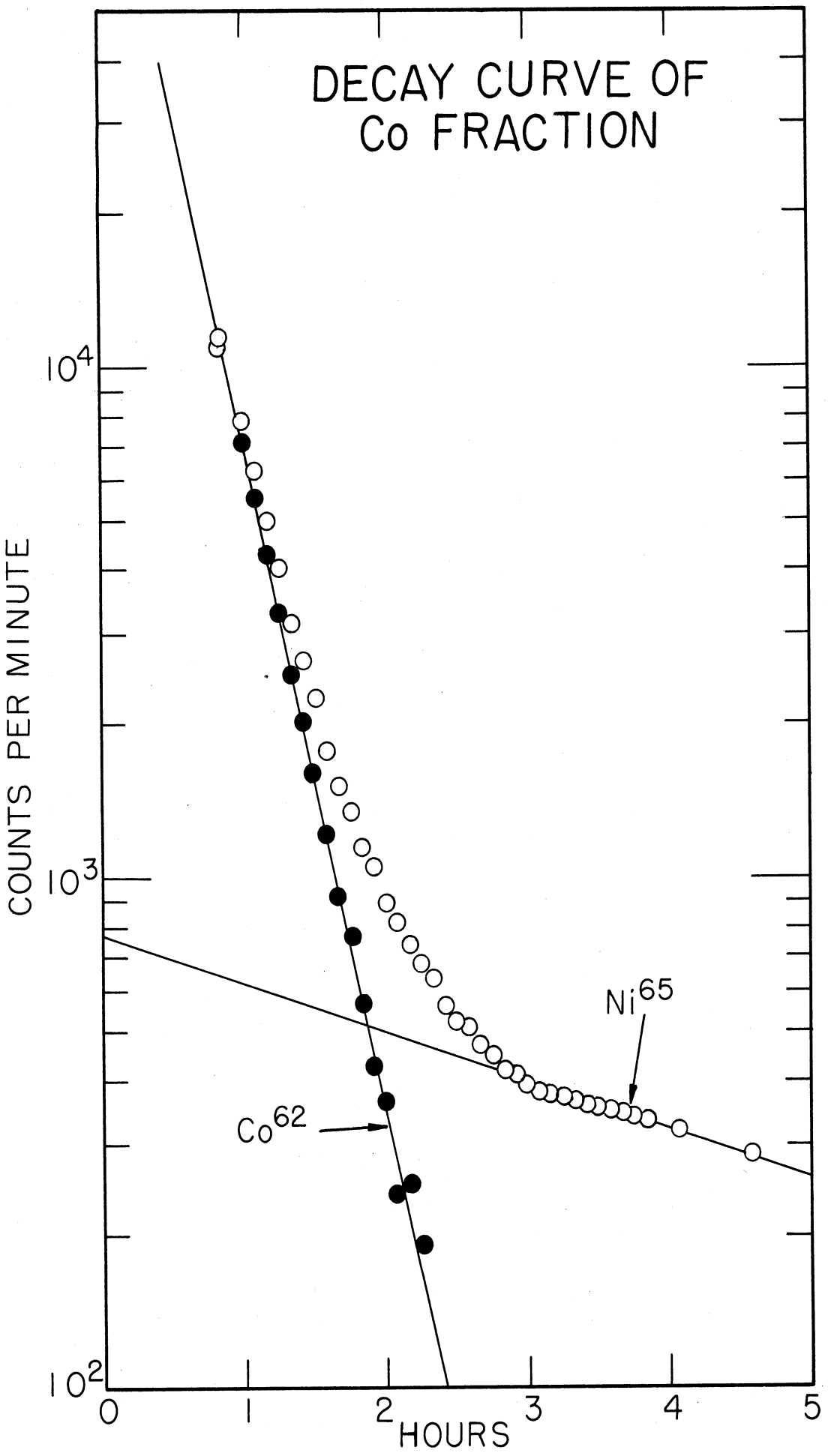

Figure 52. Decay curve of cobalt fraction

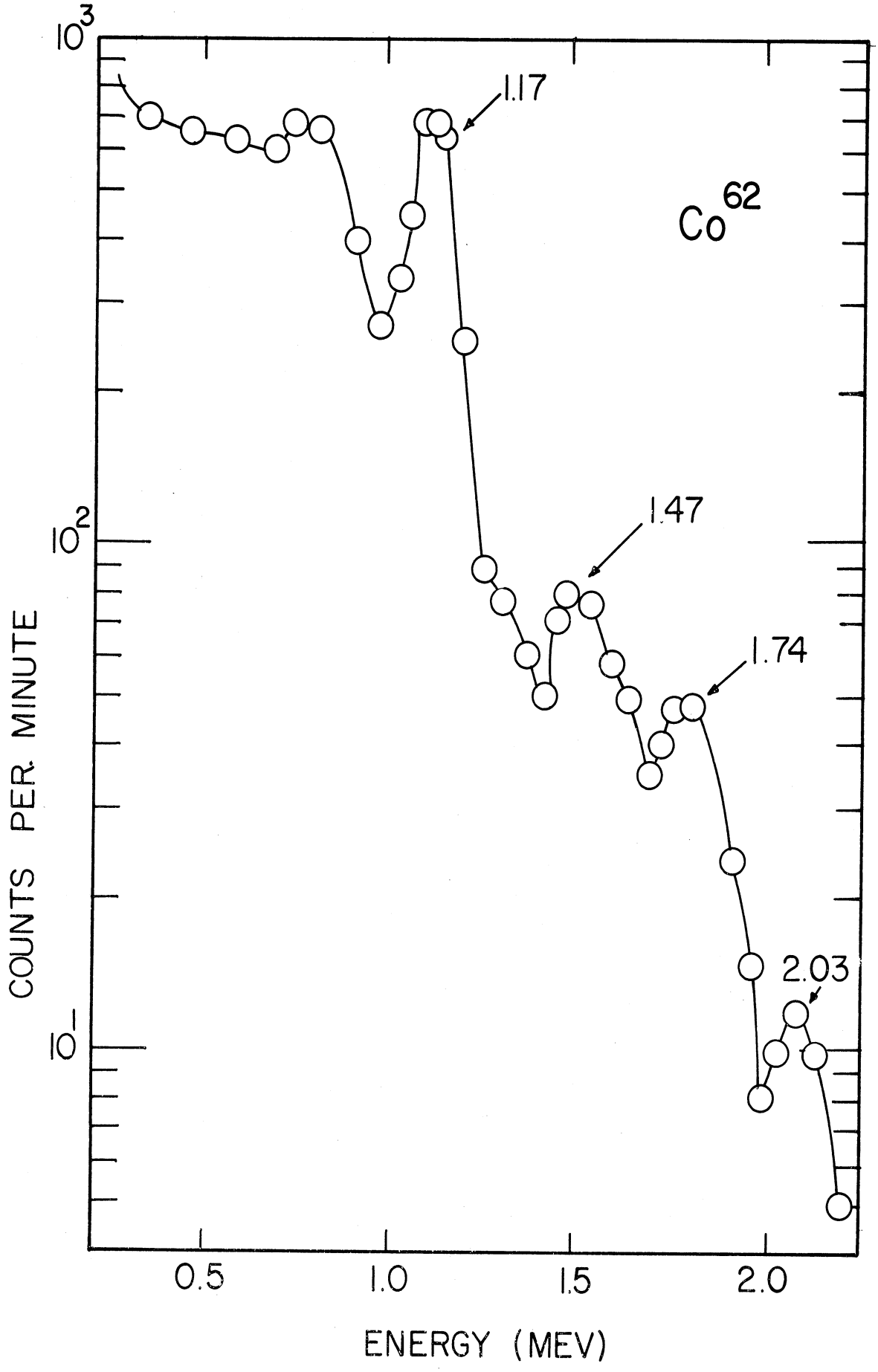

Figure 53. Gamma-ray spectrum of Co^{62}

Integration under the Speedomax curves, correcting for the NaI(Tl) crystal efficiency (92) yielded intensities of 11%, 11%, 4%, and less than 1%, respectively, for these γ rays relative to 100% for the 1.17-Mev γ ray.

A tentative decay scheme based on the γ-ray information allowed for the possibility of three β-ray groups: a 0.8, a 2.3 to 2.5, and a 2.8-Mev transition. Due to the short half-life, a complete β-ray spectrum could not be obtained on a single sample with enough points or statistical accuracy. Therefore, it was necessary to combine the results of two bombardments. Figure 54 shows the results of this combination. Each point on the curve was corrected for decay during the time of the count which ranged between 3 to 8 minutes. Then each point was corrected for decay back to the time of the start of the first count. Correction was also made for the γ-ray background in the plastic scintillator.

Since the upper portion of the β-ray spectrum yielded a Kurie plot straight down to 1.5 Mev, the possible 2.3-2.5 Mev transition was assumed to be absent, and the two portions of the Kurie plot obtained on different days could be fitted together easily. The resulting total Kurie plot, when corrected for instrument resolution, could be resolved into two components: a 0.88 ± 0.04 and a 2.88 ± 0.03 Mev transition. Relative abundances are $25 \pm 3\%$ and $75 \pm 3\%$, respectively. Errors in the energies and intensities are estimated probable errors. Log (ft) values are 4.5 and 5.8, respectively, indicating both transitions are allowed. This is borne out, in the case of the 2.88-Mev β-ray, by the shape of the Kurie plot. While the shape of the lower energy group also appears to be allowed, it is subject to the usual subtraction errors.

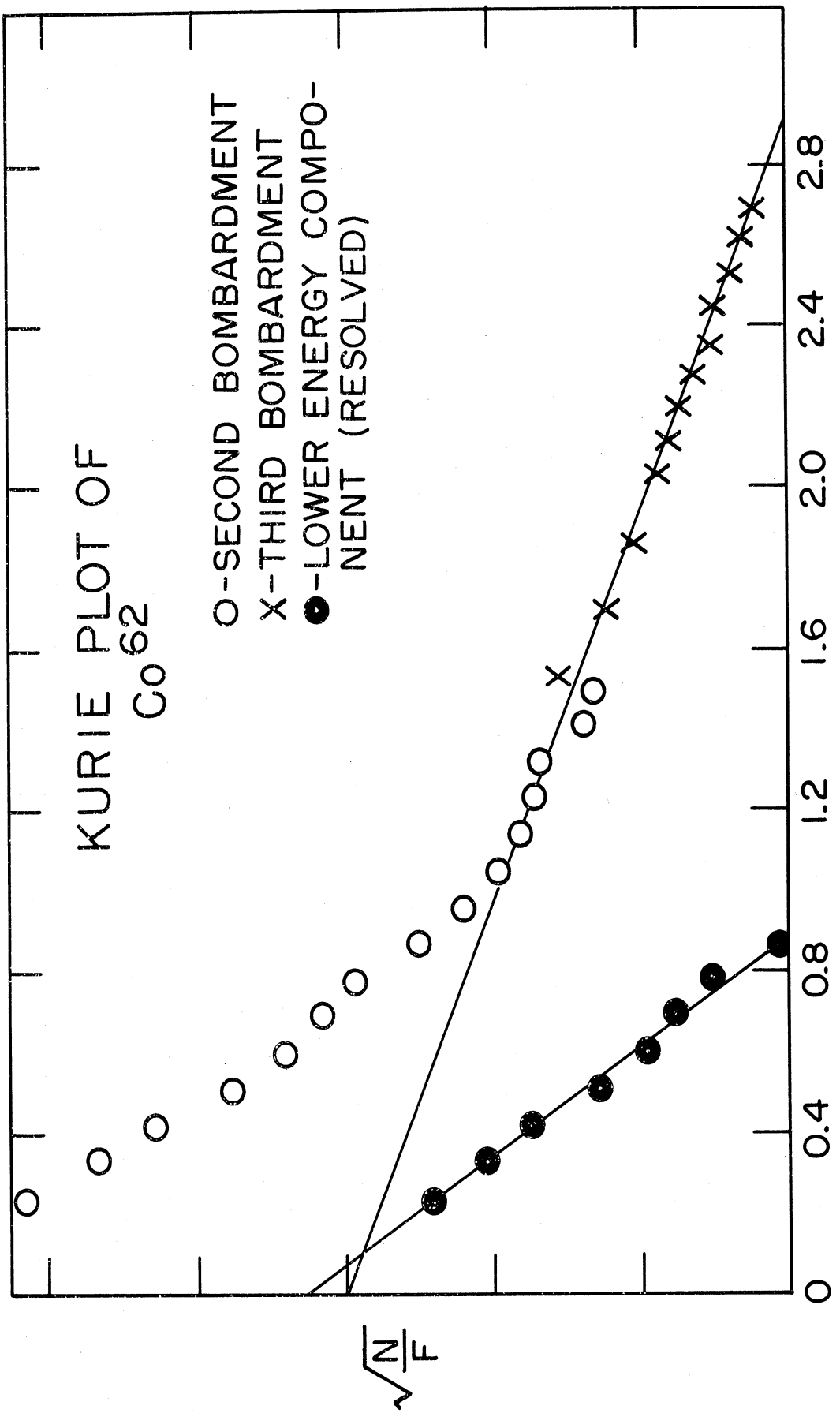

Figure 54. Kurie plot of Co^{62}.

Assuming the 2.88-Mev β group populated the 1.17-Mev γ level, the γ-ray intensities calculated from the observed β-ray intensities differed from the observed γ-ray intensities by a factor of 2. Furthermore, the total disintegration energy for Co^{62} predicted from β systematics is about 5 Mev, whereas the 2.88-Mev β and the 1.17-Mev γ transitions add up to only about 4 Mev. By assuming a cascade doublet following the higher β ray, the difficulties were resolved. Both γ rays would have an energy of 1.17 Mev, and differ in energy by less than 1-2%. The corrected percentage abundances for the 1.17 (doublet), 1.47, 1.74, 2.03, and 2.5 Mev γ-rays are then, respectively, 100% and 82% for the doublet, 18%, 18%, 7% and less than 2%.

Coincidence information was obtained by photographing the γ rays in coincidence with all β rays above 1.2 Mev. This showed only the 1.17 Mev γ-ray. γ-γ coincidence information was obtained by setting the interdicting channel on the 1.17-Mev γ-ray. The results show strong coincidences with a γ ray at 1.17 Mev, and also with higher gammas.

4. Conclusions

The above information has been correlated into the level diagram shown in Figure 55. The β rays are shown with their energies in Mev's first, followed by the % abundance and the log (ft) value. The γ rays are shown similarly with their energies in Mev's first and then the % abundance.

In the nuclide Co^{62} the ground state configuration of the protons is $(1f\ 7/2)^{-1}_{7/2}$, where the superscript -1 indicates one nucleon less than a closed shell and the subscript 7/2 indicates the resultant proton spin. The ground state configuration of the neutrons is somewhat

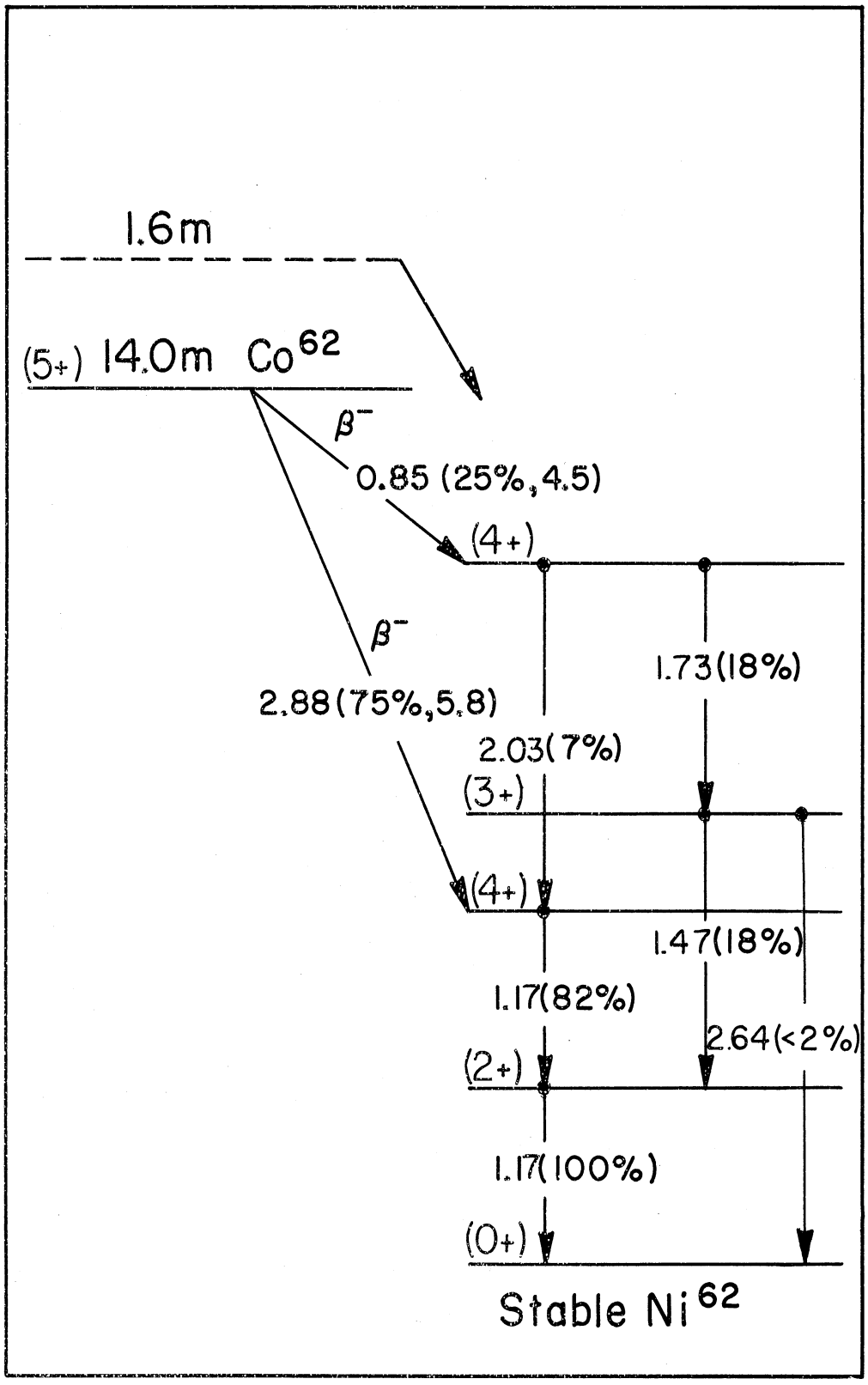

Figure 55. Decay scheme of Co^{62}

less uniquely predictable. Here both the (2p 3/2) and the (1f 5/2) levels are relatively close together in energy (91). A consideration of the other nuclides in this neutron range indicates that the probable configuration is $(2p\ 3/2)^{-1}_{3/2}\ (1f\ 5/2)^{-2}_{0}$. According to Nordheim's "weak" rule (103) the proton and neutron spins will tend to add, giving a resultant spin of 4 or 5 and even parity.

In the case of $_{28}Ni^{62}_{34}$, the (1f 7/2) proton shell is clearly filled with a resultant spin of 0. Again the neutron configuration is unclear, but is probably $(2p\ 3/2)^{-2}_{0}\ (1f\ 5/2)^{-2}_{0}$ so that the ground state of Ni^{62} would have 0 spin and even parity. The first excited state of Ni^{62} is very probably 2+, that is spin 2 and even parity. The second state at 2.34 Mev and the fourth state at 4.37 Mev are both required to have high spins and even parity since the ground state of the parent is 4+ or 5+ and both transitions are allowed. A spin of 4+ for the second state is reasonable from the shell model.

The 2.5 $\pm$ 0.2 Mev γ-ray transition cannot be a cross-over from the second excited state to the ground state, and therefore, must arise from the third excited level. Hence the order of the 1.74- and 1.47-Mev γ rays given in Figure 55 is the most likely. This would require a spin of 2 or 3 for the third level. The fact that the third level is not populated by β decay, together with the ratio of the intensities of the 1.75 and 2.03-Mev γ rays suggest the following level assignments: spin 3+ for the third level, spin 4+ for the fifth level, and spin 5+ for the ground state of Co^{62}.

The 1.6-min. isomer of Co^{62} found by Parmley (108) was not found here due to the length of time required by the chemical separation.

However, it is quite reasonable to expect that the first excited state of Co^{62} would have a proton configuration of $(1f\ 7/2)^{-1}_{7/2}$, and a neutron configuration of $(1f\ 5/2)^{-3}_{5/2}$. These would couple to give a spin of 1+, producing an isomeric state with an energy not much above the ground state. This first excited state would have a high probability of decaying directly to the ground state of Ni^{62}. For the sake of completeness this hypothetical excited level has been included in Figure 55.

B. The Isotope Y^{92}

Several representations of the decay scheme of Y^{92} have been reported in the literature, the most recent being found in the compilation of K. Way, et al. (144). This last was based primarily on the work of Cassatt and Meinke (20,21), and of Ames and his co-workers (4). Furthermore the investigation of Nb^{92} which decays by electron capture (54,66) has contributed to the knowledge of the energy levels in Zr^{92}. The half-life of Y^{92} has been determined to be approximately 3.6 hours (4,20,21). Maximum β-ray energies of 3.4, 3.5, and 3.6 Mev have been reported (4,20,21,138). The presence of three β rays of maximum energies of 1.3, 2.7, and 3.60 Mev was postulated by Ames, et al. (4). γ rays have also been measured (4,20,21,54,66). Table XVII lists the available information concerning the β rays emitted by Y^{92} and the γ rays from Zr^{92}.

Figure 56 shows the decay scheme for Y^{92} - Zr^{92} - Nb^{92} as given in reference (144). The present work was undertaken primarily because the placement of the 0.45- and the 0.21-Mev γ rays is not consistent with the available data, and the assignment of a spin of 2+ or 3+ to the ground state of Nb^{92} is unlikely from shell structure theory. A ground state spin of 2+ or 3+ would necessitate a spin of 6 or 7 for the

TABLE XVII. RADIATIONS EMITTED DURING THE DECAY OF Y^{92} AND Zr^{92}

Reference	Energy (Mev)	Relative Abundance
	γ Rays	
20, 21	0.20	10
	0.48 (double?)	11
	0.94 (double?)	19
	1.45	10
	1.9	1
	2.4	0.2
4	0.45	
	0.55	
	0.93	
	1.39	
	1.83	
54,66	0.900	
	0.930	
	1.83	
	2.35	
Present Work *	$\leq$0.03 (postulated)	6 - 12
	0.07 ± 0.004	1.9 ± 0.3
	0.14 (?)	weak
	0.21 ± 0.005	3.1 ± 0.7
	0.29 ± 0.02	3.1 ± 0.7
	0.47 ± 0.02 (double)	7.2 ± 0.5
	0.54 ± 0.02	0.5 ± 0.2
	0.90 ± 0.01	3.9 ± 0.5
	0.93 ± 0.02	11.2 ± 1.5
	1.44 ± 0.04	4.2 ± 0.5
	1.86 ± 0.05	0.5 ± 0.2
	2.40 ± 0.05	0.08 ± 0.05
	β Rays	
20, 21	3.6 (spectrum complex)	
4	1.3	11
	2.68	12
	3.60	77
Present Work *	1.26 ± 0.06	9
	1.75 ± 0.15 (complex ?)	3
	3.60 ± 0.03	88

* Errors are standard deviations, estimated for the β results.

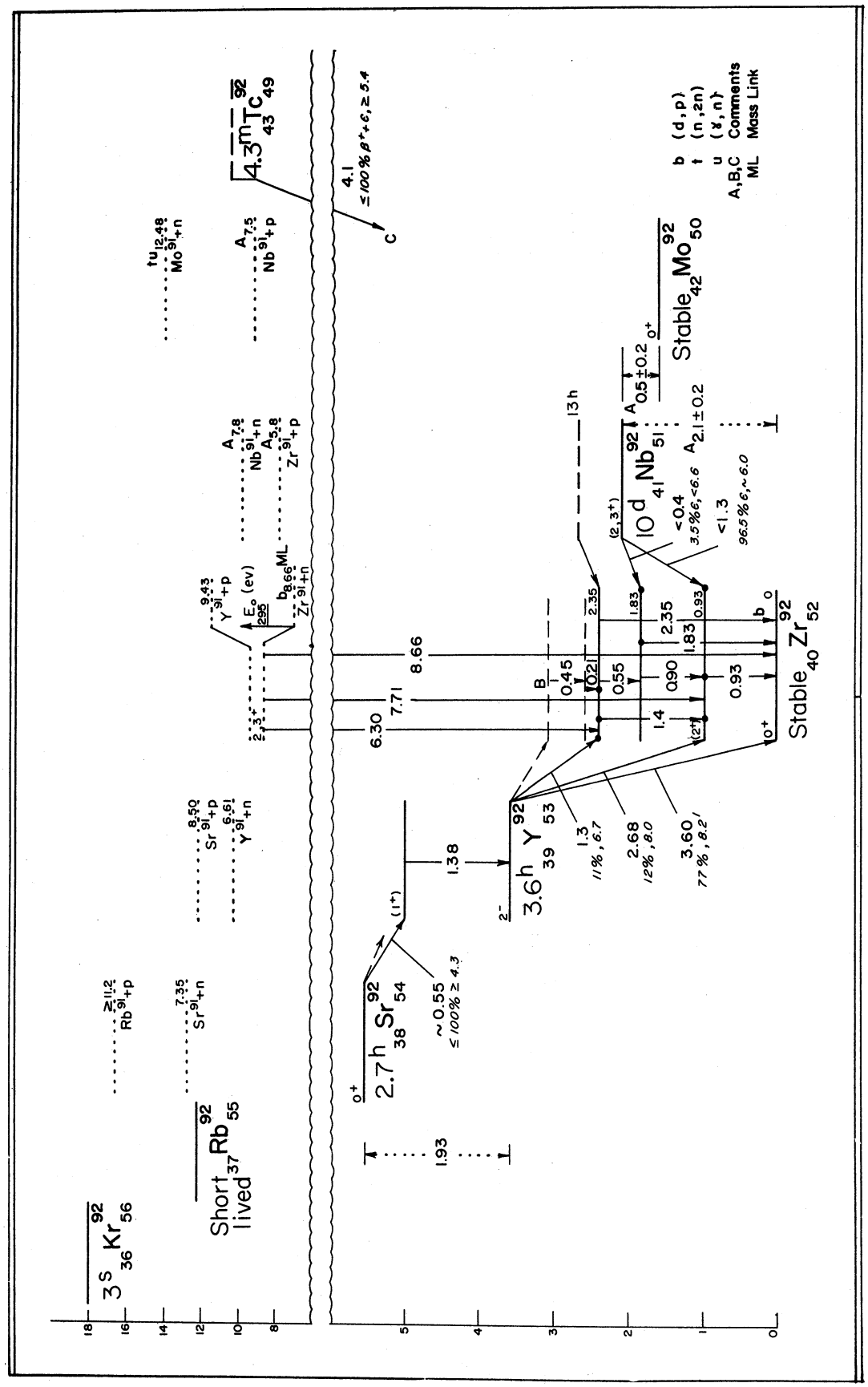

Figure 56. Decay Scheme for Y^{92} - Zr^{92} - Nb^{92} as Given by K. Way, et al.

isomeric state in Nb^{92}, whereas a low spin and odd parity would be expected from shell theory. If this isomeric state actually populates the 2.35-Mev level in Zr^{92}, as shown in Figure 56, which in turn may decay directly to the ground state, then the spin of the isomeric Nb^{92} level could not be more than 4 or 5. Finally if the ground state spin of Nb^{92} is actually 5+ or 6+, as would be expected, then the 0.93-Mev level shown in Figure 56 with a spin of 2+ would not be fed by a transition from the Nb^{92} ground state. These and other considerations indicated that a reinvestigation of this decay scheme was warranted. A search of the literature up to March, 1957 revealed no further work on this isotope. A chart of the nuclides of yttrium, zirconium, and niobium is given in Figure 57, to indicate the possible isotopes that might be produced by low-energy deuteron bombardment of zirconium.

1. Chemical Separation

The yttrium activity was produced by bombarding high-purity zirconium metal foil with 7.8 - Mev deuterons in the University of Michigan cyclotron. The foil was obtained from the Foote Mineral Company, Philadelphia, Pennsylvania, and the chemical impurities are listed in Table XVIII. A chemical separation was necessary to separate the yttrium from the zirconium and niobium activities produced by (d,n) and (d,p) reactions in the target element, as well as from products of these reactions on the impurity elements. Seven cyclotron bombardments were required to complete this study.

When the yttrium chemical separation was being planned, a possible study of the 17-minute isotope Y^{94} was considered. This study would have required a sample of zirconium enriched in the isotope Zr^{96}. Although

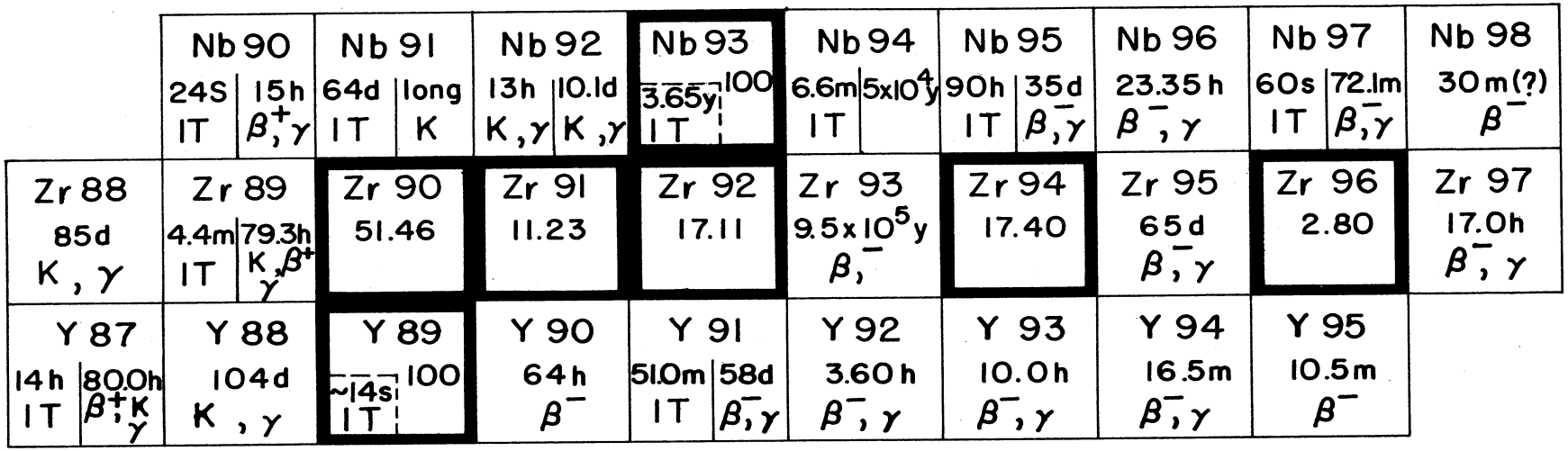

Figure 57. Chart of the isotopes of yttrium, zirconium, and niobium

it was later decided not to attempt this study due to the cost of the enriched zirconium isotopes, the chemical separation was developed with the short half-life of Y^{94} in mind.

TABIE XVIII. CHEMICAL IMPURITIES IN TYPICAL ZIRCONIUM TARGET FOIL AS DETERMINED BY SPECTROGRAPHIC ANALYSIS

Element	%	Element	%
Al	0.04 - 0.08	Mo	0.001
Ca	0.003	N	0.004 - 0.04
Cr	0.001	Pb	0.001
Cu	0.007	Si	0.02
Fe	0.01 - 0.20	Sn	0.001
Hf	2.5 - 3.0	Ti	0.04
Mg	0.003	W	0.001
Mn	0.001		

As in the case of the cobalt separation previously described, an ion-exchange separation was decided upon (78). It seemed desirable to introduce a rapid, fairly thorough separation of yttrium from zirconium and niobium before the ion-exchange stage. This initial step would then constitute the entire separation if the Y^{94} isotope were to be studied. However, this first step would be used in the more thorough separation, and hence should not introduce any inactive yttrium carrier.

The zirconium metal foil used in the Y^{92} bombardments could best be dissolved in dilute HF. Niobium and zirconium are soluble in HF, while yttrium would form the more insoluble YF_3. Therefore, if an element which forms an insoluble fluoride were to be added to the HF solution of the zirconium target foil, the radioactive yttrium would be carried down on the insoluble fluoride precipitate. The alkaline and rare earth elements would be suitable, but they would present difficulties in designing a rapid separation to remove them at a later stage. For these reasons it was decided to use lead as the carrier for yttrium.

Other advantages of lead are that its fluoride can easily be dissolved in HCl solution, and that it can be rapidly separated from yttrium on an ion exchange column. One disadvantage is that the fluoride tends to dissolve slightly when washed with water.

The principal place in the separation where some yttrium is most likely to be lost occurs in the first step where the target foil is dissolved in dilute HF. It was noted that an appreciable amount of the yttrium activity tends to adhere to the walls of the Lusteroid centrifuge tube. When the PbF_2 is precipitated, and in later washings, the precipitate should be thoroughly stirred in order to remove as much yttrium from the walls of the tube as possible. The actual chemical separation that was developed is given in Table XIX.

TABLE XIX. YTTRIUM SEPARATION CHEMISTRY

Element separated: Yttrium

Target Material: Zirconium

Type of bbdt: ~7.8 Mev deuterons

Procedure by: Gardner

Time for sep'n: ~1 hr.

Equipment required: Lusteroid centrifuge tubes, two ion exchange columns of AG 2-X8, 200-400 mesh resin obtained from Bio-Rad. Lab. Resin beds were 8 mm x 140 mm.

Yield: ~90%

Degree of purification: Estimated $>10^6$ from Nb and Zr

Advantages: Essentially carrier-free separation with high decontamination. Can be shortened to ~5 min. if carrier can be tolerated.

Procedure:

(1) Place target foil in a Lusteroid centrifuge tube containing 5 ml of 6 N HF, and 10 mg of Nb holdback carrier. (Sample dissolved immediately.)

(2) Add 10 mgs of Pb^{++}, stir precipitate, and centrifuge. (See remark 1).

(3) Wash precipitate twice with ~5 ml of ~1 N HF, centrifuging in between. Wash once with a minimum amount of H_2O.

(4) Transfer precipitate to a glass beaker. Dissolve in several ml. of conc. HCl and evaporate to dryness with a few drops of HNO_3. Take up in conc. HCl and evaporate to dryness again.

(5) Take up in several drops of conc. HCl and place on column previously washed with conc. HCl.

(6) Elute with conc. HCl. at rate of ~1-2 drops/sec. The Y will begin to come off after 3-4 mls of eluent; most will appear in another 4-6mls. (See remarks 2 and 3).

(7) If desired, the Y may be separated from the lead as follows. Concentrate the eluent from step 6 to < 1 ml, dilute with H_2O until ~5-7 N in HCl, and place on column prepared by washing with 6 N HCl. Elute with 6 N HCl. (See remark 4).

TABLE XIX. YTTRIUM SEPARATION CHEMISTRY (Cont'd)

(8) If the Pb carrier can be tolerated, along with an almost negligible amount of Nb and Zr, the precedure may be shortened to ~ 5 minutes if the sample is mounted after step 3. Filtering, using non-glass equipment, will reduce the time even further.

Remarks:

(1) Essentially all of the Y follows the Pb.

(2) A large part of the Pb will also appear in Y fraction.

(3) Any small amounts of Zr and Nb possibly present will remain on column.

(4) Pb will remain on column.

(5) General reference for this type procedure: Hicks, H. G., et al., "The Qualitative Anionic Behavior of a Number of Metals with an Ion Exchange Resin, 'Dowex 2' ", Livermore Research Laboratory Report, LRL-65, December, 1953.

2. Experimental Methods

The γ rays from Y^{92} were studied in the usual manner. The β rays were measured using the 3.6-Mev hollow plastic scintillator. In obtaining the β-ray spectrum of Y^{92}, corrections were made for the contribution of Y^{90} and Y^{88} which were produced along with the Y^{92}.

The γ - γ coincidence studies were carried out using two 1" x 1-1/2" NaI(Ti) crystals, with 1.5 gm/cm^2 Be absorbers between the source and the detectors. For β -γ coincidence studies one γ-ray detector was replaced by the 3.6-Mev β scintillator. Since the half-life of Y^{92} is relatively long, manual coincidence spectra could be obtained as well as photographic coincidence results.

3. Results

The half-life of Y^{92} was found to be 3.66 $\pm$ 0.66 hours by a least-squares analysis of the decay curve of a portion of the β-ray spectrum at $\sim$ 3.0 Mev. This is beyond the endpoint of the Y^{90} β-ray spectrum. Figure 58 shows the decay curve and the least-squares line fit. Other decay curves taken with a well-type γ-scintillation counter showed the presence of only three components, a 3.6-hour, a 65-hour, and a 105-day activity due to Y^{92}, Y^{90}, and Y^{88} respectively.

The γ rays found, and their relative intensities are listed in Table XVII. Figure 59 shows the γ-ray spectrum taken from the Speedomax strip chart recorder, while Figure 60A shows an oscilliscope picture of the same spectrum. These results reveal the presence of four intense γ rays with energies of 0.21, 0.47, 0.93, and 1.45 Mev along with several weaker transitions. The γ intensities were obtained by integration under the Speedomax curves, correcting for the NaI(Tl) crystal efficiency (92).

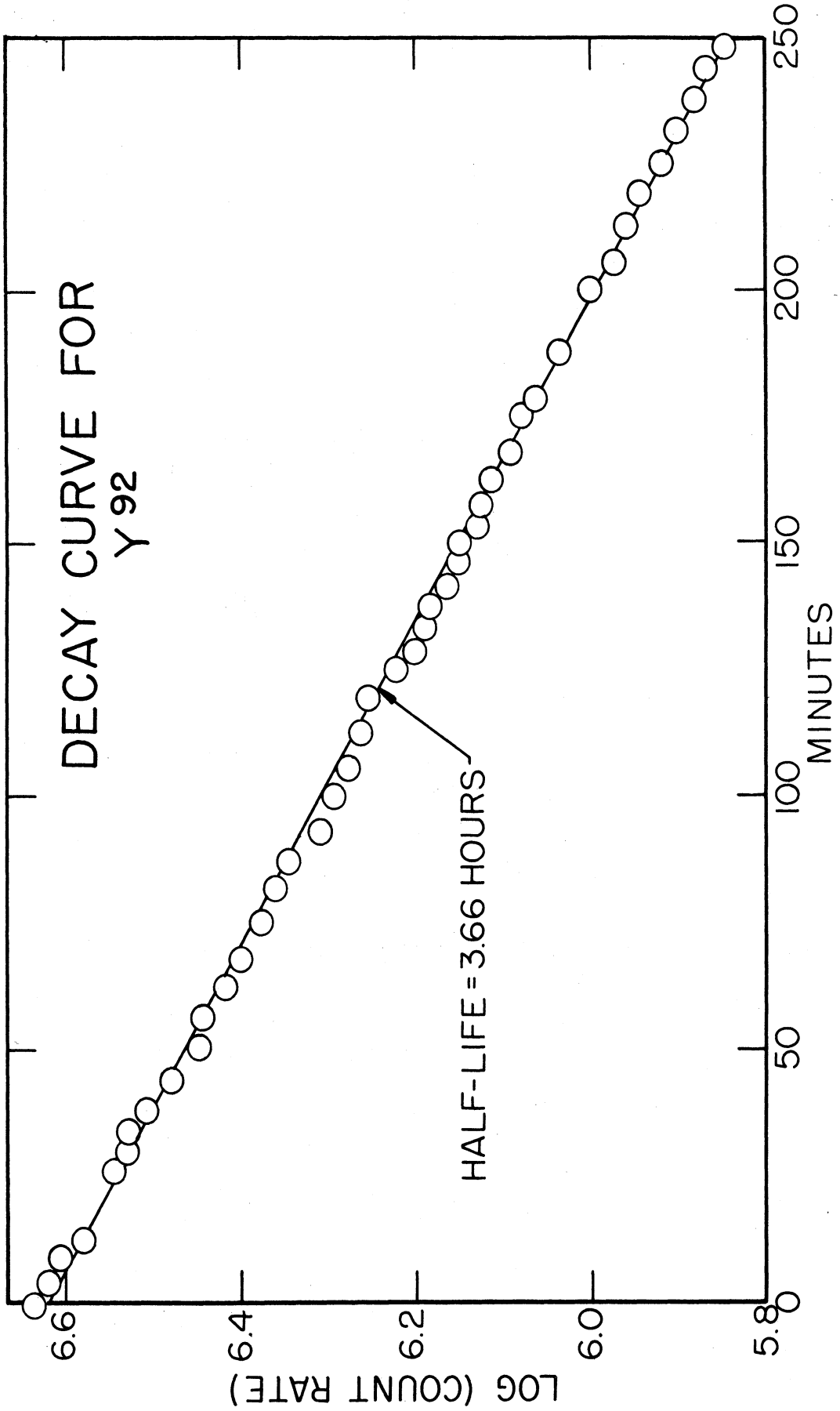

Figure 58. Decay curve of Y^{92} with least-squares line fit

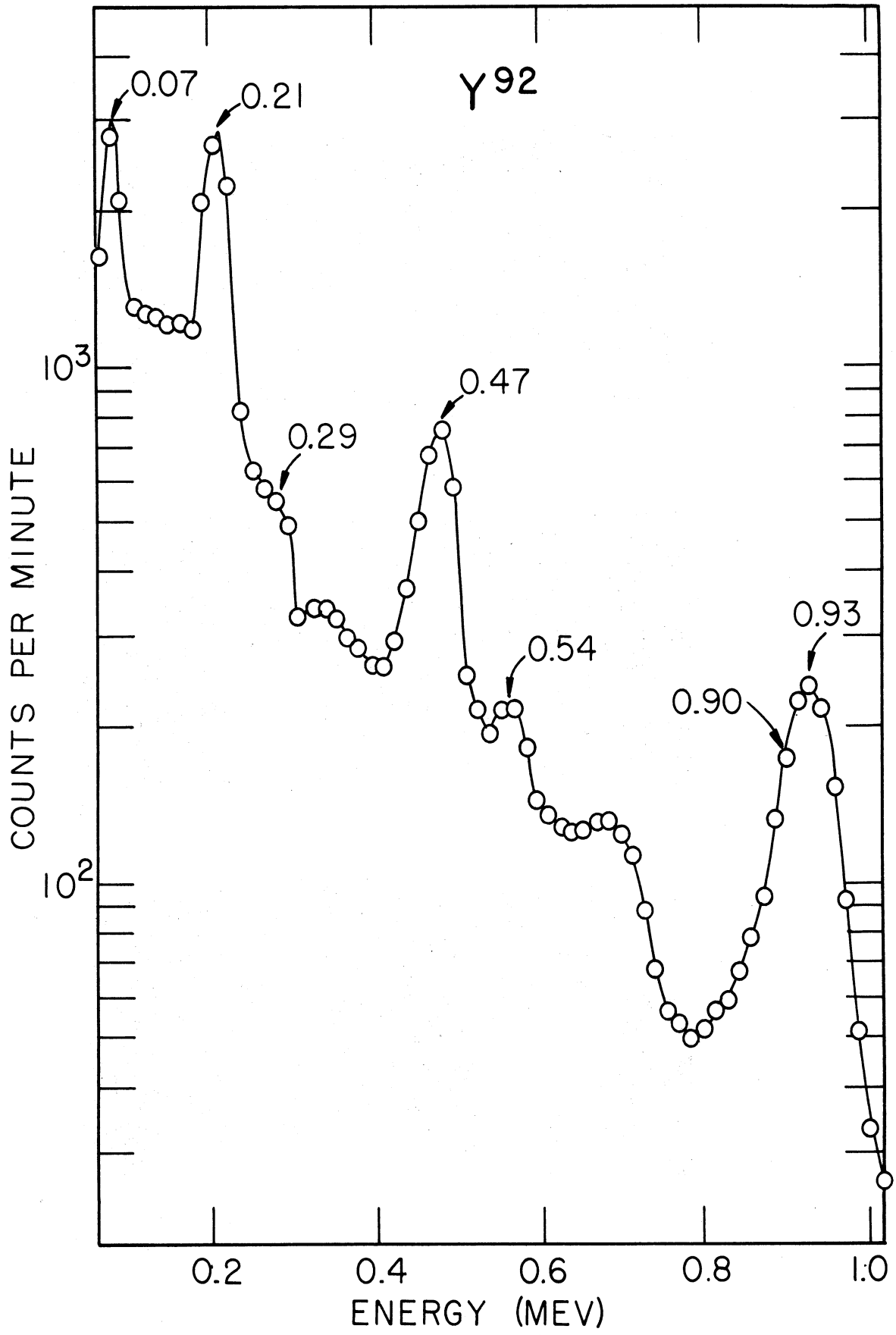

Figure 59. Gamma-ray spectrum of Y^{92}

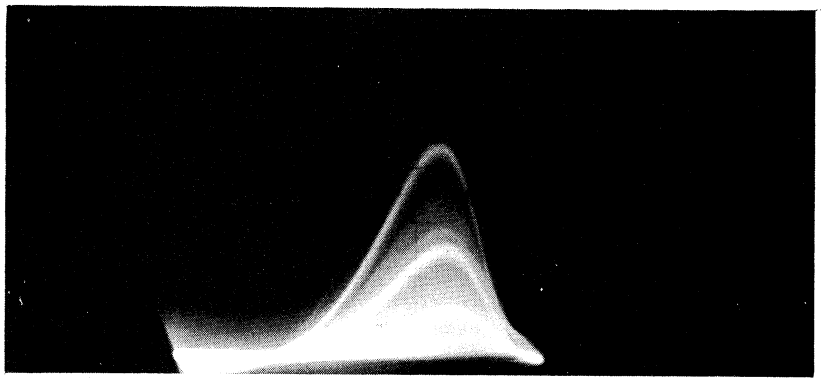

(A)

(B)

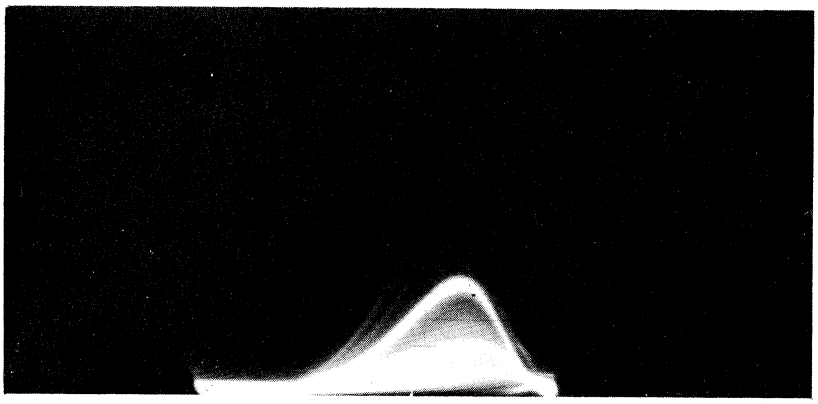

(C)

Figure 60. (A) Total Y^{92} Gamma-ray Spectrum. (B) Gamma-ray Spectrum in Coincidence with 0.47-Mev Gamma ray. (C) Gamma-ray Spectrum in Coincidence with 0.21-Mev Gamma ray.

Figure 61 gives the β-ray spectrum for Y^{92}, and has been corrected for decay as well as for the Y^{90} and the Y^{88} components. The conversion peak at ∿ 0.45 Mev should be noted. After a decay scheme had been postulated the total conversion coefficient could be estimated, and was found to be $\alpha_T \lesssim 0.20 \pm 0.12$. Using the tables of Rose, et al. (119) it was found that the measured conversion coefficient fell into the range of the following transitions: M3, M4, and E4. This indicated that the 0.47-Mev γ-ray arose from a spin change of 3 or 4 units, and originated at a meta stable state whose half-life was on the order of ∿2 milliseconds to ∿5 minutes depending on the transition involved.

Figure 62 illustrates the Kurie plot of the Y^{92} γ spectrum. Here the major transition has a maximum energy of 3.60 ± 0.03-Mev and a relative abundance of ∿ 88%. A small amount, roughly 3%, of an intermediate transition with a maximum energy 1.75 ± 0.15-Mev appeared to be present, along with a ∿ 9% of a 1.26 ± 0.06-Mev transition. The 3.60-Mev transition definitely had a "unique" first forbidden shape, but the shapes of the lower energy transitions could not be determined with accuracy. No trace of the 2.68-Mev transition found by Ames, et al. could be seen; an upper limit for this transition, consistant with the present data, would be 1 or 2%.

β-γ, γ-β and γ-γ coincidence data were obtained both by the photographic method and also by point-by-point manual sweeps. These are included in Table XX. Figure 60B is an oscilliscope photograph of the pulses in coincidence with the 0.47-Mev γ-ray. One of the more interesting features of the coincidence data is that the 0.93-Mev γ-ray does not seem to be in strong coincidence with either β transitions or other γ transitions.

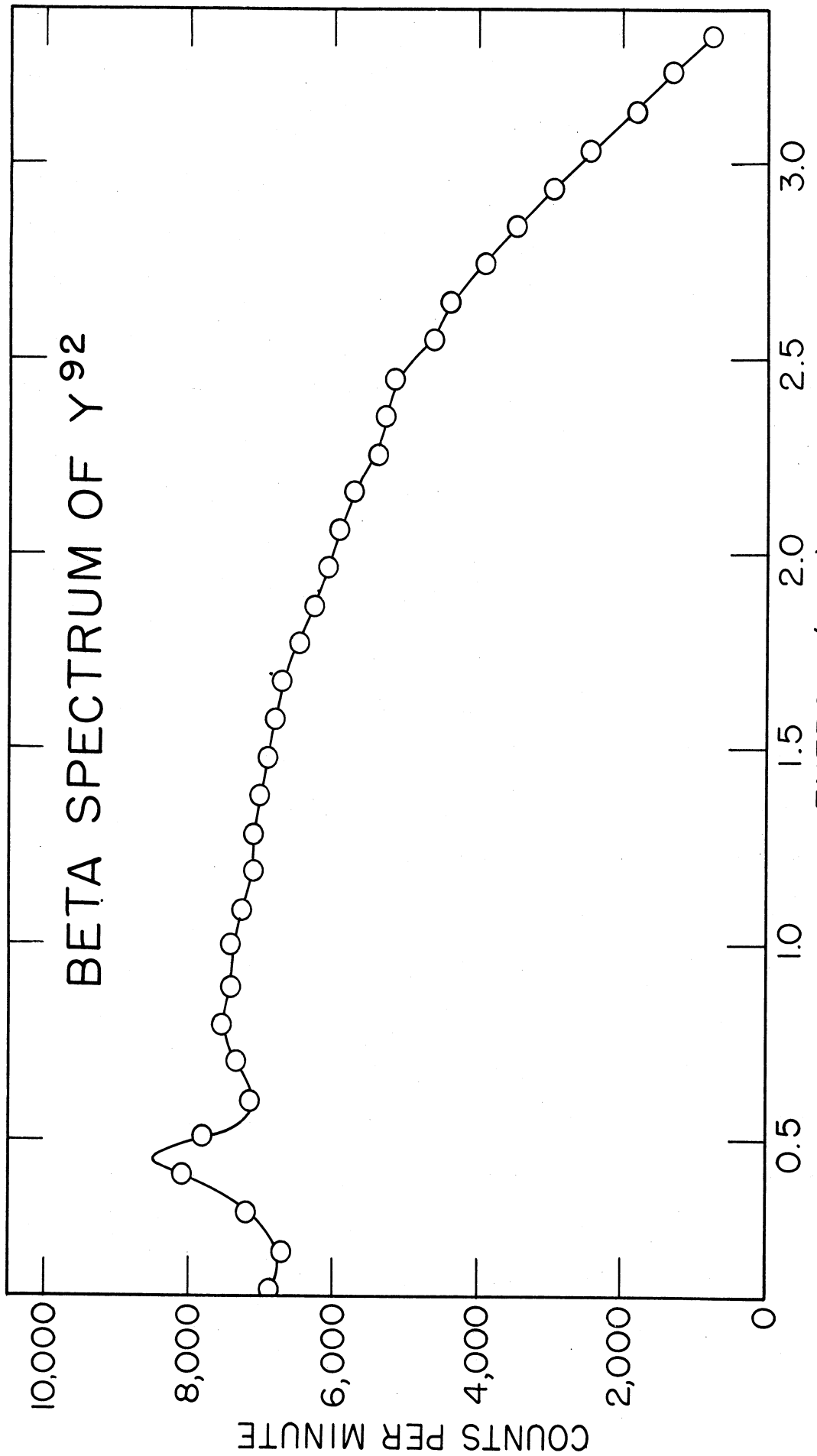

Figure 61. Beta-ray spectrum of Y^{92}

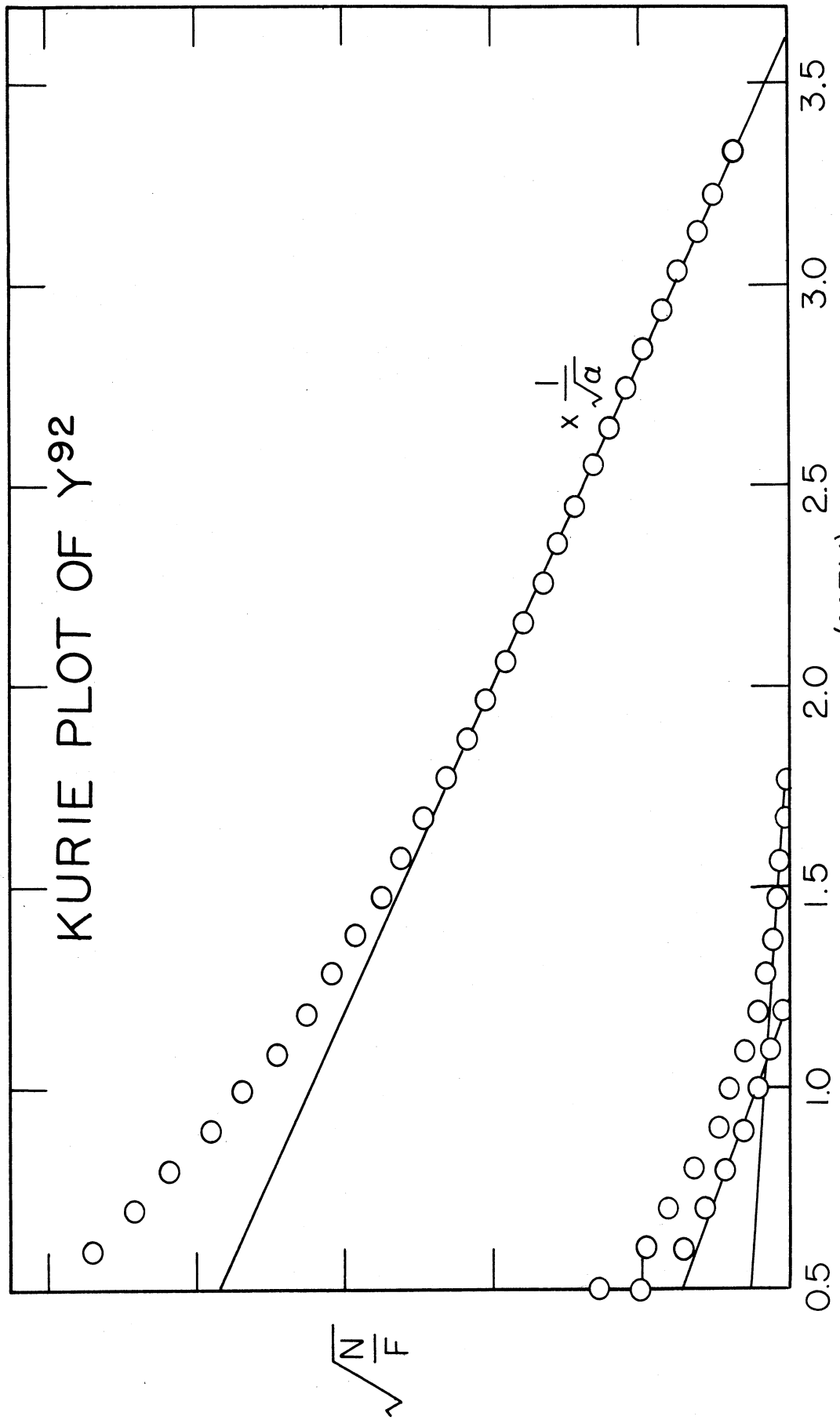

Figure 62. Kurie plot of Y^{92}. Ordinate scale for top curve differs from scale for lower curves

TABLE XX. COINCIDENCE RESULTS FOR ISOTOPE Y^{92}

Type of Coincidence	Energy of radiation (Mev)	Energy of radiation in "strong" coincidence (Mev)	Energy of radiation in "weak" or uncertain coincidence (Mev)
γ-γ	0.21	0.29, 0.47	0.14, 0.54,
			0.67, 0.93
	0.47	$\sim$0.21	0.07, 0.93,
	0.55		0.14, 0.4-0.9
	0.93		0.07, 0.47
			0.54, 0.9, 1.44
β-γ	$\sim$0.9	$\sim$0.2	γ rays below 0.21 and at least up to 0.93
	$\sim$1.6	$\sim$0.2	0.9
	$\geq$3.0	none	none
γ-β	0.45	$\leq$1.2	
	0.93		$\leq$1.6

This raises the possibility that the 0.93-Mev level is fed primarily by a transition from a state that has a lifetime in the order of 1 μ second, since the resolving time of the coincidence analyzer was 2 μ seconds.

4. Conclusions

The above information has been correlated into the level diagram shown in Figure 63. In the nuclide ${}_{39}Y^{92}_{53}$ the ground state configuration of the protons is $(2p\frac{1}{2})^1_{1/2}$, where the subscript indicates the resultant proton spin and the supercript indicates the number of nucleons in the shell. The neutron configuration is $(1d5/2)^3_{5/2}$. The resultant spin is 2-, that is, spin 2 and odd parity. This assignment is verified by the "unique" forbidden shape of the 3.60-Mev β transition. The ground state configuration of ${}_{40}Zr^{92}_{52}$ would then be $(2p\frac{1}{2})^2_o$ $(1d5/2)^2_o$ for the protons and neutrons respectively. The resultant spin is then 0 + . Now the ground state configuration of ${}_{41}Nb^{92}_{51}$ should be $(1g9/2)^1_{9/2}$ $(1d5/2)^1_{5/2}$. Here the proton and neutron spins will tend to add to give a possible spin of 5+, 6+, or 7+. A possible configuration for the first excited state of Nb^{92} would be $\left[(2p\frac{1}{2})^1_{1/2}\ (1g9/2)^2_0\right]$ $\left[(1d5/2)^1_{5/2}\right]$ yielding a spin of 2-, although a lower spin might also be produced depending upon how the (1g9/2) protons are coupled.

Assuming a ground state spin of 5+ or 6+ and a first excited state of 1- or 2-, the isomerism of Nb^{92} is understandable. However, since the first excited state of Zr^{92} almost necessarily has a spin of 2+, the electron capture from the ground state of Nb^{92} cannot proceed to this state. Two possibilities then arise. Either the first excited state in Zr^{92} is very low in energy (on the order of a few tens of kilovolts), or else it is quite close in energy to the 0.93-Mev level. The first possibility is unlikely from the systematics of the first excited states of even-even nuclei, and also because the 3.60-Mev β transition from Y^{92} clearly has the unique shape indicating a spin change of two units and a change in

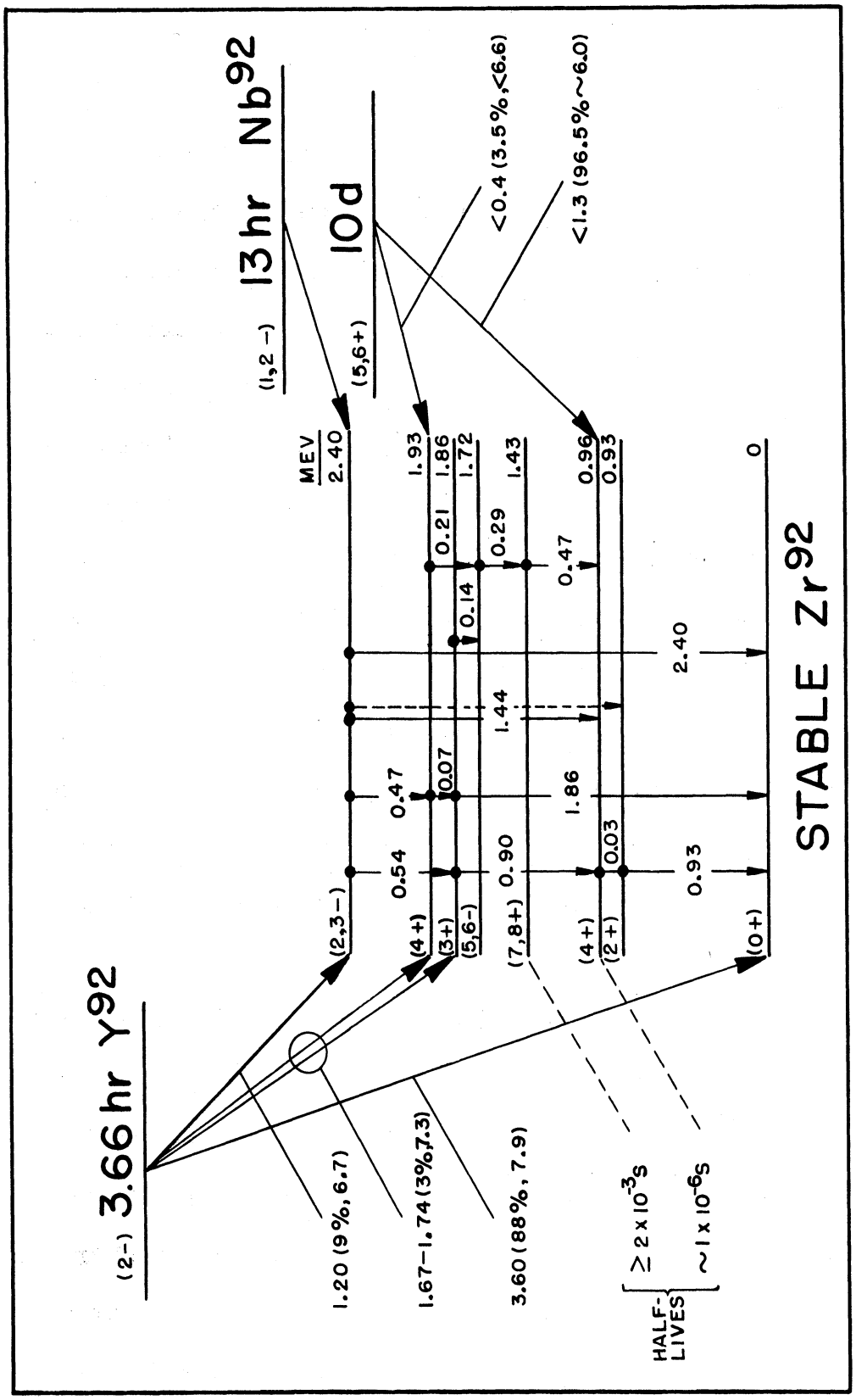

Figure 63. Decay scheme of Y^{92} - Zr^{92} - Nb^{92}

parity. Further, Griffith (48) has found the first excited state to be 0.926 Mev using inelastically scattered 4-Mev neutrons. Therefore, the second excited state in Zr^{92} was postulated to lie just above the 0.93-Mev level. Accurate γ ray spectra could not be obtained in the kilovolt region, but a reasonable order of magnitude for the difference between the first and second excited states might be $\sim$ 30 Kev or less. If the second excited Zr^{92} state has a spin of 4+, which could then be populated by electron capture from the ground state of Nb^{92}, the $\sim$ 30 kev transition might have a life time of the order of a few μ seconds as indicated by the coincidence data. While this transition should be converted to a large extent, the conversion electron peak would be too low in energy to be seen on the β-ray spectrometer that was used.

The 2.38-Mev level, being populated by transitions from both Y^{92} and the isomeric Nb^{92} level would then have a spin of 2- or 3-. This is substantiated by the presence of a 2.40-Mev γ ray. Since the 1.86-Mev level can decay directly to the ground state, a spin of 3+ is reasonable. A negative parity is unlikely because the Y^{92} β transitions to this level are in such low abundance. Therefore, the weaker electron capture from the Nb^{92} ground state cannot populate this level, but more likely reaches the 1.93-Mev level for which a spin of 4+ is likely. The 1.72-Mev level is probably not populated by either electron capture or negative β emission, indicating a spin of 5- or 6-. A high spin at this level is likely because it must lead to the 1.43-Mev level having a still higher spin. The 1.43-Mev level was postulated to be a meta-stable state leading to the converted 0.47-Mev γ transition. Therefore, a spin of 7+ or 8+ is required. The

isomeric level seems best placed at this point because of the coincidences found between the 0.21-Mev and the 0.29-Mev γ transitions. It was not possible to determine which level the 1.44-Mev γ ray populated. Either the first or second excited states or both are possible.

The decay scheme presented in Figure 63 appears to fit all of the coincidence data together with the data on β- and γ-ray intensities. A more concrete assignment of spins must await angular correlation and/or better conversion electron data.

C. The Isotope Ir^{196}

It had been noted in 1953 that an isotope of iridium, Ir^{196}, was listed in isotope tables and compilations of nuclear data (60,101) as having a half-life of $\sim$ 9 days and was supposed to decay by the emission of an $\sim$ 0.08-Mev β ray. A half-life of that order was surprising for Ir^{196} since the isotope Ir^{194} has a half-life of only 19 hours. Furthermore, the half-life and β-ray energy indicated that the transition was allowed, an unlikely occurrence for this section of the isotopic table. In January, 1954 Butement and Poe (19), who had contributed the original information on this isotope, published further information substantiating their previous findings and listed γ rays at energies of 0.58, 0.76, and $\sim$ 1.0 Mev. A search of the literature was made in 1954 and has been extended periodically through March, 1957. No further work on this isotope has been found to date. A chart of the isotopes of iridium, platinum, and gold is given in Figure 64

1. Chemical Separation

The radioactive iridium was to be produced by the (d,α) reaction from deuteron bombardment of metallic platinum foils 1.05 mils in thickness. Therefore, a chemical separation was needed to obtain the iridium free from

Au^{190}	Au^{191} 3 h K, γ	Au^{192} 4.8d β^+,K, γ	Au^{193} 4 s IT | 17 h K, γ	Au^{194} 39 h β^+,K, γ	Au^{195} 30s IT | 180d K, γ	Au^{196} 14h IT | 5.6 d β^-,K, γ	Au^{197} 100	Au^{198} 2.7d β^-, γ	Au^{199} 3.2 d β^-, γ	Au^{200} 48 m β^-, γ
Pt^{189} 10 d K, γ	Pt^{190} 0.012	Pt^{191} 3 d K, γ	Pt^{192} 0.78	Pt^{193} 3.4d IT | long	Pt^{194} 32.8	Pt^{195} 33.7	Pt^{196} 25.4	Pt^{197} 1.4h IT | 19 h β^-, γ	Pt^{198} 7.2	Pt^{199} 30m β^-, γ
Ir^{188} 40 h β^+,K, γ	Ir^{189} ~10d K, γ	Ir^{190} 3 h β^+,K, γ | ~10d K, γ	Ir^{191} 38.5	Ir^{192} 1.4m IT β^- | 74d β^-,K, γ	Ir^{193} 61.5	Ir^{194} 19 h β^-, γ	Ir^{195} 2.3h β^-, γ	Ir^{196} short	Ir^{197} 7 m β^-, γ	Ir^{198} 50s β^-, γ

Figure 64. Chart of the isotopes of iridium, platinum and gold

contamination by platinum and gold activities produced by (d, p) and (d, n) reactions on the platinum target, and also from activities produced by reactions on the impurity elements in the target. Three bombardments were obtained on "commercial grade" platinum foil, 99.5% pure, obtained from Baker and Co., Inc., Newark, New Jersey. Table XXI shows the spectrographic analysis for a typical foil. No numerical estimates of the impurities were available from Baker and Co.

TABLE XXI. SPECTROGRAPHIC ANALYSIS OF TYPICAL PLATINUM FOIL

Element	Amount	Code
Pt	M	M - major
Ir	VST +	
Os	VST	S - strong
Pd	ST	
Rh	ST	VST - very strong trace
Ru	T	
Au	T	ST - strong trace
Ag	T	
Cu	T	T - trace
Fe	ST -	
Ni	T	O - not detected
Pb	T	
Sn	T	
Zn	T	
Si	T	
Mg	T	
Ca	ST	
Mn	T	
Al	ST	

A final bombardment was obtained on a sample of platinum enriched in the isotope Pt^{198}.

The chemical separation that was finally developed is based to a certain extent on the information given in Noyes and Bray (104), and also in Meinke's compilation (93,94). Table XXII shows the separation.

TABLE XXII. IRIDIUM SEPARATION CHEMISTRY

Element separated: Iridium	Procedure by: Gardner
Target Material: Platinum metal	Time for sep'n: ~8 hours
Type of bbdt: 20-Mev deuterons	Equipment required: No special equipment

Yield: ~70%

Degree of purification: $\sim 10^6$

Advantages: Separates Ir from Pt, Au, Cu, Ni, and Zn with high decontamination factor.

Procedure:

(1) The Pt target was dissolved in boiling aqua regia and 3 mg Ir carrier and 10 mg each of the following carriers added; Cu, Ni, Zn and Au.

(2) The solution was evaporated to incipient dryness, diluted to 10 ml with water and 10 drops conc. HCl added.

(3) Au was extracted 6-8 times with ethyl acetate. (See remark 1)

(4) The aqueous phase (yellow-brown) was treated with 1-2 drops H_2NNH_2 to destroy NO_3^-. (Solution turns pale).)See remark 2)

(5) Pt was reduced with $SnCl_2$ (solution turns deep red) and extracted 6-8 times with ethyl acetate. (See remark 3)

(6) The aqueous phase was evaporated to dryness with 2-3 ml aqua regia and 5 mg Pt carrier added. The NO_3^- was removed by addition of 20 drops conc. HCl and evaporation to dryness.

(7) The residue was dissolved in 2 ml H_2O and 4 drops 6 N HCl.

TABLE XXII. IRIDIUM SEPARATION CHEMISTRY (Cont'd)

(8) The solution was saturated with solid NH_4Cl, warmed to dissolve any excess and cooled in ice for 0.5 hr. The red precipitate of Pt and Ir was washed several times with saturated NH_4Cl solution.

(9) The precipitate was dissolved in hot water, and NH_4^+, removed by evaporation to dryness with 2-3 ml aqua regia.

(10) The residue was dissolved in 2-3 ml H_2O plus 2-5 drops conc. HCl and evaporated to dryness again.

(11) The residue was dissolved in 6-8 ml H_2O and made basic to litmus with a few drops of saturated Na_2CO_3 solution (solution turns from brown to yellow).

(12) The solution was heated to boiling, 4-6 ml NaOBr solution (0.5 ml 1 $\underline{M}$ Na_2CO_3 1 ml saturated Br_2 solution) added and heating continued until the solution turned greenish-blue. (See remark 4)

(13) 1-2 drops 6 $\underline{N}$ HCl was added to the still warm solution and the solution digested until the IrO_2 coagulated.

(14) The precipitate was washed several times with H_2O, dissolved in conc. HBr and evaporated to dryness. The residue was dissolved in H_2O and mounted for counting.

Remarks:

(1) For both the Au and Pt extractions, $\frac{\text{aqueous phase}}{\text{organic phase}}$ = 2-4

(2) Metallic Pt may precipitate from hot solution.

(3) If a red precipitate forms, conc. HCl is added until it dissolves. In the presence of a large amount of Pt a series of partial reduction and extractions to remove all the Pt is preferred.

(4) The addition of a drop of 1 $\underline{M}$ Na_2CO_3 solution and/or saturated Br_2 solution may expedite the formation of the blue-green color.

It was later found in the bombardment work that it was necessary to perform the chemical separation only once. If the final iridium activity was reprocessed using the same separation, no noticeable improvement in the purity could be detected.

In the final enriched isotopes bombardment it was necessary to return the target material in a purified form. This was done as follows: The ethyl acetate containing the platinum was evaporated to dryness, and then strongly heated to drive off organic materials. In the process the Pt(II) was reduced to metallic platinum. The residue was washed repeatedly with hot concentrated and dilute HCl. The metallic platinum was dissolved in aqua regia, evaporated to dryness,and again reduced to metallic platinum by heating. After repeated washings, the metallic platinum was dissolved in aqua regia, and $PtCl_4$ formed by evaporation to dryness with HCl. The $PtCl_4$ was dissolved in water slightly acid with HCl. Next, metallic platinum was precipitated from solution by the addition of metallic zinc. The zinc was removed by dissolving in dilute HCl. The remaining platinum was washed in HCl and water, and finally dried.

2. Experimental Procedure

The three bombardments on natural platinum foil were obtained using the Argonne National Laboratory cyclotron. The cyclotron at the University of Michigan could not be used since a beam energy higher than 7.8-Mev is required to obtain useable (d, α) reaction yields at atomic numbers in the rare earth region and above. The Argonne cyclotron supplies deuterons at an energy of 20.4 Mev. Using stacks of 2 and 3 platinum foils separated by copper absorbers of appropriate thicknesses (calculated using the curves of Aron et. al., reference 5), a total of 7 platinum targets were bombarded at various energies ranging from 9.6 to 20.4 Mev.

Figure 65 shows the foil arrangements for each of the three bombardments. All platinum foils are 1.05 mils thick, while the thickness of the copper absorbers are indicated. The energy of the deuteron beam striking each platinum foil is also shown. The range and rate of energy loss of deuterons in platinum was obtained from the information for deuterons in lead, as given in Reference 5. To convert the range of deuterons in lead to the range in platinum the following formula was used.

$$R_{Pt} = R_{Pb} \frac{Z_{Pb}}{A_{Pb}} \cdot \frac{A_{Pt}}{Z_{Pt}} \qquad (113)$$

Here R is the range in mg/cm^2, Z is the atomic number, and A is the atomic weight associated with the elements represented by the subscripts. In the first bombardment, the energy of the deuteron beam striking the second platinum foil is unknown since both the first platinum foil and the 15.6 mil copper absorber showed signs of being burned.

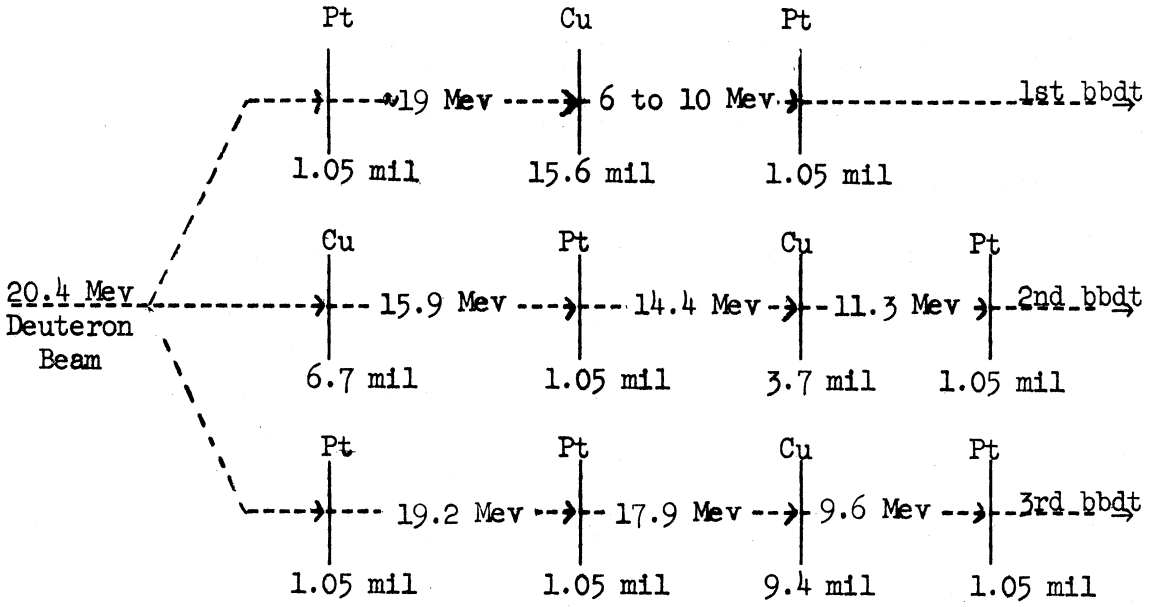

Figure 65. Foil arrangement for the three natural platinum bombardments

After the chemical separation, samples were mounted on 1/4 mil Teflon film. Decay curves were taken on 4π β-ray counters, and on γ-ray counters. Since this work was performed before the hollow scintillator β-ray spectrometer was built, data relating to β-ray spectra were obtained in two ways. The first involved the use of the 180° magnetic spectrometer described by Meinke, et. al. (97), and the second was the aluminum absorption curve method. Gamma-ray data were obtained primarily through the use of oscilloscope photographs, although Speedomax sweeps were also taken. Coincidence data were obtained manually, since the photographic method had not as yet been developed when this work was being done.

3. Results Obtained From Natural Platinum Bombardments

The decay curves of eight separate samples obtained at various bombarding energies show the presence of only three components with half-lives of 19 hours, ~8 days and 75 days. The 19-hour activity is due to Ir^{194}, while the 75-day activity comes from Ir^{192}. The latter two isotope assignments were substantiated by β-and γ -ray data presented later. A half-life of 8.3 ± 0.5 days was obtained for the intermediate lived activity by averaging the values obtained from eight decay curves. This may be compared with the value of ~ 9 days found by Butement and Poe.

Most of the above decay curves were begun ~16 hours after bombardment, and were followed for ~3 months. While activities with half-lives longer than 75 days might have been present, any appreciable amount of a half-life longer than about 5 hours and less than 75 days would have been detected. The presence of only three half-lives indicates that the chemical separation was adequate, and that the 8.3-day activity was indeed an isotope of iridium as claimed by Butement. This is further confirmed by the fact that repeating the chemical separation did not change the ratio of the three activities. Finally, the relative cross-section values for the 8.3-day activity obtained on four different samples at bombardment energies of 19.2 and 20.4 Mev were all equal to within experimental error.

Rough cross section values for the (d,γ) reaction on Pt^{194} and Pt^{196} to produce Ir^{192} (75 day) and Ir^{196} (19 hour) were obtained using Equation 114.

$$\sigma = 1.117 \times 10^{-13} \times \frac{(T1/2\ hr)\ (Co/m)\ (Mwt)}{(abund.)\ (Q)\ (Chem\ Yld.)\ (Aliquote)} \qquad (114)$$

where σ = The cross-section in barns ($10^{-24} cm^2$)

T1/2 hr = The half-life in hlurs

Co/m = The activity in counts per minute at "zero" time.

Mwt = Mass of target nuclei

Abund. = Fractional abundance of target nuclei

Q = Deuteron beam current in μ amp. hours

Assuming for the moment that the 8.3-day activity does belong to Ir^{196} (it will be shown later that this is not true), the calculated cross-sections appear in Table XXIII. The errors are estimated standard deviations. The errors in beam energy were estimated from the variations in foil thicknesses and from the initial beam distributions. The chemical yield were obtained by weighing as $IrBr_4$ an aliquote of the final iridium fraction. No corrections were made for the self absorption of the β rays in their sources. Within the stated errors, self-absorption should only affect the "Ir^{196}" cross-sections, and it will be shown later that these values must be discarded anyway since they do not actually refer to Ir^{196}.

TABLE XXIII. CROSS-SECTIONS FOR THE (d, α) REACTION ON PLATINUM

Target Nuclei	Energy of Deuterons in Mev				
	9.6 ± 1.3	11.3 ± 1.6	15.9 ± 1.5	19.2 ± 1.6	20.4 ± 0.8
Pt^{194}	$1.2\pm0.4\times10^{-5}$	$1.1\pm0.5\times10^{-4}$	$1.7\pm0.8\times10^{-4}$	$3.8\pm1.2\times10^{-4}$	$3.4\pm1.0\times10^{-4}$ $2.1\pm0.9\times10^{-4}$ $2.0\pm0.6\times10^{-4}$
Pt^{196}	$1.4\pm0.6\times10^{-4}$	$3.3\pm1.6\times10^{-4}$		$4.4\pm1.5\times10^{-4}$	$7.2\pm3.8\times10^{-4}$ $2.1\pm0.9\times10^{-4}$ $1.9\pm0.7\times10^{-4}$
"Pt^{198}"	$1.0\pm0.8\times10^{-4}$	$1.8\pm0.8\times10^{-4}$	$5.4\pm2.6\times10^{-4}$	$3.5\pm1.9\times10^{-4}$	$4.3\pm2.2\times10^{-4}$ $4.5\pm2.4\times10^{-4}$ $3.5\pm1.2\times10^{-4}$

The following information was obtained using the magnetic β-ray spectrometer:

TABLE XXIV. BETA-RAY SPECTROMETER DATA FROM NATURAL PLATINUM BOMBARDMENTS

Days After Bombardment	Beta-Ray Information
3	No β^+ Maximum β^- energy $\lesssim$ 2 Mev. Lower β^- component energy $\approx$ 0.7 Mev.
8	Very little 2-Mev β^- component left. Maximum β^- energy of principle component $\approx$ 0.7 Mev. Indication of low energy β^- component $\approx$ 0.07 - 0.1 Mev.
10-15	$\sim$ 0.08 Mev β^- component decays faster than the 0.7-Mev component

Figure 66 shows the β-ray spectrum obtained on a typical sample 8 days after bombardment. The above information is in accord with the literature values of E_{max} for Ir^{192} and Ir^{194} which emit β rays with maximum energies of 0.72 and 2.2 Mev respectively, and with Butement's observation of an ~0.08-Mev β ray ascribed to Ir^{196}. Aluminum absorption curve data confirmed the above spectrometer data. By following the decay of a portion of the β-ray spectrum at about 0.05 Mev it was found that the lowest energy group was decaying with a half-life of ~10 ± 2 days. The decay was not followed long enough to define the half-life more exactly.

Gamma-ray decay curves were obtained which showed the presence of the 8.3-day activity. Oscilloscope photographs and Speedomax sweeps showed the presence of the following γ rays which could not be ascribed to either Ir^{192} or Ir^{194}.

TABLE XXV. GAMMA RAYS FROM 8.3-DAY IRIDIUM ACTIVITY

Mev	Mev
0.064	0.378
0.097	0.407
0.1-0.29	0.448
0.341	0.548

The energy range from 0.1 - 0.29 Mev was obscured by the Compton smear from higher energy γ rays, and no accurate data could be obtained at these energies. The relative intensities of the above γ rays could not be accurately estimated due to the intense background of similar energy γ rays arising from Ir^{192}.

Most of the coincidence data that were obtained proved inconclusive again due to the interference from Ir^{192}. All that can be said is that the 0.34-Mev γ ray is in coincidence with γ rays in the range 0.40-0.45 Mev,

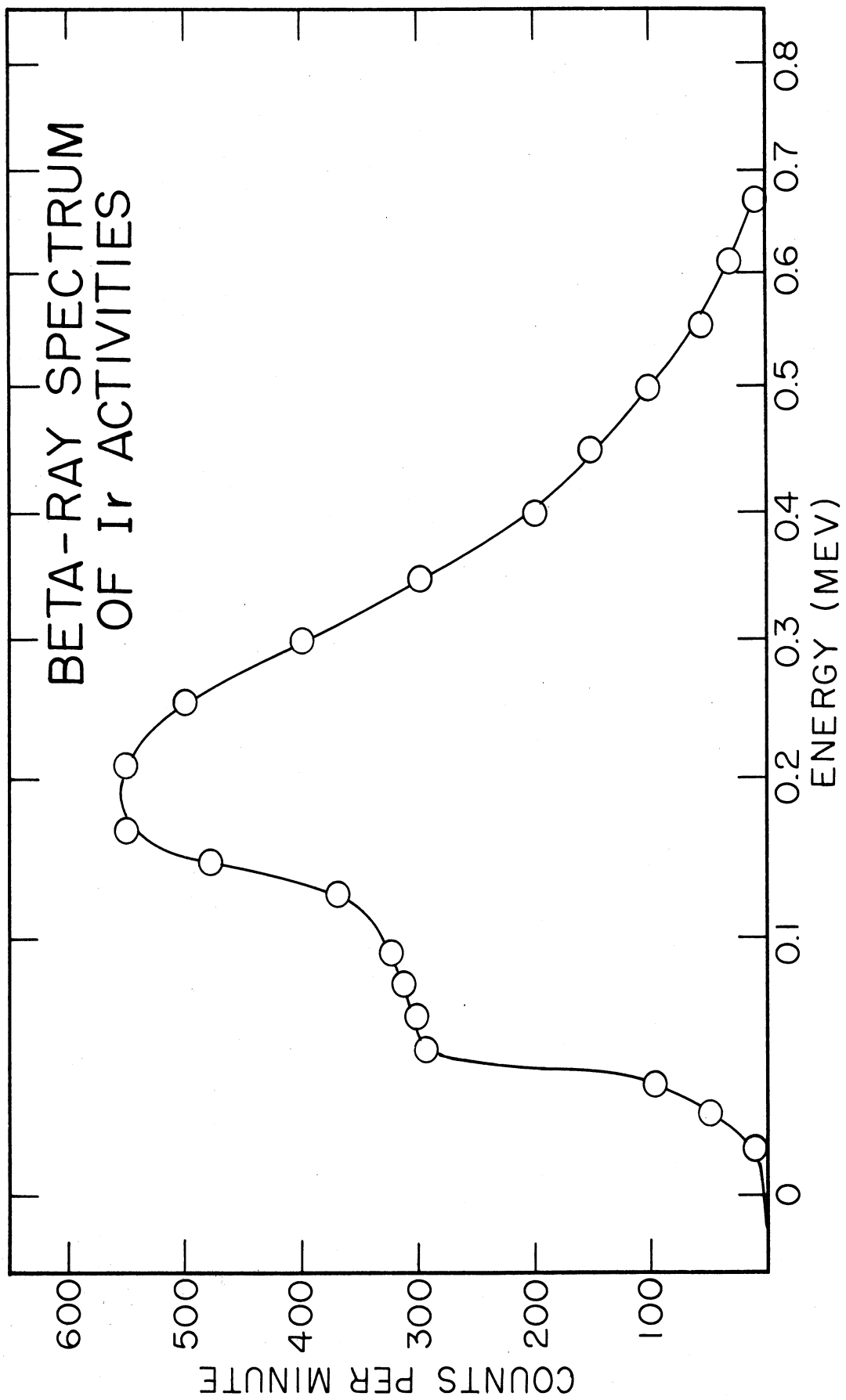

Figure 66. Beta-ray spectrum of iridium activities eight days after bombardment

and that the 0.064-Mev transition (which corresponds in energy to a Pt x-ray) is in coincidence with itself.

To summarize, the above results correlate well with those obtained by Butement and Poe who ascribed the 8.3-day activity to Ir^{196}. Even the rough cross-sections seemed to indicate that their assignment was correct. However, before a decay scheme could be formulated, better coincidence information was needed. This could not be obtained in the presence of a significant amount of Ir^{192}. Therefore, it was decided to obtain a sample of platinum enriched in the isotope Pt^{198}, the parent of Ir^{196} in the (d,α) reaction.

4. Results Obtained From the Enriched Platinum Bombardment

Table XXVI contains the analysis of the enriched platinum target. With this target the ratio of Pt^{198}/Pt^{194} was increased by a factor of 100 over the natural ratio. Fifty mgs. of the powdered platinum metal were bombarded with 23.5-Mev deuterons at the University of California cyclotron. Six days after bombardment the sample was worked up and a decay curve started.

TABLE XXVI. ANALYSIS OF ENRICHED PLATINUM ISOTOPES

	Mass Analysis		
Isotope	Atomic %	Precision	Normal Atomic %
190	<0.01		0.012
192	0.042	0.013	0.78
194	3.57	0.10	32.8
195	8.97	0.28	33.7
196	26.47	0.78	25.4
198	60.95	0.72	7.2

TABLE XXVI. ANALYSIS OF ENRICHED PLATINUM ISOTOPES (Cont'd)

Spectrographic Analysis			
Element	%	Element	%
Al	< 0.05	Mo	< 0.02
Ba	< 0.02	Na	< 0.02
Be	< 0.001	Nb	< 0.1
Ca	< 0.2	Ni	< 0.05
Co	< 0.05	Pb	< 0.1
Cr	< 0.05	Pd	< 0.04
Cu	< 0.05	Rh	< 0.04
Fe	< 0.02	Ru	< 0.1
Ir	< 0.1	Si	< 0.05
K	< 0.01	Ti	< 0.02
Li	< 0.01	V	< 0.02
Mg	< 0.02	Zr	< 0.1
Mn	< 0.02		

Only a very small amount of activity was found in the iridium fraction after bombardment. Gamma-ray data showed that the primary activity was still Ir^{192}, with the addition of a small amount of γ radiation in the 0.7-0.9 Mev range. A large amount of γ-γ coincidence information was obtained, but all of it could be explained by the presence of Ir^{192}. An excellent discussion of the decay of Ir^{192} and Ir^{194} is given by Johns and Nablo in Reference 68.

The decay curve for this bombardment was followed for 50 days. When resolved it showed only two activities to be present, the 75-day Ir^{192} and a small amount of a 3-4 day activity which probably was a mixture of Au^{196} and Au^{199}. No indication of an 8.3-day activity was found at all. The atom yield of the 3-4 day activity was less than the atom yield for Ir^{192} by a factor of ~ 6. In a normal platinum bombardment where the Ir^{192}

activity would be increased by a factor of 10, the small amount of the 3-4 day activity would have escaped attention.

5. Conclusions

While the natural platinum bombardments strongly supported Butement and Poe in their assignment of the 8.3-day activity to Ir^{196}, the enriched isotope bombardment completely disqualified this assignment. The results of this work, however, indicate that the 8.3-day activity does belong to some isotope of iridium.

The following reinterpretation of the data was made. The presence of a relatively large amount of platinum x-rays shows that the 8.3-day activity decays primarily by electron capture, with little or no positron emission as indicated by the β-ray spectrometer data. This assumption allows the assignment of the ~0.08-Mev β particles to fluorescent electrons, or conversion electrons of a low energy γ ray. This last is a logical assignment that removes the difficulty of demanding that the β decay be allowed, as would be necessary if E_{max} = 0.08 Mev and the half-life were ~8 days.

Decay by electron capture requires that the iridium isotope be on the neutron deficient side of stability. Here Ir^{189} and Ir^{190} appear as possibilities, since each has an isomer with a half-life of the right order of magnitude. Neither of these isotopes has been well characterized, but recently Aten and co-workers (6) have presented some information on Ir^{190}, and Smith and Hollander (134) have reported on Ir^{189}. Table XXVII lists their findings.

TABIE XXVII. GAMMA-RAY ENERGIES IN MEV FROM Ir^{189} AND Ir^{190}

Ir^{189}	Ir^{190}
x-ray	x-ray
0.135	0.186
0.245	0.360
	0.400
	0.540
	0.580
	0.800 weak
	1.33 weak

The γ rays found in this work permit the assumption that the observed 8.3-day activity is the result of the presence of both Ir^{189} an Ir^{190}. Ir^{189} could not be obtained by the (d,α) reaction on platinum, and Ir^{190} would have to come from Pt^{192} with a natural isotopic abundance of 0.78%. Furthermore Ir^{190} has a 3-hour isomer which would further reduce the amount of 8.3-day activity. In the enriched platinum target, Pt^{192} was reduced to 0.042%, almost a factor of 100 less than Pt^{194} which produces the 75-day Ir^{192} activity. It is quite understandable that in the enriched isotope bombardment no 8.3-day activity was found.

To account for the 8.3-day activity found in the natural platinum bombardments, it is suggested that a small amount of osmium impurity was in the platinum targets. This would produce iridium activities by the favorable (d,n) reaction. Hence both Ir^{189} and Ir^{190} could be produced from Os^{188} and Os^{189} with natural abundances of 13.3 and 16.1% respectively.

Os^{190} (26.4%) and Os^{192} (41.0%) both yield stable iridium isotopes. Os^{186}(1.6%) would produce a small amount of the 12-hour Ir^{187} which would not have been resolved from the more intense 19-hour Ir^{194}. Os^{187} (1.6%) would yield some 41-hour Ir^{188}, which would be masked to a certain extent by the Ir^{189} and the Ir^{190} activities. A re-examination of the decay curves did indicate that a small amount of the 41-hour Ir^{188} might have been present. Since the (d, n) reaction is more favorable than the (d, α) reaction by a factor of 10^2-10^3, the amount of osmium impurity needed to account for the results would only be 0.01 to 0.1%. The spectrographic analysis of the natural platinum indicates that this assumption is not unreasonable. Furthermore, Chu (25) has produced Ir^{189} and Ir^{190} by deuteron bombardment of osmium.

Concerning the true Ir^{196} activity, the present work suggests that an upper limit for the half-life would be about 5 hours. Actually, a much shorter half-life would be anticipated, perhaps in the range of minutes. That Ir^{196} does not decay with a half-life of 8.3 days eliminates a situation that would have been difficult to explain using present theories of nuclear structure.

D. The Isotope Sc^{47}

In 1953 several reports (24,27,87) appeared concerning the decay of the 3.4-day isotope Sc^{47}. In each report two β-ray transitions and one γ ray transition were found. However, the energies of these transitions varied from report to report. In Table XXVIII these values are listed. It therefore was of interest to make a careful study of this isotope, perhaps with the aid of enriched isotopes, to better determine its decay characteristics. While this work was in a preliminary stage, an excellent article

TABLE XXVIII. RADIATIONS EMITTED DURING THE DECAY OF Sc^{47}

Reference	β-ray Energy(Mev)	β-ray Abund.(%)	γ-ray Energy(Mev)	γ-ray Abund(%)
24	0.435 0.622	~66 ~34	0.185	100
27	0.64		0.160	
87	0.28 0.49	28 72	~0.22	
82	0.450 0.610	74 26	0.160	100

by Lidofsky and Fisher (82) appeared describing the decay of Sc^{47}. Since it did not appear likely that their results could be improved upon with the equipment that was available in this laboratory, the project was dropped. The chemical separation that was developed in the present work, and the results of four bombardments on TiO_2 targets are given below.

1. Chemical Separation

The radioactive scandium was produced by the bombardment of TiO_2 targets using the (d,α) reaction. The chemical separation must therefore isolate scandium in a carrier-free form from titanium and vanadium activities also produced during the bombardment. The first problem to be encountered was to find a way to dissolve the TiO_2. Attempts to dissolve TiO_2 in concentrated H_2SO_4 plus H_2O_2 were not successful, since several days were usually required to obtain a solution. It was decided then to try a fusion process.

Using $K_2S_2O_7$, obtained by heating $K_2S_2O_8$ until SO_3 fumes ceased to evolve, the fusion process required only 10-15 minutes. After the flux cooled below $\sim 200^{\circ}C$, H_2SO_4 was added. The flux was then reheated until all solids dissolved in the H_2SO_4. Upon cooling, the flux would remain liquid which facilitated its removal from the crucible.

The first attempts at a chemical separation were along the lines that Hall (51) was following in the development of his scandium separation chemistry. In this case the scandium activity was to be separated in a carrier-free form by filtering out the scandium radiocolloid on filter paper from a solution of pH 8.5. The titanium would be kept in solution by forming the complex with H_2O_2. Very little success was found with this method. The titanium was difficult to keep in solution and was constantly appearing as a dark orange-brown compound on the filter paper. Furthermore, the scandium colloid had a tendency to stick to the walls of the glassware, and also was difficult to remove from the filter paper. It seemed advisable to try another approach.

Ion-exchange techniques were to be the basis of the new separation, since Ti (IV) and V (V) will adsorb on Dowex-2 resin in 11-12 N HCl while scandium will not (78). The difficulty at this stage is that V (IV) does not adsorb on the column, and V (V) adsorbed on the resin will tend to reduce to V (IV) in concentrated HCl solutions. After trying several approaches it was found that a small amount of $KClO_3$ in the concentrated HCl solutions will keep V(V) from reducing. In fact, the V (V) adsorbs so well that both scandium and titanium may be removed from the column with 11 N HCl and the V removed later with 6 N. HCl, providing a clean separation for vanadium.

The details of the scandium chemical separation are given in Table XXIX. It will be noted that in steps 6-10 a rough separation of scandium from titanium and vanadium is made prior to the use of the ion-exchange procedure. This was done primarily to insure that no titanium contamination would be found in the scandium fraction. The final scandium fraction may contain a small amount of NaCl. If necessary the scandium may be separated from the salt by slow elution on an exchange column using concentrated HCl. The salt will come off first.

TABLE XXIX. SCANDIUM SEPARATION CHEMISTRY

Element separated: Scandium

Target Material: Titanium Oxide

Type of bbdt: 7.8 Mev deuterons

Procedure by: Gardner

Time for sep'n: ~ 2 hours

Equipment required: Ion exchange column of AG 2-X8, 200-400 mesh resin obtained from Bio-Rad Laboratories. Resin bed was 8 mm x 140 mm.

Yield: >60%

Degree of purification: $>10^6$ from V; $>10^5$ from Ti

Advantages: Carrier-free separation with high decontamination

Procedure:

(1) Prepare column by washing several times with conc. HCl, then with conc. HCl + $KClO_3$ (See remark 1).

(2) Place TiO_2 in a small porcelain crucible and add roughly 1-2 gms $K_2S_2O_7$ per 100 mgs of TiO_2. Cover and bring to dull read heat. Continue heating until TiO_2 dissolves in flux (10-15 min) (See remark 2).

(3) Cool below 200°C. and cautiously add 1-2 ml of conc. H_2SO_4.

TABLE XXIX. SCANDIUM SEPARATION CHEMISTRY (Cont'd)

(4) Heat until all solids dissolve in the H_2SO_4. Upon cooling, contents of crucible should remain liquid. If solidification occurs, add more conc. H_2SO_4 and repeat heating.

(5) Pour liquid into a beaker using a small amount of H_2O as a wash.

(6) Add solid NaOH until solution is basic to litmus and TiO_2 precipitates out as a white hydrous oxide. Stir thoroughly for a few minutes to insure that all Sc will be carried down on the TiO_2. (See remark 3)

(7) Centrifuge out the TiO_2 and salt. (Most of the V activity remains in the supernate).

(8) Wash the TiO_2 and salt several times with 1 N NaOH until all of the salt has dissolved. (See remark 4).

(9) Dissolve TiO_2 in a few drops of conc. HCl and reprecipitate with saturated Na_2CO_3 solution. (Much of the Sc goes into the supernate in this step.)

(10) Remove supernate and repeat step 9 twice more, saving the supernatents at each step and combining them in the end. (See remark 5).

(11) Total supernate is acidified with conc. HCl and evaporated down to less than 20 ml. Solution is then cooled in an ice bath and saturated with HCl gas. (Saturation is assumed complete when no more salt comes out of solution.) Centrifuge and discard salt.

(12) Continue evaporation almost to dryness. Extract residue with 5 ml of ~11 M HCl three times. Evaporate HCl solution to 5-10 ml, add ~ 5 mgs of $KClO_3$, cool in ice, and saturate with HCl gas. Centrifuge to remove any salt and then place on column prepared in step 1.

(13) Force solution through column at rate of ~1-2 drops/sec., stopping just before liquid reaches top of resin. (Do not allow top of resin to ever become dry) Some Sc will appear after first 5 ml. Elute with 11 M HCl + $KClO_3$ at rate of 1-2 drops/sec. (See remark 1)

(14) Most of Sc comes off in first 10-15 mls of 11 M HCl. Ti begins to come off after 25-30 mls of 11 M HCl. (See remark 6)

(15) A very small amount of salt may follow the Sc. This may be removed by evaporating eluent containing the Sc down to 5-10 ml, saturating it with HCl gas, and then running it through the column washed with just conc. HCl - at a much slower rate. The salt comes off first.

TABLE XXIX. SCANDIUM SEPARATION CHEMISTRY (Cont'd)

Remarks:

(1) All HCl + $KClO_3$ solutions contain just enough $KClO_3$ to impart a faint yellow color to the solution. Usually this was $\frac{0.5 \text{ mg } KClO_3}{\text{ml}}$.

(2) $K_2S_2O_7$ was made by heating $K_2S_2O_8$ until SO_3 fumes ceased to evolve.

(3) Some water may be added along with the solid NaOH, but the volume of solution should be kept small, usually 20 ml or less

(4) All of the washings in step 8 will usually contain much less than 10% of the total Sc activity.

(5) Of the total Sc activity in the TiO_2 precipitate over 60% is removed in the first reprecipitation and over 20% is removed in the second.

(6) The eluent (including original solution) is usually taken in separate units of 3-5 ml. Aliquots of these are counted to give the Sc and Ti peaks, then the center 60-70% of Sc peak is taken for analysis.

(7) General Reference for this tyee procedure: Hicks, H. G., et al., "The Qualitative Anionic Behavior of a Number of Metals with an Ion Exchange Resin, 'Dowex 2' ", Livermore Research Laboratory Report, LRL-65, Dec. 1953.

2. Bombardment Results

Four bombardments in all were obtained using natural TiO_2 powder targets. The TiO_2 was listed as grade C.P. by J. T. Baker Chemical Company, Phillipsburg, New Jersey. The bombardments were obtained to produce radioactive sources of titanium, vanadium, and scandium to be used in the development of the chemical procedure. In the fourth bombardment the target was inadvertantly destroyed in the cyclotron.

Decay curves taken on the scandium fraction from the third bombardment were followed for three months. These showed the presence of the 85-day Sc^{46} and also a shorter-lived component of ~3 days. This latter activity was due to a combination of the following activities: Sc^{44m} (2.4 day), Sc^{47} (3.43 day), and Sc^{48} (44 hour). No trace of any activities that could be assigned to vanadium or titanium was found. Oscilliscope photographs showed the presence of five γ rays. These are listed in Table XXX with their identification.

TABLE XXX. GAMMA RAYS FROM SCANDIUM FRACTION

γ-ray energy (Mev)	Isotope	Literature value of γ-ray energy Mev.
0.16	Sc^{44m}	0.16
	Sc^{47}	0.16
0.28	Sc^{44m}	0.27
0.52	Sc^{44}	annihilation radiation 0.511
0.9-0.97	Sc^{48}	0.98
	Sc^{46}	0.89
1.1-1.3	Sc^{44}	1.16
	Sc^{46}	1.12
	Sc^{48}	0.99, 1.04, 1.33

No β-ray spectral data were obtained from any bombardments.

In summary, it may be said that a chemical separation was developed that will separate scandium and vanadium in carrier-free form with good decontamination from a titanium target. A γ-ray with an energy of 0.16 Mev was found that could be assigned to the isotope Sc^{47}. The γ-ray results are in agreement with the latest evidence on the isotope Sc^{47}.

APPENDIX A

Fabrication of Hollow Plastic Scintillator

The first attempts at constructing a hollow β-ray detector involved drilling and grinding out a cone-like cavity in the center of a solid plastic scintillator. The grinding was done using dentist gem stones. After the depression had been roughed-out, the walls of the phosphor were polished with crocus cloth and rouge on felt. The phosphor was then wrapped with 1.5-mil aluminum foil.

Two detectors were made using the above process. One of these was in the form of a right circular cylinder, 3/4" in diameter and 1/2" high, while the other detector was a truncated cone 1" in diameter and 3/4" high. Both of these detectors proved unsatisfactory, primarily due to cracks, which formed from strains set up in the plastic during the hollowing-out process. These cracks reduced the resolving power below that of a solid detector. Besides, it proved almost impossible to produce a symmetrical, conical cavity with a reasonably smooth bottom within the plastic and yet retain a small entrance hole in the top. Polishing the interior surfaces was also difficult. All attempts at solvent polishing, using kerosene, acetone, alcohol, or benzene, failed. The usual result produced by these solvents is an opaque, soft, plasticized layer formed on the surface.

The following procedure was devised to produce satisfactory hollow detectors: Each detector was constructed in two parts which consist of a flat, solid, right circular cylinder used as the base, and a top piece consisting of a hollowed-out cylinder or truncated cone.

The cross-section views for the three detectors were given in **Figure 13.** As previously mentioned, the three detectors are to be used with maximum β energies of $\leq$1.5 Mev, $\leq$2.2 Mev, and $\leq$3.6 Mev.

The pieces of phosphor were machined on a lathe from a solid piece of stock rod. The plastic melts at 110°C., so the machining should be done slowly while a stream of air is played over the piece. Every effort must be made not to introduce strains into the plastic. A sharp, finely pointed tool should be used as the plastic has a tendency to chip. It is not necessary to anneal the pieces if care is taken when machining. No cracks have appeared in the pieces machined in the air stream.

Since each detector is constructed in two pieces, the polishing of the pieces is greatly facilitated. Particular care should be given the polishing of the top and bottom surfaces of the base, and the inside and bottom surfaces of the hollow piece. The point in polishing the interior surfaces of the detector is that light generated in the phosphor will escape from a rough surface more easily than from a polished surface. The polishing is accomplished using increasingly fine grades of sandpaper, ending with crocus cloth. The final finish is produced using Bon Ami on felt or soft paper tissue. If the initial polishing is done on a lathe, care should be taken not to burn or melt the plastic. Wet sandpaper may be used if desired when the polishing is done by hand.

The detectors are assembled and mounted in the following way:

1. Wipe each piece to remove any dirt or grease.

2. Apply a small amount of Dow-Corning 200 Silicone fluid to the bottom surface of the hollow section. Wipe off excess fluid.

3. Place the hollow section onto the base. Press together until excess fluid is squeezed from between the pieces. Make sure that there are no air bubbles in the junction. Just enough fluid should be used so that only a very small amount is squeezed out. Wipe off excess fluid from outside of detector.

4. Remove excess fluid from inside of piece with tissue paper wrapped around a thin dowel rod. Be careful not to scratch plastic. The fluid must be carefully removed since the β particles will loose energy passing through it that will not appear as light.

5. Cut a circular piece of Reynold's Wrap slightly larger than the top surface. Cut another piece of aluminum foil to approximate the shape of the outside surface of the phosphor. With the shiney side of the foil toward the phosphor, wrap the detector with the foil leaving the bottom face uncovered.

6. Cut away the portion of foil covering the entrance hole in the detector.

7. Tape the foil-enclosed phosphor to the aluminum collar shown in Fig. 16.

8. Mount detector on phototube with Dow-Corning 200 Silicone fluid.

9. Place phototube in preamplifier housing.

APPENDIX B

Energy Units

In the Beta Decay section of Chapter II reference was made to β energies measured in relativistic (rest mass) units. This unit is somewhat more convenient than Mev (million electron volt) units when spectra are to be corrected for forbiddenness.

The above units are related by the following equation.

$$W = \frac{E}{mc^2} + 1 \qquad (8)$$

where W is energy in relativistic units, E is energy in Mev, and mc^2 is the rest mass of the electron (0.5109 Mev). Using Figure 67 the two units may be interchanged easily.

Mev	Relativistic Units
0	1
0.5-	-2
1.0-	-3
1.5-	-4
2.0-	-5
2.5-	-6
3.0-	-7
3.5-	-8
4.0-	-9

Figure 67. Relation Between Mev and Relativistic Units

BIBLIOGRAPHY

1. Aebersold, P. C., International Conference on Peaceful Uses of Atomic Energy, Geneva, Paper 308 (USA) (1955). Importance of isotopes in technology and industry.

2. Aebersold, P. C., Rupp, A. F., Nucleonics 10, No. 1, 24-7 (1952). Radioisotope production in the United States.

3. Ageno, M., Nuovo cimento (9) 1, 33-40 (1943). Radioattivita provocata nello zirconio da bombardamento di neutroni veloci.

4. Ames, D. P., Bunker, M. W., Starner, J. W., U. S. Atomic Energy Commission, reported in Los Alamos Scientific Laboratory Classified Report WASH-75 (January 1952).

5. Aron, W. A., Hoffman, B. G., Williams, F. C., U.S. Atomic Energy Commission, Rept. AECU-663 (May 1951). Range-energy curves.

6. Aten, Jr., A. H. W., DeFeyfer, G. D., Sterk, M. J., and Wapstra, A. H., Physica 21, 740 (1955). The isomers of Os^{190} and Ir^{190}.

7. Beaufait, Jr., L. J., Lukens, Jr., H. R., U.S. Atomic Energy Commission, Rept. NP-5056 (May 1953). Handbook of radiochemical analysis. Radiochemical techniques.

8. Behrens, D. J., Brit. Atomic Energy Research Establishment, Rept. AERE-T/R-629 (January 1951). Some notes on the nature of experiments, on the statistics of counting, and on the fitting of exponential decay curves to the results of counting experiments.

9. Bernard, R., Davoine, F., Hirtz, J., Compt. rend. 232, 1826-8 (1951). Etudes de couches minces adsorbées au moyen d'éléments traceurs radioactifs.

10. Bernstein, W., Chase, R. L., Schardt, A. W., Rev. Sci. Instr. 24, 437-44 (1953). Gray wedge pulse-height analysis.

11. Birks, J. B., "Scintillation Counters," McGraw-Hill, New York, 1953.

12. Blatt, J. M., Weisskopf, V. F., "Theoretical Nuclear Physics," Wiley, New York 1952.

13. Bleuler, E., Goldsmith, G. J., "Experimental Nucleonics," Rinehart, New York, 1952.

14. Bohr, N., Nature 137, 344-8 (1936). Neutron capture and nuclear constitution.

15. Bohr, N., Wheeler, J. A., Phys. Rev. 56, 426-50 (1939). The mechanism of nuclear fission.

16. Born, H. J., Seelman-Eggebert, W., Naturwissenschaften 31, 201-2 (1943). Die Maximalenergien der Beta-Strahlen einiger bei der Uranspaltung entstehender Isotope.

17. Bracewell, R. N., J. Opt. Soc. Amer. 45, 873-6 (1955). Simple graphical method for correcting for instrumental broadening.

18. Brookhaven National Laboratory, U.S. Atomic Energy Commission, Rept. BNL-364 (AS-9) (July 1955). Annual report.

19. Butement, F. D. S., Poe, A. J., Phil. Mag. 45, 31 (1954). Radioactivity of neutron excess iridium isotopes.

20. Cassatt, W. A., Ph.D. Thesis, University of Michigan, 1954. Decay scheme and characterization study of radioactive products of deuteron reactions. (Also AECU-2958)

21. Cassatt, W. A., Meinke, W. W., Phys, Revs. 99, 760 (1955). Decay Scheme of Y^{92}.

22. Chase, R. L., U.S. Atomic Energy Commission, Rept. BNL-263 (T-42) (April 1954). Coincidence gray wedge pulse height analyzer BNL Model EH1-501.

23. Christian, D., Mitchell, R., Martin, Jr., D., Phys. Revs. 86, 946 (1952). Radioactivities of Pt and Ir from photonuclear reactions in platinum.

24. Chenz, et al., Phys. Rev. 90, 886 (1953). The disintegration of Sc^{47}.

25. Chu, T., Phys. Rev. 79, 582 (1950). New radioactive isotopes of iridium.

26. Cook, Jr., T. B., U.S. Atomic Energy Commission, Rept. AECU-1598 (July 1951). The scintillation spectrometer as a means of measuring conversion coefficients.

27. Cork, J. M., et al., Phys. Rev. 92, 367 (1953). The radioactive decay of calcium 47.

28. Cornell, R. G., U.S. Atomic Energy Commission, Rept. ORNL-2120 (September 1956). A new estimation procedure for linear combinations of exponentials.

29. Coryell, C. D., Sugarman, N., ed., "Radiochemical Studies: The Fission Products," National Nuclear Energy Series IV, Vol. 9, McGraw-Hill, New York, 1951.

30. Ibid., p. 660-2.

31. Ibid., p. 1410-16.

32. Curran, S. C., "Luminescence and the Scintillation Counter," Academic Press, New York, 1953.

33. Demichelis, F., Malvano, R., Nuovo cimento (9) 11, 49-52 (1954). Discriminatore differenziale oscillografico e sua applicazione nei circuiti a coincidenza.

34. Deming, W. E., "Statistical Adjustment of Data," Wiley, New York, 1946.

35. DerMateosian, E., Goldhaber, M., Phys. Rev. 82, 115-6 (1951). Measurement of isomeric transition energies with a scintillation spectrometer.

36. Dhar, S., Indian J. Phys. 29, 329-51 (1955). On the energy response and resolution of a scintillation counter.

37. Dunworth, J. V., Rev. Sci. Instr. 11, 167 (1940). The application of the method of coincidence counting to experiments in nuclear physics.

38. Faltings, V., Angew. Chem. 64, 605-6 (1952). Eine Anwendung der natürlichen ^{14}C-Aktivität in der Lebensmittelchemie.

39. Feenberg, E., Hammack, K. C., Phys. Rev. 75, 332 (1949). An interpretation of nuclear shell structure.

40. Feenberg, E., Hammack, K. C., Phys. Rev. 75, 1877-1893 (1949). Nuclear shell structure.

41. Feenberg, E., Trigg, G., Revs. Modern Phys. 22, 399-406 (1950). The interpretation of comparative half-lives in the Fermi theory of beta-decay.

42. Filon, L. N. G., Proc. Roy. Soc. Edin. 49, 38 (1928-29). On a quadrature formula for trigometric integrals.

43. Finston, H. G., "Radiochemical Separations Compilation," Atomic Energy Commission, National Research Council, and Brookhaven National Laboratory, 1954.

44. Flanary, J. R., Culler, F. L., International Conference on Peaceful Uses of Atomic Energy, Geneva, Paper 539 (USA) (1955). Solvent extraction separation of uranium and plutonium from fission products.

45. Freedman, M. S. et al., Rev. Sci. Instr. 27, 716 (1956). Correction for phosphor backscattering in electron scintillation spectrometry.

46. Friedlander, G., Kennedy, J. W., "Introduction to Radiochemistry," Wiley, New York, 1949.

47. Götte, H., Naturwissenschaften 29, 496-500 (1941). Neue bei der Uranspaltung auftretende Strontium- und Yittrium-Isotope.

48. Griffith, G. L., Phys. Rev. 103, 643-5 (1956). First excited states in Zr^{92} and Zr^{94}.

49. Grodzins, L., Rev. Sci. Instr. 26, 1208-9 (1955). Coincidence sorter for scintillation spectrometers.

50. Gardner, D. G.,Meinke, W. W., "Decay Scheme of Co^{62}," to be published.

51. Hall, K. L., Ph.D. Thesis, University of Michigan, 1955. Determination of (d, alpha) reaction cross sections. (Also AECU-e126).

52. Halliday, D., "Introductory Nuclear Physics," Wiley, New York, 1955.

53. Hartree, D. R., "Numerical Analysis," Clarendon Press, Oxford, 1952.

54. Hayward, R. W., Hoppes, D. D., Ernst, H., Phys. Rev. 98, 231 (1955). Disintegration of niobium-91 and -92.

55. Hendricks, S. B., Dean, L. A., Ann. Rev. Nuclear Sci. 1, 597-610 (1952). Radioisotopes in soils research and plant nutrition.

56. Heusinkveld, M., Freier, G., Phys. Rev. 85, 80-4 (1952). The production of polarized protons and the inversion of energy levels of the P 1/2 - P 3/2 doublet in Li^5.

57. Hicks, H. G., Gilbert, R. S., Stevenson, P. C., Hutchin, W. H., U.S. Atomic Energy Commission, Rept. LRL-65 (December 1953). The qualitative anionic behavior of a number of metals with an ion exchange resin, "Dowex 2."

58. Hildebrand, F. B., "Introduction to Numerical Analysis," McGraw-Hill, New York, 1956.

59. Hill, D. L., Wheeler, J. A., Phys. Rev. 89, 1102-45 (1953). Nuclear constitution and the interpretation of fission phenomena.

60. Hollander, J. M., Perlman, I., Seaborg, G. T., Revs. Modern Phys. 25, 469-73 (1953). Table of isotopes.

61. Householder, A. S., "Analyzing Exponential Decay Curves," Seminar in Scientific Computation, Nov. 1949 .

62. Householder, A. S., U.S. Atomic Energy Commission, Rept. ORNL-455 (February 1950). On Prony's method of fitting exponential decay curves and multiple-hit survival curves.

63. Hunt, W. A., Zaffarano, D. J., U.S. Atomic Energy Commission, Rept. ISC-469 (March 1954). Radioactive disintegration spectra of some short-lived nuclides.

64. Irvine, Jr,, J. W., Nucleonics 3, No. 2, 5-17 (1948). Production of radionuclides.

65. Jahnke, E., Emde, F., "Tables of Functions with Formulae and Curves," Dover Publications, New York, 1943.

66. James, R. A., Phys. Rev. 93, 288-90 (1954). Excitation functions of proton-induced reactions of Nb^{93}*.

67. Johansson, S.A.E., U.S. Atomic Energy Commission, Rept. ISC-431 (December 1953). A coincidence scintillation spectrometer.

68. Johns, M. W., and Nablo, W. V., Phys. Revs. 96, 1599 (1954). Disintegration of Ir^{192} and Ir^{194}.

69. Jordan, W. H., Ann. Rev. Nuclear Sci. 1, 207-44 (1952). Detection of nuclear particles.

70. Katcoff, S., Miskel, J. A., Stanley, C. W., Phys. Rev. 74, 631-38 (1948). Ranges in air and mass identification of plutonium fission fragments.

71. Ketelle, B. H., Phys. Rev. 80, 758 (1950). The Ca^{45} beta-distribution obtained in a split crystal scintillation spectrometer.

72. Kleinberg, J., et al., U.S. Atomic Energy Commission, Rept. LA-1566 (February 1953). Collected radiochemical procedures.

73. Kleinberg, J., et al., U.S. Atomic Energy Commission, Rept. LA-1721 (September 1954). Collected radiochemical procedures.

74. Kohl, J., Chem. Eng. Progr. 48, 611-6 (1952). Radioisotopes in progress instrumentation.

75. Konopinski, E. J., Langer, L. M., Ann. Rev. Nuclear Sci. 2, 261-304 (1953). The experimental clarification of the theory of beta-decay.

76. Kraus, K. A., Nelson, F., International Conference on Peaceful Uses of Atomic Energy, Geneva, Paper 837 (USA) (1955). Anion exchange of studies of fission products.

77. Kraus, K. A., Moore, G. E., J. Am. Chem. Soc., 75, 1460 (1953). Ion exchange studies Vi. The Divalent transition elements manganese to zinc in hydrochloric acid.

78. Kraus, A. K., Nelson, F., Smith, G. W., J. Phys. Chem. 58, 11 (1954). Ion exchange studies IX. Absorbability of a number of metals in hydrochloric acid solutions.

79. Kraushaar, Brun, Meyerhof, private communication to K. Way in June, 1955. See reference 144, page 80.

80. Kurie, F. N. D., Richardson, J. R., Paxton, H. C., Phys. Rev. 49, 368-81 (1936). The radiations emitted from artifically produced radioactive substances. The upper limits and shapes of the beta-ray spectra from several elements.

81. Lidofsky, L. J., et al. Bull. Am. Phys. Soc. 30, #3 (Washington), 1953.

82. Lidofsky, L. J., et al., Phys. Rev. 104, 759 (1956). Isobaric level structure for A = 47.

83. MacGregor, M. H., Ph.D. Thesis, University of Michigan, 1953. The decay of rubidium 87.

84. Maeder, D., Helv. Phys. Acta 20, 139-52 (1947). Elektronenröhren-Spektrograph zur Messung von Ionisationskammerimpulsen.

85. Mandeville, C. E., Schert, M. V., Nucleonics, 3, 2 (1948). Nuclear disintegration schemes and the coincidence method.

86. Margenau, H., Murphy, G. M., "The Mathematics of Physics and Chemistry," Van Nostrand, New York, 1956.

87. Marguez, L., Phys. Rev. 92, 1511 (1953). Disintegration of Ca^{47}, Sc^{47}, V^{48}, and Rh^{100}.

88. Mayer, M. G., Phys. Rev. 74, 235-39 (1948). On closed shells in nuclei.

89. Mayer, M. G., Phys. Rev. 75, 1969-70 (1949). On closed shells in nuclei.

90. Mayer, M. G., Phys. Rev. 78, 16-23 (1950). Nuclear configurations in the spin-orbit coupling model, empirical evidence.

91. Mayer, M. G., Jensen, J. H. D., "Elementary Theory of Nuclear Shell Structure," Wiley, New York, 1955.

92. McLaughlin, P. W., O'Kelly, G. D., U.S. Atomic Energy Commission, Rept. MTA-40 (September 1953). Counting efficiencies for sodium iodide crystals.

93. Meinke, W. W., U.S. Atomic Energy Commission, Rept. AECD-2738, UCRL-432 (August 1949). Chemical procedures used in bombardment work at Berkeley.

94. Meinke, W. W., U.S. Atomic Energy Commission, Rept. AECD-2750 (December 1949). Chemical procedures used in bombardment work at Berkeley.

95. Meinke, W. W., Anal. Chem. 28, 736-56 (1956). Nucleonics.

96. Meinke, W. W., Anderson, R. E., Anal. Chem. 25, 778-83 (1953). Activation analysis using low level neutron sources.

97. Meinke, W. W., Cassatt, W. A., Hall, K. L., U.S. Atomic Energy Commission, Rept. AECU-2944 (June 1954). A variable field survey beta-ray spectrometer.

98. Mitchell, A. G. C., Rev. Mod. Phys. 20, 296 (1948). Use of coincidence counting methods in determining nuclear disintegration schemes.

99. National Bureau of Standards, Applied Mathematics Series 13 (1952). Tables for the analysis of beta spectra.

100. National Bureau of Standards, Applied Mathematics Series 34 (1954). Tables of the gamma function for complex arguments.

101. National Bureau of Standards Circular No. 499, U.S. Government Printing Office, Wash., D.C. 1950. Nuclear data including supplements and cards bringing table up to date.

102. Nordheim, L. W., Phys. Rev. 75, 1894-1901 (1949). On spins, moments, and shells in nuclei.

103. Nordheim, L. W., Revs. Modern Phys. 23, 322-7 (1951). Nuclear shell structure and beta-decay. Even A nuclei.

104. Noyes, A. A., Bray, W. C., "A System of Qualitative Analysis for the Rare Elements," The MacMillan Company, New York, 1948.

105. Nuclear Chemical Research, Progress Report 4, University of Michigan, 1955.

106. Nucleonics 8, No. 5, 5-11 (1951). Industrial utilization of fission products.

107. Nussbaum, R. H., Wapstra, A. H., VanLieshout, R., Nijgh, G. J., Ornstein, L. Th. M., Physica 20, 571-2 (1954). On the decay of ^{62}Zn, ^{62}Cu and ^{62}Co.

108. Oak Ridge National Laboratory, U.S. Atomic Energy Commission, Rept. ORNL-940 (December 1950). Physics division quarterly progress report.

109. Oak Ridge National Laboratory, U.S. Atomic Energy Commission, Rept. ORNL-1092 (June 1951 , Physics division quarterly progress report.

110. Oak Ridge National Laboratory, U.S. Atomic Energy Commission, Rept. ORNL-1159 (July 1951). Instrumental research and development quarterly progress report.

111. O'Kelly, G. D., Lazar, N. H., Eichler, E., Phys. Rev. 101, 1059-63 (1956). Decay chain Ca^{49}-Sc^{49}-Ti^{49}.

112. Owen, G. E., and Primakoff, H., Phys. Rev. 74, 1406 (1948). Relation between apparent shapes of monoenergetic conversion lines and of continuous β-spectra in a magnetic spectrometer.

113. Palmer, J. P., Laslett, L. J., U.S. Atomic Energy Commission, Rept. AECU-1220 (March 1951). Beta-ray spectrometry with an anthracene scintillation spectrometer.

114. Parmley, T. J., Moyer, B. J., Lilly, R. C., Phys. Rev. 75, 619-23 (1949). The radioactivities of some high mass isotopes of cobalt.

115. Perlis, A. J., U.S. Atomic Energy Commission Rept. NP-786 (September 16, 1948). Numerical solution of linear integral equations.

116. Putnam, J. L., International Conference on Peaceful Uses of Atomic Energy, Geneva, Paper 463 (UK) (1955). Development in thickness gauges and allied instruments.

117. Rapp, K., Wallack, S., Moos, A. M., U.S. Atomic Energy Commission, Rept. NYO-685, Pt. I and II (July 1950).

118. Rose, M. E., Science 118, 635-42 (1953). Angular correlation of nuclear radiations.

119. Rose, M. E., Goertzel, G. H., Perry, C. L., U.S. Atomic Energy Commission, Rept. ORNL-1023 (June 1951). K-shell internal conversion coefficients; revised tables.

120. Sagane, R., Kojima, S., Miyamoto, G., Ikawa, M., Phys. Rev. 57, 1179-80 (1940). Artificial radioactivity induced in zirconium and molybdenum.

121. Scarborough, J. B., "Numerical Mathematical Analysis," John Hopkins Press, Baltimore, 1950, p. 460.

122. Schardt, A. W., U.S. Atomic Energy Commission, Rept. BNL-237 (T-37) (January 1954). Gray wedge pulse height analysis.

123. Scharff-Goldhaber, G., Phys. Rev. 90, 587-602 (1953). Excited states of even-even nuclei.

124. Schott, G. L., Meinke, W. W., Phys. Rev. 89, 1156-7 (1953). Assignment of Y^{92} and Y^{94*}.

125. Scott, E. J., "Transform Calculus with an Introduction to Complex Variables," Harper and Brothers, New York, 1955.

126. Seelmann-Eggebert, Naturwissenschaften 31, 510 (1943). Uber einige aktive Yttrium-Isotope.

127. Shuttleworth, R., Brit. J. Appl. Phys. 4, 326-9 (1953). The use of radioactive isotopes in metallurgy.

128. Siegbahn, K., ed., "Beta- and Gamma-Ray Spectroscopy," Interscience, New York, 1-23 (1955).

129. Ibid., p. 132-64.

130. Ibid., p. 273-91.

131. Ibid., p. 314-56.

132. Ibid., p. 433-67.

133. Siri, W. E., "Isotopic Tracers and Nuclear Radiations; with Applications to Biology and Medicine," McGraw-Hill, New York, 1949.

134. Smith, W. G., and Hollander, J. M., Phys. Rev. 98, 1258 (1955). Radiochemical Study of neutron-deficient chains in the noble metal region.

135. Snedden, I. N., "Fourier Transforms," McGraw-Hill, New York, 1951.

136. Stevenson, P. C., Hicks, H. G., Ann. Rev. Nuclear Sci. 3, 221-234 (1953). Separation techniques used in radiochemistry.

137. Stotler, H. H., U.S. Atomic Energy Commission, Rept. AECU-99 (1946). Fitting in a straight line.

138. Sugarman, N., Phys. Rev. 86, 604 (1952). Meson fission of mercury.

139. Titchmarsh, E. C., "Introduction to the Theory of Fourier Integrals," Clarendon Press, Oxford (1937).

140. Titchmarsh, E. C., "The Theory of Functions," Oxford University Press, London, 1939.

141. Tranter, C. J., "Integral Transforms in Mathematical Physics," Wiley, New York, 1956.

142. Von Kármán, T., Biot, M. A., "Mathematical Methods in Engineering," McGraw-Hill, New York, 1940.

143. Wahl, A. C., Bonner, N. A., "Radioactivity Applied to Chemistry," Wiley, New York, 1951.

144. Way, K., King, R. W., McGinnis, C. L., VanLieshout, R., U.S. Atomic Energy Commission, Rept. TID-5300 (June 1955). Nuclear level schemes A=40 - A=92.

145. Weiner, N., "The Fourier Integral and Certain of it Applications," Dover Publications, New York, 1951.

146. Whittaker, E. T., Watson, G. N., "A Course in Modern Analysis," Macmillan, New York, 1943.

147. Wiedenbeck, M. L., and Chu, K. Y., Phys. Rev. 72, 1164 (1947). Coincidence measurements. Part I, beta spectra; Part II, internal conversion.

148. Widder, D. V., "The Laplace Transform," Princeton University Press, Princeton, 1946.

149. Wilson, H. A., Phys. Rev. 77, 516-20 (1950). The spherical shell nuclear model.

150. Worthing, A. G., Geffner, J., "Treatment of Experimental Data," Wiley, New York, 1943.

151. Youden, W. J., "Statistical Methods for Chemists," Wiley, New York, 1951.